

ISSN 2312-4334

MINISTRY OF EDUCATION AND SCIENCE OF UKRAINE

East European Journal of Physics

No 1. 2021

2021

East European Journal of Physics

EEJP is an international peer-reviewed journal devoted to experimental and theoretical research on the nuclear physics, cosmic rays and particles, high-energy physics, solid state physics, plasma physics, physics of charged particle beams, plasma electronics, radiation materials science, physics of thin films, condensed matter physics, functional materials and coatings, medical physics and physical technologies in an interdisciplinary context.

Published quarterly in hard copy and online by V.N. Karazin Kharkiv National University Publishing.
ISSN 2312-4334 (Print), ISSN 2312-4539 (Online)

The editorial policy is to maintain the quality of published papers at the highest level by strict peer review.

Approved for publication by the Academic Council of the V.N. Karazin Kharkiv National University (February 22, 2021; Protocol No. 3).
EEJP registered by the order of Ministry of Education and Science of Ukraine No. 1643 of 28.12.2019, and included in the list of scientific specialized editions of Ukraine (category "A", speciality: 104, 105), which can be published results of dissertations for the Ph. D. and Dr. Sci. degree in physical and mathematical sciences.

The Journal is part of the Web of Science Core Collection (ESCI) scientometric platform and indexed by SCOPUS.

Editor-in-Chief

Azarenkov N.A., *V.N. Karazin Kharkiv National University, Kharkiv, Ukraine*

Deputy editor

Girka I.O., *V.N. Karazin Kharkiv National University, Kharkiv, Ukraine*

Executive Secretary

Hirnyk S.A., *V.N. Karazin Kharkiv National University, Kharkiv, Ukraine*

Editorial Board

Adamenko I.N., *V.N. Karazin Kharkiv National University, Ukraine*

Akulov V.P., *City University of New York, USA*

Antonov A.N., *Institute of Nuclear Research and Nuclear Energy, Sofia, Bulgaria*

Barannik E.A., *V.N. Karazin Kharkiv National University, Ukraine*

Beresnev V.M., *V.N. Karazin Kharkiv National University, Ukraine*

Berezhnuy Yu.A., *V.N. Karazin Kharkiv National University, Ukraine*

Bizyukov A.A., *V.N. Karazin Kharkiv National University, Ukraine*

Bragina L.L., *STU Kharkiv Polytechnical Institute, Ukraine*

Broda B., *University of Lodz, Poland*

Dovbnya A.M., *NSC Kharkiv Institute of Physics and Technology, Ukraine*

Dragovich B.G., *University of Belgrade, Serbia*

Duplij S.A., *Center for Information Technology (ZIV), Westfälische Wilhelms-Universität Münster, Münster, Germany*

Garkusha I.E., *NSC Kharkiv Institute of Physics and Technology, Ukraine*

Gofman Yu., *Jerusalem College of Technology, Israel*

Grekov D.L., *NSC Kharkiv Institute of Physics and Technology, Ukraine*

Karnaukhov I.M., *NSC Kharkiv Institute of Physics and Technology, Ukraine*

Kondratenko A.N., *V.N. Karazin Kharkiv National University, Ukraine*

Korchin A.Yu., *NSC Kharkiv Institute of Physics and Technology, Ukraine*

Krivoruchenko M.I., *Institute for Theoretical and Experimental Physics, Moscow, Russia*

Lazurik V.T., *V.N. Karazin Kharkiv National University, Ukraine*

Mel'nik V.N., *Institute of Radio Astronomy, Kharkiv, Ukraine*

Merenkov N.P., *NSC Kharkiv Institute of Physics and Technology, Ukraine*

Neklyudov I.M., *NSC Kharkiv Institute of Physics and Technology, Ukraine*

Noterdaeme J.-M., *Max Planck Institute for Plasma Physics, Garching, Germany*

Nurmagambetov A.Yu., *NSC Kharkiv Institute of Physics and Technology, Ukraine*

Onyschenko I.M., *NSC Kharkiv Institute of Physics and Technology, Ukraine*

Ostrikov K.N., *Plasma Nanoscience Centre Australia, Clayton, Australia*

Peletminsky S.V., *NSC Kharkiv Institute of Physics and Technology, Ukraine*

Pilipenko N.N., *NSC Kharkiv Institute of Physics and Technology, Ukraine*

Radinschi I., *Gheorghe Asachi Technical University, Iasi, Romania*

Slyusarenko Yu.V., *NSC Kharkiv Institute of Physics and Technology, Ukraine*

Smolyakov A.I., *University of Saskatchewan, Saskatoon, Canada*

Shul'ga N.F., *NSC Kharkiv Institute of Physics and Technology, Ukraine*

Tkachenko V.I., *NSC Kharkiv Institute of Physics and Technology, Ukraine*

Voyevodin V.M., *NSC Kharkiv Institute of Physics and Technology, Ukraine*

Yegorov O.M., *NSC Kharkiv Institute of Physics and Technology, Ukraine*

Editorial office

Department of Physics and Technologies, V.N. Karazin Kharkiv National University

Kurchatov av., 31, office 402, Kharkiv, 61108, Ukraine

Tel: +38-057-335-18-33,

E-mail: eejp@karazin.ua,

Web-pages: <http://periodicals.karazin.ua/eejp> (Open Journal System)

Certificate of State registration No.20644-10464P, 21.02.2014

ORIGINAL PAPERS

- How the Limit Values Work** 5
Yuri L. Bolotin, Vladimir V. Yanovsky
Як працюють граничні значення
Ю.Л. Болотін, В.В. Яновський
- Modelling of Nonlinear Thermodiffusion for a Spherically Symmetric Case** 13
Arvydas J. Janavičius, Sigita Turskienė
Модельовання нелінійної термодифузії для сферично-симетричного випадку
Арвідас Янавичюс, Сігіта Турскене
- Studies of Dosimetry Protocols for Accelerated Photons and Electrons Delivered from Medical Linear Accelerator** 20
A.K.M. Moinul Haque Meaze, Santunu Purohit, Md. Shakilur Rahman, Abdus Sattar, S.M. Enamul Kabir, Md. Kawchar Ahmed Patwary, Kamrunnahar Kali, Md. Jubayer Rahman Akhand
Дослідження протоколів дозиметрії для прискорених фотонів та електронів, медичного лінійного прискорювача
А.К.М. Мойнул Хак Миз, Сантуну Пурохит, М. Шакилур Рахман, Абдус Саттар, С.М. Энамул Кабир, М. Кавчар Ахмед Патвари, Камруннахар Кали, М. Джубайер Рахман Акханд
- Investigation on Electronic and Thermoelectric Properties of (P, As, Sb) Doped ZrCoBi** 27
Djelti Radouan, Besbes Anissa, Bestani Benaouda
Дослідження електронних термоелектричних властивостей ZrCoBi легованого (P, As, Sb)
Джелті Радуан, Бесбес Аніса, Бестані Бенауда
- Electrical and Photoelectric Properties of Heterojunctions MoOx/n-Cd1-xZnxTe** 34
Mukhailo M. Solovan, Andrii I. Mostovyi, Hryhorii P. Parkhomenko, Viktor V. Brus, Pavlo D. Maryanchuk
Електричні та фотоелектричні властивості гетеропереходів MoOx/n-Cd1-xZnxTe
М.М. Солован, А.І. Мостовий, Г.П. Пархоменко, В.В. Брус, П.Д. Мар'ячук
- Elastic Properties of Alloy ZE10 Sheets Evaluation by Kerns Texture Parameters** 43
Valentin Usov, Natalia Shkatulyak, Elena Savchuk, Nadezhda Rybak
Оцінка пружних властивостей листів сплаву ZE10 за параметрами текстури кернса
Валентин Усов, Наталя Шкатуляк, Олена Савчук, Надія Рибак
- Surface Purity Effect on Irregularities of Changes in Deformation Texture of Zr-2.5% Nb Alloy** 50
Dmitry G. Malykhin, Kostiantyn V. Kovtun, Tetiana S. Yurkova, Viktor M. Grytsyna, Gennadiy P. Kovtun, Iryna G. Tantsura, Volodymyr D. Virych, Yuri V. Gorbenko, Victor M. Voyevodin
Ефект чистоти поверхні у нерегулярностях змін текстури деформації сплаву Zr-2.5%Nb
Д.Г. Малыхин, К.В. Ковтун, Т.С. Юркова, В.М. Грицина, Г.П. Ковтун, І.Г. Танцюра, В.Д. Вірич, Ю.В. Горбенко, В.М. Воєводін
- Zone Recrystallization of Zirconium and Hafnium** 55
Oleh E. Kozhevnikov, Mykola M. Pylypenko, Maryna F. Kozhevnikova
Зонна перекристалізація цирконію та гафнію
О.Є. Кожевніков, М.М. Пилипенко, М.Ф. Кожевнікова
- Structure and Properties of ZnSnP2 with the Application in Photovoltaic Devices by Using CdS and ZnTe Buffer Layers** 63
Neeraj, Ajay S. Verma
Структура і властивості ZnSnP2 для застосування в фотоелектричних пристроях з використанням буферних шарів на основі CdS і ZnTe
Нирадж, Аджай С. Верма
- Optoelectronic Properties of Ternary Tetrahedral Semiconductors** 80
Rajesh C. Gupta, Ajay S. Verma, Khushvant Singh
Оптоелектронні властивості потрійних тетраедричних напівпровідників
Раджеш С. Гупта, Аджай С. Верма, Хушвант Сінгх

Empirical Relation for Electronic and Optical Properties of Binary Tetrahedral Semiconductors 89

Rajesh C. Gupta, Khushvant Singh, Ajay S. Verma

*Емпіричне співвідношення електронних та оптичних властивостей бінарних тетраедричних напівпровідників
Раджеш С. Гупта, Хушвант Сінгх, Аджай С. Верма*

**Study of Structural and Electronic Properties of Intercalated Transition Metal Dichalcogenides
Compound MTiS₂ (M = Cr, Mn, Fe) by Density Functional Theory** 93

Vandana B. Parmar, Aditya M. Vora

*Вивчення структурних і електронних властивостей інтеркальованих перехідних металевих дихалкогенідних
компундів MTiS₂ (M = Cr, Mn, Fe) за допомогою теорії функціональної щільності
Вандана Б. Пармар, Адітья М. Вора*

Plasma Chemical Method of Decreasing the Ethylene Impurities in the Air 99

Leonid M. Zavada, Dmytro V. Kudin

*Плазмохімічний метод зменшення домішки етилену у повітрі
Л.М. Завада, Д.В. Кудін*

HISTORY OF SCIENCE

Oleksiy Hryhorovych Sytenko: Manager, Scientist, Citizen 104

Alla Tanshina

*Олексій Григорович Ситенко: керівник, учений, громадянин
Алла Таньшина*

PACS: 04.70.Dy, 98.80.-k

HOW THE LIMIT VALUES WORK

 Yuri L. Bolotin^a,  Vladimir V. Yanovsky^{b,c,*}

^aNational Science Center "Kharkov Institute of Physics and Technology", 1, Akademicheskaya str., 61108, Kharkiv, Ukraine

^bInstitute for Single Crystals, NAS Ukraine, 60 Nauky Ave., Kharkiv, 61001, Ukraine

^cV.N. Karazin Kharkiv National University, 4 Svobody Sq., Kharkiv, 61022, Ukraine

*Corresponding Author: yanovsky@isc.kharkov.ua, tel. +380-97-614-28-13

Received November 4, 2020; accepted December 15, 2020

The efficiency of limiting quantities as a tool for describing physics at various spatio-temporal scales is shown. Due to its universality, limit values allow us to establish relationships between, at first glance, distant from each other's characteristics. The article discusses specific examples of the use of limit values to establish such relationships between quantities at different scales. Based on the principle of reaching the limiting values on the event horizons, a connection was obtained between the Planck values and the values of the Universe. The resulting relation can be attributed to relations of the Dirac type - the coincidence of large numbers that emerged from empirical observations. In the article, the relationships between large numbers of the Dirac type are established proceeding, in a certain sense, from physical principles - the existence of limiting values. It is shown that this ratio is observed throughout the evolution of the Universe. An alternative way of solving the problem of the cosmological constant using limiting values and its relation to the minimum spatial scale is discussed. In addition, a one-parameter family of masses was introduced, including the mass of the Universe, the Planck mass and the mass of the graviton, which also establish relationships between quantities differing by 120 orders of magnitude. It is shown that entropic forces also obey the same universal limiting constraints as ordinary forces. Thus, the existence of limiting values extends to informational limitations in the Universe. It is fundamentally important that on any event horizon, regardless of its scale (i.e., its gravitational radius), the universal value of limit force $c^4 / 4G$ is realized. This allows you to relate the characteristics of the Universe related to various stages of its evolution.

KEYWORDS: black hole, event horizon, entropy, limit values

The observed Universe represents a hierarchy of structures with a gigantic spread of characteristic parameters (sizes, energies) from Planck to cosmological. The search for the mysterious connection between large and small scales that describe the world around us is an exciting game of chance. "Random" coincidences caused a storm of enthusiasm and the illusion of unraveling the innermost secrets of nature. The roots of the game go back to antiquity. The first "number theory" - Kabbalah denied the possibility of random coincidences, considering numbers to be a symbol of the spiritual nature of things.

A new era in "physical numerology" began in the first half of the twentieth century, when the characteristic sizes of macro (Universe) and micro (atom, electron) objects became known. The greats entered the game: Weyl [1], Edington [2], Dirac [3].

Already in 1923, in an appendix to his book, "Space, Time, Matter", G. Weyl estimated the ratio of the radius of the Universe to the classical radius of an electron as $\sim 10^{40}$. As he writes, this suggests that the enormous numerical value of the constant is related to the difference in the sizes of the Universe and the electron. P. Dirac belongs to the observation that in the hydrogen atom the ratio of electric to gravitational forces is close to the ratio of the size of the Universe to the classical radius of the electron.

$$\frac{\text{electrical forces}(H - \text{atom})}{\text{gravitational forces}(H - \text{atom})} \approx \frac{\text{Hubble radius}}{\text{size of electron}} \quad (1)$$

No physical explanation of this result has yet been found, although it is obvious that any numerological coincidence is of interest only if it can be explained (obtained) in the framework of fundamental physical theory.

The purpose of this article is to introduce a new approach [4] to explain the relationship between different scales. We show that the so-called limit values are an effective tool for achieving this goal. Due to their universality, the limiting values make it possible to establish connections between, at first glance, distant fields of physics.

PHYSICAL MOTIVATIONS

The traditional formulation of the ultimate goal of physics (in the narrower sense of physical axiomatics) represents the derivation of physical laws from first principles. However, the search for first principles is not inferior in complexity to the original problem. An alternative way to understanding the world around us is to interpret the fundamental limit values as a factor determining the structure of physical laws. Limit values play a central role in both phenomenology and axiomatic theories. It is well known that quantum mechanics can be built on the basis of the existence of a minimum quantum of action \hbar , and the special theory of relativity - maximum speed C . From relatively recently, it became clear that a similar approach can be implemented in GR, which can be constructed by postulating the existence of a new limit value - the minimum length [5,6]

Limit values play a key role in the analysis of the measurement process in quantum mechanics. In particular, these quantities are included as parameters in the uncertainty relations, determining the permissible accuracy of measuring physical quantities.

Over the nearly century-long history of its existence, the uncertainty principle (the Heisenberg uncertainty principle (HUP)) has undergone a complex evolution related to the inclusion of gravitational interaction (generalized uncertainty principle (GUP)) and the transition to macroscopic spatial scales (extended uncertainty principle (EUP)) [7-11]

$$\begin{aligned} x\Delta p &\geq \hbar \quad (HUP) \\ \Delta x\Delta p &\geq \hbar + l_{pl}^2 \frac{\Delta p^2}{\hbar} \quad (GUP) \\ \Delta x\Delta p &\geq \hbar + l_{pl}^2 \frac{\Delta p^2}{\hbar} + \hbar \frac{\Delta x^2}{l_*^2} \quad (EUP) \end{aligned} \quad (2)$$

Here l_* is a new fundamental length scale, the value of which should be determined.

The need to modify the HUP is dictated by the fact that the HUP fails both at short and long distances. The common cause of failure is gravity: a “weak” gravitational interaction can transform into strong either at very small distances (Planck scales), or for very large masses (cosmological scales)

Probably the most important consequence of the transition from the HUP to the GUP is the appearance of a minimum spatial length

$$\Delta x_{\min} = 2\sqrt{\frac{G\hbar}{c^3}} = 2l_{pl} \quad (3)$$

and a minimum time scale

$$\Delta t_{\min} = 2\sqrt{\frac{\hbar G}{c^5}} = 2t_{pl} \quad (4)$$

GUP imposes fundamental restrictions on the accuracy $\delta l(\delta t)$ of measuring length (time) $l(t)$ regardless of the measurement method used [12-14]

$$\delta l \geq (ll_{pl}^2)^{1/3} = l_{pl} \left(\frac{l}{l_{pl}}\right)^{1/3}, \quad \delta t \geq (tt_{pl}^2)^{1/3} = t_{pl} \left(\frac{t}{t_{pl}}\right)^{1/3} \quad (5)$$

The discreteness of space-time generated by the existence of a minimum length and a minimum time is inextricably linked with the concept of an event horizon. The appearance of singularities in the theory is considered to be the first signal that the theory has gone beyond its applicability and needs to be modernized. A natural variant of such modernization is to take into account effects that have fallen from consideration, which allows us to hope (although hopes are not always justified) to make the theory free of divergences. There is also an alternative point of view, formulated by R. Penrose [15] in the form of the principle of cosmic censorship: "Nature has an aversion to naked singularity." According to this principle, the singularities of space-time appear in places that, like the inner regions of black holes, are hidden from the observer. The natural question: is it possible to generalize the principle of cosmic censorship to the level of the "principle of physical censorship", making it a universal physical principle? The existence of a minimum length allows an affirmative answer to this question, and the formation of an event horizon serves as a mechanism for generating a minimum length. In the simplest case, the Schwarzschild solution, the event horizon is a hypothetical sphere around the point of gravitational singularity, dividing the space into two causally unrelated areas. Gravitational radius - the radius of this sphere for a body of mass m

$$r_g = \frac{2mG}{c^2} \quad (6)$$

Now consider the GUP structure

$$\Delta x \geq \frac{\hbar}{\Delta p} + l_{pl}^2 \frac{\Delta p}{\hbar} \quad (7)$$

The right-hand side of this relation represents the sum of two length scales: the wavelength of the observer particle (photon, electron) $\frac{\hbar}{\Delta p}$ and its effective gravitational radius $r_g = \frac{m^*G}{c^2}$, where $m^* = E/c^2$ (E is the energy of the observer particle). Such a GUP structure suggests that quantum mechanics and gravity generate two fundamental boundaries for measurement of length: the Compton wavelength $\lambda_c = \frac{\hbar}{mc}$ and the gravitational radius corresponding to this mass, and

$$\frac{r_g}{\lambda_c} = \left(\frac{m}{m_{pl}}\right)^2 \quad (8)$$

In the macrocosm $m \gg m_{pl}$, the Compton wavelength is much smaller than the gravitational radius, which determines the ultimate accuracy in measuring the length. For the Sun $\lambda_c \approx 10^{-73} m$, $r_g \approx 3km$. In the microcosm $m \ll m_{pl}$ we are faced with the opposite situation. For the proton $\lambda_c \approx 10^{-17} m$, $r_g \approx 10^{-54} m$.

An important consequence of GUP is the appearance on the physical scene of a whole set of limit values: minimum length, minimum time, maximum force, maximum power. Consider the nature of the last two quantities. This will help to better understand the role of the event horizon as the boundary of the observed physical reality.

The assertion of the existence of a maximum (limit) force in the framework of GR as a principle was first formulated by G. Gibbons [16]. This force is equal to

$$F_{max} = \frac{c^4}{4G} \approx 3.25 \times 10^{43} N \tag{9}$$

The limit does not depend on the nature of the forces and is satisfied for gravitational, electromagnetic, nuclear and any other forces. It is interesting to note that, up to a factor of 2π , the reciprocal of the ultimate force coincides with the coefficient in front of the pulse energy tensor in the field equations of GR.

The statement about the existence of maximum power is absolutely equivalent to this.

$$P_{max} = \frac{c^5}{4G} \approx 9.07 \times 10^{51} W \tag{10}$$

Both of these quantities are components of a 4-vector $F^\eta = \frac{dp^\eta}{dt}$. Maximum force and maximum power are invariants: this follows from the invariance of the quantities c and G . The dependence on time, generally speaking, is not excluded.

Note that the above statements are valid only in space-time dimension $N + 1$ for $N = 3$ [17]. For $N > 3$ maximum force increases with mass as $M^{\frac{N-3}{N-2}}$. As a result, such spatial dimensions allow unlimited gravitational forces. Lack of horizon leads to naked singularities can arise in more than three dimensions

COSMOLOGICAL APPLICATIONS

The surfaces on which the maximum force (maximum momentum flux) or maximum power (maximum energy flux) is realized are event horizons. Any attempt to exceed the force limit creates a horizon that prevents a further increase in force.

It is fundamentally important that on any event horizon, regardless of its scale (i.e., its gravitational radius), maximum force c^4 / G is realized. Therefore, for the Planck and current cosmological horizons

$$G \frac{m_{pl}^2}{l_{pl}^2} \approx G \frac{M_U^2}{R_U^2} \rightarrow \frac{m_{pl}}{l_{pl}} \approx \frac{M_U}{R_U} \tag{11}$$

Here $M_U \approx 10^{52} kg$ is the mass of the observable Universe, and $R_U = R_H = cH_0^{-1} \approx 10^{26} m$ is the current Hubble radius. This relation is performed no worse (1).

The accuracy of relation (11) depends on how close the radius of the observable Universe R_U is to the radius of the event horizon of mass M_U . In fact, since $\frac{m_{pl}}{l_{pl}} = \frac{c^2}{G}$, it is necessary for (11) to satisfy. $R_U \approx \frac{M_U G_U}{c^2}$. To evaluate the fulfillment of this approximate equality, we use the first Friedmann equation

$$\begin{aligned} H^2 &= \frac{8\pi G}{3} \rho \rightarrow \rho = \frac{3H^2}{8\pi G}; \\ M_{Uv} &= \frac{4\pi}{3} R_H^3 \frac{3H^2}{8\pi G} = \frac{c^2 R_H}{2G}; \\ R_U = R_H &= \frac{2GM_U}{c^2} = r_g \end{aligned} \tag{12}$$

We now consider the asymptotic behavior of the relation $\frac{m_{pl}}{l_{pl}} \approx \frac{M}{R}$ in the framework of SCM for $t \rightarrow \infty$. In this limit

$$\begin{aligned} M_U &= \frac{4}{3} \pi R_H^3 \rho_\Lambda, \quad \rho_\Lambda = \frac{\Lambda c^4}{8\pi G}, \\ R_H &= \frac{c}{H} = c \sqrt{\frac{3}{\Lambda c^2}} = \sqrt{\frac{3}{\Lambda}}, \end{aligned} \tag{13}$$

Hence

$$\left. \frac{M_U}{R_H} \right|_{l \rightarrow \infty} \approx \frac{c^2}{G} = \frac{m_{Pl}}{l_{Pl}} \tag{14}$$

Those, this ratio is satisfied throughout the evolution of the Universe.

Limit values can be used as an alternative way of finding a solution to the problem of the cosmological constant. For this, the condition for limiting the concentration of energy can be used, in other words, the condition for preventing the formation of an event horizon: the total energy contained in a region with a linear size L should not exceed the mass of a black hole of the same size. If the volume is filled with energy in the form of a cosmological constant, then this condition can be written in the form [18]

$$L^3 \rho_\Lambda \leq M_{BH} \sim L m_{Pl}^2 \tag{15}$$

Here ρ_Λ is the energy density in volume L^3 . If this inequality is violated, a black hole is formed with an event horizon that prevents a further increase in the energy density.

We apply inequality (15) to the Universe as a whole. In this case, it is natural to identify the IR scale with the Hubble radius H^{-1} , and ρ_Λ is understood as density of the dominant component filling the Universe, i.e. dark energy in the form of a cosmological constant. Then for the upper limit of the energy density we find

$$\rho_\Lambda \sim L^{-2} m_{Pl}^2 \sim H^2 m_{Pl}^2 \tag{16}$$

Given that

$$\begin{aligned} m_{Pl} &\approx 1.2 \times 10^{19} \text{ GeV}; \\ H_0 &\approx 1.6 \times 10^{-42} \text{ GeV} \end{aligned} \tag{17}$$

finally get

$$\rho_\Lambda \sim 10^{-46} \text{ GeV}^4 \tag{18}$$

This value is close (the difference is only two orders of magnitude and not 120) with the observed density of dark energy. Let us now try at a more fundamental level to understand what our hopes are for solving the problem of the cosmological constant along this path. If we treat the cosmological constant as the energy of zero-point oscillations of a vacuum, then

$$\begin{aligned} \rho_{vac} &= \frac{1}{2} \int_0^\infty \frac{d\vec{k}}{(2\pi)^3} \sqrt{k^2 + m^2} = \frac{1}{4\pi^2} \int_0^\infty k^2 dk \sqrt{k^2 + m^2}, \\ \rho_{vac} &\sim \frac{k_{max}^4}{16\pi^2}; k_{max} \sim M_{Pl} \rightarrow \rho_{vac} \approx 10^{74} \text{ GeV} \end{aligned} \tag{19}$$

Within the framework of this model, the only way to bring this gigantic value of the density of dark energy closer to the observed one is to reduce the value of ultraviolet cutoff k_{max} or, what is the same, to degrade the spatial resolution k_{max}^{-1} . Within the framework of the proposed approach, it seems natural to switch from cutoff $k_{max} \sim m_{Pl}$ to cutoff associated with the existence of a minimum length.

In any effective quantum field theory, defined in a spatial region with a characteristic size l and using ultraviolet cutoff k_{max} , entropy is $S \propto l^3 k_{max}^3$. According to the holographic principle [19], the cutoff value must satisfy the inequality

$$S \leq S_{BH} \approx \left(\frac{l}{l_{Pl}} \right)^2 \tag{20}$$

Consider now a size box l (IR-scale) filled with a substance with a UV-cutoff scale k_{max}^{-1} . Then the entropy of such a system $S \propto l^3 k_{max}^3$ and

$$l^3 k_{max}^3 \leq \left(\frac{l}{l_{Pl}} \right)^2 \tag{21}$$

It is natural to identify the UV- scale with a minimum uncertainty of length measurement $\delta l = k_{max}^{-1}$. In this case, the last ratio is immediately transformed into $\delta l \leq l_{Pl}^{2/3} l^{1/3}$. For $l = R_u$ we can determine the scale of UV-cutoff.

According to SCM, quantum mechanics plays a fundamental role in the early Universe, which is described by Planck units built from functional constants \hbar, c, G . In the late Universe ($z \rightarrow -1$), the evolution of the scale factor is determined by the cosmological constant, whose relative density $\Omega_\Lambda \rightarrow 1$. A “game” with fundamental constants allows a transition to a new set of Planck variables. Since a cosmological constant plays such a fundamental role in the dynamics of the

Universe, let us consider the transition from the initial set of Planck units m_{Pl}, l_{Pl}, t_{Pl} built on fundamental constants \hbar, c, G to a new set $m_\Lambda, l_\Lambda, t_\Lambda$ built on constants Λ, c, G [20]

$$\begin{aligned} m_\Lambda &= \left(\frac{\hbar_\Lambda c}{G} \right)^{1/2} = \frac{c^3}{G(8\pi\Lambda)^{1/2}} = 5.90 \times 10^{56} \text{ GeV}; \\ l_\Lambda &= \left(\frac{G\hbar_\Lambda}{c^3} \right)^{1/2} = \left(\frac{8\pi c^2}{\Lambda} \right)^{1/2} = 4.38 \times 10^{28} \text{ cm}; \\ t_\Lambda &= \left(\frac{G\hbar_\Lambda}{c^5} \right)^{1/2} = \left(\frac{8\pi}{\Lambda} \right)^{1/2} = 1.46 \times 10^{18} \text{ s} \\ \hbar_\Lambda &= \frac{8\pi c^5}{G\Lambda} \end{aligned} \tag{22}$$

The new units perfectly reproduce the mass, size and lifetime of the observed Universe, but solving the problem of the cosmological constant, they give rise to the problem of Planck constant,

$$\hbar_\Lambda = 7.35 \times 10^{122} \hbar = 7.75 \times 10^{88} \text{ J} \cdot \text{s} \tag{23}$$

All the same 120 orders! Just the difficulty is “buried” in another place, and, apparently, to solve the problem of the cosmological constant, one should look for fundamentally new approaches.

WEINBERG MASS

We now turn to the original idea of S. Weinberg [21] to take into account the influence of the dynamics of the Universe at the level of fundamental constants. To do this, he constructed the mass of a hypothetical particle, using, in addition to the fundamental constants \hbar, c, G the Hubble parameter H

$$m_w = \left(\frac{\hbar^2 H}{Gc} \right)^{1/3} \tag{24}$$

A set of constants (\hbar, c, G, H) , generally speaking, does not provide an unambiguous choice of mass. Therefore, a natural question arises: what physical considerations lead to such a choice of mass?
Surface gravity at the Hubble Horizon

$$a_g = G \frac{M_U}{R_H^2} \approx cH \tag{25}$$

"Surface" acceleration for a quantum particle of mass m and size $r = \hbar / mc$

$$a_{gp} = G \frac{m}{r^2} = \frac{Gm^3 c^2}{\hbar^2} \tag{26}$$

If the Hubble sphere represents the event horizon, and the Weinberg particle is a microscopic black hole, then $a_g = a_{gp}$ and

$$a_g = a_{gp} \rightarrow m_w = (\hbar^2 H / cG)^{1/3} \tag{27}$$

Note that in SCM $H(t \rightarrow \infty) = \sqrt{\Lambda / 3}$. Hence,

$$m_w(t \rightarrow \infty) = (\hbar^2 \sqrt{\Lambda} / \sqrt{3}cG)^{1/3} \tag{28}$$

Weinberg mass admits a curious interpretation [22]. The self-gravitational potential energy E_g of this quantum of mass m (and size its Compton wavelength \hbar / mc) is given by

$$E_g = Gm^2 / (\hbar / mc) = Gm^3 c / \hbar \tag{29}$$

Substituting (24) into (29) we obtain

$$E_g \approx H\hbar = \hbar c / R_H \tag{30}$$

Since the age of the Universe $1 / H$ which is today the maximum time and, therefore H minimum frequency, the value $E_g \approx H\hbar$ can be interpreted as a quantum of the minimum gravitational energy. At a phenomenological level, it is natural to interpret it as the minimum graviton energy.

Let us now consider in more general terms the structure of the set of parameters (\hbar, c, G, H) . The most important characteristic of this set is the dimensionless parameter

$$I \equiv \frac{c^5}{\hbar H^2 G} \approx 10^{120} \quad (31)$$

The dimensionless parameter has a simple physical meaning: he represents maximum number of gravitons in the Universe. Indeed,

$$I = \left(\frac{c^5}{G} H^{-1} \right) / \hbar H = (P_{\max} H^{-1}) / E_g \quad (32)$$

Using a parameter I , a one-parameter mass family can be constructed

$$M_\gamma = \frac{\hbar H}{c^2} \left(\frac{1}{\hbar H^2} \frac{c^5}{G} \right)^\gamma \quad (33)$$

From this relation it follows that $m_w = M_{1/3}$. Note that the Planck mass is also present in this family and corresponds to the choice: $\gamma = 1/2$, $M_{1/2} = \frac{\hbar H}{c^2} \left(\frac{1}{\hbar H^2} \frac{c^5}{G} \right)^{1/2} = \sqrt{\frac{\hbar c}{G}} = m_{pl}$.

The mass spectrum (32) contains four masses that are independent of one of the parameters of the set (\hbar, c, G, H) : the Planck mass $m_{pl} = \frac{\hbar H}{c^2} I^{1/2}$, the mass of the graviton $\frac{\hbar H}{c^2} I^0$, the mass of the Universe $M_{\gamma=1} = \frac{c^3}{HG} = \left(\frac{c^5}{G} H^{-1} \right) / c^2$ and $M_{2/5} = \left(\frac{\hbar^3 H}{G^2} \right)^{1/5}$.

THERMODYNAMIC CONSTRAINTS

Let us show now that the entropy forces [23] satisfy the same limiting restrictions as ordinary forces. Consider a particle of mass m approaching the event horizon of the black hole of the mass M ($m \ll M$). On the horizon, this particle will experience acceleration

$$a = GMm / R_{Sh}^2 m = \frac{c^4}{4GM} \quad (34)$$

Assume that the force causing the acceleration is of entropic origin. Entropic force is a macroscopic force that arises in systems with many degrees of freedom, as a consequence of the universal tendency to achieve maximum entropy. Entropic force is determined by the condition

$$F_{ent} = T \times 2\pi k_B \frac{mc}{\hbar} \quad (35)$$

Acceleration caused by this force

$$a_{ent} = T \times 2\pi k_B \frac{c}{\hbar} \quad (36)$$

Equating (34) and (36), we reproduce the well-known expression for the temperature of the black hole horizon

$$T = \frac{\hbar c^3}{8\pi G k_B M} \quad (37)$$

For entropic force, a universal constraint is retained $F \leq \frac{c^4}{4G}$. Really,

$$F_{ent} = T \times 2\pi k_B \frac{mc}{\hbar} = \frac{\hbar c^3}{8\pi G k_B M} \times 2\pi k_B \frac{mc}{\hbar} = \frac{m}{M} \frac{c^4}{4G} \quad (38)$$

Since $\frac{m}{M} < 1$ then $F_{ent} \leq \frac{c^4}{4G}$.

Consider a Schwarzschild black hole with parameters M, R . Let $R \rightarrow R + l_{\min} = R + 2l_{pl}$. Then $\Delta M = \frac{l_{pl} c^2}{G}$.

Correspondingly the change in the energy of a black hole

$$\Delta E = \Delta M c^2 = \frac{l_{pl} c^4}{G} = l_{pl} F_{\max} \quad (39)$$

The number of bits on the horizon of a black hole of radius R

$$N = \frac{4\pi R^2}{4l_{Pl}^2} = \pi \frac{R^2}{l_{Pl}^2} \quad (40)$$

Increasing the amount of information on the event horizon for $R \rightarrow R + 2l_{Pl}$,

$$\Delta N = 4\pi \frac{R}{l_{Pl}} \quad (41)$$

Let the energy required to create (erase) one bit is E_L . Then

$$\Delta E = E_L \Delta N \quad (42)$$

Substituting (39), (41) into (42) we obtain

$$E_L = \frac{l_{Pl}^2 c^4}{4\pi GR} \quad (43)$$

Given that $R = \frac{2GM}{c^2}$ and $M = \frac{\hbar c^3}{8\pi k_B GT}$ finally get

$$E_L \approx k_B T \quad (44)$$

in accordance with the Landauer principle [24].

CONCLUDING REMARKS

Historical experience teaches that the most interesting discoveries in physics occur during the transition to new characteristic scales of quantities that describe the problem under study. The boundary of the region in which a certain paradigm operates is determined by fundamental constants. For example, the transition from classical mechanics to relativistic is controlled by the speed of light, and the transition from classical mechanics to quantum is controlled by the Planck constant. The transition to the Planck scale is much more complicated, both quantitatively (this area is separated from the parameters currently achieved by tens of orders of magnitude) and qualitatively. (Is the concept of continuous space-time compatible with quantum mechanics). These difficulties make us look for workarounds to solve the problem. One of these areas may be the physics of limit quantities. Some specific examples of the use of limit values were considered in this paper. It is fundamentally important that on any event horizon, regardless of its scale (i.e., its gravitational radius), the universal value of limit force $c^4 / 4G$ is realized. This allows you to relate the characteristics of the Universe related to various stages of its evolution.

ORCID IDs

 Yuri L. Bolotin, <https://orcid.org/0000-0001-8164-5668>;  Vladimir V. Yanovsky, <https://orcid.org/0000-0003-0461-749X>

REFERENCES

- [1] H. Weyl, *Annalen der Physik*, **364**(10), 101–133 (1919), <https://doi.org/10.1002/andp.19193641002>.
- [2] A. Eddington, *Proceedings of the Cambridge Philosophical Society*, **27**(1), 15–19 (1931), <https://doi.org/10.1017/S0305004100009269>.
- [3] P.A. Dirac, *The cosmological constants*, *Nature*, **139**, 323 (1937), <https://doi.org/10.1038/139323a0>.
- [4] Yu.L. Bolotin, A.V. Tur, and V.V. Yanovsky, <https://arxiv.org/abs/2005.03984v1>.
- [5] T. Jacobson, *Phys. Rev. Lett.* **75**, 1260 (1995), <https://doi.org/10.1103/PhysRevLett.75.1260>.
- [6] C. Schiller, *International Journal of Theoretical Physics*, **44**, 1629-1647 (2005), <https://doi.org/10.1007/s10773-005-4835-2>.
- [7] G.Veneziano, *Europhys. Lett.* **2**(3), 199 (1986), <https://doi.org/10.1209/0295-5075/2/3/006>.
- [8] E. Witten, *Phys. Today*, **49**, 24 (1996), <https://doi.org/10.1063/1.881493>.
- [9] J. Polchinski, *String Theory*, (Cambridge University Press, Cambridge, 1998), pp. 402, <https://doi.org/10.1017/CBO9780511816079>.
- [10] R. Adler, P. Chen, and D. Santiago, *Gen. Rel. Grav.* **33**, 2101-2108 (2001), <https://doi.org/10.1023/A:1015281430411>.
- [11] S. Mignemi, *Mod. Phys. Lett. A*, **25**, 1697-1703 (2010), <https://doi.org/10.1142/S0217732310033426>.
- [12] H. Salecker, and E. Wigner, *Phys. Rev.* **109**, 571 (1958), https://doi.org/10.1007/978-3-662-09203-3_15.
- [13] F. Karolyhazy, *Nuovo Cim. A*, **42**, 390 (1966), <https://doi.org/10.1007/BF02717926>.
- [14] Y. Ng, *Phys. Rev. Lett.* **86**, 2946 (2002), <https://doi.org/10.1103/PhysRevLett.88.139902>.
- [15] R. Penrose, *Ann. N.Y. Acad. Sci.* **224**, 125-134 (1973), <https://doi.org/10.1111/j.1749-6632.1973.tb41447.x>.
- [16] G. Gibbons, *Found. Phys.* **32**, 1891 (2002), <https://doi.org/10.1023/A:1022370717626>.
- [17] J.D. Barrow, <https://arxiv.org/abs/2005.06809v1>.
- [18] A. Cohen, D. Kaplan, and A. Nelson, *Phys. Rev. Lett.* **82**, 4971 (1999), <https://doi.org/10.1103/PhysRevLett.82.4971>.
- [19] G. 't Hooft, <https://arxiv.org/abs/gr-qc/9310026v2>.
- [20] P-H. Chavanis, *Eur. Phys. J. Plus*, **129**, 222 (2014), <https://doi.org/10.1140/epjp/i2014-14222-0>.
- [21] S. Weinberg, *Gravitation and Cosmology*, (JohnWiley & Sons, New York, NY, 1972).
- [22] I. Gkigkitzis I. Haranas, and S. Kirk, *Astrophys. Space Sci.* **348**, 553–557 (2013), <https://doi.org/10.1007/s10509-013-1581-4>.
- [23] E.P. Verlinde, *On the origin of gravity and the laws of Newton*, *JHEP* 1104:029, 2011, [https://doi.org/10.1007/JHEP04\(2011\)029](https://doi.org/10.1007/JHEP04(2011)029).
- [24] R. Landauer, *IBM Journal of Research and Development*, **5**(3), 183-191 (1961), <https://doi.org/10.1147/rd.53.0183>.

ЯК ПРАЦЮЮТЬ ГРАНИЧНІ ЗНАЧЕННЯ

Ю.Л. Болотін^a, В.В. Яновський^{b,c}

^aННЦ "Харківський фізико-технічний інститут" НАН України, Харків, Україна

^bІнститут монокристалів НАН України, Харків, Україна

^cХарківський національний університет імені В.Н. Каразіна, Харків, Україна

Показана ефективність граничних величин як інструменту для опису фізики на різних просторово-часових масштабах. Завдяки своїй універсальності, граничні значення дозволяють встановлювати взаємозв'язки між, на перший погляд, далекими один від одного характеристиками. У статті розглянуті конкретні приклади використання граничних значень для встановлення таких зв'язків між величинами на різних масштабах. Виходячи з принципу досягнення граничних значень на горизонтах подій отримано зв'язок між планківськими величинами та величинами всього Всесвіту. Отримане співвідношення можна віднести до співвідношень діраківського типу – збігу великих чисел, які з'являлися з емпіричних спостережень. У статті співвідношення між великими числами типу діраківських, встановлюються виходячи, в певному сенсі, з фізичних принципів - існування граничних величин. Показано, що це співвідношення дотримується на всьому протязі еволюції Всесвіту. Обговорюється альтернативний спосіб вирішення проблеми космологічної сталої з використанням граничних величин і зв'язок її з мінімальним просторовим масштабом. Крім цього введено одно параметричне сімейство мас, яке включає в себе масу Всесвіту, масу Планка і масу гравітону, яке також встановлює зв'язок між величинами які відрізняються на 120 порядків. Показано, що ентропійні сили також підкоряються тим же універсальним обмеженням на граничні значення, як і звичайні сили. Тим самим існування граничних величин поширюється на інформаційні обмеження у Всесвіті. Принципово важливо, що на будь-якому горизонті подій, незалежно від його масштабу (тобто його гравітаційного радіуса), реалізується універсальне значення граничної сили $c^4 / 4G$. Це дозволяє зв'язати характеристики Всесвіту, що відносяться до різних етапах її еволюції.

КЛЮЧОВІ СЛОВА: чорна діра, горизонт подій, ентропія, граничні значення

PACS: 66.30.J-, 66.30.-h, 51.20.+d

MODELLING OF NONLINEAR THERMODIFFUSION FOR A SPHERICALLY SYMMETRIC CASE

Arvydas J. Janavičius[†],  Sigita Turskienė*

*Institute of Regional Development, Šiauliai University, Lithuania
P. Višinskio st. 25, LT-76351*

*Corresponding Author: turskienes@gmail.com

[†]E-mail: AYanavy@gmail.com

Received December 4, 2020; revised February 13, 2021, accepted February 15, 2021

The paper discusses the properties of the nonlinear thermodiffusion equation corresponding to the heat transfer processes occurring with a finite velocity in gas from a high intensity source. In the previous papers A. J. Janavičius proposed the nonlinear diffusion equation which provided a more exact description of impurities diffusion by fast moving vacancies generated by X-rays in Si crystals. This is similar to the heat transfer in gas with constant pressure by molecules carrying a greater average kinetic energy based on the nonlinear thermodiffusion of gas molecules from hot regions to the coldest ones with a finite velocity by random Brownian motions. Heat transfer in gas must be compatible with the Maxwell distribution function. Heat transfer in gas described by using nonlinear thermodiffusion equation with heat transfer coefficients directly proportional to temperature T . The solution of the thermodiffusion equation in gas was obtained by using similarity variables. The equation is solved by separating the linear part of the equation that coincides with Fick's second law. The obtained results coincide with Ya.B. Zeldovich's previously published solutions of nonlinear equations by changing the respective coefficients.

KEYWORDS: nonlinear thermodiffusion, high intensity source, similarity solution, temperature profiles, spherically symmetric case

In the previous papers we have discussed the nonlinear diffusion of impurities in semiconductors [1-2], nonlinear thermodiffusion in gas [2-3] and heat transfer in metals by electrons [4] using mathematical methods of similarity variables [1] for the solution of the nonlinear equation. The obtained results are important for engineering calculations of heat transfer in gas at constant pressure.

It is assumed that the process of thermal transmittance in gas is similar to nonlinear diffusion process of impurities described as Brownian movement of atoms in solids spreading with a finite velocity. Heat transfer can be described by using a modified theory of nonlinear diffusion in solids [1]. In this case the frequency of the jumps of diffusing molecules [2] depends upon the coordinates and changing molecules concentration n and temperature T according law of ideal gas defining pressure $p = nkT$.

The coefficient of thermal conductivity of gas can be expressed in the following way [2], [6]

$$K = \frac{1}{3} \lambda \bar{v} c_v \rho = D_w(T) c_v \rho = \frac{k \bar{v}}{2 \sqrt{2} \pi d^2}, \quad \lambda = \frac{1}{\sqrt{2} \pi d^2 n}, \quad \bar{v} = \sqrt{\frac{8RT}{\pi \mu}}. \quad (1)$$

Here λ is the mean value of a free path of diffusing molecules, \bar{v} - the mean velocities of molecular movement, c_v - the molar heat capacity at constant volume, ρ - the density of gas, n - the number of molecules per unit volume, k - Boltzmann constant, T - temperature of gas, μ - molar mass, R - gas constant, d - the distance between centers of the diffusing molecules of the gas, $D_w(T)$ - the thermodiffusion function of impurities in gas for the isobaric process.

The equation of thermodiffusion in gases can be obtained with the coefficient $D_w(T)$, which is proportional to the temperature [7] of gas. Similarly, as in the case of nonlinear diffusion in crystal silicon [1] by using (1), the coefficient $D_w(T)$ can be introduced

$$D_w(T) = \frac{K(T)}{\rho \cdot c_p} = \frac{1}{3} \frac{c_v}{c_p} \lambda \bar{v} = \frac{1}{3} \frac{c_v}{c_p} \bar{v} \frac{k T_s}{\sqrt{2} \pi d^2 p} \frac{T(r,t)}{T_s} = D_{ws} \frac{T(r,t)}{T_s} \quad (2)$$

The constant pressure $p = n(r,t)kT(r,t) = n_s(r,t)kT_s(r,t)$ at slow impurities transmission in gas with decreasing temperature $T(r,t)$ is compensated by increasing the concentration $n(r,t)$ of impurities in gases with heating from the spherical source of temperature T_s .

Here D_{ws} is the thermodiffusion proportionality constant for the nonlinear thermodiffusion function $D_w(T)$ for the specific heat capacity c_p of gas at the constant pressure p , K_s - the coefficient of thermal conductivity at source. From the theory of Brownian motion follows that the diffusion velocity and the maximum penetration depth of impurity atoms

and heat transfer velocity must be finite. Consequently [1], the thermodiffusion coefficient $D_w(r, t)$, defined by thermodiffusion constant at source D_{ws} , is directly proportional to the temperature

$$D_w(T) = D_w(r, t) = \frac{D_{ws}}{T_s} T(r, t) = D_{wn} T(r, t), \quad D_{ws} = D_{wn} T_s \quad (3)$$

which requires that the first Fick law must be improved by introducing the heat flux [1], [2] according the radial direction

$$j = -D_{wn} T(r, t) \frac{T(r + \Delta r, t) - T(r, t)}{\Delta r} \approx -D_{wn} T \frac{dT}{dr} \quad (4)$$

with the finite length Δr of the jumps with the finite velocity [1] of diffusing particles. It can be assumed that the jump length of the diffusing atoms or molecules from one equilibrium position to another in solids or fluids has the definite value L .

In gases L may be the average free path of diffusing particles. From the conservation the number of diffusing particles

$$\oint_S D_w \cdot \text{grad}(T) dS = \int_V \frac{\partial T}{\partial t} dV, \quad D_w = D_{wn} T(x, y, z, t) \quad (5)$$

and the theorem of Gauss' [6]

$$\int_V \text{div}(D_w \cdot \text{grad}(T)) dV = \int_V \frac{\partial T}{\partial t} dV \quad (6)$$

the following nonlinear thermodiffusion equation is obtained

$$\text{div}(D_w \text{grad}(T)) = \frac{\partial}{\partial x} \left(D_w \frac{\partial T}{\partial x} \right) + \frac{\partial}{\partial y} \left(D_w \frac{\partial T}{\partial y} \right) + \frac{\partial}{\partial z} \left(D_w \frac{\partial T}{\partial z} \right) = \frac{\partial T}{\partial t}. \quad (7)$$

By using the nonlinear diffusion equation [5], [6] the following thermodiffusion equation in spherical coordinates can be obtained

$$\frac{\partial T}{\partial t} = -\text{div}(-D_w(T) \text{grad}(T)), \quad j_p = -D_w(T) \frac{\partial T}{\partial r} = -D_{wn} T \frac{\partial T}{\partial r}. \quad (8)$$

The equation (6) for temperature $T(r, t)$, $0 \leq r \leq r_0$, $0 \leq t \leq t_0$ can be rewritten in the spherical case

$$\frac{\partial T}{\partial t} = \frac{D_{wn}}{T_s r^2} \left(\frac{\partial}{\partial r} \left(T r^2 \frac{\partial T}{\partial r} \right) \right) = \frac{D_{wn}}{T_s} \left(T \frac{\partial^2 T}{\partial r^2} + \frac{2}{r} T \frac{\partial T}{\partial r} + \left(\frac{\partial T}{\partial r} \right)^2 \right), \quad (9)$$

which mathematically coincides with the nonlinear diffusion equation [2].

The numerical calculations provided in [2] give the dependence $n(r, t)$ as a straight line in the region $0 \leq r \leq r_0$, $0 \leq t \leq t_0$. The temperature $T(r, t)$ dependence was obtained in a similar way [7].

The jump of hotter molecules or particles of impurities with a greater kinetic energy in the region $r + \Delta r$ with lower temperature is only possible if exists hotter at the point r .

This requirement is equivalent to the approval that thermodiffusion and diffusion must occur with finite value jumps and velocities. This is very important in defining coefficients of thermal conductivity [3], [7] and diffusion [1], [2].

The nonlinear heat conduction equation [8] presented for one dimensional case

$$\frac{\partial E}{\partial t} = \frac{\partial}{\partial x} \left(k_e(E) \frac{\partial E}{\partial x} \right), \quad (10)$$

using energy density E , which cannot be directly measured, is not perspective viable as equation (9) for temperature $T(r, t)$, which can be measured directly for calculation thermal conductivity [9].

The aim of the article is to get the nonlinear equation describing the flow of atoms and molecules in gases by the thermodiffusion for a spherically symmetric case and to find its approximate analytical solution.

THE NONLINEAR THERMODIFFUSION EQUATION FOR A SPHERICALLY SYMMETRIC CASE

The solution of (9) can be obtained by introducing similarity variable [5] ξ and function $f(\xi)$

$$T(\xi) = T_s f(\xi), \quad \xi = \frac{r}{\sqrt{D_{wn} T_s \cdot t}} = \frac{r}{\sqrt{D_{ws} t}},$$

$$0 \leq \xi \leq \xi_0, \quad 0 \leq r \leq r_0, \quad r_0 = \xi_0 \sqrt{D_{ws} T_s \cdot t} = \xi_0 \sqrt{D_{ws} t}, \quad (11)$$

which depends on the thermodiffusion constant D_{ws} at source with temperature T_s . By substituting (11) into (9) the following nonlinear differential equation can be obtained

$$f \frac{\partial^2}{\partial \xi^2} f + \frac{2}{\xi} f \frac{\partial f}{\partial \xi} + \frac{1}{2} \xi f \frac{\partial f}{\partial \xi} + \left(\frac{\partial f}{\partial \xi} \right)^2 - \frac{1}{2} \xi f \frac{\partial f}{\partial \xi} + \frac{1}{2} \xi \frac{\partial f}{\partial \xi} = 0. \quad (12)$$

The nonlinear equation (12) can be solved approximately by separating first three terms like the linear equation of hot molecules diffusion [2] can occur with the different lengths Δr of the some average frequency of jumps as at linear heat transmittance approach

$$f_l \left(\frac{\partial^2 f_l}{\partial \xi^2} + \frac{2}{\xi} \frac{\partial f_l}{\partial \xi} + \frac{1}{2} \xi \frac{\partial f_l}{\partial \xi} \right) \approx 0, \quad \left(\frac{\partial^2 f_l}{\partial \xi^2} + \frac{2}{\xi} \frac{\partial f_l}{\partial \xi} + \frac{1}{2} \xi \frac{\partial f_l}{\partial \xi} \right) \approx 0. \quad (13)$$

The part of nonlinear equation (12) is transformed to linear (13) and obtained the following expression representing thermodiffusion only by nonlinear processes

$$\left(\frac{\partial f}{\partial \xi} \right)^2 - \frac{1}{2} \xi \cdot f_l \frac{\partial f_l}{\partial \xi} + \frac{1}{2} \xi \frac{\partial f}{\partial \xi} = 0, \quad \frac{\partial f}{\partial \xi} - \frac{1}{2} \xi \cdot f_l + \frac{1}{2} \xi = 0. \quad (14)$$

The first [2] and the third terms in (14) represent a nonlinear diffusion or thermodiffusion. The second term in (14) represents the connection with linear thermodiffusion (13) and nonlinear equation (14) by introducing the term $P(\xi) = \frac{1}{2} \xi \cdot f_l$, which will be demonstrated below gets small numerical values in the region $0 \leq \xi \leq 2$.

APPROXIMATE ANALYTICAL SOLUTION

The term $P(\xi) = \frac{1}{2} \xi \cdot f_l$ of nonlinear equation (14) can be excluded. Thus, a simplified equation is obtained

$$\frac{\partial f}{\partial \xi} + \frac{1}{2} \xi = 0, \quad \frac{\partial f}{\partial \xi} \neq 0. \quad (15)$$

The equation (15) is solved for the source point temperature T_s and environment temperature T_e

$$f(\xi) = 1 - \frac{1}{4} \xi^2, \quad T(\xi) = T_s f(\xi), \quad 0 \leq \xi \leq \xi_e, \quad T_e = T_s \left(1 - \frac{1}{4} \xi_e^2 \right),$$

$$\xi_e^2 = 4 \frac{T_s - T_e}{T_s} \quad (16)$$

by satisfying the boundary conditions for the maximum distance r_e of heat penetration

$$f(\xi_e) = 0, \quad \xi_e = \frac{r_e}{\sqrt{D_{ws} t}}, \quad r_e = 2 \sqrt{D_{ws} t} \sqrt{\frac{T_s - T_e}{T_s}}, \quad (17)$$

and by satisfying the boundary condition for temperature T_s at the source point $r = 0$, $\xi = 0$

$$f(0) = 1, \quad T(0) = T_s f(0) = T_s. \quad (18)$$

The solution of the linear thermodiffusion equation (13) can be expressed [2] by similarity variables

$$F(\xi) = \frac{T(\xi)}{T_s} = \frac{\Delta \xi}{\xi} \operatorname{erfc} \left(\frac{\xi - \Delta \xi}{2} \right) \quad (19)$$

where the radius of source is $\Delta \xi$.

The nonlinear thermodiffusion equation (14)

$$\frac{\partial f_n}{\partial \xi} - \frac{1}{2} \xi \cdot f_n + \frac{1}{2} \xi = 0 \quad (20)$$

can be solved analytically by introducing a new variable

$$z = \xi - \xi_e, \quad \xi = z + \xi_e,$$

$$\frac{\partial f_n}{\partial z} - \frac{1}{2}(z + \xi_e)f_n + \frac{1}{2}(z + \xi_e) = 0 \tag{21}$$

The equation (21) can be modified to the following form

$$\frac{1}{1-f_n} \frac{\partial(1-f_n)}{\partial z} = \frac{1}{2}(z + \xi_e), \tag{22}$$

which is easy to integrate

$$f_n = 1 - C \cdot \exp[0.25z^2 + 0.5\xi_e z]. \tag{23}$$

The obtained solution of the equation must satisfy the boundary condition for maximum heat penetration depth

$$f_n(0) = 0, \quad z = 0, \quad \xi = \xi_e = 2, \quad C = 1. \tag{24}$$

For the heat penetration from the point source a multiplier for the obtained solution of the equation must be introduced

$$f_n(z) = \frac{e}{e-1} (1 - \exp(0.25z^2 + 0.5 \cdot \xi_e \cdot z)), \quad \frac{2.7183}{2.7183-1} = 1.582. \tag{25}$$

The comparison of solutions (Table) $f_n(\xi)$ of nonlinear thermodiffusion equation (25) and $f(\xi)$ of simplified equation (16) shows the coincidence of both numerical solutions which depend on similarity variables ξ .

Table.

ξ	0	0.5	1	1.5	2
$f_n(\xi)$	1	0.9624	0.8347	0.5606	0
$f(\xi)$	1	0.9844	0.7500	0.5625	0

RESULTS AND DISCUSSION

The nonlinear diffusion equation is derived [10] by taking into account the local variations of impurities temperature in the solvent within a mechanism of diffusion driven by random impurities particles collisions with solvent molecules of density at average frequency

$$v(x, y, z, t) = \sigma \cdot N(x, y, z, t) \cdot u \cdot \sqrt{2} \tag{26}$$

and relative velocity (1) $u\sqrt{2} = v\sqrt{2}$ with solvent molecules of density N . Here σ is the collision cross-section of diffusing particles. In real thermodiffusion process the collisions frequency depends not only on the distribution $N(x, y, z, t)$ but also on the distribution of impurities or hot molecules with velocities [6] as well as on temperature.

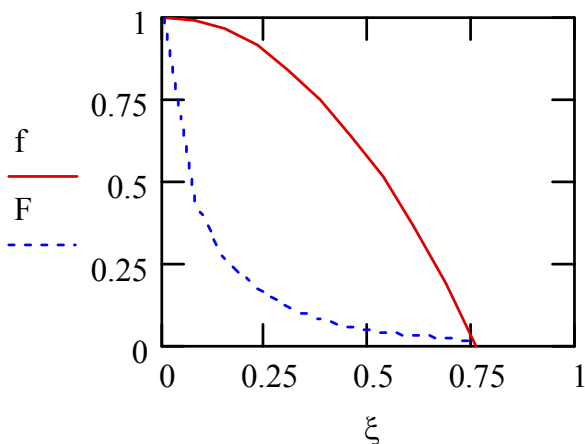


Figure 1. Profiles of nonlinear (16) $f(\xi) = \frac{T}{T_s}$ and linear (19) $F(\xi)$ solutions of equation for the point source with temperature $T_s = 300,15$ K and environment temperature $T_e = 280,15$ K when thermodiffusion coefficient [9] $D_{\text{vis}} = 2.172 \cdot 10^{-2} \text{ m}^2 / \text{ s}$ and time is 100 s.

The presented profiles of $f(\xi)$ and $P(\xi)$ in Fig. 2 as well as the results presented in Table 1 show that the term $P(\xi) = \frac{1}{2}\xi \cdot f_i$ gets small numerical values in the equation (14), and, consequently, can be removed. The linear effects in equations (12), (13) and nonlinear equations (15), (20) can be separated.

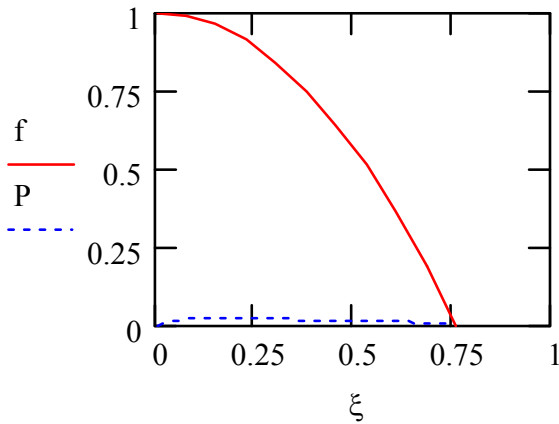


Figure 2. Profiles of nonlinear (16) solution $f(\xi) = \frac{T}{T_s}$ and term (14) $P(\xi) = \frac{1}{2}\xi \cdot f_i$ for the point source with temperature $T_s = 300,15$ K, environment temperature $T_e = 280,15$ K when thermodiffusion coefficient [9] $D_{ws} = 2.172 \cdot 10^{-2} m^2 / s$ and time is 100 s.

Concentration profiles (Fig. 3) illustrate the obtained parabolic form of nonlinear equation (16) $f(\xi) = \frac{T}{T_s}$ and linear equation (19) $F(\xi)$ solutions.

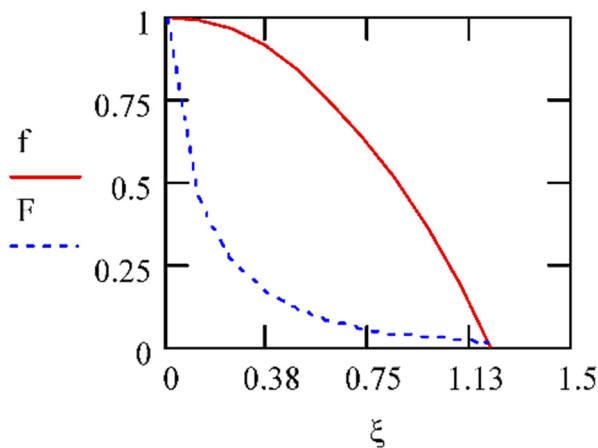


Figure 3. Concentration profiles of nonlinear (16) $f(\xi) = \frac{T}{T_s}$ and linear (19) $F(\xi)$ solutions of equations for the point source with temperature $T_s = 300,15$ K, environment temperature $T_{e0} = 250,15$ K when thermodiffusion coefficient [9] $D_{ws} = 2.172 \cdot 10^{-2} m^2 / s$ and thermodiffusion time is 100 s.

It can be explained by taking into account the distribution function [6] of hot molecules with velocities c

$$\frac{\Delta n}{n} = \frac{4 \cdot c_m^3 \exp\left(\frac{-mc^2}{2kT}\right)}{\sqrt{\pi}} \cdot c^2 \cdot \Delta c, \tag{27}$$

possessing the most probable molecular velocity c_m and average velocity \bar{v} [6]

$$c_m = \sqrt{\frac{2kT}{m}}, \quad \bar{v} = \sqrt{\frac{8kT}{\pi m}}, \quad \bar{v} = \frac{2}{\sqrt{\pi}} c_m. \tag{28}$$

The average value \bar{v} in (28) must be substituted by the temperature $T = \frac{1}{2}T_s$. Gas densities n at this temperature collide with the hottest molecules $2n_s$ when they satisfy the condition $n = 2n_s$, which formats the front of temperature. The dependence of density distribution of hot molecules c_m and T_s can explain the formation of the barrier of hot molecules with greater kinetic energies

$$\frac{mc^2}{2} = \frac{3}{2}kT \quad (29)$$

and hot shock waves [11] according (16), (17) and Fig. 4 rapidly spreading in space.

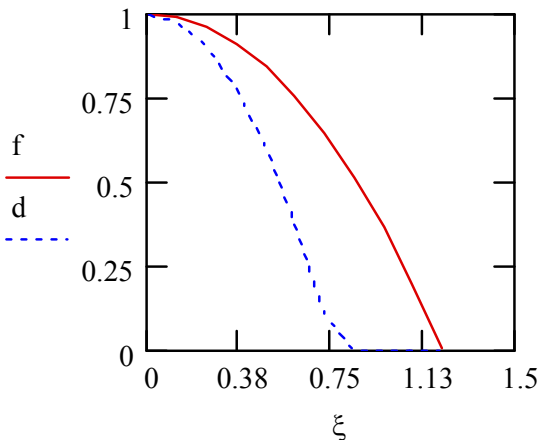


Figure 4. Temperature profiles of functions (16), (17) $f(\xi) = \frac{T}{T_s}$ and $d(\xi)$ for the same nonlinear solutions (16) of the point source with temperature $T_s = 300,15$ K, environment temperatures $T_{e0} = 250,15$ K and $T_e = 280,15$ K respectively for presented temperatures functions $f(\xi)$ and $d(\xi)$ when thermodiffusion coefficient [9] at source is $D_{ws} = 2.172 \cdot 10^{-2} m^2 / s$ for the time interval of 100 s.

In Fig. 4 heat penetration depths (17) from the same source are equal to $r_e = 2\sqrt{D_{ws}t} \sqrt{\frac{T_s - T_e}{T_s}}$ and can be similarly explained.

All graphs are presented by using computer algebra system MathCAD.

CONCLUSIONS

The flow of atoms and molecules by nonlinear diffusion [1] and thermodiffusion is defined by the finite length Δr jumps of the hot molecules (4) as well as the finite velocity [1] by using a thermodiffusion coefficient proportional to the temperature (2), (8). The obtained temperature parabolic graphs [11-12] of the nonlinear solutions in Fig. 4 are generated by hot atoms or molecules velocities probability (27), (28) and their dependence on temperature.

The approximate analytical solution of nonlinear thermodiffusion equation for the point source in the spherical case is very complicated and was solved by excluding the linear diffusion equation (13) from the nonlinear equation (12). This can be physically realized only when the third term on the right side of (9) defining diffusion [2] on the frontier $\frac{D_{ws}}{T_s} \left(\frac{dT}{dr} \right)^2$ is significantly greater than the first term representing the self-diffusion from the source having high intensity of impurities. This can be similar to superdiffusion of impurities by vacancies [13-14] at room temperature in the crystal silicon irradiated with X-rays.

In this case the obtained nonlinear equation (15), solved analytically (16), as can be seen in Fig. 4, by using similarity variables, can be applied with sufficient accuracy.

Nonlinear thermal conductivity in gas [3] was considered in one dimensional case with thermal diffusion coefficient (2) proportional to the gas temperature. Similar equations only for one dimensional case were solved analytically for more complicated thermodiffusion coefficients [15-16] $D = k + m \cdot T^n$, $k > 0$ by using similarity variables.

The analytical solution of a more complicated task of nonlinear thermodiffusion equation for a spherically symmetric case by using similarity variable and separation of linear processes has been successfully achieved.

ORCID IDs

 Sigita Turskienė, <https://orcid.org/0000-0002-2019-6712>

REFERENCES

- [1] A.J. Janavičius, Physics Letters A, **224**, 159-162 (1997), [https://doi.org/10.1016/S0375-9601\(96\)00794-3](https://doi.org/10.1016/S0375-9601(96)00794-3).
- [2] A.J. Janavičius, and A.Poškus, Acta Phys. Pol. A, **107**, 519-521 (2005), <http://dx.doi.org/10.12693/APhysPolA.107.519>.
- [3] A.J. Janavičius, and S. Turskienė, Proc. of the Lithuanian Mathematical Society, Ser. A, **57**, 24-28 (2016), <http://dx.doi.org/10.15388/LMR.A.2016.05>.
- [4] A.J. Janavičius, and S. Turskienė, Acta Phys. pol. A, **110**, 511-521 (2006), <http://dx.doi.org/10.12693/APhysPolA.110.511>.
- [5] V.I. Rudakov, and V.V. Ovcharov, International Journal of Heat and Mass Transfer, **45**(4), 743-753 (2002), [https://doi.org/10.1016/S0017-9310\(01\)00204-6](https://doi.org/10.1016/S0017-9310(01)00204-6).
- [6] G. Joos, and I.M. Freeman, *Theoretical Physics*, (Dover Publications Inc., New York, 1986).
- [7] A.J. Janavičius, and S. Turskienė, Latvian Journal of physics and technical sciences, **55**, 34-42 (2018), <https://doi.org/10.2478/lpts-2018-0019>.
- [8] M.E. Glikzman, *Diffusion in solids*, (Wiley, New York, 2000), pp. 472.

- [9] L.L. Goldin, *Laboratory works in physics*, (Science, Novosibirsk, 1983). (in Russian)
- [10] A.J. Janavičius, G. Lūža, and D. Jurgaitis, *Acta Phys. Pol. A*, **105**, 475-483 (2004), <http://dx.doi.org/10.12693/APhysPolA.105.475>.
- [11] Ya.B. Zeldovich, and Yu.P. Raizer, *Physics of Shock Waves and High-Temperature, Hydrodynamic Phenomena*, (Dover Publications, 2003).
- [12] A.J. Baškys, D.J. Zanevičius, O.N. Kolomojec, and A.J. Janavičius, *Algebraic Devices-Technological Model for production Integral Schemes*, *Microelectronics Ser. 3*, **4**(307), 44-47 (1989). (in Russian)
- [13] A.J. Janavičius, S. Balakauskas, V. Kazlauskienė, A. Mekys, R. Purlys, and J. Storasta, *Acta Phys. Pol. A*, **114**, 779 (2008), <http://dx.doi.org/10.12693/APhysPolA.114.779>.
- [14] A.J. Janavičius, et al, PCT publication number WO/2014/062045, PCT declaration number PCT/LT2013/000017, Declaration in USA No. 14/436,934 (2016).
- [15] C.J. van Duyn, and L.A. Peletier, *Nonlinear Analysis: Theory, Methods & Applications*, **1**(3), 223-233 (1977), [https://doi.org/10.1016/0362-546X\(77\)90032-3](https://doi.org/10.1016/0362-546X(77)90032-3).
- [16] V.D. Djordjevic, and Th.M. Atanackovic, *Journal of Computational and Applied Mathematics*, **222**(2), 701-714 (2008), <https://doi.org/10.1016/j.cam.2007.12.013>.

МОДЕЛЮВАННЯ НЕЛІНІЙНОЇ ТЕРМОДИFUZІЇ ДЛЯ СФЕРИЧНО СИМЕТРИЧНОГО ВИПАДКУ

Арвидас Й. Янавичюс, Сігіта Турскієне

Институт регіонального розвитку, Університет Шяуляй, Литва

вул. П. Вішинсько, 25, LT-76351

У статті розглядаються властивості нелінійного рівняння термодифузії, що відповідає процесам теплообміну, які відбуваються з кінцевою швидкістю в газі від джерела високої інтенсивності. У попередніх роботах А. Янавичюс запропонував нелінійне рівняння дифузії, яке надало більш точний опис дифузії домішок за допомогою швидкорухомих вакансій, породжених рентгенівським випромінюванням у кристалах Si. Це є подібним до теплопередачі в газі з постійним тиском молекулами, які несуть більшу середню кінетичну енергію, на основі нелінійної термодифузії молекул газу з гарячих областей у найхолодніші з кінцевою швидкістю випадковими броунівськими рухами. Теплообмін у газі повинен бути сумісним із функцією розподілу Максвелла. Теплопередача в газі описана за допомогою нелінійного рівняння термодифузії з коефіцієнтами теплопередачі, які є прямо пропорційними температурі T . Рішення рівняння термодифузії в газі було отримано з використанням змінних подібності. Рівняння вирішується відокремленням лінійної частини рівняння, яка відповідає другому закону Фіка. Отримані результати співпадають з рішеннями Я. Зельдовича нелінійних рівнянь, що були опубліковані раніше, шляхом зміни відповідних коефіцієнтів

КЛЮЧОВІ СЛОВА: нелінійна термодифузія, джерело високої інтенсивності, рішення подібності, температурні профілі, сферично симетричний випадок

PACS: 29.20.Ej; 87.50.sj; 87.55.Qr

STUDIES OF DOSIMETRY PROTOCOLS FOR ACCELERATED PHOTONS AND ELECTRONS DELIVERED FROM MEDICAL LINEAR ACCELERATOR

 A.K.M. Moinul Haque Meaze^{a,*},  Santunu Purohit^a,  Md. Shakilur Rahman^b,
 Abdus Sattar^a,  S.M. Enamul Kabir^c,  Md. Kawchar Ahmed Patwary^d,
 Kamrunnahar Kali^d,  Md. Jubayer Rahman Akhand^e

^aDepartment of Physics, University of Chittagong, Bangladesh

^bSecondary Standard Dosimetry Laboratory, Bangladesh Atomic Energy Commission, Savar, Dhaka, Bangladesh

^cNational Institute of Cancer Research, Dhaka, Bangladesh

^dDepartment of Physics, Comilla University, Bangladesh

^eBangladesh Military Academy, Bhatiary, Chittagong, Bangladesh

*Corresponding Author: meaze@cu.ac.bd; mhqmeeaze@yahoo.com

Received October 22, 2020, accepted December 15, 2020

We focus on the comparative study of dosimetry protocols in radiotherapy for accelerated photon and electron delivered from medical linear accelerator (LINAC). In this study, a comparison between the protocols (TRS 398, DIN 6800-2 and TG 51) for both the electron and photon delivered from Clinac 2300CD and Clinac DHX 3186 were performed. We used photon beams with energies of 6 and 15 MV and electron beams of 4, 6, 9, 12, 15 and 18 MeV for both Medical Linac. In case of Clinac the maximum deviations for the relative dose at D_{\max} for the photon beam (15 MV) among the protocols was observed to be 1.18% between TRS-398 and TG-51, 1.56% between TG-51 and DIN 6800-2; and 0.41% between TRS-398 and DIN 6800-2. Conversely, these deviations were 3.67% between TRS-398 and TG-51, 3.92% between TG-51 and DIN 6800-2 for 4 MeV and 0.95% between TRS-398 and DIN 6800-2 in the case of Clinac 2300 CD for the PTW Markus and Exradin A10. For the measurement of the maximum absorbed dose depth to water using three protocols, the maximum deviations were observed between TRS 398 and TG-51 as well as TG51 and DIN 6800-2.

KEYWORDS: TRS (Technical Report Series), TG (Task Group), DIN (Deutsches Institut für Normung).

Approximately 60% of cancer patients are referred for external beam radiotherapy, for which the most commonly used equipment is a medical LINAC that produces an electron beam and photon beam [1]. The precise planning of the treatment depends on the tumor type, size, position, stage, and health condition of patients [1, 2]. By considering various uncertainty components associated with beam calibration factors, a study of the uncertainty in determining of the absorbed dose to water had been carried out by C. Pablo *et al.* [3] Their results showed a typical uncertainty in the determination of absorbed dose to water during beam calibration approximately 1.3% for photon beams and 1.5% for electron beams ($k = 1$ in both cases). M. S. Huq *et al.* [4] performed a study by comparing International Atomic Energy Agency Technical Report Series No. 398 (IAEA TRS-398) and AAPM TG-51 absorbed dose to water protocols in the dosimetry of high-energy photon and electron beams. They compared the two protocols in two ways: (i) by analyzing the differences of the basic data included in the two protocols for photon and electron beam dosimetry in detail and (ii) by performing experiments in clinically accelerated photon and electron beams and determining the absorbed dose to water following the recommendations of the two protocols [4]. For electron beams, the ratios TG-51/TRS-398, of the absorbed dose to water D_w were observed to be lie between 0.994 and 1.018 depending upon the chamber and electron beam energy used, with mean values of 0.996, 1.006, and 1.017 respectively, for the cylindrical, well-guarded and not well-guarded plane-parallel chambers [4]. A dosimetric study comparing NCS report-5, IAEA TRS-381, AAPM TG-51 and IAEA TRS-398 in three clinical electron beam energies was carried out by H. Palmans *et al.* [5]. In their work, they compared dosimetry for three clinical electron beam energies using two NE2571-type cylindrical chambers, two Markus-type plane-parallel chambers and two NACP-02-type plane-parallel chambers [5]. Another comparison of high-energy photon and electron dosimetry for various dosimetry protocols was performed by F. Araki *et al.* [6] They calculated the absorbed dose to water calculated according to the Japanese Association of Radiological Physics, IAEA TRS-277 and IAEA TRS-398 protocols, and compared it to that calculated using the TG-51 protocol. A comparison of protocols for external beam radiotherapy beam calibrations was carried out by S S Al-Ahababi *et al.* [7] where they used the IAEA TRS-398, AAPM TG-51 and IPEM 2003 protocols. The comparisons were carried out by delivering electron beams of nominal energies of 6, 9, 12, 16 and 20 MeV using Physikalisch-Technische Bundesanstalt (PTW) Markus and NACP-02 plane-parallel chambers.

Different group of dosimetrists did experiments several times to ensure lower uncertainty, best suited protocols and improvement of protocols for the commissioning of medical Linac and more precisely healthcare purposes. The aims of our work is to analyze the dosimetry applying three different most preferable protocols maintaining the QA parameters for high energy photon and electron beams delivered from the medical linear accelerator (Clinac). Different ionization chambers were used to calculate the absorbed dose to water and a comparison among chambers was investigated. For each chamber the absorbed dose to water was calculated using three different protocols. Sometimes in same reference conditions absorbed dose differs from Clinac to Clinac because of wall material of jaws. To confirm that dose variations

we use two different medical LINAC and same chamber response with LINAC in this research work. This study will be helpful for defining more accurate dosimetry and developing more general protocol for ensuring patient safety during treatment planning.

METHODS AND MATERIALS

Absorbed dose to water calibration in ^{60}Co

The calibrations in terms of absorbed dose to water are available only for ^{60}Co gamma radiation [8]. The reference point of the chamber was at $5\text{g}/\text{cm}^2$ water depth. The size of the radiation field (50% isodose level) at the reference plane was $10\text{ cm}\times 10\text{ cm}$ [9 – 12]. The PTW Markus chamber was set up for determining the calibration factor in a water phantom, and then the Physikalisch-Technische Bundesanstalt (PTW) UNIDOSE electrometer was used to obtain the dose rate. From these dose rates the calibration factor was measured using the IAEA TRS-398 protocol. The same procedure was used to calibrate the Exradin A10 and IBA FC65-G (2009) chambers. The descriptions of different protocols are presented in Table 1.

Table 1. Description of different protocols [10, 13, 14]

Criteria	Chamber Type	TRS 398		AAPM TG-51		DIN 6800-2	
		Electron	Photon	Electron	Photon	Electron	Photon
Chamber position	Cylindrical	At $Z_{ref} + r/2$	At Z_{ref}	At Z_{ref}	At Z_{ref}	At $Z_{ref} + r/2$	At $Z_{ref} + r/2$
	Plane parallel	At Z_{ref}		At Z_{ref}		At Z_{ref}	
Beam quality	Cylindrical	specified by the half-value of the depth dose in water R_{50}	specified by the tissue phantom ratio $\text{TPR}_{20,10}$	specified by the half-value of the depth dose in water R_{50}	specified by $\%dd(10)_x$	specified by the half-value of the depth dose in water R_{50}	specified by $Q = 1.2661 \frac{M_{20}}{M_{10}} - 0.0595$
	Plane parallel						
Value of T_o	Cylindrical	20 °C		22 °C		20 °C	
	Plane parallel						
Ion recombination correction factor	Cylindrical	$K_s = a_0 + a_1 \left(\frac{M_1}{M_2}\right) + a_2 \left(\frac{M_1}{M_2}\right)^2$		$P_{\text{ion}} = \frac{1 - \frac{V_H}{V_L}}{\frac{M_{\text{raw}}^H}{M_{\text{raw}}^L} - \frac{V_H}{V_L}}$		$K_s = \frac{U_1 - 1}{\frac{U_2}{U_1} - \frac{Mu_1}{Mu_2}}$	
	Plane parallel						
Chamber positioning correction	Cylindrical	none		none		$K_r = 1 + \delta \cdot r/2$	

RESULTS

Calibration of Ionization Chambers

The calibration factors of Markus, A10 and FC65-G are listed in Table 2.

Table 2. Calibration factors of Markus, A10 and FC65-G

Chamber Model	Chamber Serial No.	Calibration factor in Gy/nc		Variation (%)
		Certified by (Physikalisch-Technische Bundesanstalt) PTB	Experimentally found	
PTW23343 Markus	3941	0.5448	0.5349	1.8200
Exradin A10	XC110304	0.6087	0.6047	0.6600
IBA FC65-G	2009	0.0476	0.0477	0.1900

**Absorbed dose to water for Photon beam
Absorbed dose to water according to different protocols**

TRS 398	$M_Q = M_{raw} \times K_{TP} \times K_{elec} \times K_{pol} \times K_s$ $D_{w,Q} = M_Q \times N_{D,w,Q_0} \times K_Q$
TG 51	$M = M_{raw} \times P_{TP} \times P_{elec} \times P_{pol} \times P_{ion}$ $K_Q = P_{gr}^Q \times K_{R_{50}}$ $K_{R_{50}} = K'_{R_{50}} \times K_{ecal}$ $D_{w,Q} = M \times N_{D,w,Q_0} \times K_Q$
DIN 6800-2	$M_Q = M \times K_\rho \times K_p \times K_r \times K_s$ $k_E = k'_E \times k''_E$ $k'_E = 1.106 - 0.1312 (R_{50})^{0.214}$ $k''_E = 0.982 (P_{cav})_{R_{50}}$ $(P_{cav})_{R_{50}} = 1 - 0.037e^{-0.27R_{50}}$ $D_{w,Q} = M_Q \times N_{D,w,Q_0} \times K_Q$

a. Beam quality.

The measurement of K_Q using three different protocols are presented in Table 3.

Table 3. Measurement of K_Q

Energy (MV)	K_Q		
	IAEA TRS-398	AAPM TG-51	DIN 6800-2
6	0.996	0.992	0.993
15	0.981	0.976	0.977

b. Comparison among protocols.

To make a comparison among protocols, we considered three main correction factors: pressure temperature correction, ion recombination correction and polarity correction factors. The values of these parameters are listed in Table 4.

Table 4. Values of pressure temperature, ion recombination and polarity correction factor

K_p				
Chamber	IAEA TRS 398	AAPM TG 51	DIN6800-2	
FC65-G (2005)*	1.0078	1.0013	1.0081	
FC65-G (2009)*	1.0080	1.0015	1.0082	
k_s				
Chamber	Energy (MV)	IAEA TRS 398	AAPM TG-51	DIN 6800-2
FC65-G (2005)*	6	1.0048	1.0050	1.0054
	15	1.0063	1.0065	1.0078
FC65-G (2009)*	6	1.0027	1.0028	1.0027
	15	1.0061	1.0064	1.0065
k_{pol}				
Chamber	Energy (MV)	IAEA TRS-398	AAPM TG-51	DIN 6800-2
FC65-G (2005)*	6	1.0018	1.0018	1.0011
	15	1.0009	1.0009	0.9993
FC65-G (2009)*	6	1.0017	1.0017	1.0011
	15	1.0009	1.0009	1.0006

*Here FC65-G (2005) and (2009) represents serial number.

A comparison of the maximum dose depths (D_{max}) measured with three different protocols is presented in Table 5.

Table 5. Comparison of maximum dose depth (D_{max}) measured with three different protocols

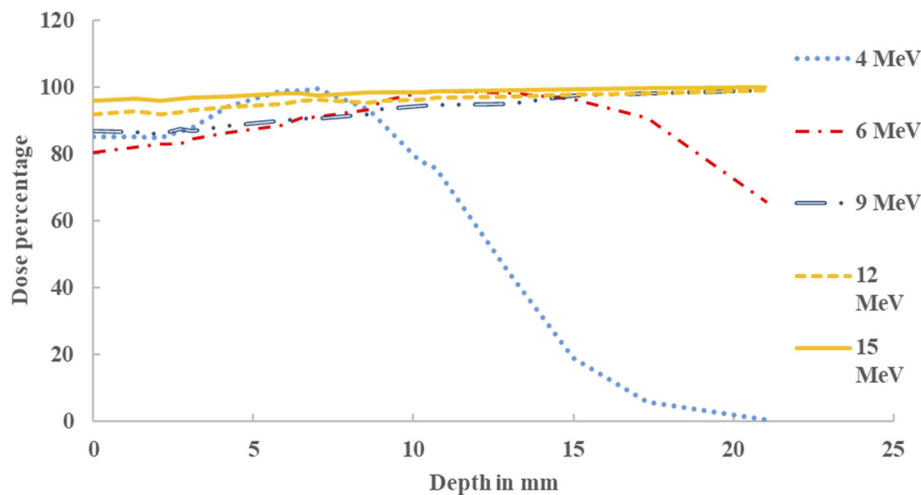
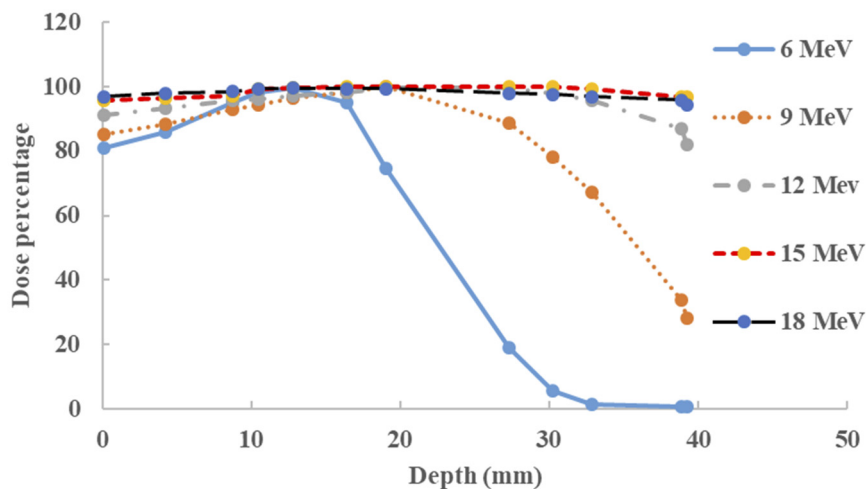
Chamber	Energy (MV)	D_{max}			Deviation (%) in between		
		IAEA TRS-398	AAPM TG51	DIN 6800-2	TRS-398 & AAPM TG51	AAPM TG51 & DIN6800-2	DIN 6800-2 & TRS-398
FC65-G (2005)	6	9.962×10^{-03}	9.859×10^{-03}	9.940×10^{-03}	1.03	0.82	0.22
	15	9.882×10^{-03}	9.765×10^{-03}	9.917×10^{-03}	1.18	1.56	0.36
FC65-G (2009)	6	9.847×10^{-03}	9.745×10^{-03}	9.872×10^{-03}	1.03	1.29	0.26
	15	9.816×10^{-03}	9.700×10^{-03}	9.856×10^{-03}	1.18	1.56	0.41

We found that the percentage of the depth dose increases with increasing of energy, and the maximum dose D_{max} decreases. This is because the main influencing correction factor K_Q decreases with increasing energy. The variation of the maximum dose depth at D_{max} for FC65G (2005) and FC65G (2009) according to IAEA TRS 398 and AAPM TG 51 was found to be 1.18% and 1.03% in 15 and 6 MV photon energies respectively. However, in DIN 6800-2 the variation of dose at D_{max} for FC65G (2005) and FC65G (2009) was found to be less than 0.5% in both 6 and 15 MV photon energies.

Absorbed dose to water for Electron beam

a. PDD Curves.

The PDD curves were observed at energies of 4, 6, 9, 12 and 15 MeV for Clinac 2300CD, and at energies of 6, 9, 12 and 15 MeV for DHX-3186. All comparative curves for limited length are shown in Figures 1 and 2. Since the electron beam has significantly low penetration power the reference depth for an electron is close to the phantom water surface.

**Figure 1.** PDD curves for 4, 6, 9, 12 and 15 MeV electron beams delivered from 2300CD Clinac**Figure 2.** PDD curves for 6, 9, 12, 15 and 18 MeV electron beams delivered from DHX-3186 Clinac

The dose percentage with respect to the energy and depth is presented in Table 6.

Table 6. Dose percentage with respect to energy and depth

Clinac	Energy (MV)	Z _{ref} (cm)	Dose (%)
2300CD	4	0.64	99.60
	6	1.29	99.70
	9	2.02	100.00
	12	2.89	99.30
	15	3.69	97.80
DHX-3186	6	1.29	99.80
	9	2.02	100.00
	12	2.89	99.50
	15	3.69	98.70

Comparison among protocols

The PTW TM23343 Markus chamber was used to compare three protocols IAEA TRS 398, AAPM TG51 and DIN 6800-2. The correction factors for the electron beam are listed in table 7.

Table 7. Measurement of the correction factors for the electron beam

k _s				
Clinac	Energy (MV)	IAEA TRS 398	AAPM TG-51	
2300CD	4	1.0088	1.0084	
	6	1.0086	1.0089	
	9	1.0089	1.0092	
	12	1.0081	1.0083	
	15	1.0078	1.0080	
DHX-3186	6	1.0099	1.0102	
	9	1.0110	1.0113	
	12	1.0082	1.0086	
	15	1.0123	1.0126	
	18	1.0073	1.0075	
K _Q				
Clinac	Energy (MeV)	K _Q		
		IAEA TRS-398	AAPM TG-51	DIN 6800-2
2300CD	4	0.930	0.9705	0.9262
	6	0.922	0.9507	0.9135
	9	0.913	0.9356	0.9042
	12	0.904	0.9226	0.8957
	15	0.897	0.9129	0.8889
DHX-3186	6	0.922	0.9507	0.9135
	9	0.913	0.9356	0.9042
	12	0.904	0.9226	0.8957
	15	0.897	0.9129	0.8889
	18	0.892	0.9061	0.8838

Uncertainty in Dose Measurement

For the photon beam the total uncertainty in the measurement of absorbed dose to water was approximately similar for FC65-G (2005) and (2009) which was ± 0.57% (*k* = 1) for both 6 and 15 MV. Our work provides better result than that of Castro P *et al*³. For electron beam using the PTW TM23343 chamber, the total uncertainty in the absorbed dose to water in Clinac 2300CD were ± 1.74%, ± 1.09%, ± 0.92%, ± 0.85% and ± 0.82% for 4, 6, 9, 12 and 15 MeV respectively and that in Clinac DHX-3186 were ± 1.09%, ± 0.94%, ± 0.86%, ± 0.84% and ± 0.80% for 6, 9, 12, 15 and 18 MeV respectively (*k* = 1). In contrast using the Exradin A10 chamber for electron dosimetry, the total uncertainty in the absorbed dose to water in Clinac 2300CD were ± 1.67%, ± 0.97%, ± 0.78%, ± 0.69% and ± 0.65% for 4, 6, 9, 12 and 15 MeV respectively and that in Clinac DHX-3186 were ± 0.96%, ± 0.78%, ± 0.76%, ± 0.68% and ± 0.69% for 6, 9, 12, 15 and 18 MeV respectively (*k* = 1).

DISCUSSIONS

In general, the discrepancies in the values of beam quality, K_Q and D_{max} for various protocols exhibited in a decreasing trend for the electron beam with the increase of energy. In contrast, for the comparative study with various chambers, the variation in D_{max} also exhibited in a decreasing trend with energy for both the accelerated photon and electron. The vital influencing factor for deviations among the protocols as well as between the chambers was the beam quality conversion factor K_Q . The deviation can be resolved if the chambers can be calibrated at their respective electron or photon beam quality rather than at ^{60}Co . Our measured correction factors, according to the TG-51, TRS-398 and DIN 6800-2 protocols were in good agreement with previous published works [4, 6, 14, 15, 16].

CONCLUSIONS

In this study, it was experimentally observed that the TRS 398 protocol is in good agreement with DIN 6800-2 rather than TG51 because of the measurement technique and correction factors included with the protocol. The experimental uncertainty (Type A and B) included in the measurement is below that of the previously published and recommended works [6, 17]. In this work we found that, some uncertainties would be minimized if the chambers calibrated with the photon beam delivered from the medical LINAC rather than the ^{60}Co beam.

Compliance with Ethical Standards: This article does not contain any studies with human participants performed by any of the authors.

Funding: None

Conflict of Interest: All authors declare that they have no conflict of interest

ORCID IDs

-  AKM Moinul Haque Meaze, <https://orcid.org/0000-0002-1526-2113>;
  Santunu Purohit, <https://orcid.org/0000-0002-0029-995X>;
 Md. Shakilur Rahman, <https://orcid.org/0000-0002-7873-7999>;
  Abdus Sattar, <https://orcid.org/0000-0003-3863-7253>;
 SM Enamul Kabir, <https://orcid.org/0000-0002-9684-4966>;
  Kamrunnahar Kali, <https://orcid.org/0000-0002-9284-9516>;
 Md. Kawchar Ahmed Patwary, <https://orcid.org/0000-0002-6150-9113>;
 Md. Jubayer Rahman Akhand, <https://orcid.org/0000-0002-4406-0369>

REFERENCES

- [1] K.A. Paskalev, J.P. Seuntjens, H.J. Patrocinio, and E.B. Podgorsak, *Med Phys.* **30**(2), 111–118 (2003), <https://doi.org/10.1118/1.1536290>.
- [2] A.J. D. Scott, A.E. Nahum, and J.D. Fenwick, *Am. Assoc. Phys. Med.* **35**(10), 4671-4684 (2008), <https://doi.org/10.1118/1.2975223>.
- [3] P. Castro, F.G Vicente, C. Minguez, A. Floriano, D. Sevillano, L. Perez, and J.J. Torres. *Appl. Clinical Medical Phys.* **9**(1), 70-86 (2008), <https://dx.doi.org/10.1120%2Fjacmp.v9i1.2676>.
- [4] M.S. Huq, P. Andreo, and H. Song. *Physics in Medicine and Biology*, **46**(11), 2985-3006 (2001), <https://doi.org/10.1088/0031-9155/46/11/315>.
- [5] H. Palmans, L. Nafaa, N. Patoul, J-M. Denis, M. Tomsej, and S. Vynckier, *Physics in Medicine and Biology*, **48**(9), 1091-1107 (2003), <https://doi.org/10.1088/0031-9155/48/9/301>.
- [6] F. Araki, and H.D. Kubo, *Med Phys.* **29**(5), 857-868 (2002), <https://doi.org/10.1118/1.1470208>.
- [7] S.S. Al-Ahbab, D.A. Bradley, M. Beyomi, Z. Alkatib, S. Adhaheri, M. Darmaki, and A. Nisbet, *Appl Radiat. Isot.* **70**(7), 1331-1336 (2012), <https://doi.org/10.1016/j.apradiso.2011.11.065>.
- [8] *Radiotherapy Ionization Chamber Calibration Procedures at the IAEA Dosimetry Laboratory*, http://www-naweb.iaea.org/nahu/dmrip/documents/DOLP.011_Appendix_3A_to_Calibration_certificate_rev6.pdf.
- [9] J. Medin, P. Andreo, and S. Vynckier, *Phys Med Biol.* **45**(11), 3195-3211 (2000), <https://doi.org/10.1088/0031-9155/45/11/306>.
- [10] S.R.M. Mahdavi, M. Mahdavi, H. Alijanzadeh, M. Zabihzadeh, and A. Mostaar, *Iran J. Radiat. Res.* **10**(1), 43-51 (2012), <https://www.sid.ir/FileServer/JE/92620120106.pdf>.
- [11] *Absorbed Dose Determination in External Beam Radiotherapy: An International Code of Practice for Dosimetry based on Standards of Absorbed Dose to Water. TRS No.398.* (International Atomic Energy Agency, Vienna, 2001), https://www-pub.iaea.org/MTCD/Publications/PDF/TRS398_scr.pdf.
- [12] *Calibration of dosimeters used in radiotherapy. TRS No.374.* (International Atomic Energy Agency, Vienna, 1994), https://inis.iaea.org/collection/NCLCollectionStore/_Public/26/037/26037970.pdf.
- [13] P.R. Almond, P.J. Biggs, B.M. Coursey, W.F. Hanson, M.S. Huq, R. Nath, and D.W.O. Rogers, *Med Phys.* **26**(9), 1847-1870 (1999), <https://doi.org/10.1118/1.598691>.
- [14] G.A. Zakaria, W. Schuette, and C. Younan, *Biomed Imaging Interv. J.* **7**(2), 1-10 (2011), <https://www.ncbi.nlm.nih.gov/pmc/articles/PMC3265153/pdf/biij-07-e15.pdf>.
- [15] G.A. Zakaria, and W. Schütte, *Zeitschrift für medizinische physik*, **13**(4), 281-289 (2003), <https://doi.org/10.1078/0939-3889-00182>.
- [16] G.A. Zakaria, and W. Schütte, *J. Med Phys.* **32**(1), 3-11 (2007), <https://doi.org/10.4103/0971-6203.31143>.
- [17] D.I. Thwaites, B. Mijnheer, and J.A. Mills, in: *Radiation Oncology Physics: A Handbook for Teachers and Students*, edited by E.B. Podgorsak (International Atomic Energy Agency, Vienna, 2005), pp. 407-450, <http://www-naweb.iaea.org/nahu/DMRP/documents/Chapter12.pdf>.

**ДОСЛІДЖЕННЯ ПРОТОКОЛІВ ДОЗИМЕТРІЇ ДЛЯ ПРИСКОРЕНИХ ФОТОНІВ І ЕЛЕКТРОНІВ
ВІД МЕДИЧНОГО ЛІНІЙНОГО ПРИСКОРЮВАЧА**

**АКМ Мойнул Гаку Миз^a, Сантуну Пурохіт^a, М. Шакілур Рахман^b, Абдус Саттар^a, С.М. Енамул Кабір^c,
М. Кавчар Ахмед Патварі^d, Камруннахар Калі^d, М. Джубайер Рахман Аханд^e**

^aФізичний факультет, Університету Читтагонгу, Бангладеш

^bДруга стандартна дозиметрична лабораторія, Комісія з атомної енергії Бангладеш, Савар, Дакка, Бангладеш

^cНаціональний інститут досліджень раку, Дакка, Бангладеш

^dФізичний факультет, Університет Комілла, Бангладеш

^eВійськова Академія Бангладеш, Бхатіарі, Читтагонг, Бангладеш

Особливу увагу в цій статті зосереджено на порівняльному дослідженні дозиметричних протоколів променевої терапії для прискорених фотонів та електронів, що надходять з лінійного медичного прискорювача (LINAC). У цьому дослідженні було проведено порівняння між протоколами (TRS 398, DIN 6800-2 і TG 51) як для електрона, так і для фотона, що надійшли з Clinac 2300CD і Clinac DHX 3186. Ми використовували пучки фотонів з енергіями 6 та 15 МВ та електронні пучки з енергіями 4, 6, 9, 12, 15 та 18 МеВ для обох медичних лінійних прискорювачів. У випадку з Clinac максимальні відхилення відносної дози при D_{max} для пучка фотонів (15 МВ) серед протоколів становило 1,18% між TRS-398 і TG-51, 1,56% між TG-51 і DIN 6800-2, та 0,41% між TRS-398 та DIN 6800-2. І навпаки, ці відхилення становили 3,67% між TRS-398 і TG-51, 3,92% між TG-51 і DIN 6800-2 для 4 МеВ, і 0,95% між TRS-398 і DIN 6800-2 у випадку Clinac 2300 CD для PTW Markus та Exradin A10. При вимірюванні максимальної глибини поглинутої дози у воді за допомогою трьох протоколів спостерігались максимальні відхилення між TRS 398 та TG-51, а також TG51 та DIN 6800-2.

КЛЮЧОВІ СЛОВА: TRS (Серія технічних звітів), TG (Цільова група), DIN (Німецький інститут стандартизації).

PACS: 71.20.Dg; 71.15.Mb; 71.20.-b; 72.20.Pa

INVESTIGATION ON ELECTRONIC AND THERMOELECTRIC PROPERTIES OF (P, As, Sb) DOPED ZrCoBi

 Djelti Radouan^{a,*},  Besbes Anissa^b,  Bestani Benaouda^b

^aTechnology and Solids Properties Laboratory, University of Mostaganem (UMAB) - Algeria

^bSEA2M Laboratory, University of Mostaganem (UMAB) - Algeria

*Corresponding Author: djeltired@yahoo.fr, Radouane.djelti@univ-mosta.dz

Received October 9, 2020; revised December 3, 2020; accepted December 4, 2020

Since the last decade, the half-Heusler (HH) compounds have taken an important place in the field of the condensed matter physics research. The multiplicity of substitutions of transition elements at the crystallographic sites X, Y and (III-V) elements at the Z sites, gives to the HH alloys a multitudes of remarkable properties. In the present study, we examined the structural, electronic and thermoelectric properties of $\text{ZrCoBi}_{0.75}\text{Z}_{0.25}$ ($Z = \text{P, As, Sb}$) using density functional theory (DFT). The computations have been done parallel to the full potential linearized augmented plane wave (FP-LAPW) method as implemented in the WIEN2k code. The thermoelectric properties were predicted via the semi-classical Boltzmann transport theory, as performed in Boltztrap code. The obtained results for the band structure and densities of states confirm the semiconductor (SC) nature of the three compounds with an indirect band gap, which is around 1eV. The main thermoelectric parameters such as Seebeck coefficient, thermal conductivity, electrical conductivity and figure of merit were estimated for temperatures ranging from zero to 1200K. The positive values of Seebeck coefficient (S) confirm that the $\text{ZrCoBi}_{0.75}\text{Z}_{0.25}$ ($x = 0$ and 0.25) are a p-type SC. At the ambient temperature, $\text{ZrCoBi}_{0.75}\text{P}_{0.25}$ exhibit the large S value of 289 $\mu\text{V/K}$, which constitutes an improvement of 22% than the undoped ZrCoBi , and show also a reduction of 54% in thermal conductivity (κ/τ). The undoped ZrCoBi has the lowest ZT value at all temperatures and by substituting bismuth atom by one of the sp elements (P, As, Sb), a simultaneous improvement in κ/τ and S have led to maximum figure of merit (ZT) values of about 0.84 obtained at 1200 K for the three-doped compounds.

KEYWORDS: First-principle, GGA, Doped-semiconductor, Seebeck coefficient, figure of merit

The half-Heusler (HH) semiconductors have attracted substantial interest of researchers, they are considered as alternative and green energy sources because they have the capacity to transform waste heat into electric energy. A significant change in their thermoelectric properties can be observed by the incorporation of a dopant at various concentration rates. Many researches on the thermoelectric properties of HH compounds show moderately high ZT of ≈ 1.0 in the mid to high temperature ranges (700–1000 K) [1] which makes them as potential candidates for high efficiency power generation. Recently, several experimental [2-4] and theoretical [5-7] studies have been focused on the doped HH alloys, these last can be utilized in a broad temperature region and a good part of their raw materials are non-toxic, abundant and cheap [8-11]. The single doping remains one of the effective process, which adjust the electrical power factor and reduce the thermal conductivity [12]. C.C. Hsu et al., [13] have studied the $\text{ZrFe}_x\text{Co}_{1-x}\text{Sb}$ HH and they show that for $x=0.2$, the maximum ZT value of 0.036 was obtained at 900K, they attribute this to reduction of thermal conductivity because the point defects, mass alterations and strain field effects induced by doping vigorously scatter the thermal phonons. Y.Lei et al. [14] have explored the impact of Sb doping on thermoelectric properties of TiNiSn HH, they noted that the ZT value is moderately improved from 0.30 for undoped alloy to 0.44 for a dopant concentration of 3%. R. Akram et al [15] find that the incorporation of 1.5% of Sb in $\text{Hf}_{0.25}\text{Zr}_{0.75}\text{NiSn}$ HH enhanced the electrical properties by increasing the carrier concentration and reducing the thermal conductivity. A maximal ZT value of 0.83 was achieved at 923 K, which constitute 67% of improvement compared to the undoped sample value. In another work [16], the $\text{La}_x\text{Zr}_{1-x}\text{NiSn}$ compounds, was synthesized by induction melting combined with plasma-activated sintering, the x-ray diffraction confirms that for all x-concentration of La, the structures remain cubic with space group F-43m. A particular drop in thermal conductivity was found following doping by La, thus leading to ZT of 0.53 at 923 K, which represent an enhancement of about 37% compared to the pristine sample. In the present work, we studied the electronic and thermoelectric properties of sp elements (P, As, Sb)-doped ZrCoBi half-Heusler alloy. A brief commentary on the band structure and densities of states are given. A particular emphasis was placed on the thermoelectric properties investigated by the semi-classical Boltzmann theory.

COMPUTATIONAL METHOD

The computations are performed by the full potential linearized augmented plane wave (FP-LAPW) method [17-18] based on DFT [19] as implemented in Wien2K package [20]. The generalized gradient approximation (GGA) [21] is employed for the exchange-correlation potential. The muffin-tin sphere radii RMT were chosen as equal to 1.85, 2.1 and 2.5 a.u for the Zr, Co and (Bi / P, As, Sb) atoms respectively. For convergence, the energy cut off = -6.0 Ry, $G_{\text{max}}=12$, $l_{\text{max}}=10$ and $\text{RMT} \cdot K_{\text{max}}=7$ are used. The $22 \times 22 \times 22$ k-point mesh is used for electronic properties calculation. The self-consistency is achieved up to 0.0001 Ry. The space group of cubic ZrCoBi is 216 (F-43m). According to reference [22], the compound is stable in paramagnetic phase and the atomic coordinates are (0, 0, 0), (0.25, 0.25, 0.25) and (0.5, 0.5, 0.5) for Zr, Co and Bi respectively. With the aim of creating 25 % concentration of doping in

ZrCoBi lattice, the supercell $1 \times 1 \times 1$ containing twelve atoms is constructed. The dopant elements (Phosphor, Arsenic and Antimony) was substituted at the Bismuth site. The space group number of this generated super cell is 215 (P-43m) which contains 4 Zr atoms, 4 Co atoms and 4 Bi atoms. For the four Bi atom, the one who is situated at the (0, 0, 0) position was replaced with (P/As/Sb) atom without disturbing the other eleven atoms (4 Zr, 4 Co and 3 Bi) in the supercell. The semi-classical Boltzmann approach [23] as given in the BoltzTraP code associated to a fine grid mesh of $(46 \times 46 \times 46)$ were employed to investigate the thermoelectric response of compounds doped and undoped.

RESULTS AND DISCUSSION

Structural and electronic properties

The crystal structure of the perfect ZrCoBi HH and the doped $ZrCoBi_{0.75}Z_{0.25}$ ($Z = P, As, Sb$) are plotted by the CrystalMaker 2.7 software [24]. The undoped structure of ZrCoBi (Fig.1a) is formed by three interpenetrating fcc sublattices, which are occupied by Zr, Co and Bi elements. Its lattice constant obtained from optimization is in good agreement with the value of 6.22 Å, achieved by G. Surucu [22] using the GGA-PBE.

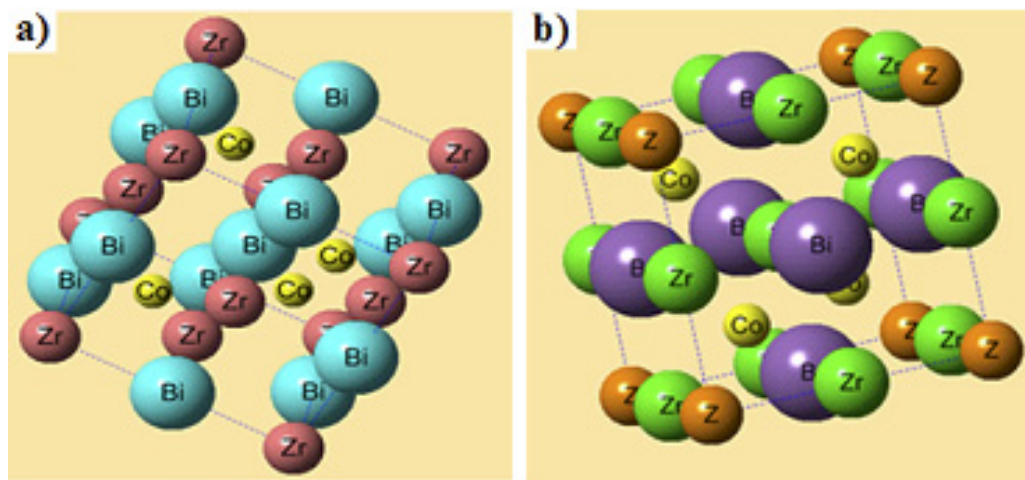


Figure 1. a) - Crystal structure of half-Heusler semiconductor ZrCoBi, b) - 12 atom simple cubic model of $ZrCoBi_{0.75}Z_{0.25}$ ($Z = P, As, Sb$) structure.

The crystal structures of $ZrCoBi_{0.75}Z_{0.25}$ ($Z = P, As, Sb$) are cubic with the space group of P-43m; the structure can be regarded as four interpenetrating fcc sublattices (Fig. 1b). The calculated structural properties such as lattice constants a , bulk modulus B , first derivatives B' and equilibrium energies E_{min} are recapitulated in Table 1.

Table 1.

Calculated lattice constant $a_0(\text{Å})$, bulk modulus $B(\text{GPa})$, derivative of the bulk modulus, $B'(\text{GPa})$, minimum total energy per unit cell E_{min} (Ry) and Gap energy (eV)

Compounds	Space group	A (Å)	B (GPa)	B'	E_{min} (Ry)	Gap (eV)
Undoped - ZrCoBi	216 F-43m	6.23	120.31	4.94	-53148.552763	0.990
$ZrCoBi_{0.75}P_{0.25}$	215 P-43m	6.12	131.34	5.23	-170115.352819	1.018
$ZrCoBi_{0.75}As_{0.25}$		6.14	128.07	5.10	-173953.361417	1.008
$ZrCoBi_{0.75}Sb_{0.25}$		6.19	124.95	4.95	-182398.455731	0.996

The lattice constants for $ZrCoBi_{0.75}P_{0.25}$, $ZrCoBi_{0.75}As_{0.25}$, $ZrCoBi_{0.75}Sb_{0.25}$, show increase from P to Sb dopant. The three doping elements are electronegative and their atomic radii in increasing order is P, As and Sb. Fig. 2(a–d) show the calculated electronic band structure with high symmetric Brillouin zone W-L- Γ -X-W-K for undoped ZrCoBi and $ZrCoBi_{0.75}Z_{0.25}$ ($Z = P, As, Sb$) Half-Heusler using the GGA approach. For the pristine case, the Fermi level lies inside the forbidden gap and the valance band maxima (VBM) and conduction band minima (CBM) occur at the L and X points, thus generating an indirect band gap of about 0.99 eV, which confirms the semiconducting nature of compound. The introduction of sp elements (P, As, Sb) ions into ZrCoBi shifts the bottom point of the conduction band towards a higher energy than the undoped ZrCoBi, thus increasing the band gap. The values to 0.996 eV, 1.008 eV and 1.018 eV are obtained for $ZrCoBi_{0.75}Sb_{0.25}$, $ZrCoBi_{0.75}As_{0.25}$ and $ZrCoBi_{0.75}P_{0.25}$ respectively. The VBM and the CBM are located at the L and Γ points, which indicates the change in momentum of the electrons during their transitions from VBM to CBM. Consequently, all the $ZrCoBi_{0.75}Z_{0.25}$ ($Z = P, As, Sb$) compounds are indirect band gap semiconductors. In order to study the positioning of the orbital's in the electronic band structure as well as the electrons involving in the shaping of the band gap, the total anacd partial density of states (TDOS/PDOSS) of pure and sp element (P, As, and Sb) doped ZrCoBi are investigated between -4 and 4 eV Fig. 3(a-d). The dashed line displays the Fermi energy level (EF). We can see that the

top of the VB is mainly determined by the hybridization of d-Zr, d-Co, P-Bi and p-P states, whereas the bottom of the CB is formed primarily by the d-states of Co and Zr. From [- 4 to - 2eV], the anion d-Zr, d-Co, P-Bi and p-P states depict the lowest bands, these states are separated the main valence state (d-Co) by a small gap. The (PDOS) in this energy range is more pronounced for P-doped ZrCoBi than for As-doped ZrCoBi or Sb-doped ZrCoBi. The density of states near the Fermi level for the $ZrCoBi_{0.75}Z_{0.25}$ (Z = P, As, Sb) HH, can be attributed to d-d orbitals hybridization between transition metals (Zr/Co). The p-orbitals of the Z atom contribute only slightly to the electronic properties. The offset of the valence bands toward the low energies is more larger for $ZrCoBi_{0.75}Z_{0.25}$ (Z = P, As, Sb) than that for undoped-ZrCoBi, while the conduction bands remain almost in the same energy range (Fig. 3a). We observe that with increasing in atomic number of dopant element a shift of the main peak (d-Co) towards higher energies occurs [P (-1.22 eV)/As (-1.08 eV)/Sb (-1.04 eV)].

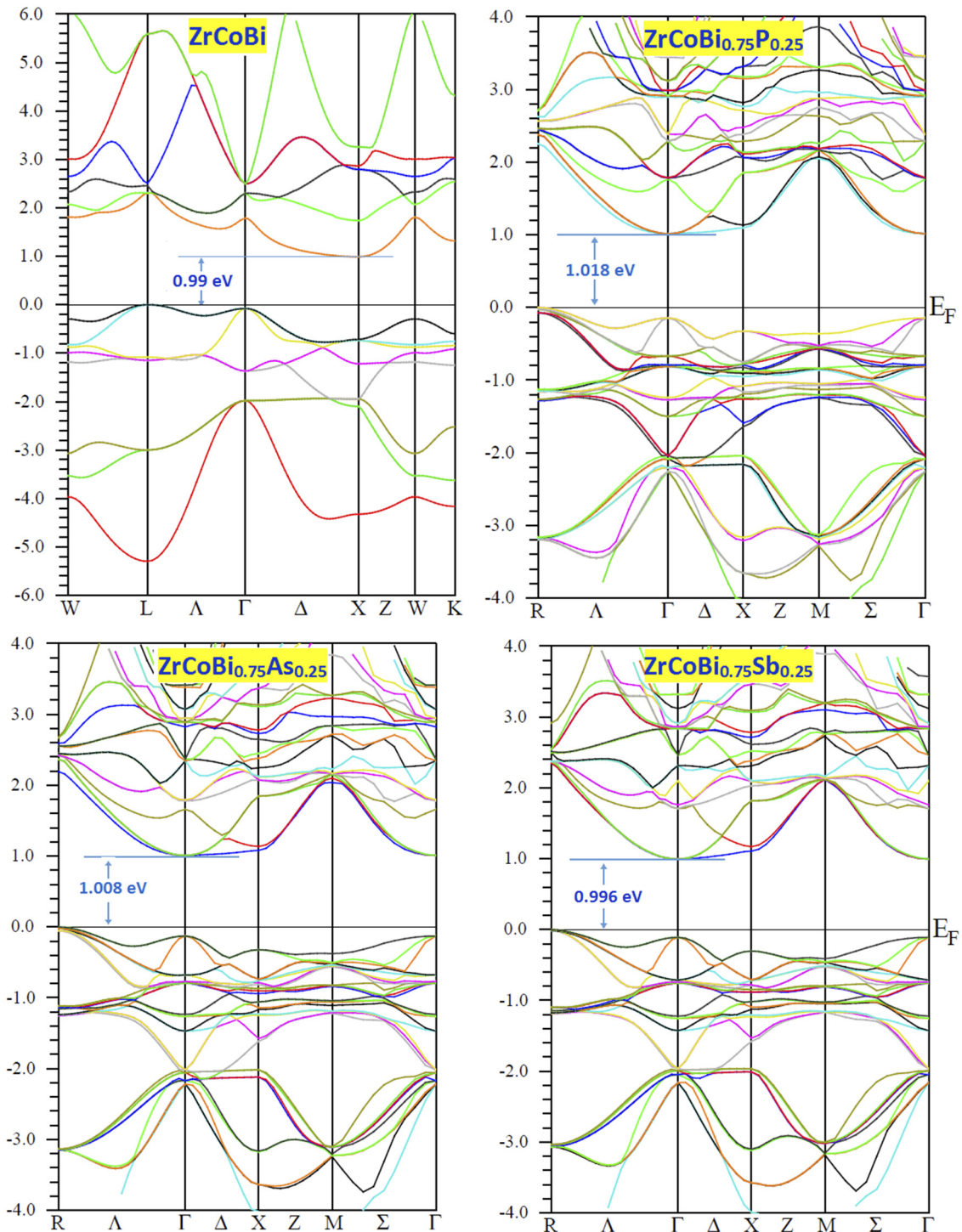


Figure 2. Band structure for a) undoped ZrCoBi, b) $ZrCoBi_{0.25}P_{0.25}$, c) $ZrCoBi_{0.25}As_{0.25}$ and d) $ZrCoBi_{0.25}Sb_{0.25}$.

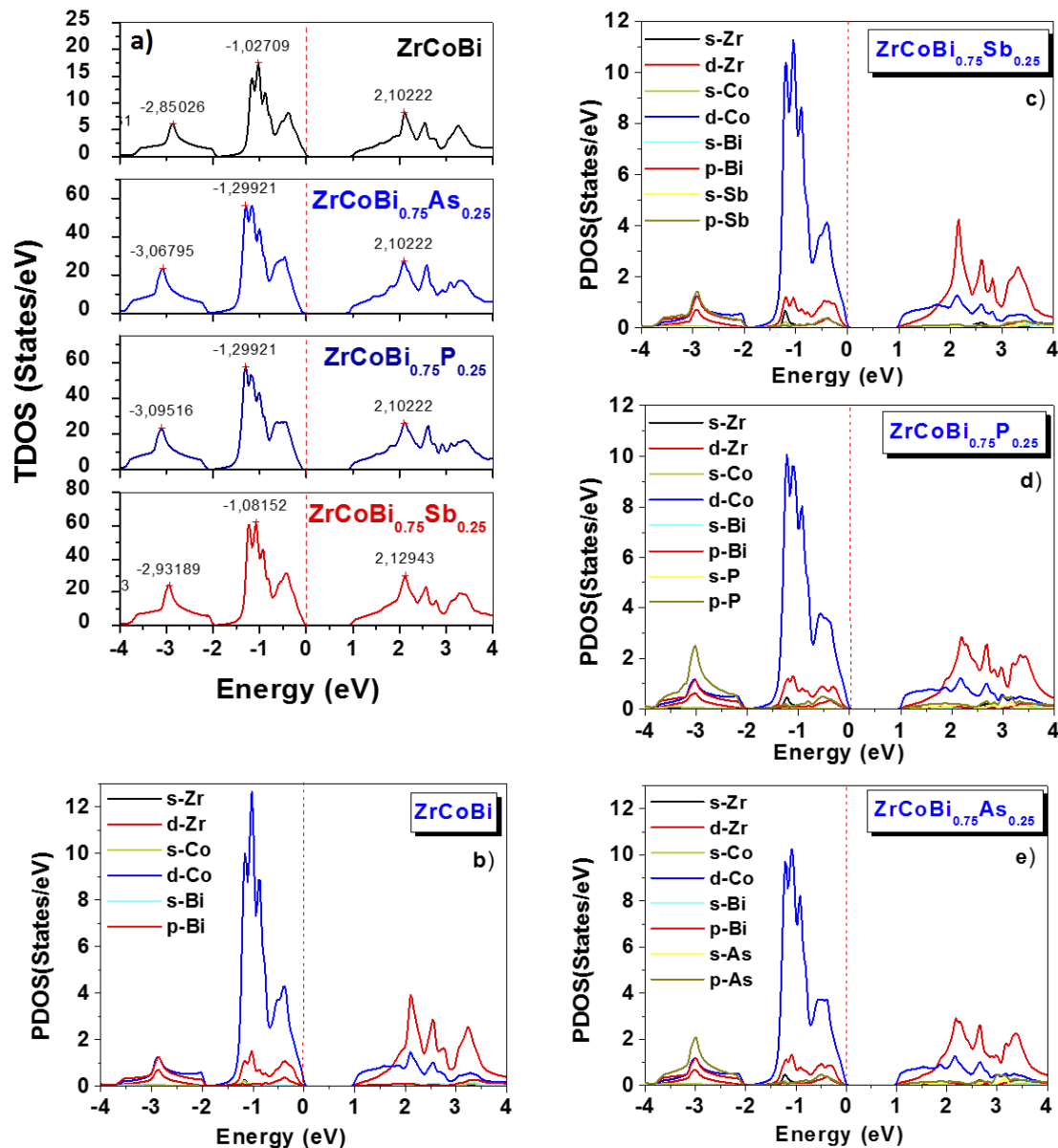


Figure 3. a) - Total density of states (TDOS), b-d) - Partial densities of states (PDOS)

Thermoelectric properties

The appropriate choice of the doping as well as its concentration remain among the principal factors which maximize the ZT of semiconductors and which make them suitable for the thermoelectric applications. The transport properties will be computed with BoltzTraP code under a constant relaxation time approximation of the charge carriers. The main thermoelectric parameters, such as Seebeck coefficient (S), electrical conductivity (σ/τ), thermal conductivity (κ/τ) and figure of merit (ZT) will be investigated as function of temperature [25-26]. The temperature reliance of S is shown in Fig. 4c. It is observed that beyond temperature of 400 K, the Seebeck coefficient (S) decrease steadily with the increase of temperature for the ZrCoBi_{0.75}Z_{0.25} (Z = P, As, Sb) HH. This limitation of S at high temperature can be attributed to the bipolar effects which occur for wide-bandgap semiconductors and which result in an increase of thermal conductivity [27]. Among the three doped compounds, the P-doped ZrCoBi exhibit the large Seebeck coefficient of 289 $\mu\text{V/K}$ between 300 to 400 K, this obtained value of S has been improved by 22% than the undoped ZrCoBi. With the increased of the atomic mass of the doping element, a diminution of S was observed. The positive values of Seebeck coefficient confirm that the ZrCoBi_{0.75}Z_{0.25} (Z = P, As, Sb) are p-type semiconductors. The obtained values of S around room temperature are larger to those reported by several doped and undoped HH compounds such TiCoSn_xSb_{1-x} [28], FeV_{1-x}Hf_xSb [29], PdZrGe [30] ScRhTe [31]. Our compounds are good thermoelectric materials (TM), because according to J.W. Sharp [32], the best TM are highly doped semiconductors with a Seebeck coefficient located in the domain 150 – 250 $\mu\text{V K}^{-1}$. The ability of the ZrCoBi_{0.75}Z_{0.25} (Z = P, As, Sb) HH to transfer heat is investigated in this section by the computation of its thermal conductivity (κ/τ). Fig. 4b shows temperature dependence of κ/τ of doped and undoped ZrCoBi.

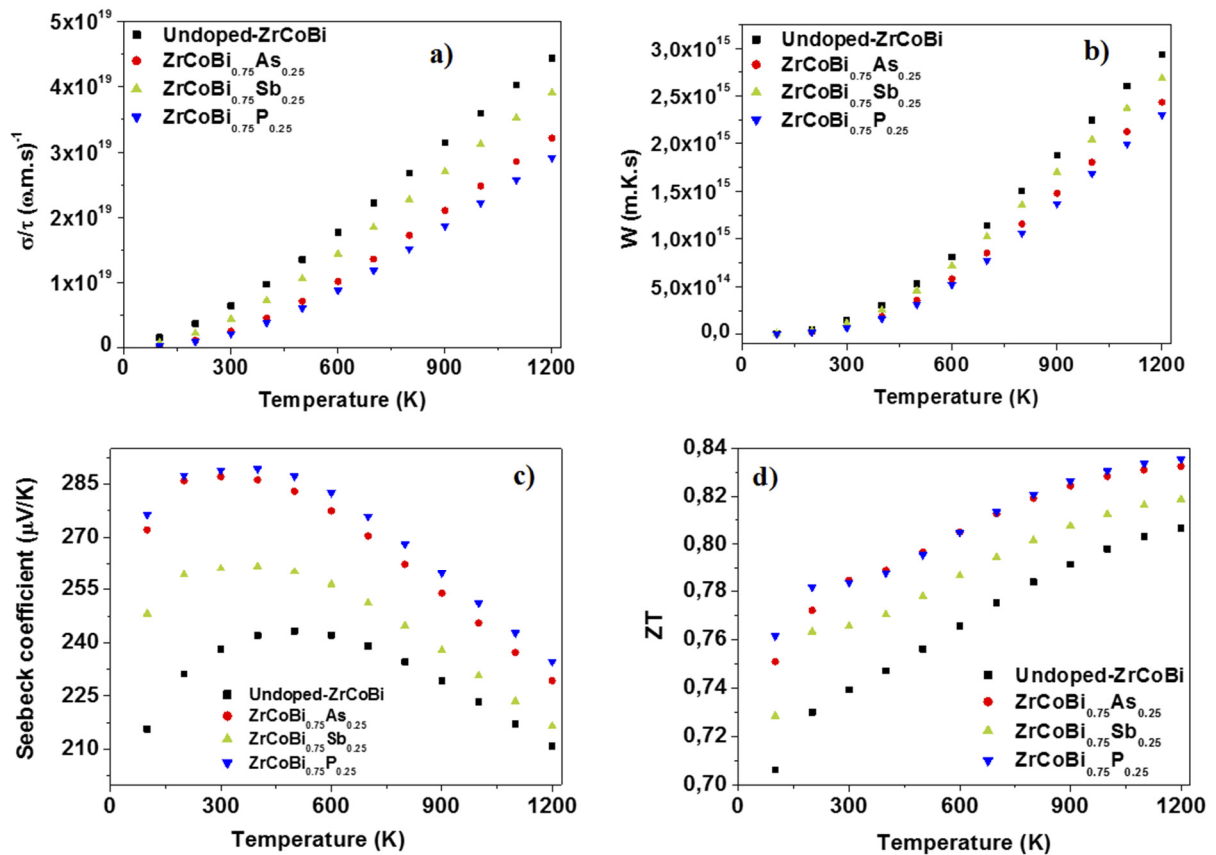


Figure 4. Thermoelectric properties versus temperature
 a) Electrical conductivity b) Thermal conductivity c) Seebeck coefficient and d) figure of merit

We can see that doping reliance of the κ/τ showed a decreasing value comparatively to the undoped ZrCoBi, which is advantageous for improving the ZT value. After 400 K, the κ/τ , which is directly allied with electrical conductivity, augments with temperature in a very linear trend and the slope of the κ/τ curves increases with increasing the Z-atomic number. The κ/τ which is also influenced by the evolution of charge-carrier concentration, show at 300 K a value of about $5.9 \cdot 10^{13}$ W/m.K.s which is comparable with that of $\text{Pb}_7\text{Bi}_4\text{Se}_{13}$ [33], CdSe, CdTe [34]. In comparison with undoped ZrCoBi, a reduction of nearly 23% in the κ/τ was obtained at 1200 K by the substitution of the Bismuth site by the Phosphor. Around the ambient temperature, the κ/τ is weak then it sudden increases with the increasing in temperature this is due to electron-phonon scattering [35]. With an increase from $5.91 \cdot 10^{12}$ mKs at 100 K to $2.69 \cdot 10^{15}$ mKs at 1200 K, and with value of $6.50 \cdot 10^{13}$ W/mKs at room temperature (300 K), the $\text{ZrCoBi}_{0.75}\text{Sb}_{0.25}$ constitutes a good thermal conductor. The effectiveness of thermoelectric devices requires a sufficiently high electrical conductivity (σ/τ) to achieve a high figure of merit (ZT). Fig. 4(a) shows the temperature dependence of σ/τ for the $\text{ZrCoBi}_{0.75}\text{Z}_{0.25}$ compounds. The σ/τ displays exponential growth with increasing temperature due to the increase in the number of carriers. The $\text{ZrCoBi}_{0.75}\text{Sb}_{0.25}$ exhibits the highest value of σ/τ comparatively to $\text{ZrCoBi}_{0.75}\text{As}_{0.25}$ and $\text{ZrCoBi}_{0.75}\text{P}_{0.25}$, because the antimony shows the greater atomic weight to that of arsenic and phosphor. The increase in atomic weight augments the number of electronic layer and nucleus grip on the valence electrons then becomes weak. Several electrons are pushed toward the conduction band leading to improve the σ/τ values [23]. At room temperature, the σ/τ is of $4.41 \cdot 10^{18}$, $2.52 \cdot 10^{18}$ and $2.09 \cdot 10^{18}$ ($\Omega \cdot \text{m} \cdot \text{s}$)⁻¹ for $\text{ZrCoBi}_{0.75}\text{Sb}_{0.25}$, $\text{ZrCoBi}_{0.75}\text{As}_{0.25}$ and $\text{ZrCoBi}_{0.75}\text{P}_{0.25}$ respectively. These values increase with the temperature and reaches the maximum of $3.91 \cdot 10^{19}$, $3.21 \cdot 10^{19}$ and $2.91 \cdot 10^{19}$ ($\Omega \cdot \text{m} \cdot \text{s}$)⁻¹ at 1200 K. The increasing trend of σ/τ displayed for doped ZrCoBi and undoped ZrCoBi is in agreement with previous studies done on the semiconductors compounds [36-37]. The calculated values of figure of merit versus temperature are presented in Fig. 4d. There is a continuous increase in ZT with increasing temperature. The undoped ZrCoBi has the lowest ZT value at all temperatures and by substituting bismuth atom by one of the sp elements (P, As, Sb), an increase of the ZT was observed. A maximum ZT = 0.85 was obtained at 1200 K with a 25% P-substitution at the Bi-site. At low temperature (100 K), the deviation of ZT between the doped and undoped structures is much more marked. The high values of the Seebeck coefficient as well as the electrical conductivity of $\text{ZrCoBi}_{1-x}\text{Z}_x$ alloys did not translate into high values of ZT because of rather high thermal conductivity. The difference in mass and radius between Bi and Z are responsible for the high thermal conductivity. However, others adjustment remains necessary for more improvement let's quote the concentration of the dopant element which should be optimized to decrease more the density of transport electrons also the use of second substituting atom (co-doping) with larger mass can reduce the thermal conductivity [38]. Despite that, the figure of merit and Seebeck

coefficients values obtained and which have been widely improved by doping we can conclude that ours doped compounds have the capacity to transform waste heat into electric energy and may be also used in various thermoelectrically devices.

CONCLUSION

By using the first-principle density-functional theory within the supercell approach, we have studied the $\text{ZrCoBi}_{0.75}\text{Z}_{0.25}$ ($Z = \text{P, As, Sb}$) half-Heusler, a particular emphasis was placed on the thermoelectric properties. The calculated band structures reveal that the doped and undoped-ZrCoBi are indirect band gap semiconductors. The substitution of the Bi site by P, As and Sb is found effective in decreasing thermal conductivity and increasing the Seebeck coefficient and figure of merit value. Comparatively to undoped-ZrCoBi, the $\text{ZrCoBi}_{0.75}\text{P}_{0.25}$ show improvements of 22% and 54% of its Seebeck coefficient and thermal conductivity respectively. An enhancement of ZT values of 7.8% and 6.1% have been observed at 100K and 300K between the undoped-ZrCoBi and P-doped ZrCoBi half-Heusler. In order to further boost the performance of these alloys, future work will focus on single doping with very low dopant concentration as well as on co-doping.

ORCID IDs

 Djelti Radouan, <https://orcid.org/0000-0002-0762-5818>;  Besbes Anissa, <https://orcid.org/0000-0002-2853-1909>;
 Bestani Benaouda, <https://orcid.org/0000-0002-1104-0900>

REFERENCES

- [1] T. Zhu, C. Fu, H. Xie, Y. Liu, and X. Zhao, *Adv. Energy Mater.* **5**, 1-13 (2015), <https://doi.org/10.1002/aenm.201500588>.
- [2] I.P. Ezekiel, and T. Moyo, *Journal of Alloys and Compounds*, **749**, 672-680 (2018), <https://doi.org/10.1016/j.jallcom.2018.03.349>.
- [3] A. Karati, S. Mukherjee, R.C. Mallik, R. Shabadi, B.S. Murty, and U.V. Varadaraju, *Materialia*, **7**, 100410 (2019), <https://doi.org/10.1016/j.mtla.2019.100410>.
- [4] A. Bandyopadhyaya, S.K. Neogia, A. Paul, C. Meneghini, I. Dasgupta, and S. Ray, *Journal of Alloys and Compounds*, **764**, 656-664 (2018), <https://doi.org/10.1016/j.jallcom.2018.06.065>.
- [5] T.C. Chibueze, A.T. Raji, and C.M.I. Okoye, *Chemical Physics*, **530**, 110635 (2020), <https://doi.org/10.1016/j.chemphys.2019.110635>.
- [6] Z. Wendan, L. Yong, L. Yunsheng, W. Jiahua, H. Zhiling, and S. Xiaohong, *Chemical Physics Letters*, **741**, 137055 (2020), <https://doi.org/10.1016/j.cplett.2019.137055>.
- [7] J. Shen, L. Fan, C. Hu, T. Zhu, J. Xin, T. Fu, D. Zhao, and X. Zhao, *Materials Today Physics*, **8**, 62-70 (2019), <https://doi.org/10.1016/j.mtphys.2019.01.004>.
- [8] A. Bhardwaj, and D.K. Misra, *J. Mater. Chem. A*, **2**, 20980-20989 (2014), <https://doi.org/10.1039/C4TA04661G>.
- [9] E. Lkhagvasuren, S. Ouardi, G.H. Fecher, G. Auffermann, G. Kreiner, W. Schnelle, and C. Felser, *Optimized thermoelectric performance of the n -type half-Heusler material TiNiSn by substitution and addition of Mn*, *AIP Advances*, **7**, 045010 (2017), <https://doi.org/10.1063/1.4979816>.
- [10] S. Chen, and Z. Ren, *Mater. Today*, **16**(10), 387-395 (2013), <https://doi.org/10.1016/j.mattod.2013.09.015>.
- [11] S.J. Poon, D. Wu, S. Zhu, W. Xie, T.M. Tritt, P. Thomas, and R. Venkatasubramanian, *J. Mater. Res.* **26**, 2795-2802 (2011), <https://doi.org/10.1557/jmr.2011.329>.
- [12] J. Shen, C. Fu, Y. Liu, X. Zhao, and T. Zhu, *Energy Storage Materials*, **10**, 69-74 (2018), <https://doi.org/10.1016/j.ensm.2017.07.014>.
- [13] C.-C. Hsu, and H.-K. Ma, *Materials Science and Engineering B*, **198**, 80-85 (2015), <https://doi.org/10.1016/j.mseb.2015.03.015>.
- [14] Y. Lei, C. Cheng, Y. Li, R. Wan, and M. Wang, *Ceramics International*, **43**, 9343-9347 (2017), <https://doi.org/10.1016/j.ceramint.2017.04.100>.
- [15] R. Akram, Y. Yan, D. Yang, X. She, G. Zheng, X. Su, and X. Tang, *Intermetallics*, **74**, 1-7 (2016), <https://doi.org/10.1016/j.intermet.2016.04.004>.
- [16] R. Akram, Q. Zhang, D. Yang, Y. Zheng, Y. Yan, X. Su, and X. Tang, *Journal of electronic materials*, **44**(10), 3563-3570 (2015), <https://doi.org/10.1007/s11664-015-3882-6>.
- [17] O.K. Andersen, *Phys. Rev. B*, **42**, 3060 (1975), <https://doi.org/10.1103/PhysRevB.12.3060>.
- [18] D.J. Singh, *Planes Waves, Pseudo-potentials and the LAPW Method*, (Kluwer Academic Publishers, Boston, 1994).
- [19] P. Hohenberg, and W. Kohn, *Phys. Rev. B*, **136**, 864-871 (1964), <https://doi.org/10.1103/PhysRev.136.B864>.
- [20] P. Blaha, K. Schwarz, G.K.H. Madsen, D. Kvasnicka, and J. Luitz, *WIEN2k, An Augmented Plane Wave Plus Local Orbitals Program for Calculating Crystal Properties*, (Vienna University of Technology, Austria, 2001), pp. 269, http://www.wien2k.at/reg_user/textbooks/usersguide.pdf.
- [21] J.P. Perdew, K. Burke, and M. Ernzerhof, *Phys. Rev. Lett.* **77**, 3865 (1996) 68, <https://doi.org/10.1103/PhysRevLett.77.3865>.
- [22] G. Surucu, M. Isik, A. Candan, X. Wang, and H.H. Gullu, *Physica B*, **587**, 412146 (2020), <https://doi.org/10.1016/j.physb.2020.412146>.
- [23] G.K.H. Madsen, D.J. Singh, *Comput. Phys. Commun.* **175**, 67-71 (2006), <https://doi.org/10.1016/j.cpc.2006.03.007>.
- [24] CrystalMaker software Ltd, Begbroke, Oxfordshire OX5 1PF, UK, <http://www.crystalmaker.com>.
- [25] R. Hasan, and S.-C. Ur, *Transactions on Electrical and Electronic Materials*, **19**(2), 106-111 (2018), <https://doi.org/10.1007/s42341-018-0024-x>.
- [26] T. Wu, W. Jiang, X. Li, S. Bai, S. Liufu, and L. Chen, *Journal of Alloys and Compounds*, **467**(1-2), 590-594 (2009), <https://doi.org/10.1016/j.jallcom.2007.12.055>.
- [27] G.J. Snyder, and E.S. Toberer, *Nat. Mater.* **7**(2), 105-114 (2008), <https://doi.org/10.1038/nmat2090>.
- [28] T. Sekimoto, K. Kurosaki, H. Muta, and S. Yamanaka, *Journal of Alloys and Compounds*, **407**, 326-329 (2006), <https://doi.org/10.1016/j.jallcom.2005.06.036>.
- [29] A. El-Khouly, A. Novitskii, A.M. Adam, A. Sedegov, A. Kalugina, D. Pankratova, D. Karpenkov, and V. Khovaylo, *Journal of Alloys and Compounds*, **820**, 153413 (2020), <https://doi.org/10.1016/j.jallcom.2019.153413>.

- [30] B. Anissa, D. Radouan, B. Benaouda, and A. Omar, Chinese Journal of Physics, **56**, 2926–2936 (2018), <https://doi.org/10.1016/j.cjph.2018.09.027>.
- [31] K. Kaur, and J. Kaur, Journal of Alloys and Compounds, **715**, 297-303 (2017), <https://doi.org/10.1016/j.jallcom.2017.05.005>.
- [32] J.W. Sharp, in: *Encyclopedia of Condensed Matter Physics*, edited by F. Bassani, G.L. Liedl, and P. Wyder, (Academic Press, Cambridge, MA, 2005), pp. 173-180, <https://doi.org/10.1016/B0-12-369401-9/00507-6>.
- [33] S. Azam, S. Goumri-Said, S.A. Khan, H. Ozisik, E. Deligoz, M.B. Kanoun, and W. Khan, Materialia, **10**, 100658 (2020), <https://doi.org/10.1016/j.mtla.2020.100658>.
- [34] M. Naseri, D.M. Hoat, J.F. Rivas-Silva, and G.H. Coccoletz, Optik, **210**, 164567 (2020), <https://doi.org/10.1016/j.ijleo.2020.164567>.
- [35] V.F. Gantmakher, Reports on Progress in Physics, **37**(3), 317 (1974), <https://doi.org/10.1088/0034-4885/37/3/001>.
- [36] A.A. Khan, I. Khan, I. Ahmad, and Z. Ali, Materials Science in Semiconductor Processing, **48**, 85-94 (2016), <https://doi.org/10.1016/j.mssp.2016.03.012>.
- [37] S. Azam, M. Umer, U. Saeed, W. Khan, M. Irfan, Z. Abbas, and I.V. Kityk, Journal of Molecular Graphics and Modelling, **94**, 107484 (2020), <https://doi.org/10.1016/j.jmkgm.2019.107484>.
- [38] M.A.A. Mohamed, E.M.M. Ibrahim, N.P. Rodriguez, S. Hampel, B. Büchner, G. Schierning, K. Nielsch, and R. He, Acta Materialia, **196**, 669–676 (2020), <https://doi.org/10.1016/j.actamat.2020.07.028>.

ДОСЛІДЖЕННЯ ЕЛЕКТРОННИХ ТЕРМОЕЛЕКТРИЧНИХ ВЛАСТИВОСТЕЙ ZrCoBi ЛЕГОВАНОГО (P, As, Sb)

Джелті Радуан^a, Бесбес Аніса^b, Бестані Бенауда^b

^aЛабораторія технологій та властивостей твердих речовин, Університет Мосаганему (UMAB) – Алжир

^bЛабораторія SEA2M, Університет Мосаганему (UMAB) – Алжир

Протягом останнього десятиріччя напів-Гайслерові сполуки (НН) займають важливе місце в галузі досліджень фізики конденсованої речовини. Численність заміщень перехідних елементів на кристалографічних ділянках X, Y та (III-V) елементів на Z-ділянках надає сплавам напів-Гайслера (НН) безліч надзвичайних властивостей. У цьому дослідженні ми вивчали структурні, електронні та термоелектричні властивості ZrCoBi_{0.75}Z_{0.25} (Z = P, As, Sb), використовуючи теорію функціоналу щільності (DFT). Розрахунки проводились паралельно з використанням метода повного потенціалу лінеаризованої розширеної плоскої хвилі (FP-LAPW), який був реалізований в коді WIEN2k. Термоелектричні властивості були прогнозовані за допомогою напівкласичної теорії транспорту Больцмана, яка була реалізована в коді Больцтрапа. Отримані результати для зонної структури та щільностей станів підтверджують напівпровідникову (SC) природу трьох сполук із непрямым проміжком енергетичної зони, який становить близько 1 eV. Основні термоелектричні параметри, такі як коефіцієнт Зеебека, теплопровідність, електропровідність та порівняльний показник якості, були оцінені для температур від нуля до 1200K. Позитивні значення коефіцієнта Зеебека (S) підтверджують, що ZrCoBi_{0.75}Z_{0.25} (x = 0 та 0,25) є SC типу p. При температурі навколишнього середовища ZrCoBi_{0.75}P_{0.25} демонструє значну величину (S), яка складає 289 μV/K, що означає покращення на 22% порівняно з нелегованим ZrCoBi, а також демонструє зменшення теплопровідності на 54% (κ/τ). Нелегований ZrCoBi має найнижче значення ZT при будь-яких температурах, і, при заміщенні атома вісмуту одним із sp-елементів (P, As, Sb), одночасне покращення κ/τ та S призводить до досягнення максимальних значень порівняльного показника якості (ZT) ~ 0,84, отриманого при 1200 K для трьох легованих сполук.

КЛЮЧОВІ СЛОВА: першооснова, GGA, легований напівпровідник, коефіцієнт Зеебека, порівняльний показник якості

PACS: 68.65.Pq, 68.55.Jk, 68.37.Hk, 68.37.-d, 71.20.-b, 71.20.Nr

ELECTRICAL AND PHOTOELECTRIC PROPERTIES OF HETEROJUNCTIONS MoO_x/n-Cd_{1-x}Zn_xTe

 Mykhailo M. Solovan^a,
  Andrii I. Mostovyi^a,
  Hryhorii P. Parkhomenko^{a,*},
 Viktor V. Brus^b,
  Pavlo D. Maryanchuk^a

^aYuriy Fedkovych Chernivtsi National University
2 Kotsyubinsky Str., 58012 Chernivtsi, Ukraine

^bNazarbayev University, 53 Kabanbay Batyr, 010000, Nur-Sultan City, Kazakhstan

*Corresponding Author: h.parkhomenko@chnu.edu.ua

Received December 21, 2020; revised February 17, 2021; accepted February 18, 2021

The paper presents the results of studies of the optical and electrical properties of MoO_x/n-Cd_{1-x}Zn_xTe semiconductor heterojunctions made by depositing MoO_x films on a pre-polished surface of n-Cd_{1-x}Zn_xTe plates (5 × 5 × 0.7 mm³) in a universal vacuum installation Leybold - Heraeus L560 using reactive magnetron sputtering of a pure Mo target. Such studies are of great importance for the further development of highly efficient devices based on heterojunctions for electronics and optoelectronics. The fabricated MoO_x/n-Cd_{1-x}Zn_xTe heterojunctions have a large potential barrier height at room temperature ($\phi_0 = 1.15$ eV), which significantly exceeds the analogous parameter for the MoO_x/n-CdTe heterojunction ($\phi_0 = 0.85$ eV). The temperature coefficient of the change in the height of the potential barrier was experimentally determined to be $d(\phi_0)/dT = -8.7 \cdot 10^{-3}$ eV K, this parameter is four times greater than the temperature coefficient of change in the height of the potential barrier for MoO_x/n-CdTe heterostructures. The greater value of the potential barrier height of the MoO_x/n-Cd_{1-x}Zn_xTe heterojunction is due to the formation of an electric dipole at the heterointerface due to an increase in the concentration of surface states in comparison with MoO_x/n-CdTe heterostructures, and this is obviously associated with the presence of zinc atoms in the space charge region and at the metallurgical boundary section of the heteroboundary. In MoO_x/n-Cd_{1-x}Zn_xTe heterojunctions, the dominant mechanisms of current transfer are generation-recombination and tunneling-recombination with the participation of surface states, tunneling with forward bias, and tunneling with reverse bias. It was found that MoO_x/n-Cd_{1-x}Zn_xTe heterojunctions, which have the following photoelectric parameters: open circuit voltage $V_{oc} = 0.3$ V, short circuit current $I_{sc} = 1.2$ mA/cm², and fill factor $FF = 0.33$ at an illumination intensity of 80 mW/cm² are promising for the manufacture of detectors of various types of radiation. The measured and investigated impedance of the MoO_x/n-Cd_{1-x}Zn_xTe heterojunction at various reverse biases, which made it possible to determine the distribution of the density of surface states and the characteristic time of their charge-exchange, which decrease with increasing reverse bias.

KEYWORDS: heterojunction, molybdenum oxide, Cd_{1-x}Zn_xTe, impedance, surface states.

Телурид кадмію та тверді розчини на його основі Cd_{1-x}Zn_xTe є перспективними матеріалами для виготовлення приладів напівпровідникової мікроелектроніки [1]. Близькі до оптимальних значень для фотоелектричного перетворення енергії ширини заборонених зон $E_g = 1,5$ eV (CdTe) та $E_g = 1,5 - 1,55$ eV (CdZnTe) і високий коефіцієнт поглинання світла ($\alpha = 10^5$ см⁻¹ при енергії фотонів $h\nu \geq E_g$) сприяють застосуванню цих напівпровідників для створення сонячних елементів.

В свою чергу, оксиди перехідних металів, зокрема оксид молібдену, є одним з найбільш перспективним електронним матеріалом. Прозорі провідні шари широко використовуються для виготовлення приладів електроніки, оптоелектроніки та сонячної енергетики. В останні роки інтенсивно досліджуються напівпровідникові гетеропереходи на основі оксидів тонких плівок. MoO_x прозорий в області видимого спектра, а також відносно добре проводить струм [2,3]. Відомо, що матеріали з великою роботою виходу здатні утворювати омичний контакт із широкозонними напівпровідниками р-типу провідності. Проте тонкі плівки з великою роботою виходу, нанесені на підкладки n-типу провідності, утворюють високоякісні випрямляючі діоди Шотткі або гетеропереходи [4,5]. Тому цікаво виготовити гетеропереходи де широкозонна провідна плівка оксиду молібдену забезпечить ефективне поглинання сонячного випромінювання фотоактивним шаром поглинача в широкому спектральному діапазоні.

Розвиток фізики і технології напівпровідникових гетеропереходів – один із основних напрямків досліджень у галузі сучасного матеріалознавства і напівпровідникового приладобудування. На даний час різні гетеропереходи широко застосовуються в електроніці, телекомунікаційних системах, лазерах і фотовольтаїці [6].

Таке зацікавлення до напівпровідникових приладів на основі гетеропереходів вимагає розвитку точних методів для дослідження їх електричних і фотоелектричних властивостей [7,8]. Однак, внаслідок деяких причин дослідження електричних властивостей гетеропереходів суттєво ускладнене порівняно з гомопереходами.

У більшості гетеропереходів неможливо уникнути розбіжності періодів кристалічних ґраток, що викликає появу різних поверхневих станів, в основному у вигляді дислокацій невідповідності. Поверхневі дефекти створюють енергетичні рівні в межах забороненої зони. Вони можуть працювати як рекомбінаційні центри або пастки, які чинять великий вплив на електричні властивості напівпровідникових приладів на основі гетеропереходів [9,10].

Імпеданс спектроскопія – це потужний інструмент для дослідження напівпровідникових матеріалів і структур на їх основі [9]. Цей метод дозволяє аналізувати окремо вплив різних компонент еквівалентної схеми напівпровідникової структури. Імпеданс спектроскопія широко використовується для дослідження

напівпровідникових гетеропереходів, які є набагато складнішими для аналізу у порівнянні з гомопереходами, в основному внаслідок наявності поверхневих станів [9].

З вище сказаного очевидно, що створення гетероструктур MoO_x/n-Cd_{1-x}Zn_xTe та дослідження їх фізичних властивостей на постійному та змінному струмі є актуальною задачею.

ЕКСПЕРИМЕНТАЛЬНА ЧАСТИНА

Для виготовлення гетероструктури використовували кристали Cd_{1-x}Zn_xTe, з малим вмістом Zn, які були вирощені методом Бріджмена і мали мале значення питомого опору $\rho \approx 10^2$ Ом·см.

Структури виготовлялись нанесенням плівок MoO_x на попередньо поліровану поверхню пластин n-Cd_{1-x}Zn_xTe (розміром $5 \times 5 \times 0,7$ мм³) в універсальній вакуумній установці Leybold - Heraeus L560 за допомогою реактивного магнетронного розпилення мішені чистого Мо в атмосфері суміші аргону і кисню, при постійній напрузі. Молібденова мішень – це пластина діаметром 100 мм і товщиною 5 мм. Розміщується вона на столику магнетрона з водяним охолодженням. Підкладка з Cd_{1-x}Zn_xTe розміщується над магнетроном на столику, який обертається. Це робиться для того, щоб забезпечити нанесення однорідних плівок. Перед початком процесу напilenня у вакуумній камері понижають тиск до 10⁻⁴ Па.

Формування газової суміші Ar і O₂, в необхідних пропорціях відбувається з двох окремих балонів, перед процесом напilenня.

Для видалення забруднення поверхні мішені і підкладки, використовували короткочасне бомбардування іонами Ar. Під час процесу напilenня, парціальні тиски у вакуумній камері встановлюються 0,34 Па для Ar і 0,024 Па для O₂. Потужність магнетрона - 120 Вт. Процес напilenня проходив протягом 10 хвилин, при температурі підкладки 250 °С.

Були напilenі тонкі плівки MoO_x на скляні та керамічні підкладки, для визначення оптичних і електричних параметрів тонких плівок. Отримані плівки володіли провідністю n-типу. Виміряні значення питомої електропровідності і концентрації носіїв заряду становили $\sigma = 10$ Ом⁻¹·см⁻¹ і $n = 4,8 \cdot 10^{17}$ см⁻³, при 295 К.

Методом магнетронного розпилення молібдену формували фронтальний електричний контакт з тонкою плівкою оксиду молібдену, при температурі підкладки 150 °С. При формуванні тилового електричного контакту до підкладки n-CdZnTe осаджували шар Cu шляхом відновлення з водного розчину CuSO₄ з подальшим вплавленням індію.

РЕЗУЛЬТАТИ ТА ЇХ ОБГОВОРЕННЯ

Електричні та фотоелектричні властивості

Як видно з рис. 1, при освітленні білим світлом інтенсивністю 80 мВт/см², зворотний струм I_{light} зростає у порівнянні з його величиною у темряві I_{dark} . З ВАХ освітленого гетеропереходу MoO_x/n-Cd_{1-x}Zn_xTe (рис. 1) видно, що він володіє такими фотоелектричними параметрами: напруга холостого ходу $V_{oc} = 0,3$ В, струм короткого замикання $I_{sc} = 1,2$ мА/см² і коефіцієнт заповнення FF = 0,33 при інтенсивності освітлення 80 мВт/см².

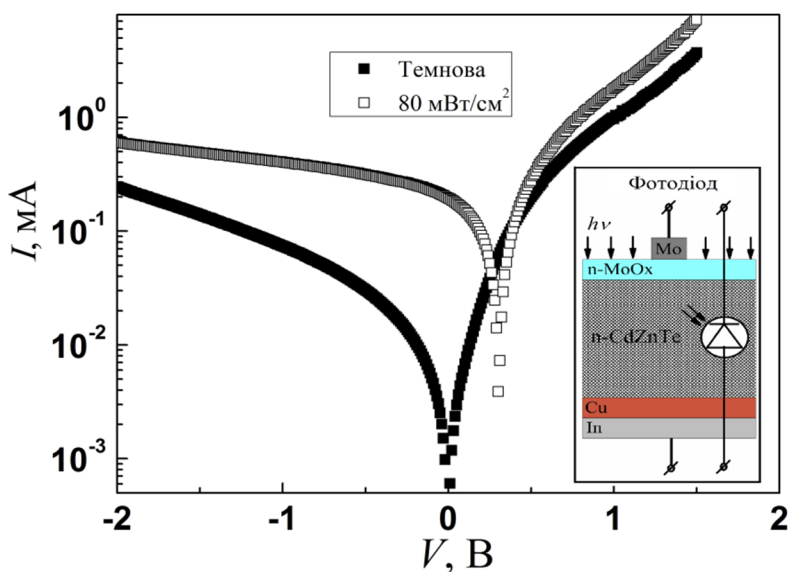


Рис. 1. ВАХ гетеропереходу MoO_x/n-Cd_{1-x}Zn_xTe неосвітленого та при інтенсивності освітлення 80 мВт/см². На вставці приведено структурну схему гетероструктури MoO_x/n-Cd_{1-x}Zn_xTe.

Четвертий квадрант ($V_{oc} \geq V \geq 0$) освітленої ВАХ є найбільш важливим, так як він визначає всі фотоелектричні параметри (рис. 2). Враховуючи рівняння, яке описує струм через гетероструктуру у темнових умовах, ми можемо записати вираз для освітленої ВАХ на основі еквівалентної схеми гетеропереходу (вставка рис. 2) з урахуванням впливу послідовного R_s і шунтуючого R_{sh} опорів:

$$I = I_{ph} - I_0 \left[\exp \left(\frac{e(V - IR_s)}{nkT} \right) - 1 \right] - \frac{V + IR_s}{R_{sh}},$$

де I_0 - струм насичення, n - показник неідеальності, а R_s та R_{sh} послідовний і шунтуючий опори (вставка. рис. 2), I_{ph} - фотострум.

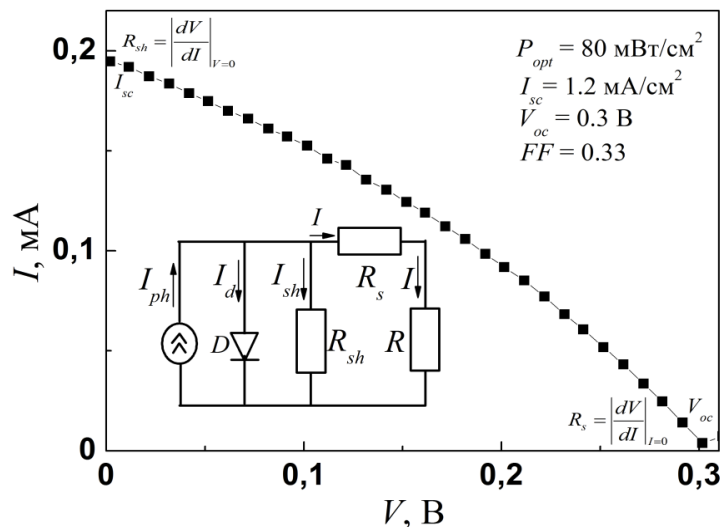


Рис. 2. Четвертий квадрант освітленої ВАХ $\text{MoO}_x/\text{n-Cd}_{1-x}\text{Zn}_x\text{Te}$.
 На вставці наведено еквівалентну схему освітленого гетеропереходу.

На рис. 3 представлено темнові вольт-амперні характеристики гетероструктури $\text{MoO}_x/\text{n-Cd}_{1-x}\text{Zn}_x\text{Te}$ при різних температурах, у напівлогарифмічному масштабі. Досліджувана структура володіє яскраво вираженою діодною характеристикою з коефіцієнтом випромінювання $k \approx 10^2$.

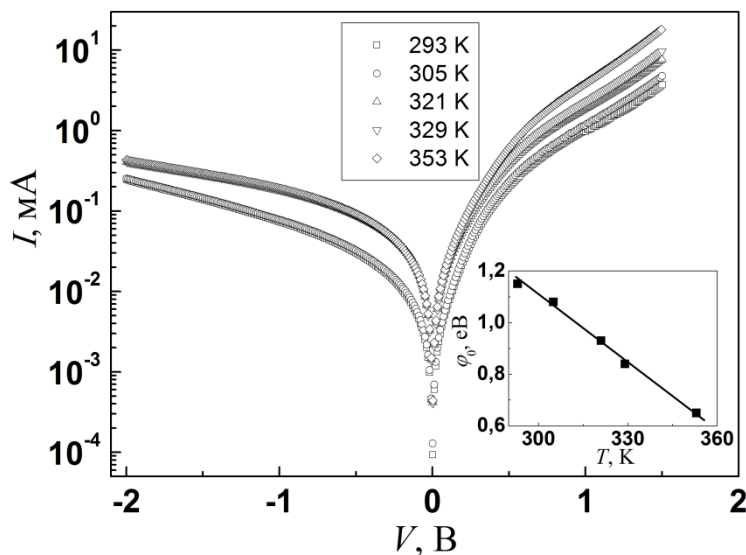


Рис. 3. Темнові ВАХ гетероструктури $\text{n-MoO}_x/\text{n-Cd}_{1-x}\text{Zn}_x\text{Te}$ при різних температурах у напівлогарифмічному масштабі.
 На вставці - температурна залежність висоти потенціального бар'єру.

Прямі гілки ВАХ досліджуваної структури, виміряні при різних температурах, наведені на рис. 3. Для них характерно зменшення напруги, при якій спостерігається швидке зростання струму з підвищенням температури, внаслідок зниження потенціального бар'єру, обумовленого різницею потенціалів та збільшення концентрації електронів. Шляхом екстраполяції лінійних ділянок вольт-амперних характеристик до перетину з віссю напруг, визначені значення висоти потенціального бар'єру φ_0 гетеропереходу при різних температурах (вставка рис. 3).

Варто відмітити, що визначена висота потенціального бар'єру гетеропереходу $\text{MoO}_x/\text{n-Cd}_{1-x}\text{Zn}_x\text{Te}$ при кімнатній температурі ($\varphi_0 = 1,15$ еВ) значно перевищує аналогічний параметр для гетеропереходу $\text{MoO}_x/\text{n-CdTe}$ ($\varphi_0 = 0,85$ еВ). Експериментально визначений температурний коефіцієнт зміни висоти потенціального бар'єра

становив $d(\varphi_0)/dT = -8.7 \cdot 10^{-3}$ eV/K, однак даний параметр більший у чотири рази від температурного коефіцієнта зміни висоти потенціального бар'єра для гетероструктур MoO_x/n-CdTe. Більше значення висоти потенціального бар'єру гетеропереходу MoO_x/Cd_{1-x}Zn_xTe обумовлене формуванням електричного диполя на гетерограниці, внаслідок збільшення концентрації поверхневих станів в порівнянні з гетероструктурою MoO_x/n-CdTe, а це очевидно пов'язано з наявністю атомів цинку в області просторового заряду та на металургійній межі поділу гетерограниці. Невеликий вміст атомів цинку практично не змінює ширину забороненої зони твердого розчину Cd_{1-x}Zn_xTe по відношенню до CdTe. Тому можна припустити, що наявність атомів цинку призводить до формування енергетичних рівнів розміщених в околі гетерограниці MoO_x/Cd_{1-x}Zn_xTe, які формують вище згаданий електричний диполь, а збільшення температурного коефіцієнта зміни висоти потенціального бар'єру обумовлене зменшенням цього диполя при зростанні температури через виснаження енергетичних рівнів, які його утворюють. Формування електричного диполя на гетерограниці також спостерігалось нами при виготовленні гетероструктури TiN/p-Cd_{1-x}Zn_xTe [11].

Механізми струмопереносу

Аналіз прямих гілок ВАХ структур MoO_x/n-Cd_{1-x}Zn_xTe, побудованих в напівлогарифмічному масштабі, показав, що на залежності $\ln I = f(V)$ спостерігається три прямолінійні ділянки, що свідчить про три домінуючі механізми струмопереносу. Отримані значення коефіцієнта неідеальності n для трьох ділянок напруг (рис. 4): n змінюється від 3,6 до 3,3 ($3kT/e < V < 0,3$ В) з підвищенням температури від 294-350 К, становить $n \approx 6$ ($0,3 < V < 0,6$ В) і становить $n > 10$ ($V > 0,6$ В).

Значення показника неідеальності в області напруг $3kT/e < V < 0,3$ В близькі до 2 дають можливість припустити, що основний механізм струмопереносу визначається генераційно-рекомбінаційними процесами в області просторового заряду, а саме n змінюється від 3,6 до 3,3 з підвищенням температури в інтервалі 295-358 К (вставка рис. 4), це свідчить про те, що у вище запропонований домінуючий механізм струмопереносу, який обумовлений генераційно-рекомбінаційними процесами в області просторового заряду, роблять внесок електрично активні поверхневі стани розміщені на металургійній межі розділу досліджуваного гетеропереходу [12,13].

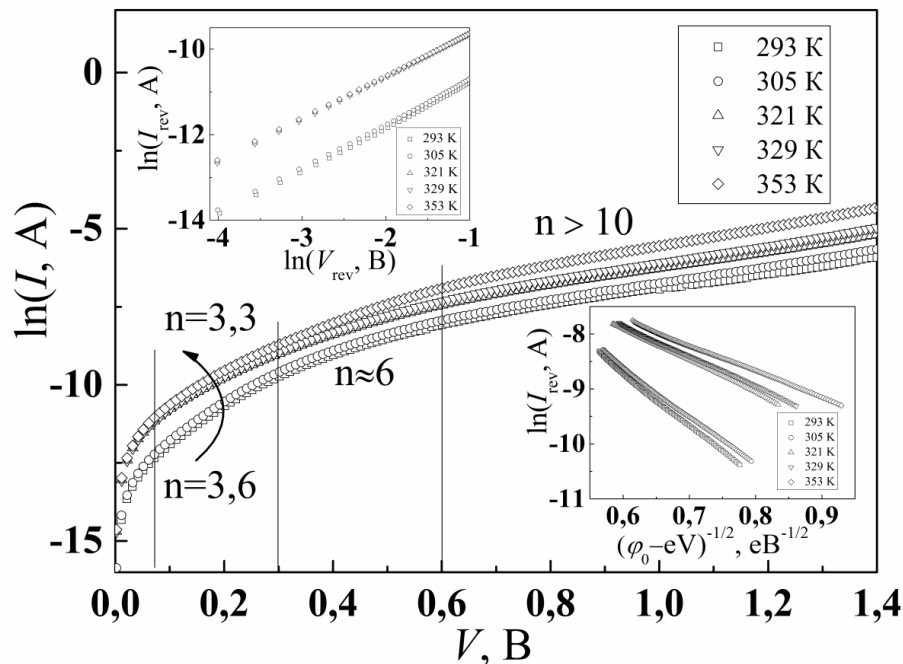


Рис. 4. Темнові ВАХ гетероструктури n-MoO_x/n-Cd_{1-x}Zn_xTe при різних температурах у напівлогарифмічному масштабі. На вставках - приведено залежності, які описують механізми струмопереносу через гетероструктуру при зворотному зміщенні.

При збільшенні прямого зміщення показник неідеальності зростає до $n \approx 6$ ($0,3 < V < 0,6$ В), це свідчить про наявність тунельного струму [14], оскільки потенціальний бар'єр ще достатньо великий для прямого тунелювання носіїв заряду, єдиним фізично обґрунтованим механізмом струмопереносу у досліджуваній області напруг є тунельно-рекомбінаційні процеси за участі поверхневих станів [14], а при збільшенні прямого зміщення $V > 0,6$ В показник неідеальності ще зростає і становить більше 10, це свідчить що настають умови сприятливі для прямого тунелювання носіїв заряду через потенціальний бар'єр.

Проведений аналіз механізмів струмопереносу через досліджувану гетероструктуру MoO_x/n-Cd_{1-x}Zn_xTe показав, що при малих зворотних напругах $3kT/e < V_{rev} < 0,5$ В залежність струму від напруги описується степеневим законом $I \sim V^m$, побудувавши залежності $\ln(I_{rev}) = f(\ln V_{rev})$ визначено значення $m = 1$ (вставка рис.4).

Це відповідає струмам витоку через шунтуючий опір, а при більших зворотних зміщеннях, апроксимація зворотних гілок ВАХ прямими лініями в координатах $\ln(I_{rev})=f(\varphi_0-eV)^{-1/2}$ (вставка рис. 4) свідчить про домінування тунельного механізму струмопереносу [14].

Імпеданс спектроскопія

Імпеданс напівпровідникових гетеропереходів $\text{MoO}_x/\text{n-Cd}_{1-x}\text{Zn}_x\text{Te}$ розглянуто при наявності послідовного R_s і шунтуючого R_{sh} опорів, паразитної індуктивності L і континууму поверхневих станів. Еквівалентна схема досліджуваного гетеропереходу представлена на рис. 5.

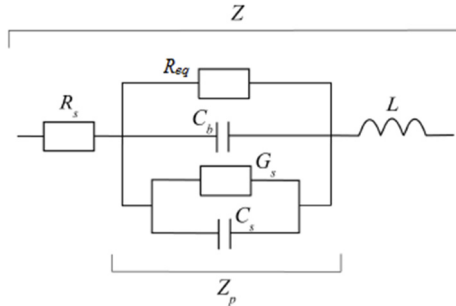


Рис. 5. Еквівалентна схема напівпровідникового гетеропереходу при наявності континууму поверхневих станів: R_s – послідовний опір, $R_{eq}=R_{sh}R_b/(R_{sh}+R_b)$ – еквівалентний опір, R_{sh} – шунтуючий опір, R_b – бар’єрний опір, C_b – бар’єрна ємність, G_s – провідність континууму поверхневих станів, C_s – ємність континууму поверхневих станів, L – індуктивність.

Відомо, що комплексна провідність континууму поверхневих станів описується наступним виразом [15]:

$$Y_s = \frac{eN_{ss}S}{2\tau_m} \ln(1 + \omega^2\tau_m^2) + i \frac{eN_{ss}S}{\tau_m} \arctan(\omega\tau_m), \quad (1)$$

де N_{ss} – розподіл густини поверхневих станів [$\text{см}^{-2} \text{eB}^{-1}$], τ_m – характеристичний час у рамках моделі континууму поверхневих станів, S – площа напівпровідникового гетеропереходу, e – заряд електрона, ω – циклічна частота змінного сигналу. Таким чином, компоненти гілки континууму поверхневих станів: провідність G_s та ємність C_s визначаються виразами (2) і (3), відповідно:

$$G_s = \frac{eN_{ss}S}{2\tau_m} \ln(1 + \omega^2\tau_m^2), \quad (2)$$

$$C_s = \frac{eN_{ss}S}{\omega\tau_m} \arctan(\omega\tau_m). \quad (3)$$

Варто відмітити, що вираз (1) записаний з урахуванням рівномірного розподілу густини поверхневих станів в околі kT/e в околі рівня Фермі, а не в межах усїєї забороненої зони, що прийнятно для багатьох реальних систем.

Остаточно можна записати вираз для імпедансу напівпровідникового гетеропереходу при наявності послідовного R_s і шунтуючого опору R_{sh} , паразитної індуктивності і континууму поверхневих станів N_{ss} , τ_m [16,17,18]:

$$Z = R_s + \frac{4\omega\tau_m B \left\{ \frac{\omega\tau_b A}{2B} \left[eN_{ss} S \tau_b (A^2 + 4B^2) + 2\tau_m C_b A (1 + \omega^2\tau_b^2) \right] + \omega^3 \tau_b^4 q N_{ss} S \frac{A(A^2 + 4B^2)}{2B} + 4\omega\tau_m \tau_b C_b B (1 + \omega^2\tau_b^2) \right\}}{\omega^2 \left[q N_{ss} S \tau_b (A^2 + 4B^2) + 2\tau_m C_b A (1 + \omega^2\tau_b^2) \right]^2 + \left[eN_{ss} S \omega^2 \tau_b^2 (A^2 + 4B^2) + 4\omega\tau_m C_b B (1 + \omega^2\tau_b^2) \right]^2} +$$

$$+ i \omega L - \frac{4\omega\tau_m B \left\{ \omega^2 \tau_b^2 \left[\frac{eN_{ss} S (A^2 + 4B^2)}{\omega^2} + 2\tau_m C_b A (1 + \omega^2\tau_b^2) \right] + \omega^3 \tau_b^4 q N_{ss} S (A^2 + 4B^2) + 4\omega^2 \tau_m \tau_b C_b B (1 + \omega^2\tau_b^2) \right\}}{\omega^2 \left[eN_{ss} S \tau_b (A^2 + 4B^2) + 2\tau_m C_b A (1 + \omega^2\tau_b^2) \right]^2 + \left[eN_{ss} S \omega^2 \tau_b^2 (A^2 + 4B^2) + 4\omega\tau_m C_b B (1 + \omega^2\tau_b^2) \right]^2} =$$

$$= Z' + iZ'' \quad (4)$$

де $\tau_b = R_{eq}C_b$, $A = \ln(1 + \omega^2\tau_m^2)$, $B = \arctan(\omega\tau_m)$, Z' і Z'' - дійсна і уявна частина імпедансу напівпровідникових гетеропереходів, розглянутих у рамках моделі континууму поверхневих станів.

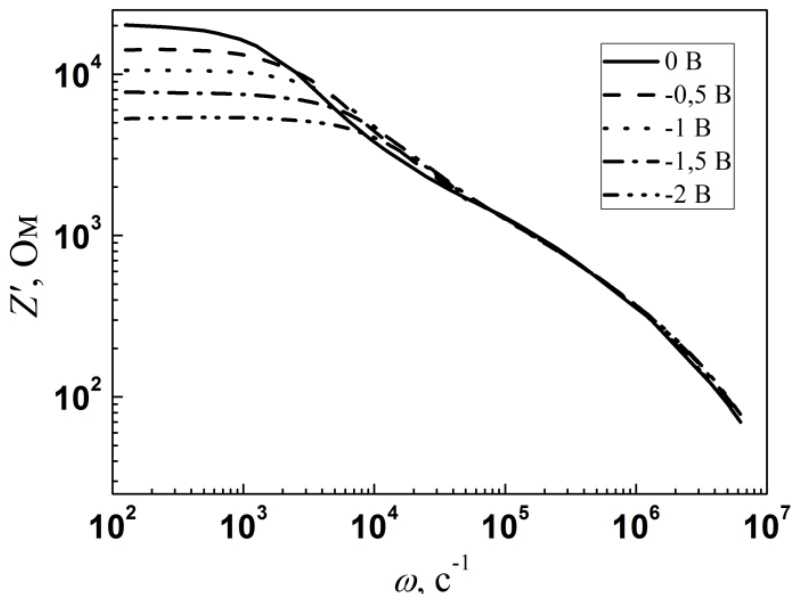


Рис. 6. Спектральний розподіл дійсної компоненти імпедансу гетеропереходу MoOx/n-Cd1-xZnxTe при різних зворотних зміщеннях.

Спектральний розподіл дійсної і уявної частини імпедансу гетеропереходу MoOx/n-Cd1-xZnxTe при різних зворотних зміщеннях показано на рис. 6 і 7, відповідно. З рисунків видно, що вплив континууму поверхневих станів на дійсну та уявну частину імпедансу спостерігається лише при циклічній частоті змінного сигналу $\omega \leq 1/\tau_m = 1 \cdot 10^5 \text{ c}^{-1}$, це свідчить про те, що поверхневі стани відносно повільні і не встигають перезаряджатися, тобто не встигають слідувати за високочастотним змінним сигналом.

Комплексна провідність паралельної гілки еквівалентної схеми, зображеної на рис. 5, Y_p описується виразом через дійсну і уявну частини імпедансу Z' і Z'' , а на основі виразів для дійсної частини провідності записують наступне рівняння [19,20]:

$$\frac{1}{\omega} \left[\frac{Z' - R_s}{[Z' - R_s]^2 + [Z'' - \omega L]^2} - \frac{1}{R_{sh}} \right] = \frac{eN_{ss}S}{2\omega\tau_m} \ln(1 + \omega^2\tau_m^2). \tag{5}$$

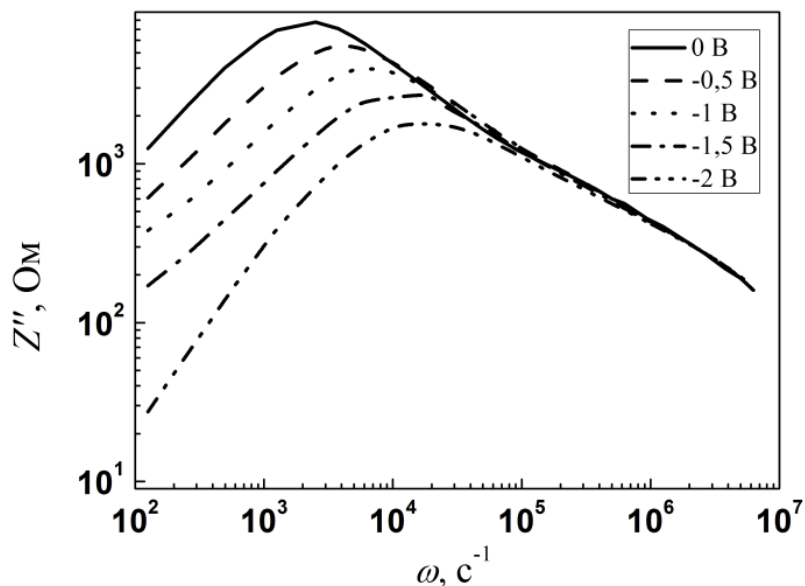


Рис. 7. Спектральний розподіл уявної компоненти імпедансу гетеропереходу n-MoOx/n-Cd1-xZnxTe при різних зворотних зміщеннях.

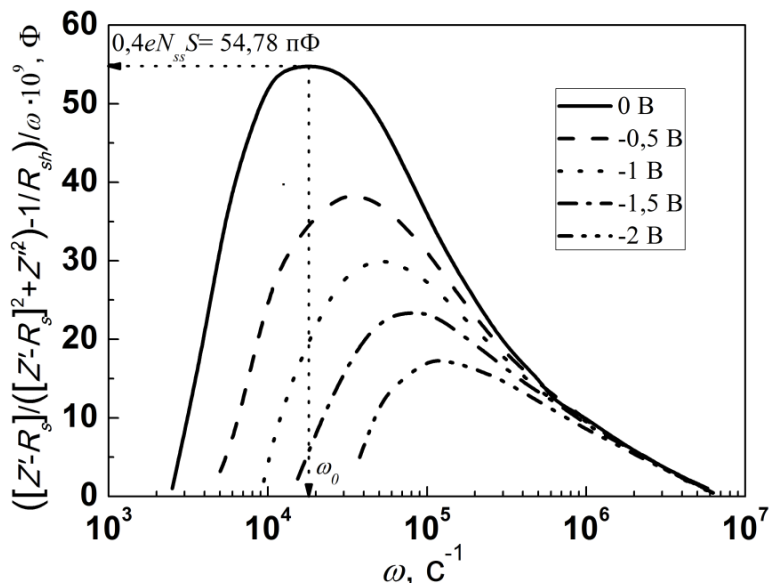


Рис. 8. Визначення параметрів пов'язаних з поверхневими станами в рамках моделі континууму поверхневих станів.

З виразу (5) видно, що із графіка $\{[Z'-R_s]/([Z'-R_s]^2 + [Z''-\omega L]^2) - 1/R_{sh}\}/\omega$ від ω можна визначити обидва параметри пов'язані з континуумом поверхневих станів при фіксованому зміщенні:

$$\tau_m = \frac{1.977}{\omega_0}, \tag{6}$$

$$N_{ss} = \frac{\left\{ \frac{1}{\omega} \left[\frac{(Z' - R_s)}{(Z' - R_s)^2 + (Z'' - \omega L)^2} - \frac{1}{R_{sh}} \right] \right\}}{0.402eS}. \tag{7}$$

Використовуючи рівняння (6-7) та (рис. 8) визначено розподіл густини поверхневих станів N_{ss} та характеристичного часу τ_m у залежності від прикладеного зовнішнього зміщення, які приведено на рис. 9.

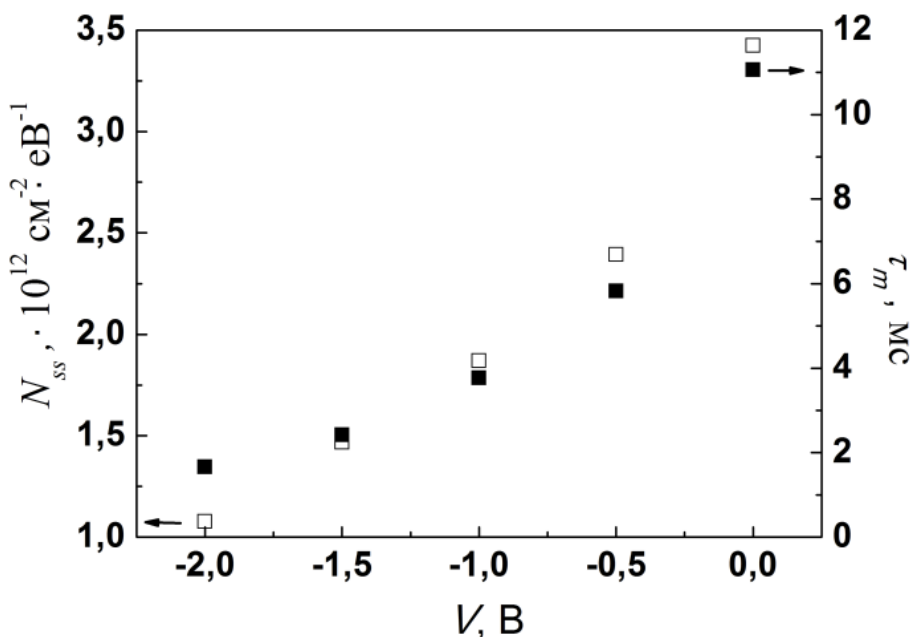


Рис. 9. Розподіл густини поверхневих станів N_{ss} та характеристичного часу τ_m

З рис. 9 видно, що зі збільшенням зворотного зміщення зменшується густина поверхневих станів N_{ss} та характеристичний час їх перезарядки τ_m , що обумовлено зміщенням положення рівня Фермі в межах забороненої зони кадмій цинк телуру на гетерограниці $\text{MoO}_x/\text{n-Cd}_{1-x}\text{Zn}_x\text{Te}$.

ВИСНОВКИ

Встановлено, що виготовлені гетеропереходи MoO_x/n-Cd_{1-x}Zn_xTe володіють великою висотою потенціального бар'єру при кімнатній температурі ($\phi_0 = 1,15$ eВ), яка значно перевищує аналогічний параметр для гетеропереходу MoO_x/n-CdTe ($\phi_0 = 0,85$ eВ). Експериментально визначений температурний коефіцієнт зміни висоти потенціального бар'єра становив $d(\phi_0)/dT = -8,7 \cdot 10^{-3}$ eВ/К, однак даний параметр більший у чотири рази від температурного коефіцієнта зміни висоти потенціального бар'єра для гетероструктур MoO_x/n-CdTe. Більше значення висоти потенціального бар'єру гетеропереходу MoO_x/n-Cd_{1-x}Zn_xTe обумовлене формуванням електричного диполя на гетерограниці, через збільшення концентрації поверхневих станів в порівнянні з гетероструктурою MoO_x/n-CdTe, а це очевидно пов'язано з наявністю атомів цинку в області просторового заряду та на металургійній межі поділу гетерограниці.

Показано, що в гетеропереходах MoO_x/n-Cd_{1-x}Zn_xTe домінуючими механізмами струмопереносу є генераційно-рекомбінаційний та тунельно-рекомбінаційний за участі поверхневих станів та тунельний при прямому зміщенні та тунелювання при зворотному зміщенні. Встановлено, що гетеропереходи MoO_x/n-Cd_{1-x}Zn_xTe, які володіють такими фотоелектричними параметрами: напруга холостого ходу $V_{oc} = 0,33$ В, струм короткого замикання $I_{sc} = 1,2$ мА/см² і коефіцієнт заповнення FF = 0,33 при інтенсивності освітлення 80 мВт/см² є перспективними для виготовлення детекторів різного типу випромінювань.

Досліджено імпеданс гетеропереходу MoO_x/n-Cd_{1-x}Zn_xTe при різних зворотних зміщеннях, що дало змогу визначити розподіл густини поверхневих станів та характеристичний час їх перезарядки, які зменшуються при зростанні зворотного зміщення.

ORCID IDs

-  Mykhailo M. Solovan, <https://orcid.org/0000-0002-1077-5702>;
  Andrii I. Mostovyi, <https://orcid.org/0000-0001-9634-0058>
 Hryhorii P. Parkhomenko, <https://orcid.org/0000-0001-5358-1505>;
  Viktor V. Brus, <https://orcid.org/0000-0002-8839-124X>
 Pavlo D. Maryanchuk, <https://orcid.org/0000-0002-5523-4280>

REFERENCES

- [1] K. Zanio, *Semiconductors and semimetals*. (Academic Press, 1978).
- [2] R. Singh, R. Sivakumar, S.K. Srivastava, and T. Som, *Applied Surface Science*, **507**, 144958 (2020), <https://doi.org/10.1016/j.apsusc.2019.144958>.
- [3] Y. Sun, C.J. Takacs, S.R. Cowan, J.H. Seo, X. Gong, A. Roy, and A.J. Heeger, *Advanced materials*, **23**(19), 2226-2230 (2011), <https://doi.org/10.1002/adma.201100038>.
- [4] C. Gretener, J. Perrenoud, L. Kranz, C. Baechler, S. Yoon, Y.E. Romanyuk, S. Buecheler, and A.N. Tiwari, *Thin Solid Films*, **535**, 193-197 (2013), <https://doi.org/10.1016/j.tsf.2012.11.110>.
- [5] C. Battaglia, S.M. De Nicolas, S.De Wolf, X. Yin, M. Zheng, C. Ballif, and A. Javey, *Applied Physics Letters*, **104**(11), 113902 (2014), <https://doi.org/10.1063/1.4868880>.
- [6] Zh.I. Alferov, *Semiconductors*, **32**, 1-14 (1998), <https://doi.org/10.1134/1.1187350>.
- [7] V.V. Brus, *Solar Energy*, **86**, 786-791 (2012), <https://doi.org/10.1016/j.solener.2011.12.009>.
- [8] H.A. Mohamed, *Journal of applied Physics*, **113**(9), 093105 (2013), <https://doi.org/10.1063/1.4794201>.
- [9] E. Barsoukov, and J.R. Macdonald (Eds.). *Impedance spectroscopy: theory, experiment, and applications*. (John Wiley & Sons, 2018).
- [10] J. Chen, and N.G. Park, *Advanced Materials*, **31**(47), 1803019 (2019), <https://doi.org/10.1002/adma.201803019>.
- [11] M.N. Solovan, V.V. Brus, P.D. Maryanchuk, M.I. Ilashchuk, and Z.D. Kovalyuk, *Semicond. Sci. Technol.* **30**, 075006 (2015), <https://doi.org/10.1088/0268-1242/30/7/075006>.
- [12] L.N. Skvortsova, V.N. Batalova, K.A. Bolgaru, I.A. Artyukh, and A.A. Reger, *Russian Journal of Applied Chemistry*, **92**(1), 159-165 (2019), <https://doi.org/10.1134/S10704272190100221>.
- [13] P.M. Gorley, Z.M. Grushka, V.P. Makhniy, O.G. Grushka, O.A. Chervinsky, P.P. Horley, Yu.V. Vorobiev, and J. Gonzalez-Hernandez, *Phys. Stat. Sol. (C)*, **5**, 3622-3625 (2008), <https://doi.org/10.1002/pssc.200780149>.
- [14] V.V. Brus, M.I. Ilashchuk, Z.D. Kovalyuk, P.D. Maryanchuk, K.S. Ulyanytsky, *Semicond. Sci. Technol.* **26**, 125006 (2011), <https://doi.org/10.1088/0268-1242/26/12/125006>.
- [15] E.H. Nicollian, and A. Goetzberger, *Bell System Tech. J.* **46**, 1055-1133 (1967), <https://doi.org/10.1002/j.1538-7305.1967.tb01727.x>.
- [16] V.V. Brus, *Semicond. Sci. Technol.* **27**, 035024 (2012), <https://doi.org/10.1088/0268-1242/27/3/035024>.
- [17] M.P. Hughes, K.D. Rosenthal, N.A. Ran, M. Seifrid, G.C. Bazan, and T.Q. Nguyen, *Advanced Functional Materials*, **28**(32), 1801542 (2018), <https://doi.org/10.1002/adfm.201801542>.
- [18] M.M. Shehata, and K. Abdelhady, *Applied Physics A*, **124**(9), 591 (2018), <https://doi.org/10.1007/s00339-018-2006-6>.
- [19] V.V. Brus, *Semicond. Sci. Technol.* **28**, 025013 (2013), <https://doi.org/10.1088/0268-1242/28/2/025013>.
- [20] T. Kamas, V. Giurgiutiu, and B. Lin, *Smart Materials and Structures*, **24**(11), 115040 (2015), <https://doi.org/10.1088/0964-1726/24/11/115040>.

ЕЛЕКТРИЧНІ ТА ФОТОЕЛЕКТРИЧНІ ВЛАСТИВОСТІ ГЕТЕРОПЕРЕХОДІВ MoO_x/n-Cd_{1-x}Zn_xTe

М.М. Солован^а, А.І. Мостовий^а, Г.П. Пархоменко^а, В.В. Брус^б, П.Д. Мар'янчук^а

^аЧернівецький національний університет імені Юрія Федьковича

вул. Коцюбинського 2, 58012 Чернівці, Україна

^бУніверситет імені Назарбаєва, 53 Кабанбай Батир, 010000, Нур-Султан, Казахстан

У роботі представлено результати досліджень оптичних і електричних властивостей напівпровідникових гетеропереходів MoO_x/n-Cd_{1-x}Zn_xTe виготовлених нанесенням плівок MoO_x на попередньо поліровану поверхню пластин n-Cd_{1-x}Zn_xTe

(розміром $5 \times 5 \times 0,7$ мм³) в універсальній вакуумній установці Leybold - Heraeus L560 за допомогою реактивного магнетронного розпилення мішені чистого Мо у середовищі аргону і кисню. Такі дослідження мають велике значення для подальшої розробки високоєфективних приладів на основі гетеропереходів для електроніки і оптоелектроніки. Виготовлені гетеропереходи $\text{MoO}_x/\text{n-Cd}_{1-x}\text{Zn}_x\text{Te}$ володіють великою висотою потенціального бар'єру при кімнатній температурі ($\varphi_0 = 1,15$ eV), яка значно перевищує аналогічний параметр для гетеропереходу $\text{MoO}_x/\text{n-CdTe}$ ($\varphi_0 = 0,85$ eV). Експериментально визначений температурний коефіцієнт зміни висоти потенціального бар'єра становив $d(\varphi_0)/dT = -8,7 \cdot 10^{-3}$ eV/K, даний параметр більший у чотири рази від температурного коефіцієнта зміни висоти потенціального бар'єра для гетероструктур $\text{MoO}_x/\text{n-CdTe}$. Більше значення висоти потенціального бар'єру гетеропереходу $\text{MoO}_x/\text{n-Cd}_{1-x}\text{Zn}_x\text{Te}$ обумовлене формуванням електричного диполя на гетерограниці, через збільшення концентрації поверхневих станів в порівнянні з гетероструктурою $\text{MoO}_x/\text{n-CdTe}$, а це очевидно пов'язано з наявністю атомів цинку в області просторового заряду та на металургійній межі поділу гетерограниці. В гетеропереходах $\text{MoO}_x/\text{n-Cd}_{1-x}\text{Zn}_x\text{Te}$ домінуючими механізмами струмопереносу є генераційно-рекомбінаційний та тунельно-рекомбінаційний за участі поверхневих станів та тунельний при прямому зміщенні та тунелювання при зворотньому зміщенні. Встановлено, що гетеропереходи $\text{MoO}_x/\text{n-Cd}_{1-x}\text{Zn}_x\text{Te}$, які володіють такими фотоелектричними параметрами: напруга холостого ходу $V_{oc} = 0,3$ В, струм короткого замикання $I_{sc} = 1,2$ мА/см² і коефіцієнт заповнення $FF = 0,33$ при інтенсивності освітлення 80 мВт/см² є перспективними для виготовлення детекторів різного типу випромінювань. Виміряний і досліджений імпеданс гетеропереходу $\text{MoO}_x/\text{n-Cd}_{1-x}\text{Zn}_x\text{Te}$ при різних зворотних зміщеннях, що дало змогу визначити розподіл густини поверхневих станів та характеристичний час їх перезарядки, які зменшуються при зростанні зворотного зміщення.

КЛЮЧОВІ СЛОВА: гетероперехід, оксид молібдену, $\text{Cd}_{1-x}\text{Zn}_x\text{Te}$, імпеданс, поверхневі стани

PACS: 81.40.Jj

ELASTIC PROPERTIES OF ALLOY ZE10 SHEETS EVALUATION BY KERNS TEXTURE PARAMETERS

 Valentin Usov^{a,*},  Natalia Shkatulyak^{a,†},  Elena Savchuk^{b,††}, Nadezhda Rybak^{a,†††}

^aSouth Ukrainian National Pedagogical University named after K. D. Ushinsky

Str. Staroportofrankovskaya, 26, Odessa, 65020, Ukraine

^bNational University "Odessa Maritime Academy", Str. Didrikhson, 8, Odessa, 65000, Ukraine

*Corresponding Author: E-mail address: valentinusov67@gmail.com

[†]E-mail: shkatulyak56@gmail.com, ^{††}E-mail: z9816@yandex.ua, ^{†††}E-mail: tesha1994@mail.ru

Received 18 December, 2020; accepted February 18, 2021

The ZE10 magnesium alloy with the rare-earth metal additives, which contribute to a better forming of the alloy, was used as studied material. The ZE10 magnesium alloy with the rare-earth metal additives, which contribute to a better forming of the alloy, was used as studied material. Sheet material is usually straightened on roller levelers to relieve residual stresses and improve flatness. The metal is subjected to alternating deformation by bending when straightening. The changes in the structure, crystallographic texture and, as a result, physical and mechanical properties occur in the metal are often not taken into account in the future. The elastic modulus is an important parameter, for example, in the production of products using bending. In this work, the elastic modulus of sheets of magnesium alloy ZE10 was estimated in three main directions. A starting sheet was obtained by extruding an ingot, then rolling in the longitudinal direction and then rolling with a change in direction by 90° after each pass in combination with heating to 350°C. The original sheets were subsequently subjected to alternate folding. Evaluations were made of the elastic modulus of the original sheet, as well as the sheets after 0.5, 1.0, 3.0 and 5.0 alternating bending cycles. To estimate the elastic modulus, we used the Kearns texture parameters, which we calculated from the inverse pole figures, as well as the elastic constants of the single crystal of the ZE10 alloy found by us. The maximum deviation of the calculated and experimental values of the elastic modulus did not exceed 5.2%. Strong correlations and quadratic regression equations have been established between the values of the elastic modulus, mechanical characteristics (tensile strength, yield stress, elongation), on the one hand, and the above-mentioned parameters of the Kearns texture, on the other hand. The approximation reliability coefficients are 0.76 - 0.99.

KEYWORDS: magnesium alloy, alternating bending, Kearns texture parameters, elastic modulus, tensile strength, ultimate tensile strength, relative elongation

Magnesium, as the lightest metal suitable for the manufacture of structures, is the most attractive for use in the aviation and space industries [1]. However, the practical use of pure magnesium is difficult due to unsatisfactory forming during plastic deformation [1]. A crystallographic texture of the central basal type mainly is formed during rolling of Mg, in which the crystallites are oriented with their hexagonal axis perpendicular to the rolling plane [2]. As a result, for example, during subsequent stamping or deep drawing, the material is destroyed. Therefore, in practice, structural materials are used not pure magnesium but magnesium-based alloys. In this case, aluminum, zinc, zirconium, lithium, as well as rare earth metals or less common metals (LCM) are used as alloying elements [3]. Such additives to magnesium in alloys contribute to an easier plastic flow of the metal during deformation due to an increase in the role of prismatic and pyramidal sliding and a decrease in the contribution of the basal one [4].

The alloy of magnesium with zinc, zirconium and rare earth metals ZE10 is one of the most promising for practical application of magnesium alloys. Before use, sheet material is usually straightened on roller straightening machines [5]. With such processing sheet or roll metal subjected to the alternating bending (AB) experiences periodic tensile-compression deformations. This helps to reduce residual stresses and favors the creation of a flat sheet [5]. Earlier it was shown that as a result of alternating bending, the original texture and, as a consequence, the physical and mechanical characteristics of the sheet are changed [6] that should be taken into account in the manufacture of products.

The alternating bending render most significant impact on the structural parameters and mechanical properties, which are sensitive to small deformations during tensile tests. These are texture, yield stress and twins [6, 7]. The texture in [6, 7] was represented using inverse pole figures (IPF) of the direction (ND) to the rolling plane (IPF ND). The linear equations of regression with approximation reliability coefficients of at least 0.7 were established between the normalized values of pole density exceeding one on IPF ND, on the one hand, and values of the yield strength, ultimate tensile strength and elongation, averaged over all direction of the sheets, on the other hand [6, 7]. At the same time, it seems more correct to compare the values of properties and texture characteristics measured in the same corresponding directions. The use of Kearns texture parameters allows carry out this comparison [8].

The Kearns texture parameters for materials with a hexagonal structure can be calculated both from their full direct pole figures, and from the inverse pole figures (IPF) of the corresponding directions in the sheet - normal direction (ND), rolling direction (RD), and transversal direction (TD) [8]. Moreover, knowledge of the Kearns texture parameters and the values of the properties of single crystals along and across the hexagonal axis allow calculating the tensor properties (for example, elasticity) of a polycrystalline sample in three mutually perpendicular directions [8].

This work aimed the Kearns texture parameters to find and evaluating on this base the elastic and mechanical properties of sheets of magnesium alloy ZE10 after industrial processing and subsequent alternating bending (AB). Such approach to evaluating of the elastic and mechanical properties of sheets of magnesium alloy ZE10 has not been used before.

MATERIALS AND METHODS

Sheets of ZE10 magnesium alloy (1.3% Zn, 0.15% Zr, 0.2% rare earth metals (REM), among REM mainly cerium) were obtained by processing [9], which consisted of ingot extrusion at a temperature of 350°C, after which a slab 6 mm thick and 60 mm wide was obtained. Next, the slab was rolled sequentially in the longitudinal direction to a thickness of 4.5 mm in 2 passes in combination with heating to 350 ° C after each pass. Further rolling to a thickness of 2 mm was performed in the transverse direction in combination with heating to 350°C after each pass. The degree of deformation for each pass was approximately 10 %. From a thickness of 2 mm, the direction of rolling was changed by 90° after each pass with a degree of deformation of approximately 10 % in combination with heating to 350°C, and thus obtained sheets with a thickness of 1 mm (original sheets).

The alternating bending (AB) was simulated on a manual bending device that included three rollers. The diameter of the bending roller was 50 mm. The speed of metal movement during bending was ~ 150 mm/s. The study was performed after 0.5; 1.0, 3.0 and 5.0 cycles. One cycle of alternating bending consisted of bending in one direction (0.25 cycles), straightening to a flat state (0.5 cycles), bending in the other direction (0.75 cycles) and straightening (1.0 cycle).

The three series of samples for mechanical testing in every from the three direction namely rolling direction (RD), diagonal direction (DN, i. e. at an angle of 45° to the RD), and transverse direction (TD) were cut out from original sheet as well as from the sheets after bending for 0.5, 1, 3 and 5 cycles. Mechanical tests of abovementioned samples were performed at room temperature on the tensile-testing machine Zwick Z250 / SN5A with a force sensor at 20 kN. The total length of the samples was 90 mm. The length and width of the working part of the samples was 30 mm and 12.5 mm, respectively.

For the Young's modulus measuring were cut out the samples through every 15° from the rolling direction (RD) up to the transverse direction (TD) (by three samples in every direction) from original sheet as well as from the sheets after AB. The length and width of the samples were respectively 100 mm and 10 mm.

The Young's modulus was measured dynamically by the frequency of natural bending oscillations of flat specimens. The error Young's modulus measuring did not exceed 1% [10].

The average value by three series of measured and tested specimens in each according direction were taken as values of the elastic and mechanical properties.

Samples to the texture study were cut also.

Before studying the texture, the samples were chemically polished to a depth of 0.1 mm to remove the distorted surface layer. The crystallographic texture was investigated on the two surfaces of the sheets, as well as in the rolling direction of the samples after above number of the RB cycles by means of the inverse pole figures (IPF) of the normal direction (ND IPF) and the rolling direction (RD IPF) on a DRON-3m diffractometer in filtered K α -Mo X-ray. A typesetting sample was used to record of RD IPF. The sample without texture was made of fine recrystallized sawdust of the investigated alloy. Morris normalization was used in the construction of the IPFs [11].

EXPERIMENTAL RESULTS AND DISCUSSION

The experimental IPFs of the alloy under study are shown in Fig. 1. The texture of the initial sample of the ZE10 alloy (Fig. 1a,b) is characterized by a wide preferential scattering of normal's to the basal plane in the TD. The maximum deflection angle is 90°. Intermediate maxima of the deviation of the hexagonal prism from the ND are observed both towards the TD at 40° and towards the RD by 40°, in contrast to the texture, which is usually formed in Mg, Ti, and Zr.

Changes in the character of texture scattering are observed depending on the number of AB cycles (Fig. 1c - m). The pole density values on the IPFs change also. The observed changes in the pole density distribution at different stages of the AB indicate the occurrence of deformation processes of sliding and twinning [6, 7].

The Kearns texture parameters are often used to quantify the texture of hexagonal materials [8]. These coefficients, f_j (index j means the corresponding direction ND, RD or TD in the sample) show the degree of coincidence of the c -axes of the crystalline hexagonal cells of grains with a given geometric direction in a polycrystalline material and can be found by the IPFs according to the ratio

$$f_j = \langle \cos^2 \alpha_i \rangle_j = \sum_i A_i P_{ji} \cos^2 \alpha_i, \quad (1)$$

where $P_{ji} = \frac{I_i/I_R}{\sum_{\Delta} (A_i \cdot I_i/I_R)}$; I_i/I_R is the ratio of the integral intensity of the i -th reflex on the j -th IPF to the corresponding value of the intensity of the reflex of the sample without texture I_R ; A_i is statistical weights of the i -th reflex ($\sum A_i P_{ji} = 1$) [12]. Conditionally A_i determined by the fraction of the surface area of the stereographic triangle around

the normal to the i -th reflex of the corresponding IPF; α_i is the angle of deviation from the c axis of the i -th crystallographic direction for the j -th direction in the sample.

For hexagonal single crystal, the value of some properties connecting two vector quantities or a tensor with a scalar quantity is determined [13] as:

$$P(\varphi)_{ref} = P_c \cos^2 \varphi + P_a (1 - \cos^2 \varphi) \quad (2)$$

Where $P(\varphi)_{ref}$ is property in the selected direction, P_a and P_c are the properties of a single crystal in a direction perpendicular and parallel to the direction $[0002]$, respectively, φ is the angle between the selected direction and $[0002]$.



Figure 1. Experimental IPFs of the alloy ZE10: (a, b) are IPFs of the original sheet; (c - e) are IPFs after 0.5 of the RB cycle; (f - h) are IPFs after 1 of the RB cycle; (i - k) are IPFs after 3 of the RB cycles; (l - n) are IPFs after 5 of the RB cycles; (a, c, f, i, l) are IPFs of ND; (b, e, h, k, n) are IPFs of RD; (d, g, i, m) correspond to the stretched out sides of the sheets; (c, e, h, l) correspond to the compressed sides of the sheets

Assuming that crystallites in a polycrystalline contribute to the volumetric property in proportion to their volume fraction, V_i , the contribution to the volumetric property of crystals whose axes c are oriented at an angle of inclination φ to the chosen direction can be written in the form:

$$P(\varphi_i)_{ref} = P_c V_i \cos^2 \varphi_i + P_a V_i (1 - \cos^2 \varphi_i). \quad (3)$$

Summing over the entire volume, we get:

$$P(\varphi_i)_{ref} = P_c \sum_i V_i \cos^2 \varphi_i + P_a \sum_i V_i (1 - \cos^2 \varphi_i). \quad (4)$$

Since $\sum_i V_i = 1$, and $\sum_i V_i \cos^2 \varphi_i = f_j$ is the Kearns texture parameter, we can write

$$P(\varphi_i)_{ref} = f_j P_c + (1 - f_j) P_a \tag{5}$$

To find the Kearns texture parameters by formula (1), we used the IPFs in Fig. 1, the values of A_i were taken from [12]. To calculate the angles between the crystallographic planes of a hexagonal single crystal using the known formulas [14], it is necessary to know the ratio of the crystal lattice parameters c/a of the alloy under study. According to our data, for magnesium alloy ZE10 (c/a) = 1.622. A similar result was also obtained by the authors of [15].

Kerns showed [8] that if a material property can be described by a tensor (for example, elasticity), then it obeys relation (5). In this case, the sum of f_j in the three main directions of the sample should be equal to one and a value of $f_j = 1/3$ in each direction determines the isotropic case. Thus, if the Kearns texture parameters found from ND IPF (f_{ND}) and RD IPF (f_{RD}) are known, then can find the Kearns parameter for the third direction in the sheet - the transverse direction (TD) - f_{TD} by the ratio:

$$f_{ED} + f_{TD} + f_{RD} = 1 \tag{6}$$

The Kearns texture parameters calculated from ND IPF (f_{ND}) and RD IPF (f_{RD}) in Fig. 1 as well as f_{TD} found using relation (6) are given in Table. 1.

Table 1. Kearns texture parameters

Cycles number, n	Kearns texture parameters				
	$f_{ND}^{(1)}$	$f_{ND}^{(2)}$	$f_{ND}^{(av)}$	f_{RD}	f_{TD}
0	0.340	0.340	0.340	0.176	0.484
0.5	0.322	0.324	0.323	0.203	0.474
1.0	0.322	0.318	0.320	0.208	0.472
3.0	0.326	0.306	0.316	0.217	0.467
5.0	0.323	0.315	0.319	0.153	0.528

Analysis of the distribution of pole density on the ND IPFs of opposite sides of the sheets after a different number cycles of AB showed certain inconsistencies (Fig. 1, c, d; f, g; i, j; l, m). The cause of these discrepancies is due to the fact that when bent to one side, the metal layers on the convex side of the sheet are subjected to tensile deformation. At the same time, the corresponding metal layers on the concave side of the sheet are deformed by compression. The deformation processes are alternated when the sign of bending is periodical changed. Similar inconsistencies in the distribution of the pole density on the IPFs of the outer and inner sides of the strips obtained after cutting along the axis and subsequent straightening of the tube made of Zr-2.5% Nb alloy were found earlier in [16].

The noted inconsistencies are reflected on the values of the Kearns texture parameters, calculated from the ND IPFs of opposite sides of the sheets after the AB ($f_{ND}^{(1)}$, and $f_{ND}^{(2)}$, Table 1). For further analysis of the AB effect on the properties of investigated alloy in the ND to the sheets plane were used of the Kearns texture parameters averaged over both sides of the sheets after the corresponding number of AB cycles.

The values of the modulus of elasticity, measured every 15° in the rolling plane of the sheets of investigated alloy, are presented in Table 2.

Tables 3-5 show the experimental values of ZE10 alloy mechanical characteristics: ultimate tensile strength σ_{UTS} , yield strength σ_{YS} and relative elongation $\epsilon = \Delta l / l$.

Table 2. Experimental elastic modulus E_{exp} after alternating bending of ZE10 alloy sheets

Angle with the RD, deg.	Elastic modulus E_{exp} , GPa				
	Number of the AB cycles, n				
	0	0.5	1.0	3.0	5.0
0	46.3	46.0	45.8	45.0	44.8
15	44.3	44.0	43.8	43.5	43.7
30	43.5	43.1	43.0	43.1	42.8
45	43.1	43.0	42.8	42.7	42.5
60	43.3	43.2	43.0	42.5	42.5
75	43.6	43.5	43.1	43.0	42.8
90	43.9	43.8	43.0	43.3	43.3

Table 3. Ultimate tensile strength σ_{UTS} after alternating bending of ZE10 alloy sheets

Angle with the RD, deg.	Ultimate tensile strength σ_{UTS} , MPa				
	Number of the AB cycles, n				
	0	0.5	1.0	3.0	5.0
0	246.0	250.0	252.0	256.0	250.0
45	231.0	219.0	219.0	221.0	229.0
90	216.0	221.0	225.0	234.0	214.0

Table 4. Yield strength σ_{YS} after alternating bending of ZE10 alloy sheets

Angle with the RD, deg.	Yield strength σ_{YS} , MPa				
	Number of the AB cycles, n				
	0	0.5	1.0	3.0	5.0
0	174.0	174.0	102.0	89.0	173.0
45	132.0	99.0	88.0	100.0	89.0
90	91.0	88.0	89.0	91.0	96.0

Table 5. Relative elongation $\varepsilon = \Delta l / l$ after alternating bending of ZE10 alloy sheets

Angle with the RD, deg.	Relative elongation $\varepsilon = \Delta l / l$, %				
	Number of the AB cycles, n				
	0	0.5	1.0	3.0	5.0
0	23.1	21.0	20.5	19.1	28.3
45	28.0	36.1	19.1	35.6	25.0
90	33.4	32.6	33.0	31.0	34.3

Let us estimate the value of the elasticity modulus of the alloy under study in three directions of the sheets: RD, TD and ND. For this we are used the Kerns texture parameters (Table 1) and the single crystal elastic constants of the alloy under study. Earlier in [17], we found the values of the elastic constant S_{11} and the combination of the elastic constants

$$a = S_{13} - S_{11} + 0.5S_{44}, \quad (7)$$

$$b = S_{11} + S_{33} - 2S_{13} - S_{44}. \quad (8)$$

According to [17]

$$(S_{11} = 2.287; a = -0.100; b = 0.128) \cdot 10^{-11} Pa^{-1}. \quad (9)$$

Simple transformations of relations (7) - (9) made it possible to calculate the elastic constant of $S_{33} = 2.22 \cdot 10^{-11} Pa^{-1}$.

A relation was obtained in [18] that makes it possible to express the elastic modulus in terms of the Miller indices, the ratio c/a , and the elastic constants of a hexagonal single crystal:

$$E(hkl) = \frac{\left[h^2 + \frac{(h+2k)^2}{3} + \left(\frac{a}{c} l \right)^2 \right]}{\left[S_{11} \left(h^2 + \frac{(h+2k)^2}{3} \right)^2 + S_{33} \left(\frac{a}{c} l^4 \right) + (S_{44} + 2S_{33}) \left(h^2 + \frac{(h+2k)^2}{3} \right) \left(\frac{a}{c} l \right)^2 \right]}. \quad (10)$$

As a result of substitution of the corresponding quantities of S_{11} , S_{33} , h , k , l , c , and a into relation (10), we obtain that

$$E(001) = E_c = \frac{1}{S_{33}} = 45.147 \text{ GPa}, \quad (11)$$

$$E(100) = E(110) = E_a = \frac{1}{S_{11}} = 43.730 \text{ GPa}. \quad (12)$$

Now let us estimate the value of the elastic modulus of the sheets of the investigated alloy in three directions of the sheet E_{RD} , E_{TD} , and E_{ND} by a relation of the type (8), using the values of the elastic modulus of the single crystal along and across the hexagonal axis of the ZE10 alloy (11) and (12), as well as the corresponding of the Kerns texture parameters (Table 1). The calculation results are presented in the Table 6. The experimental values of the modulus of elasticity for

convenience of comparison are also given in the Table 6. It is seen that the maximum deviation of the calculated and experimental values of the elastic modulus was 5.2%.

We could not experimentally measure the elastic modulus in the normal direction E_{ND} to the rolling plane due to the small sheet thickness (1 mm). The value of the E_{ND} in the original sheet of the ZE10 alloy estimated earlier us in [16] was 43.8 GPa. The value of the E_{ND} obtained in this work (Table 6) deviates from the above value by 0.9% (Table 6).

Unfortunately, it is impossible to estimate the value of the mechanical characteristics of the alloy under study using the Kearns texture parameters, similar to the above calculations for the elastic modulus, since data on the strength and plastic properties of the single crystal of the alloy ZE10 are missed in the literature.

Table 6. Experimental and calculated elastic modulus after alternating bending of ZE10 alloy sheets

Number of the AB cycles, n	E_{RD}^{exp} , GPa	E_{RD}^{calc} , GPa	$\Delta E/E_{exp}$, %	E_{TD}^{exp} , GPa	E_{TD}^{calc} , GPa	$\Delta E/E_{exp}$, %	E_{ND}^{calc} , GPa
0	46.3	43.9	5.2	43.9	44.4	-1.1	44.2
0.5	46.0	44.0	4.3	43.8	44.4	-1.4	44.2
1.0	45.8	44.0	3.9	43.5	44.0	-1.1	44.2
3.0	45.0	44.1	2.0	43.3	44.4	-2.5	44.2
5.0	44.8	44.0	1.8	43.3	44.5	-2.8	44.2

It is known that one of the main causes for the appearance of anisotropy in the physical and mechanical properties of polycrystalline metallic materials is the crystallographic texture formed during deformation. As mentioned above, Kearns texture parameters are often used to quantify the texture of hexagonal materials [19].

Let us analyze the observed changes in the studied characteristics (Tables 2-5) in connection with the crystallographic texture, represented by the Kearns texture parameters (Table 1). The analysis was showed that there are strong correlations between the values of the modulus of elasticity, mechanical characteristics, on the one hand, and the above-mentioned Kearns texture parameters, on the other hand. The corresponding regression equations and approximation reliability coefficients are represented by the relations (13) - (20):

$$E_{RD}^{exp} = -1514.6 f_{RD}^2 + 563.9 f_{RD} - 6.0; R^2 = 0.99 \quad (13)$$

$$E_{TD}^{exp} = -846.2 f_{TD}^2 + 841.4 f_{TD} - 165.1; R^2 = 0.90 \quad (14)$$

$$\sigma_{YSRD}^{exp} = -48102.0 f_{RD}^2 + 16566.0 f_{RD} - 1239.5; R^2 = 0.76 \quad (15)$$

$$\sigma_{YSTD}^{exp} = 2047.1 f_{TD}^2 + 1932.7 f_{TD} + 545.8; R^2 = 0.84 \quad (16)$$

$$\sigma_{UTSRD}^{RD} = 4640.5 f_{RD}^2 - 1584.7 f_{RD} + 381.0; R^2 = 0.99 \quad (17)$$

$$\sigma_{UTSRD}^{exp} = 17176.0 f_{TD}^2 - 17387.0 f_{TD} + 4606.3; R^2 = 0.94 \quad (18)$$

$$\epsilon_{RD}^{exp} = 1437.3 f_{RD}^2 - 664.0 f_{RD} + 96.0; R^2 = 0.98 \quad (19)$$

$$\epsilon_{TD}^{exp} = -1916.6 f_{TD}^2 + 1952.8 f_{TD} - 462.5; R^2 = 0.84 \quad (20)$$

CONCLUSION

The crystallographic texture of the original sample of polycrystalline magnesium alloy ZE10 after ingot extrusion, further rolling in the longitudinal direction and subsequent rolling with a direction change by 90° after each pass in combination with heating to 350°C is characterized by a wide predominant scattering of normal's to the basal plane in the TD with a maximum angle deviations of 90° and intermediate maxima of the deviation of the hexagonal prism from the ND both towards the TD by 40° and towards the RD by 40°, in contrast to the texture, which is usually formed in Mg, Ti and Zr.

Inconsistencies in the distribution of pole density on the ND IPF after a different number cycles of alternating bending are caused by alternating deformation by stretching and compression, respectively, on the convex and concave sides of the sheets results to a mismatch of the Kearns texture parameters, which were calculated from the ND IPF of opposite sides of the sheets.

Evaluations of the elastic modulus in three main directions of the original sheet of magnesium alloy ZE10, as well as sheets after 0.5; 1.0; 3.0; and 5.0 cycles of alternating bending were carried out using the Kearns texture parameters and the elastic constants of the alloy single crystal. The maximum deviation of the calculated and experimental values does not exceed 5.2%.

Strong correlations the elastic modulus and mechanical characteristics values with Kerns texture parameters established and quadratic regression equations with approximation reliability coefficients of 0.76 - 0.99 were found.

The presented results may be useful to develop a technology for obtaining improved characteristics of the shaping and minimal anisotropy of mechanical characteristics of magnesium alloys sheets.

ORCID IDs

© Valentin Usov, <https://orcid.org/0000-0001-7855-5370>; © Nataliia Shkatulyak, <https://orcid.org/0000-0003-4905-001X>
 © Elena Savchuk, <https://orcid.org/0000-0002-4249-6505>

REFERENCES

- [1] M. Millikin, <https://www.greencarcongress.com/2018/01/20180131-epfl.html>
- [2] J. Wu, L. Jin, J. Dong, F. Wang, and S. Dong, *J. Materials Science & Technology*, **42**, 175-189 (2020), <https://doi.org/10.1016/j.jma.2013.02.002>
- [3] B. Prasad, and P.P. Bhingole, *Advanced Materials Proceedings*, **2**(11), 734-744 (2017), <https://doi.org/10.5185/amp.2017/859>, <https://www.vbripress.com/amp/articles/fullArticle-pdf/203>
- [4] K.K. Alaneme, and E.A. Okotete, *J. of Magnesium and Alloys*, **5**, 460–475 (2017), <https://doi.org/10.1016/j.jma.2017.11.001>
- [5] ARKU Inc., 7251 E. Kemper Road, Cincinnati, OH 45249, <https://www.arku.com/us/arku-magazine/detail/sheet-metal-leveling-methods-us/>
- [6] N.M. Shkatulyak, V.V. Usov, N.A. Volchok, et. al, *The Physics of Metals and Metallography*, **115**(6) 609–616 (2014), <https://link.springer.com/article/10.1134/S0031918X1406012X>
- [7] N.M. Shkatulyak, S.V. Smirnova, and V.V. Usov, *International Journal of Metals*, **2015**, Article ID 349810 (2015), <https://doi.org/10.1155/2015/349810>.
- [8] J.J. Kearns, <https://ntrl.ntis.gov/NTRL/dashboard/searchResults/titleDetail/WAPDTM472.xhtml>
- [9] WIPO Patent Application WO/2011/146970, <http://www.sumobrain.com/patents/wipo/Magnesium-based-alloy-wrought-applications/WO2011146970A1.html>
- [10] Standard Test Method for Dynamic Young's Modulus, Shear Modulus, and Poisson's Ratio by Impuls Excitation of Vibration, http://forlab.pt/wp-content/uploads/2015/08/E1876_mvuj8965.pdf
- [11] P.R. Morris, *Journal of Applied Physics*, **30**(4), 595-596 (1959), <https://aip.scitation.org/doi/10.1063/1.1702413>
- [12] N.V. Ageev, A.A. Babareko, and S.Ya. Betsofen, *Izv. Ross. Akad. Ser. Met.*, **1**, 94–103 (1974). [in Russian]
- [13] J.F. Nye, *Physical properties of crystals their representation. Their representation by tensors and matrices*, (Oxford: University Press, 2006), pp. 131-149, <http://93.174.95.29/main/7258F1CE1EEE4CD628566F4EA21CDD58>
- [14] C. Tannous, <https://hal.archives-ouvertes.fr/hal-02268849v2/document>
- [15] Y. Liu, W. Li, and Y. Li, *International Journal of Minerals, Metallurgy and Material*, **16**(5), 559-563 (2009), [https://doi.org/10.1016/S1674-4799\(09\)60096-0](https://doi.org/10.1016/S1674-4799(09)60096-0)
- [16] V. Grytsyna, D. Malykhin, T. Yurkova, K. Kovtun, T. Chernyayeva, G. Kovtun, I. Tantsura, and V. Voyevodin, *East Eur. J. Phys.* **3**, 38-45 (2019), <https://doi.org/10.26565/2312-4334-2019-3-05>
- [17] S.V. San'kova, N.M. Shkatulyak, V.V. Usov, and N.A. Volchok, Article ID 142920, 6 pages, (2014), <https://www.hindawi.com/journals/ijmet/2014/142920/>
- [18] J.-M. Zhang, Y. Zhang, K.-W. Xu, and V. Ji, *Thin Solid Films*, **515**, 7020-7024 (2007), <https://doi.org/10.1016/j.tsf.2007.01.045>.
- [19] J.J. Kearns, *Journal of Nuclear Materials*, **299**(2), 171–174 (2001), [https://doi.org/10.1016/S0022-3115\(01\)00686-9](https://doi.org/10.1016/S0022-3115(01)00686-9)

ОЦІНКА ПРУЖНИХ ВЛАСТИВОСТЕЙ ЛИСТІВ СПЛАВА ZE10 ЗА ПАРАМЕТРАМИ ТЕКСТУРИ KERN'S

Валентин Усов^а, Наталя Шкатуляк^а, Елена Савчук^б, Надія Рибак^а

^аПівденноукраїнський національний педагогічний університет імені К.Д. Ушинського
вул. Старопортофранківська, 26, Одеса 65020, Україна

^бНаціональний університет «Одеська морська академія», вул. Дідріхсона, 8, Одеса 65000, Україна

Матеріалом для дослідження послужив сплав ZE10 магнію з добавками рідкісноземельних металів, які сприяють кращій формозміни сплаву. Листовий матеріал після прокатки зазвичай випрямляють на роликівих правильних машинах для зняття залишкових напружень і поліпшення площинності. В процесі правки метал піддається знакозмінній деформації вигином. Не дивлячись на незначну деформацію в процесі правки, в металі відбувається помітні зміни структури, кристалографічної текстури і, як наслідок, фізико-механічних властивостей, що часто не враховується в подальшому. Модуль пружності є важливим параметром, наприклад, при виробництві виробів за допомогою гнуття. У даній роботі нами була проведена оцінка модуля пружності листів магнієвого сплаву ZE10 за трьома основними напрямками. Вихідний лист був отриманий шляхом екструзії злитка, подальшим вальцюванням в поздовжньому напрямку та наступним вальцюванням зі зміною напрямку вальцювання на 90 ° після кожного проходу в поєднанні з нагріванням до 350° С. Вихідні листи в подальшому піддавалися знакозмінному вигину. Нами були проведені оцінки модулів пружності вихідного листа, а також листів після 0,5, 1,0, 3,0 і 5,0 циклів знакозмінного вигину. Для оцінки модуля пружності використані параметри текстури Кернса, розраховані нами зі зворотних полюсних фігур, а також знайдені нами пружні постійні монокристала сплаву ZE10. Максимальне відхилення розрахункових і експериментальних значень модуля пружності не перевищувало 5,2 %. Нами було встановлено сильні кореляційні зв'язки та квадратні рівняння регресії між значеннями модуля пружності, механічних характеристик (межа міцності, границя текучості, відносне подовження), з одного боку, і згаданими вище параметрами текстури Кернса, з іншого боку. Коефіцієнти надійності апроксимації склали 0,76 - 0,99.

КЛЮЧОВІ СЛОВА: магнієвий сплав, знакозмінний вигин, параметри текстури Кернса, модуль пружності, межа міцності при розтягуванні, межа плинності при розтягуванні, відносне подовження.

PACS: 28.41.Qb, 81.40.Ef, 61.10.Nz, 61.72.Hh

SURFACE PURITY EFFECT ON IRREGULARITIES OF CHANGES IN DEFORMATION TEXTURE OF Zr-2.5% Nb ALLOY

 **Dmitry G. Malykhin^{a,*}**,  **Kostiantyn V. Kovtun^c**,  **Tetiana S. Yurkova^a**,
 **Viktor M. Grytsyna^a**,  **Gennadiy P. Kovtun^{a,b}**, **Iryna G. Tantsura^a**, **Volodymyr D. Virych^a**,
Yuri V. Gorbenko^a,  **Victor M. Voyevodin^{a,b}**

^aNSC "Kharkiv Institute of Physics & Technology" NASU, Kharkiv, 61108, st. Akademicheskaya 1, Ukraine

^bV.N. Karazin Kharkiv National University, Kharkiv, 61022, Svobody Sq. 4, Ukraine

^cPublic enterprise «NTC «Beryllium», NASU, Kharkiv, 61108, st. Akademicheskaya 1, Ukraine

*Corresponding Author: dmitr.malykhin@gmail.com

Received September 16, 2020; revised November 9, 2020; accepted December 5, 2020

This work is a continuation of a series of works on the study of regularities and structural mechanisms of changes in characteristics of crystallographic texture during cold deformation of plates made of Zr2.5%Nb alloy. Effects of influence of surface cleanliness of the plates on the textural regularities during their rolling were investigated. For this, longitudinal fragments of the tube $\varnothing 15.0 \times 1.5$ mm² were used, flattened, annealed at 580°C in a vacuum of 1.5...3.0 Pa and rolled along the axis of the original tube with various degrees of deformation up to 56%, which is likened to longitudinal rolling of plates. Techniques of maximally uniform straightening of tube fragments were used. An analysis of the results of studies of textural changes during cross rolling of plates, straightened from rings of the same tube and pretreated under similar conditions, is also carried out. To analyze the results, the method of inverse pole figures was used, which, in these studies, is distinguished by the possibility of achieving satisfactory accuracy in calculating the integral characteristics of texture. On this basis, the Kearns textural coefficient was calculated along the normal to the plates' plane. Corrections were introduced for texture dissimilarity along the thickness of the plates, which is caused by the unbending of the preliminary blanks. Additionally, the analysis of texture distributions was carried out using original techniques. According to the results obtained – as a result of X-ray measuring from the plates' surface – oscillations of the course of changes in the texture coefficient were revealed. This is associated with an alternating process of relaxation of residual stresses during deformation. It has been established that this effect is initiated from the near-surface regions, is associated with a near-surface impurity, and in some cases can penetrate to a considerable depth of the plates. The twinning nature of such regularities is confirmed and active systems of twins are noted.

KEYWORDS: zirconium alloys, rolling, X-ray diffraction, texture, stresses, twinning.

This work is a supplement to the cycle of X-ray studies of regularities of changes in the crystallographic texture during cold deformation of zirconium and its alloys [1-3]. A feature of such works is the implementation of X-ray studies of rolling textures from their moderate level and the use of the method of inverse pole figures (IPFs) with an increased accuracy of determining the quantitative texture characteristics.

In the course of the research, a task was formed to study an effect of stress relaxation in Zr-2.5%Nb alloy, expressed in the instability of the process of texture changes after deformation, as well as to analyze conditions for manifestation of this effect. Preliminary studies have established that this effect is initiated on the surface of deformed plates [4]. Comparison of the results of works [2-4] gives reason to assume that this is due to surface impurities. Such a circumstance can occur under usual conditions of materials machining.

In view of this, this work is aimed at continuing the study of stress relaxation effects associated with the state of surface of hcp metals of the titanium subgroup. It is focused on the X-ray study of structural mechanisms of deformation, directly related to stress relaxation, and also on conditions of its manifestation. The results obtained can contribute to study of laws of plastic deformation of hcp metals used in nuclear, aircraft, aerospace engineering and medicine.

The main subject of the research is the Kearns texture parameter (TP) [1,2,5]. Many characteristics of zirconium alloys and other metals with hcp lattice are associated with it. According to changes in this parameter with the degree of deformation by rolling of alloys and using other methods, the analysis of textural dynamics – redistribution of the crystallographic axes "c" of the material and characteristic features of such changes – is provided.

EXPERIMENTAL

For the research, the material of $\varnothing 15.0 \times 1.5$ mm² tube of Zr-2.5%Nb alloy was used. The measurements of texture characteristics were performed on the DRON4-07 X-ray diffractometer in CuK α radiation with the Bragg-Brentano scheme.

According to preliminary studies, the texture of the tube turned out to be similar to the usual rolling texture of plates which rolling direction coincides with the tube axis [2]. A distinctive feature was its fan-like shape – the moderate character of its distribution along cross section of the tube.

Sample blanks were cut from the tube in the form of longitudinal fragments. Further, they were straightened to flat shape. To straighten them as uniformly as possible, they were deformed using tubes of different diameters.

After that, the obtained plates were annealed at 580 °C for 24 hours in a vacuum of 1.5...3.0 · 10⁻³ Pa. Further, the plates were deformed by cold rolling within 6 ... 55% along their length. The degree of deformation from sample to

sample was achieved in one act. Up to 40% of the total deformation, this was carried out with a step of 6...10%. Technological breaks were made between the acts of rolling from ten to forty minutes for size measurements. As a result, a series of 6 samples was obtained. In view of the texture feature of the original tube, the deformation of the plates was considered as longitudinal rolling.

The investigated surfaces of the plates were etched by 10...15 μm in a reagent with a volumetric combination of water, nitric and hydrofluoric acid in a ratio of 9:5:1.5.

We also present and analyze the results of studies of plates straightened from rings of the same tube, with similar preparation conditions, including the degree of rolling with other details, and subsequent etching [4]. In view of the texture feature of the original tube, deformation for this series of samples was considered as cross rolling.

Texture of the plates was investigated by the method of inverse pole figures (IPFs) [6]. The essence of the method is to analyze quantitative proportions in $(hkil)$ crystallographic orientations of hcp lattice of the material along selected direction of sample. In this case, this is the direction of the normal to its surface. An analogue of this distribution is the density of poles (P_{hkil}), which was determined from the intensities of the recorded X-ray reflections ($hkil$) with certain normalization: it should give the value of unity for all $(hkil)$ in case of a textureless material.

The texture parameter (TP) is calculated using the obtained set $\{P_i\}$ [7]:

$$f_j = \langle \cos^2 \alpha_i \rangle_j = \sum_i A_i P_{ij} \cos^2 \alpha_i, \quad (1)$$

where α_i is the angle between the base normal of reflecting grains – this is "c" axis of hcp cell – and the measurement direction (j), normal to the plate plane (NN); A_i is statistical weight of i -th reflection – solid-angular size of the neighborhood related to i -th crystallographic orientation of grains [7].

In order to take into account the texture differences between the sides of the plates – the outer and inner surfaces of the original tube – the measurements were made from both sides. In this regard, the appropriate designations were adopted: "front" and "back" side of the plates.

As a result of repeated measurements of cross-rolled plates, satisfactory texture homogeneity was noted on the surfaces of the tube and the plates (this is reflected in the subsequent graphs). In this case, in determining the TP ($0 \leq f \leq 1$), the random error as a whole was ± 0.003 . Systematic error may have an increased value due to texture inhomogeneity along the plate thickness.

RESULTS AND DISCUSSION

Figure 1a,c shows the TP values on the both sides of the alloy plates for each degree of longitudinal and cross deformation. Significant differences are observed in the data measured from different sides of the plates.

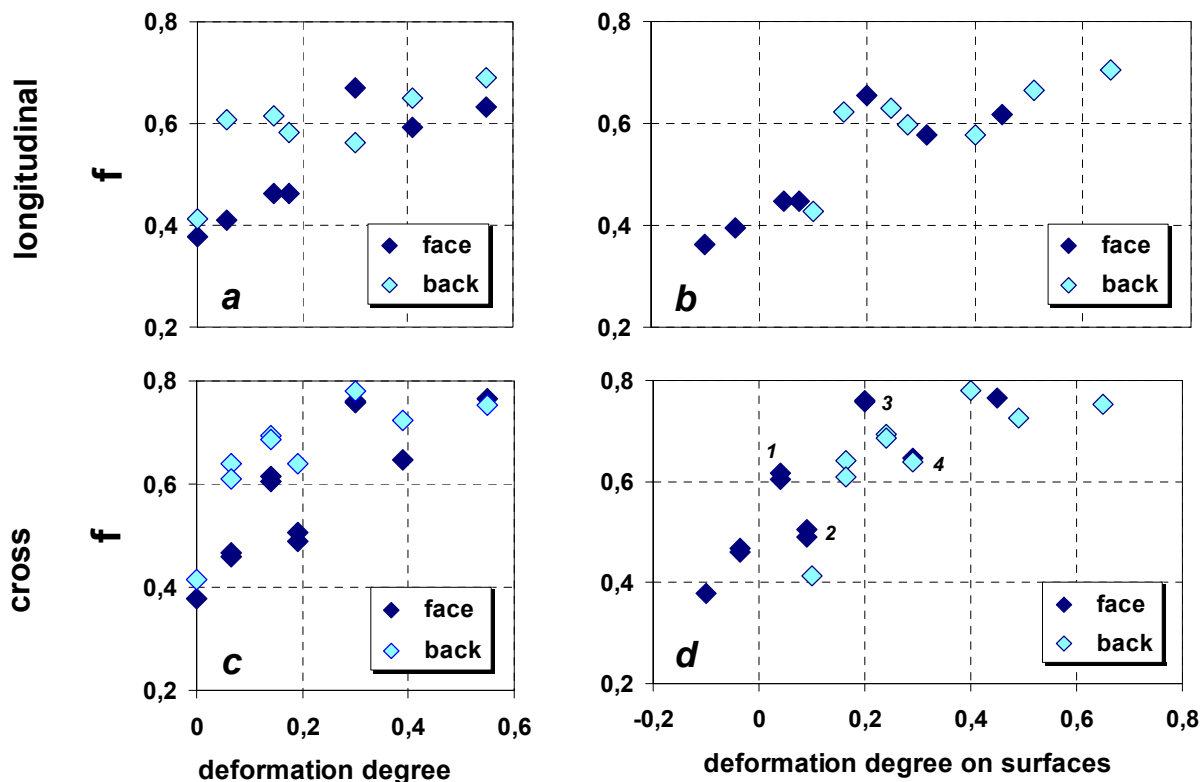


Figure 1. TP changes with degree of deformation by longitudinal (a, b) and cross rolling (c, d; [4]) of Zr-2.5%Nb alloy plates (a, c) and near-surface layers on their both sides (b, d).

According to the experience of work [2,4], the deformation degrees were corrected taking in account its inhomogeneity along the thickness of the plates. The correction was calculated based on the values of the thickness and diameter of the original tube – and was introduced as a deformation of the medium on the surface of the original plates similarly to rolling. As a result, more regular graphs of TP changes with deformation of the plates medium were obtained (Fig. 1b,d). For graph 1b, the optimal regularity was achieved by additionally introducing a correction of $\pm 0,015$ to the TP values (“-” for the front side). The numbers in Figure 1d refer to the following discussion.

As a result, as in the case of cross rolling of plates with specific preparation conditions (see **Experimental**) [4], during longitudinal rolling of such a material, oscillations in the TP changes are also observed (Fig. 1b). And at the same time, the inaccuracy of introducing corrections to deformation also did not exceed $\pm 0.5\%$. However, in view of the fact that the both cross rolling and effect of unbending deformation of the original rings act in a single geometric direction, the additivity of introduction of the correction with achievement of optimal regularity of the corresponding graph in this case is quite obvious. As for longitudinal rolling, we will discuss it below.

Visual analysis of Figures 1b,d shows a qualitative coincidence of the features of the graphs in the neighborhood of $\varepsilon = 0.1$ (10% deformation on the surfaces). Following the conclusions of work [4], this feature can be directly attributed to the relaxation of viscoelastic stresses which remained after annealing of straightened blanks and affected texture of the material. Further in Fig. 1b, there is an oscillation of TP with a period of $\Delta\varepsilon \approx 0.4$ (40%), while for cross rolling (Fig. 1d) this period is approximately 0.2. We will also discuss these details below.

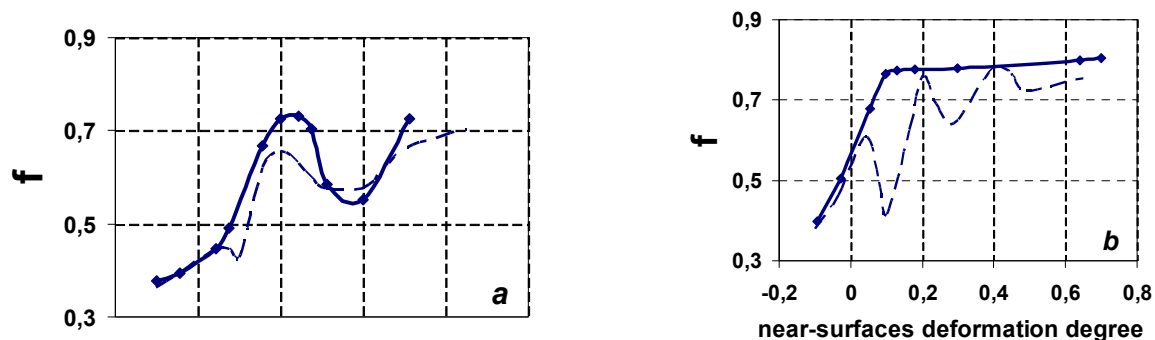


Figure 2. Changes in graphs of TP dependence on degree of longitudinal (a) and cross rolling (b [4]) after etching of the plates to a depth of $\approx 30 \mu\text{m}$ (solid lines)

As mentioned at the beginning and noted in [4], TP oscillations during cross rolling of plates are associated with relaxation of residual stresses, and it is initiated on the surfaces of the plates. Comparing the conditions of sample preparation in the present studies and in [2,3], we can conclude that the surface relaxation of residual stresses, expressed in the effect of oscillations, is associated in this case with interstitial impurities on the surface of deformed samples. In this case, the nature of the data obtained during longitudinal rolling, first of all, gives grounds to clarify two points: how significant is the relaxation of stresses in changes in TP in the free state of the plates (for example, during half an hour); what are the limits of propagation of the TP oscillation effect into the depth of the plates.

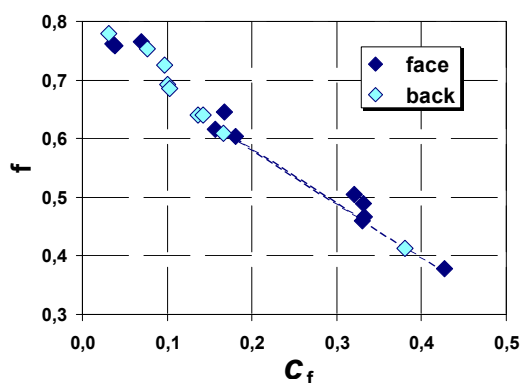


Figure 3. Relation of TP values with content of fraction could be twinned by cross rolling of plates

According to Figure 2a, in longitudinally rolled plates, the effect of irregularity of the TP graph, associated with textural effect of stress relaxation, penetrates to a considerable depth on both sides of the plates.

Following the approaches provided in [2,3], the analysis of the relationship between changes in TP and the distributions of orientations of the crystallographic axes "c" under conditions of stress relaxation in deformed plates of the alloy was carried out. The data obtained is shown here for cross rolling.

In particular, the participation in such changes of the fraction of grains could be twinned during deformation is analyzed. Figure 3 shows a comparison of TP (Fig. 1c,d) with the relative portion (C_f) of such a fraction.

As for the first point, the idea of stress relaxation in the periods between the acts of cross rolling of the plates was induced by a “reverse” in the changes in TP on their front surface, which manifested itself almost in every act (Fig. 1d) [4]. However, during longitudinal rolling (Fig. 1b), this character is not felt so clearly, and with increased deformations, the experimental points fit into a sinusoid with a doubled period, which does not give grounds to consider free relaxation to be a significant effect of TP changes.

As for the second point, i.e. the depth of propagation of the relaxation effect, then in [4] it was noted that on the front surface of cross-rolled plates the effect was limited to $30 \mu\text{m}$ depth. At the same time, the irregularity effect partially remained on the back side.

This study is supplemented with results obtained for longitudinally rolled plates with similar preparation conditions, etched up to $65 \mu\text{m}$ (Fig. 2a, solid lines). Dashed lines in Figure 2 mark the initial graphs (Fig. 1b, d).

The graph on Fig. 3 repeats the character inherent in deformed alloy plates prepared under normal conditions [2], i.e., practically, in absence of both residual stresses and the effect of their relaxation.

Thus, in relation to the effect of TP oscillations, the conclusion is repeated that twinning is significantly dominant in this process. In this case, all the points lying on the drawn straight line (Fig. 3) refer to the intervals of TP increase (Fig. 1d) and indicate the exclusive activity of the $\{10\bar{1}2\}[\bar{1}011]$ system of tensile twins with participation possibly of $\{11\bar{2}1\}[\bar{1}\bar{1}26]$ system [8]. Their combination rotates the "c" axes by an angle $\approx 90^\circ$, which gives the derivative for the straight line equal to -1.

The points located above the straight line (Fig. 3) refer to the TP return intervals (Fig. 1b,d). They are probably associated with compression twins, which do the counter-rotation of "c" axes at an angle $\approx 60^\circ$ [8] (derivative > -1). To confirm this, Figure 4 shows the graphs of the pole density distribution on the base of $(h0\bar{h}l)$ reflections. It is given for 14...39% of cross rolling in a logarithmic scale and represented by $\cos^2\alpha$ (Fig. 4a). Figure 4b shows similar distributions for usual conditions of sample preparation – without the TP oscillations [3]. The both figures refer to the face of the plates. The graphs in each figure are located with arbitrary intervals along the ordinate axis.

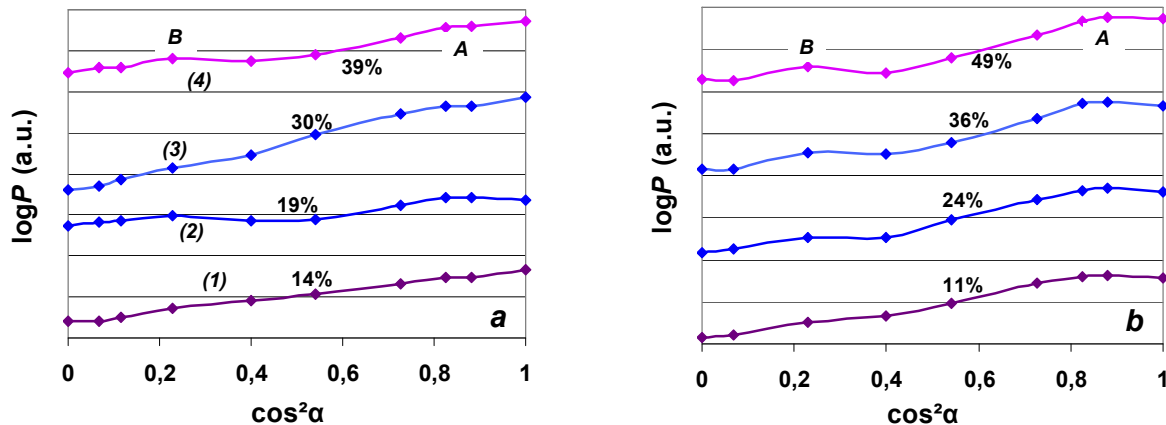


Figure 4. Density distribution of poles $P_{(h0\bar{h}l)}$ for deformed alloy plates in conditions of stress relaxation effects (a) and without it (b [3]).

A characteristic basis of the graphs in Figure 4b, as also was noted in [1,3], is their linear course. The conditional maxima at points A and B were associated with twinning effects. The rising of the graphs in the neighborhood of point A ($\cos^2\alpha \approx 1$; $\alpha \approx 0$) was associated with the result of action of tensile twins on the base of the $\{10\bar{1}2\}[\bar{1}011]$ system. Point B was associated with reverse rotations of the "c" axes at an angle $\Delta\alpha \approx 60^\circ$ ($\cos^2\alpha \approx 0.25$) created by compression twins.

The qualitative difference in Figure 4a is manifested in the oscillations of the character of the graphs from one to next, which uniquely accords with the TP oscillations in Fig. 1d; (marked with the corresponding numbering "1"- "4").

In view of the foregoing, the TP oscillations, like any its changes in the deformation process [3], are associated with twinning effects. In this case, this is a mutually counter-directional alternating action of both classes of twins: compression twins – it can be particularly seen from the local rise of graphs (2) and (4) in the neighborhood of point B – and tensile twins, what is expressed in the rise of graphs (1) and (3) in the neighborhood of A (Fig. 4a).

It can reasonably be argued that independent action of each of the two classes of the twins begins with reaching a certain threshold level in the distribution of initiating stresses (lattice distortions) between these classes, and ends with a reverse redistribution, giving rise to another class. In this case, just as in [3], the turns of "c" axes mainly occur along the fan of their orientations, which is inherent in the texture of the original tube. This was established as a result of the analysis of the rocking curves of the deformed plates. This justifies the principle of introducing deformation corrections when obtaining graph 1b: when straightening the blanks and subsequent deforming of the plates, the crystallographic rotations of the grains are carried out in a single plane. This is the cross-sectional plane of the original tube. However, in view of the existing differences in the rates of TP changes during deformation by longitudinal and cross rolling (with a multiplicity of 1:2 [2]), it remains unclear why such a correction for longitudinal rolling is equal to 0.1, not 0.2. In this regard, it remains to formally state that under conditions of accumulation of viscoelastic stresses during straightening of the blanks, longitudinal rolling initially sets its own regularity to TP changes.

Taking into account the conditions and features of the accumulation of residual stresses and the manifestation of the effect of their relaxation, it can be concluded that surface purity plays a role in this.

Obviously, it makes no sense to assume that only the main acting twins, and, consequently, other twins, play an immediate role in the stress accumulation. It remains to attribute the stress accumulation effects to the influence of surface impurities directly on gliding processes. This is mainly the effect of oxygen, the concentration of which on the surface of the initial plates exceeded 0.2 wt% in this experiment and was limited to 0.14 wt% in [2, 3].

Although under normal conditions of deformation, twinning and prismatic gliding in hcp metals of the titanium subgroup act simultaneously and in a balanced manner, there is reason in these studies to consider twinning as more active. This can explain the feature of the initial changes in TP in Figure 2b (solid line; cross rolling [4]), the rate of which, according to [3], should be considered, as well as in Fig. 1d [3], overestimated by about two times. Obviously,

despite the significant elimination of the surface layer in the alloy plates, the influence of the surface contamination effect on the deformation texture extends beyond the near-surface layer. This is especially confirmed by Fig. 2a.

SUMMARY

Surface effects of stress relaxation in the plates made from a Zr-2.5%Nb alloy tube $\varnothing 15.0 \times 1.5$ mm² have been studied using the X-ray method of inverse pole figures (IPFs). Effects of oscillations of texture characteristics at cold deformation of plates by longitudinal and cross rolling have been investigated. The following results have been obtained.

The oscillations of the Kearns' texture parameter with degree of deformation of alloy plates are associated with a mutually counter-directional alternating action of tensile and compression twin classes.

The sequence of the action of twins is associated with the threshold effects of stress accumulation in the material, which is due to the near-surface impurity and its influence on the microstructural gliding processes.

When the plates are deformed in the presence of impurities, the activity of twinning systems is increased, which has a significant effect on the characteristics of texture changes.

Influence of surface impurities on the process of texture changes can extend to a significant depth of the material.

ORCID IDs

 Dmitry G. Malykhin, <https://orcid.org/0000-0003-0259-0211>;  Kostiantyn V. Kovtun, <https://orcid.org/0000-0002-0524-5053>
 Tetiana S. Yurkova, <https://orcid.org/0000-0003-1264-640X>;  Viktor M. Grytsyna, <https://orcid.org/0000-0003-4341-007X>
 Gennadiy P. Kovtun, <https://orcid.org/0000-0003-4242-7697>;  Victor M. Voyevodin, <https://orcid.org/0000-0003-2290-5313>

REFERENCES

- [1] G.P. Kovtun, K.V. Kovtun, D.G. Malykhin, T.S. Yurkova, and T.Yu. Rudycheva, East Eur. J. Phys. **4**(3), 44-50 (2017), <https://doi.org/10.26565/2312-4334-2017-3-05>.
- [2] V.M. Grytsyna, D.G. Malykhin, T.S. Yurkova, K.V. Kovtun, T.P. Chernyayeva, G.P. Kovtun, V.V. Korniyeva, O.O. Slabospitskaya, I.G. Tantsura, and V.N. Voyevodin, East Eur. J. Phys. **2**, 39-45 (2019), <https://doi.org/10.26565/2312-4334-2019-2-06>.
- [3] V. Grytsyna, D. Malykhin, T. Yurkova, K. Kovtun, T. Chernyayeva, G. Kovtun, I. Tantsura, V. Voyevodin, East Eur. J. Phys. **3**, 38-45 (2019), <https://doi.org/10.26565/2312-4334-2019-3-05>.
- [4] V.M. Grytsyna, D.G. Malykhin, T.S. Yurkova, K.V. Kovtun, T.P. Chernyayeva, G.P. Kovtun, and V.N. Voyevodin, Problems of Atomic Science and Technology, **5**(117) 69-74 (2018), https://vant.kipt.kharkov.ua/ARTICLE/VANT_2018_5/article_2018_5_69.pdf.
- [5] J. Kearns, *Thermal expansion and preferred orientation in Zircaloy, USAEC WAPD-TM-472*, (Westinghouse Electric Corporation, Pittsburg, Pa. USA, 1965).
- [6] G.B. Harris, Quantitative measurement of preferred orientation in rolled uranium bars, Phil. Mag. **43**(336), 113-123 (1952), <https://doi.org/10.1080/14786440108520972>.
- [7] P.R. Morris, J. Appl. Phys. **30**(4), 595 (1959), <https://doi.org/10.1063/1.1702413>.
- [8] E. Tenckhoff, J. ASTM Int. **2**(4), 1-26 (2005), <https://doi.org/10.1520/JAI12945>.

ЕФЕКТ ЧИСТОТИ ПОВЕРХНІ У НЕРЕГУЛЯРНІСТЯХ ЗМІН ТЕКСТУРИ ДЕФОРМАЦІЇ СПЛАВУ Zr-2.5%Nb

Д.Г. Малихін^а, К.В. Ковтун^с, Т.С. Юркова^а, В.М. Грицина^а,

Г.П. Ковтун^{а,б}, І.Г. Танцюра^а, В.Д. Вірич^а, Ю.В. Горбенко^а, В.М. Восводін^{а,б}

^аННЦ «Харківський фізико-технічний інститут» НАНУ, Україна, 61108, г. Харків, ул. Академічна 1

^бХарківський національний університет ім. В.Н. Каразіна, Україна, 61022, м. Харків, майдан Свободи, 4

^сДП «НТЦ «Берилій» НАНУ, Україна, 61108, м. Харків, вул. Академічна 1

Дана робота є продовженням циклу робіт з досліджень закономірностей і структурних механізмів змін характеристик кристалографічної текстури при холодній деформації пластин зі сплаву Zr2,5%Nb. Досліджувалися ефекти впливу чистоти поверхні пластин на закономірності текстурних змін у процесі їх прокатки. Для цього використано поздовжні фрагменти труби $\varnothing 15.0 \times 1.5$ мм², які випрямлені до плоскої форми, відпалені при 580°C у вакуумі 1,5 ... 3,0 Па і прокатані уздовж осі вихідної труби з деформацією різних ступенів до 56%, що вважалося аналогічним поздовжній прокатці пластин. Використано прийоми максимально рівномірного випрямлення фрагментів труби. Проведено також аналіз результатів досліджень текстурних змін при поперечній прокатці пластин, випрямлених з кілець такої ж труби і попередньо оброблених в подібних умовах. Для аналізу результатів використано метод зворотних полюсних фігур, що відрізняється в даних дослідженнях можливістю досягнення задовільної точності розрахунку інтегральних характеристик текстури. На цій основі проведено розрахунок текстурного параметру Кернса уздовж нормалі до площини пластин. Введено поправки на текстурну неоднорідність вздовж товщини пластин, що пов'язано з розгинанням попередніх заготовок. Додатково проведено аналіз текстурних розподілів із застосуванням оригінальних прийомів. Згідно з отриманими результатами – в результаті зйомок з поверхні пластин – виявлено осциляції ходу змін текстурного параметра. Осциляції зв'язуються зі знакозмінним процесом релаксації залишкових напружень в процесі деформації. Встановлено, що цей ефект ініціюється з приповерхневих областей, пов'язаний з приповерхневою домішкою і в деяких випадках може проникати на значну глибину пластин. Підтверджено двійникову природу таких закономірностей і відзначено активні системи двійників.

КЛЮЧОВІ СЛОВА: цирконієві сплави, прокатка, рентгенографія, текстура, напруження, двійникування.

PACS: 81.10.-h

ZONE RECRYSTALLIZATION OF ZIRCONIUM AND HAFNIUM

 **Oleh E. Kozhevnikov***,
  **Mykola M. Pylypenko**,
  **Maryna F. Kozhevnikova**

*NSC "Kharkiv Institute of Physics & Technology" NASU
1, Academichna str., 61108, Kharkiv, Ukraine*

**Corresponding Author: kozhevnikov@kipt.kharkov.ua*

Received December 4, 2020; revised February 21, 2021; accepted February 22, 2021

The work studied the possibility of obtaining of the high-purity samples of zirconium and hafnium by the method of zone recrystallization of round rods with electron-beam heating in a vacuum of $1 \cdot 10^{-4}$ Pa. Some meltings were carried out in a constant electric field with the variability of its connection. It is shown that the simultaneous passage of several refining processes (evaporation of highly volatile metallic impurities, zone recrystallization with directional displacement of impurities to the end of the sample, electrotransport) made it possible to efficient refining of zirconium both from metallic impurities and from interstitial impurities. The best degree of purification was achieved when zone melting carrying out in an electric field directed opposite to the zone movement. In this case, the displacement of interstitial impurity ions coincided with the direction of movement of the liquid zone. Samples of zirconium with a purity of 99.89 wt. % were obtained (the concentration of aluminum was reduced by 5, iron - 11, copper - 45, chromium - 75, silicon - 10, titanium - 2.5, oxygen - 3.3, nitrogen - 3, carbon - 2 times). The hafnium samples refined by the zone recrystallization method were characterized by a purity of 99.85 wt. %. The concentrations of both all metal impurities and interstitial impurities were significantly reduced (concentration in wt% oxygen was 0.011, carbon - 0.0018, nitrogen - $5 \cdot 10^{-5}$). A study of gas evolution from samples of iodide hafnium and refined hafnium was carried out. It was found that the maximum gas release peak fell on the temperature range of 500 ... 550 °C. The use of an integrated approach, including high-temperature heating, stages of zone melting at different rates, and thermal cycling in the range of the polymorphic transformation temperature, made it possible to obtain single-crystal hafnium samples. According to X-ray diffraction data, the parameters of the hafnium crystal lattice were determined: $a = (0.31950 \pm 5 \cdot 10^{-5})$ nm and $c = (0.50542 \pm 5 \cdot 10^{-5})$ nm (at 298 K), which corresponds to the density $\rho = 13.263$ g/cm³ and axial ratio $c/a = 1.5819$.

KEYWORDS: zirconium, hafnium, zone recrystallization, electrotransport, thermal cycling, impurity composition, microhardness

In the next 30 years, the thermal neutron reactors will continue to occupy a dominant position among nuclear power units. The basic material for the active zones of such reactors are zirconium-based alloys, which have an optimal combination of nuclear, corrosion, mechanical, thermal and other physicochemical characteristics. An improvement of zirconium materials will increase the efficiency of existing power units, increase the depth of fuel burnup, extend the design life, ensure operational reliability and safety [1, 2]. The industrial production of zirconium (Zr) has led to an increase in the production of hafnium (Hf). A great deal of experience has been accumulated in the chemical separation of zirconium and hafnium, the technology of manufacturing materials with the required physical and mechanical characteristics has been improved, statistics have been accumulated on the duration of operation and the evolution of the properties of products operating in the cores of nuclear reactors.

Zirconium and hafnium belong to the elements of IVB group of Mendeleev's periodic table. The chemical properties of these metals are very similar, but the main applications in reactor construction are not the same due to the different neutron-physical characteristics. Hafnium is characterized by a high thermal neutron absorption cross section (105 ± 5 b), which is three orders of magnitude higher than that of zirconium. Under radiation exposure, the hafnium absorption cross section decreases very slowly. This is due to the isotopic composition of hafnium and the peculiarities of isotope transmutation in the neutron flux. Therefore, it finds application in the manufacture of controls for control and protection systems of reactors. Hafnium has good mechanical and corrosive properties over a wide temperature range [3].

The interstitial and metallic impurities (O, C, Si, P, Mg, K, Ca, Cl, F, Ni, H, etc.) have a negative effect on the structure and properties of zirconium and hafnium even in small amounts. This can lead to a change in mechanical and corrosion characteristics, as well as to changes in deformation and heat treatment modes. Therefore, experimenters are always interested in obtaining high-purity metal samples. The study of the characteristics of such samples makes it possible to more correctly assess the physical and mechanical properties associated with an own nature of metals.

The crystallization processes from melts are one of the main methods for refining metals and obtaining single crystals. They are used at the final stage of cleaning to remove small concentrations of impurities. Since zirconium and hafnium are characterized by high melting points and chemical activity, special physical purification methods are required. The conducting of zone melting in a vacuum allows cleaning both as a result of the zone separation of impurities and as a result of the evaporation process of impurities having a high saturated vapor pressure at the melting point of the base material.

The article discusses the possibilities of effective refining of zirconium and hafnium by the zone recrystallization method, including the use of electrotransport, the results of studies of the obtained samples are presented.

MATERIALS AND METHODS

In the presented work, the process of refining zirconium and hafnium was carried out by the zone recrystallization method, including in an electric field, on a crucibleless electron-beam zone melting facility in a vacuum. A description of the process and experimental setup was presented in detail in an article [4].

The starting materials for the experiments were zirconium with a purity of 99.7 wt. % and hafnium with a purity of 99.58 wt. %, obtained by the method of industrial iodide refining. The results of the content of impurities were obtained by laser mass spectrometry using an EMAL-2 analyzer. The limiting sensitivity of the analysis method for metal impurities was $\sim 10^{-5} \dots 10^{-6}$ at. %.

The use of the LECO TC-600 gas analyzer made it possible to determine the content of nitrogen and oxygen in the samples with an accuracy of $5 \cdot 10^{-8}$ at.%. The device was calibrated with certified LECO samples.

The visual inspection of thin sections was carried out using an MMP-4 microscope. The microhardness was measured on a PMT-3 microhardness meter at loads of 0.05 and 0.1 kgf. The value of the microhardness numbers was recorded by ten measurements, the error did not exceed 5%.

ZONE RECRYSTALLIZATION METHOD

The principle of zone refining is based on the practical use of the phenomenon of different solubility of impurities in the liquid and solid phases of the base material [5]. An important characteristic in the process description is the impurity distribution coefficient k , which is the ratio of the impurity concentration in the solid phase C_S to the concentration in the melt C_L :

$$k = C_S / C_L . \quad (1)$$

It is distinguishing between the concepts of equilibrium distribution coefficient k_0 and effective distribution coefficient k_e . When solving most problems, the equilibrium coefficient k_0 is determined from the "base-impurity" state diagrams or by the ratio of the maximum solubility of an impurity to its concentration at the point of invariant transformation [6,7]. However, with such estimation methods, k_0 values can be calculated only in the case of a significant concentration of impurities in the base material.

When calculating the equilibrium distribution coefficient k_0 in the case of low impurity concentrations it is convenient to use the theoretical methods of calculations based on the thermodynamic constants of the equation of ideal solutions. According to this concept it be can use a special case of the Schroeder – Le Chatelier equation for refractory metals [8]:

$$\ln \frac{C_{L_i}}{C_{S_i}} = - \frac{\Delta H_i}{R} \left(\frac{1}{T_b} - \frac{1}{T_{G_i}} \right) = \theta_i \quad (2)$$

$$\frac{C_{L_i}}{C_{S_i}} = e^{\theta_i} \text{ and } k_{0_i} = 1/e^{\theta_i}$$

where ΔH_i is the molar heat of fusion of the i -th impurity (J/mol), R is the universal gas constant ($R = 8.314$ J/mol·K), T_b is the melting temperature of the basic substance ($T_{Zr} = 2125$ K; $T_{Hf} = 2500$ K), T_{G_i} is the estimated value of the melting temperature of the base-impurity alloy, which is selected from the state diagram "base metal - impurity".

For phase diagrams characterized by a continuous series of solid solutions, peritectic-type diagrams throughout the concentration range, as well as for impurities whose diagrams with the base metal are unknown, T_{G_i} is chosen equal to the melting temperature of the impurity element. In the case of phase diagrams with a number of eutectic and peritectic transformations value T_{G_i} is selected in order to meet the minimum transformation temperature of eutectic or peritectic type.

When conducting zone melting process, moving crystallization front pushes dissolved impurity faster than it can evenly distribute in the melt. Before crystallization front occurs, enriched impurity region called the diffusion layer. The diffusion layer thickness δ is dependent on the impurity diffusion capacity, the melt viscosity, the nature of the fluid motion, and the crystallization speed and it can be changed depending on the conditions of the melt mixing. The more intensive the stirring, the thinner the diffusion layer adjacent to the crystallized metal. The layer thickness δ can vary from 10^{-3} cm with vigorous stirring to 10^{-1} cm with weak stirring.

Therefore, the main characteristic of the zone separation is the effective distribution coefficient k_{ei} , which for the i -th impurity can be calculated using the Barton-Prim-Slichter relation:

$$k_{ei} = \frac{1}{1 + \left(\frac{1}{k_{0_i}} - 1 \right) \cdot e^{-\frac{\nu \delta}{d}}} \quad (3)$$

where ν is the zone speed, δ is the diffusion layer thickness, and d is the impurity diffusion coefficient in the melt [5].

The value of the impurity diffusion coefficient d for most cases is in the range from 10^{-4} to 10^{-5} cm²/s. The width of the diffusion layer δ in the case of moderate mixing of the melt in the liquid zone is assumed to be 0.01 cm. Therefore, $\delta/d \approx 200$ s/cm. The ratio $v\delta/d$ is called the reduced crystallization rate (it is a dimensionless quantity).

When zone melting of refractory metals is carrying out in vacuum, in addition to cleaning the material as a result of zone redistribution, refining also occurs due to the evaporation of impurities having a high saturated vapor pressure at the melting point of the base material. Thus, at the melting temperature of zirconium ($T_{Zr} = 2125$ K) or hafnium ($T_{Hf} = 2500$ K), one should expect a decrease in the concentration of a number of metallic impurities (Al, Ca, Cu, Fe, Mn, Ni, Si, Ti, etc.). The reduced evaporation coefficient g_i for the i -th impurity (it is a dimensionless quantity) can be expressed by the formula:

$$g_i = \frac{2\alpha_i \gamma_i p_i^0 V l}{17.16 \cdot v r \sqrt{\frac{A_i T_b}{\eta_i}}}, \quad (4)$$

where α_i is the Langmuir coefficient; p_i^0 is the saturated vapor pressure at a melting temperature, torr; γ_i is the activity coefficient; A_i is the atomic weight in the condensed phase; η_i is the number of atoms in a vapor molecule; $V = A_b/\rho_b$ - atomic (molar) volume of the main component; r is the radius of the molten zone, l is the length of the zone, and v is the velocity of the zone [9].

After several passes of zone melting with a low speed of zone movement (1 or 2 mm/min), in the middle part of the refined sample a region of quasi-stationary concentration is established. The concentration of the i -th impurity after the n -th number of passes C_{ni} in the quasi-stationary region is related to the initial concentration of C_{oi} by the ratio, which is valid only when considering the case of low concentrations of impurities:

$$\tilde{N}_{ni} / C_{oi} = \left(\frac{k_{ei}}{k_{ei} + g_i} \right)^n. \quad (5)$$

The passing of a direct electric current through the metal sample leads to the displacement of both matrix ions and impurity ions to the anode or cathode. The current passing through the phase boundary changes the value of the effective distribution coefficient k_e due to the addition of the electric transport component to the diffusion flux. In the case of zone melting in an electric field equation (3) for the effective impurity distribution coefficient k_{ei}' takes the form:

$$k_{ei}' = \frac{1 + \frac{v'}{v}}{1 + \left[\frac{1}{k_{oi}} \left(1 + \frac{v'}{v} \right) - 1 \right] \cdot e^{-\frac{v\delta}{D_i} \left(1 + \frac{v'}{v} \right)}}, \quad (6)$$

where D_i is the diffusion coefficient of the impurity ion; v' is the speed of movement of the impurity ion.

RESULTS AND DISCUSSION

To obtain high-purity samples of zirconium or hafnium the method of vertical crucibleless zone melting (ZM) of round rods in a vacuum of $1 \cdot 10^{-4}$ Pa with electron-beam heating was chosen. The advantages of this technique include: the ability to grow single crystals of refractory metals and alloys with a melting point above 2000 K, no crucible, creation of a narrow heating area by focusing the electron beam, high specific power concentration [10].

The process of cleaning of metals was carried out in several stages. After the initial billet was heated (for the purpose of degassing) and carrying out the ZM at different speeds (from 16 to 1 mm/min), the samples were obtained in the form of cylindrical rods with a length of 100 to 300 mm and a diameter of up to 10 mm (Fig. 1).



Figure 1. The samples of zirconium before (a) and after (b) zone recrystallization

Calculations of the equilibrium coefficient k_{oi} and effective distribution coefficient k_{ei} allowed us to conclude that when carrying out the zone melting, due to the different solubility of impurities in the liquid and solid phases of zirconium, it is possible to carry out refining from the majority of metallic impurities (Al, Be, Fe, Ca, Si, Mn, Cu, etc.).

Small amounts of these impurities lower the melting point of zirconium, and for them $k_{oi} < 1$ [11]. For effective refining of zirconium from metal impurities with $k_{ei} < 1$, two or three passes of the zone melting with a low speed $v = 2$ mm/min are sufficient (Table 1).

The estimates of the values of the reduced evaporation coefficient g_i and the assumed concentration of impurities C_{ni} in the quasi-stationary region were carried out for the stages of zone melting at different rates according to formulas (5) and (6). The performed calculation of C_{ni} for a speed of 2 mm/min showed that those impurities for which $g_i > 1.2$ will be effectively removed during the evaporation process (Al, Be, Ca, Si, Cu, Mn, Pb, Cr).

Also Table 1 shows the calculations of the equilibrium distribution coefficient $k_{o,lim}$, taken from the article [12].

Table 1. The calculated values of equilibrium coefficient k_{oi} and effective distribution coefficient k_{ei} , reduced evaporation coefficient g_i , assumed concentration C_{ni} for the i -th impurity in Zr, and results of chemical analysis of zirconium samples after zone melting

Element	C_{oi} , wt. %	k_{oi}	$k_{o,lim}$ [12]	k_{ei}	g_i at $v=2$ mm/min	C_{ni} after two passes with $v=2$ mm/min	Chemical analysis after ZM
Zr	99.7	1	1	1	$2.2 \cdot 10^{-6}$	–	99.87
Al	$2.2 \cdot 10^{-4}$	0.46	<0.42	0.62	7.21	$1.4 \cdot 10^{-6}$	$7 \cdot 10^{-6}$
Be	$<1 \cdot 10^{-5}$	0.60	<1	0.74	5.35	$1.5 \cdot 10^{-7}$	$<1 \cdot 10^{-5}$
Hf	0.075	1.23	>1	1.1	$8 \cdot 10^{-8}$	0.075	0/052
Fe	$8.5 \cdot 10^{-3}$	0.54	0.27	0.70	0.21	0.005	$7.5 \cdot 10^{-4}$
Ca	$2 \cdot 10^{-5}$	0.62	–	0.76	118.4	$8 \cdot 10^{-10}$	$1.3 \cdot 10^{-5}$
Si	$2.3 \cdot 10^{-4}$	0.43	<1	0.59	7.07	$1.4 \cdot 10^{-6}$	$7 \cdot 10^{-5}$
Mn	$4.5 \cdot 10^{-5}$	0.68	<1	0.80	144.4	$1.4 \cdot 10^{-9}$	$<5 \cdot 10^{-6}$
Cu	$9.5 \cdot 10^{-4}$	0.54	0.101	0.70	1.34	$1 \cdot 10^{-4}$	$<1 \cdot 10^{-5}$
Mo	$<6 \cdot 10^{-5}$	0.77	0.392	0.87	$8.7 \cdot 10^{-8}$	$6 \cdot 10^{-5}$	$<6 \cdot 10^{-5}$
Ni	$4 \cdot 10^{-3}$	0.49	<1	0.65	11.46	$1.1 \cdot 10^{-5}$	$2 \cdot 10^{-3}$
Nb	$<5 \cdot 10^{-5}$	0.92	0.634	0.95	$5.5 \cdot 10^{-9}$	$5 \cdot 10^{-5}$	$<5 \cdot 10^{-5}$
Pb	$<1 \cdot 10^{-4}$	0.50	<1	0.66	74.37	$7.7 \cdot 10^{-9}$	$<1 \cdot 10^{-4}$
Ti	$5 \cdot 10^{-4}$	0.83	<1	0.90	0.001	$5 \cdot 10^{-4}$	$5 \cdot 10^{-4}$
Cr	$3.5 \cdot 10^{-3}$	0.68	<1	0.80	5	$6.5 \cdot 10^{-5}$	$5 \cdot 10^{-6}$

In order to obtain large metal grains, the experiments were carried out using slow heating and cooling of the ingot (stage of thermal cycling) in the range of polymorphic transformation temperature, which for zirconium is 1138 K. Thermal cycling was carried out for 4...6 hours. Metallographic studies showed the presence of large metal grains with sizes from 5 to 10 mm. The use of a complex purification procedure, including preliminary heating, stages of vacuum zone melting and thermal cycling, made it possible to obtain samples of zirconium with a purity of 99.87 wt. %.

The concentration of impurities was significantly reduced (for example, the concentration of Hf decreased by 1.5, O – by 2.7, C – by 1.6 times, metal impurities – by 1.5...700 times) (Table 1).

The study of the possibility of zirconium refining by the method of vacuum electron-beam melting was also carried out in an electric field (ZMEF method), included both in the direction of the zone melting and against the course of the zone. The process of directional bias of interstitial impurities during electrotransport takes place actively both in the β -phase and in the molten metal zone. When the field was connected against the course of the melting, the ions of interstitial impurities, characterized by a negative value of effective charge of the impurity ion Z^* , were displaced to the positive pole (anode) (according to the results of work [13]). Moreover, in this case, the movement of ions coincided with the direction of movement of the liquid zone. This significantly increased the efficiency of refining by the ZMEF method. In work [14], the parameters of the ZMEF process were calculated for interstitial impurities: the values of the impurity ion mobility U , the diffusion coefficient D , the movement velocity of the impurity ion v' , the effective impurity distribution coefficient k_e' . In carrying out the calculations, the values of the melting parameters were used: the electric field strength $E = 0.013$ V/cm, the melting speed $v = 0.066$ cm/s (Table 2).

Table 2. The results of calculating the parameters of the ZMEF process for interstitial impurities in zirconium

Impurity	Z^* [13]	$U, 10^{-5}, \text{cm}^2/(\text{V}\cdot\text{s})$	$D, 10^{-6}, \text{cm}^2/\text{s}$	$ v' , 10^{-7}, \text{cm/s}$	k_e at ZM	k_e'	k_e'
						$\vec{E} \uparrow \vec{v}$	$\vec{E} \downarrow \vec{v}$
O	-1	1.8	3.3	2.34	1.15	1.01	0.99
C	-0.2	0.9	8.25	1.17	0.95	0.96	0.95
N	-0.7	1.2	3.14	1.56	1.03	1.01	0.99

The refining of zirconium from gas-forming impurities took place at various stages of the experiments. Thus, hydrogen was evaporated in the form of gaseous molecules (H_2 , H_2O) during preliminary heating and melting at a high speed. The carbon was volatilized as CO and CO_2 molecules. The refining process also took place due to the displacement of metal carbides into the end of the ingot. Nitrogen was evaporated in the form of N_2 gas molecules during high-temperature heating and zone melting. A decrease in the oxygen content occurred at the stages of heating and ZM as a result of the formation of gaseous molecules (CO , CO_2 , H_2O). Oxygen removal could also occur due to the displacement of refractory oxides (for example, ZrO_2 , HfO_2) during recrystallization to the end of the sample. In the purest samples of zirconium, the concentration of oxygen was reduced by 3.3, nitrogen – 3, carbon – 2 times. The results of the analysis of the elemental composition showed an insignificant content of a number of metallic impurities in the refined ingots, which were removed during the simultaneous passage of the processes of evaporation, zone recrystallization and melting with electric transport. Thus, the concentration of aluminum was reduced by 5, iron – 11, nickel – 2, copper – 45, chromium – 75, silicon – 10, titanium – 2.5 times. There was a slight decrease in the concentration of hafnium (from 0.075 to 0.05 wt %). The content of molybdenum and niobium after heats did not change and remained at the level of $2 \cdot 10^{-4}$ and $1 \cdot 10^{-4}$ wt.% respectively. The purity of the refined samples was characterized by a value of 99.89 wt. % by zirconium content.

When carrying out a cycle of works on zone recrystallization of hafnium, the coefficients k_{0i} , k_{ei} , g_i , C_{ni} , k_e' were calculated using formulas (2-5) (Table 3). A detailed description of the calculations was given in the articles [15, 16]. Also Table 3 shows the calculations of the equilibrium distribution coefficient $k_{0,lim}$, taken from the the article [12].

Table 3. The calculated values of equilibrium coefficient k_{0i} and effective distribution coefficient k_{ei} , reduced evaporation coefficient g_i , assumed concentration C_{ni} for the i -th impurity in Hf, and results of chemical analysis of hafnium samples after zone melting

Element	C_{0i} wt. %	k_{0i}	$k_{0,lim}$ [12]	k_{ei}	g_i at $v=2$ mm/min	C_{ni} after two passes with $v=2$ mm/min	Chemical analysis after ZM
Hf	99.58	1	1	1	0.001	-	99.75...99.8
Zr	0.23	0.85	0.73	0.91	0.0099	0.225	0.21
Al	0.003	0.42	0.71	0.58	402.8	$6.3 \cdot 10^{-9}$	$<1 \cdot 10^{-5}$
W	0.0002	0.81	0.49	0.89	$2.8 \cdot 10^{-5}$	0.0002	0.00013
Fe	0.007	0.68	0.12	0.80	11.45	$3 \cdot 10^{-5}$	$4 \cdot 10^{-4}$
Ca	0.01	0.58	-	0.72	1502	$2.3 \cdot 10^{-9}$	$<7 \cdot 10^{-6}$
Si	0.004	0.26	0.42	0.40	89.72	$7.9 \cdot 10^{-8}$	$<4 \cdot 10^{-5}$
Mg	0.003	0.47	-	0.63	$3.85 \cdot 10^4$	$8 \cdot 10^{-13}$	$<5 \cdot 10^{-6}$
Mn	0.0003	0.64	0.29	0.78	$3.84 \cdot 10^3$	$1.2 \cdot 10^{-11}$	$<1 \cdot 10^{-5}$
Cu	0.002	0.53	-	0.68	95.44	$1 \cdot 10^{-7}$	$1 \cdot 10^{-5}$
Mo	0.07	0.80	0.71	0.88	$7.7 \cdot 10^{-3}$	0.069	0.02
Ni	0.01	0.53	0.05	0.68	11.17	$3.3 \cdot 10^{-5}$	$1 \cdot 10^{-4}$
Nb	0.006	0.91	0.70	0.95	$8.8 \cdot 10^{-4}$	$6 \cdot 10^{-3}$	0.004
Ti	0.003	0.76	0.66	0.86	1.37	$4.4 \cdot 10^{-4}$	$2 \cdot 10^{-4}$
Cr	0.003	0.66	0.74	0.79	79.13	$2.9 \cdot 10^{-7}$	$<2 \cdot 10^{-5}$

It was found that for the refining of hafnium, the zone melting method will be most efficiently applied when several stages of experiments are carried out sequentially, namely: 1) high-temperature heating, 2) zone melting at a big speed (16 or 8 mm/min) to remove highly volatile metallic impurities, 3) melting at a low speed (2 or 1 mm/min) for the display of the effect of impurity displacement of together with the movement of the liquid zone, 4) thermal cycling in the temperature range of polymorphic transformation. All operations must be carried out in a vacuum of at least $1 \cdot 10^{-4}$ Pa.

Zone recrystallization made it possible to obtain hafnium samples with a purity of 99.88 wt. %. The oxygen and carbon concentrations were lowered 1.5 times (from 0.03 to 0.02 wt. % in oxygen, from 0.04 to 0.022 wt. % in carbon), zirconium - from 0.23 to 0.065 wt. %.

The use of the MX 7304A mass spectrometer made it possible to study the outgassing from hafnium iodide and refined hafnium samples (the weight of the samples was 0.93 g). The experiments had shown that the maximum peak of gas release was in the temperature range of 500...550 °C. In this temperature range, the total gas pressure during heating of the refined sample was observed to be 10 times lower than during heat treatment of hafnium iodide (Fig. 2).

The change in the partial pressure of gases released from the hafnium iodide sample is shown in the diagram (Fig. 3, a). In the experiment, the amount of evolved gas in relation to the chamber volume was 0.0063 %. When the sample was heated to a temperature of 300 °C, there was a slight increase in pressure, which is explained by the degassing of the original sample; gas evolution with a mass number of 18 (water vapor) prevailed. When heated from 300 °C to 550 °C, the pressure increased due to the activation of the process of gas evolution with mass numbers 18 (H_2O), 28 (carbon monoxide CO and nitrogen N_2), 44 (carbon dioxide CO_2). When heated above 700 °C, the total gas pressure stabilized at the level of $1.2 \cdot 10^{-5}$ mm Hg.

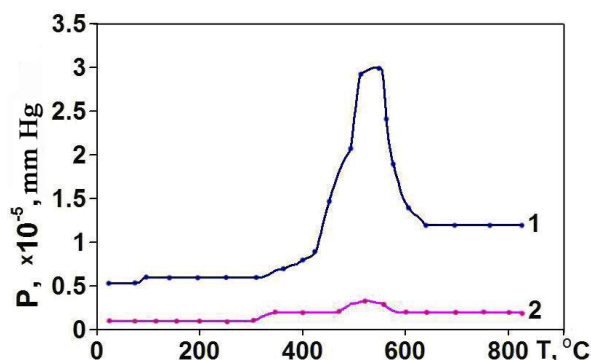


Figure 2. Gas evolution from samples of initial hafnium iodide (1) and refined hafnium (2)

The gas evolution from a sample of refined hafnium under heating is insignificant (total pressure $P \approx 3 \cdot 10^{-6}$ mm Hg). The distribution of the partial pressure of gases is shown in Fig. 3, b. When heated to a temperature of 350 °C...400 °C, some activation of the process of gas evolution with a mass number of 18 (H_2O) was observed.

The study of gas evolution made it possible to optimize the temperature regime of the stage of preliminary heating of the hafnium sample. It is recommended to carry out heating in the range from 400 °C to 600 °C.

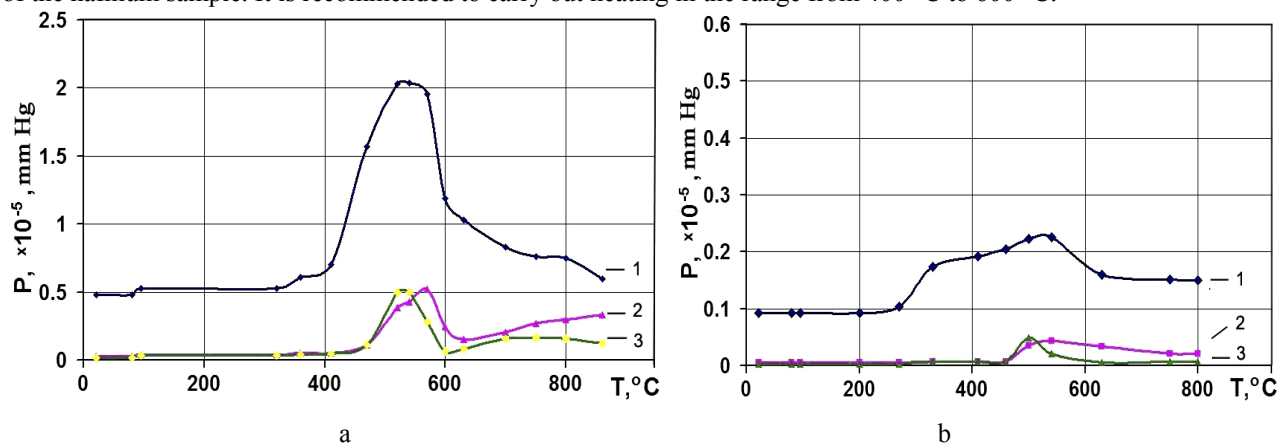


Figure 3. Partial pressure of gases released from samples of hafnium iodide (a) and refined hafnium (b), with mass numbers: 1) 18 (H_2O), 2) 28 (N_2 , CO), 3) 44 (CO_2)

Vickers microhardness measurements of the samples showed that if for the initial hafnium iodide $H_{\mu} = 2700...2850$ MPa, then for the sample after zone melting with a high speed $H_{\mu} = 2050...2200$ MPa, for the sample after two passes at a speed of 2 mm/min the value decreased to $H_{\mu} = 1200...1400$ MPa.

The refining of hafnium by the ZMEF method was carried out with a variability of connection (in the direction and against the movement of zone melting). Samples were cut from the purest part of the refined ingot 100 mm long for testing. The results of chemical analysis of refined hafnium samples indicate an insignificant content of Al, Ca, Cu, Si, Ti, which were removed during the joint passage of the processes of zone recrystallization and evaporation. The concentration of iron was significantly reduced at the stages of zone melting (Table 4) [16].

Table 4. Results of chemical analysis of hafnium samples

Materials	Concentration of a chemical element, wt. %											
	Hf	Zr	O	N	C	Al	Fe	Ca	Cu	Mo	Si	Ti
Hafnium iodide	99.58	0.23	0.03	0.003	0.04	0.003	0.007	0.01	0.002	0.07	0.004	0.003
Hf after ZM	99.75	0.21	0.02	$4 \cdot 10^{-4}$	0.022	$1 \cdot 10^{-5}$	$4 \cdot 10^{-4}$	$7 \cdot 10^{-6}$	$1 \cdot 10^{-5}$	0.02	$4 \cdot 10^{-5}$	$2 \cdot 10^{-4}$
Hf ZMEF $\vec{E} \uparrow \uparrow \vec{v}$	99.81	0.17	0.013	$8 \cdot 10^{-5}$	0.0021	$< 2 \cdot 10^{-6}$	$5 \cdot 10^{-6}$	$< 3 \cdot 10^{-6}$	$< 3 \cdot 10^{-6}$	0.01	$< 1 \cdot 10^{-5}$	$< 5 \cdot 10^{-5}$
Hf ZMEF $\vec{E} \uparrow \downarrow \vec{v}$	99.85	0.12	0.011	$5 \cdot 10^{-5}$	0.0018	$< 2 \cdot 10^{-6}$	$2 \cdot 10^{-4}$	$< 3 \cdot 10^{-6}$	$< 3 \cdot 10^{-6}$	0.008	$< 1 \cdot 10^{-5}$	$< 5 \cdot 10^{-5}$

In this work, the special attention was paid to the study of the distribution of interstitial impurities in hafnium after various stages of melting. Refining is especially effective when melting in an electric field coinciding with the direction of zone movement. The simultaneous passage of refining processes (evaporation of highly volatile impurities in vacuum, zone recrystallization, electrotransport) significantly increased the efficiency of hafnium purification from all types of impurities. High-purity hafnium samples with a low content of interstitial impurities were obtained. The oxygen concentration was 0.011, carbon - 0.0018, nitrogen - $5 \cdot 10^{-5}$ wt %.

In Fig. 4 (a, b) it is can see a zone with a low concentration of oxygen and carbon (within 20...60 mm along the length of the ingot), closer to the end sections is slightly higher concentration. The redistribution of oxygen along the length of the ingot indicates the effect of an electrotransport. A significant decrease in the concentrations of carbon and nitrogen after ZMEF occurred as a result of evaporation and displacement during recrystallization (Table 4).

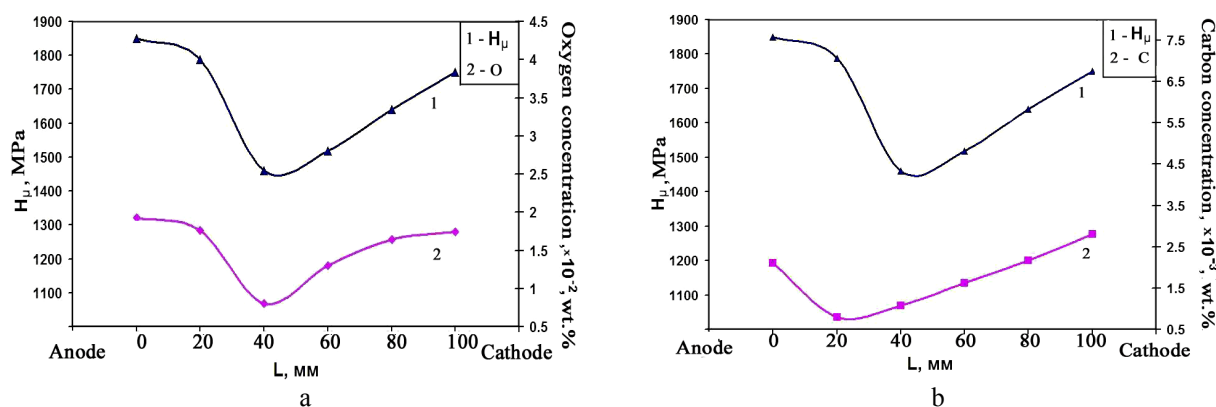


Figure 4. Dependence of the microhardness of hafnium on the impurity concentration after the ZMEF for: a) oxygen, b) carbon. The directions of the zone melting and the electric field coincided

The value of microhardness directly depends on the concentration of interstitial impurities (the minimum of microhardness falls on the minimum concentrations), and this dependence is most characteristic in relation to oxygen, the content of which is much higher than that of carbon and nitrogen. So, the minimum value of microhardness $H_{\mu} = 1460$ MPa was observed at an oxygen concentration of 0.008 wt. %.

In order to obtain large grains of hafnium, experiments were carried out using slow heating and cooling of the ingot in the range of the polymorphic transformation temperature of 2033 K (thermal cycling stage). The experiment was carried out for 4...6 hours. Metallographic studies showed the presence of large grains up to 25 mm long, elongated along the ingot. By the method of electrical discharge cutting an ingot of hafnium was divided into cylindrical columns with a length of 10...12 mm and a diameter of 8...10 mm. The ends of the samples were ground and etched to reveal the microstructure. The optical method using an MMP-4 microscope was used to visually study thin sections and photograph the grain structure.

The orientation of the single crystals with the separation of hcp lattice directions $[0001]$, $[10\bar{1}0]$ was carried out on diffractometer DRON-1.0. The orientation accuracy was within ± 1.5 , the crystal mosaic was $\pm 4'..5'$. Single-crystal samples had an arbitrary shape with a thickness of ~ 3 mm along the selected crystallographic directions. The parameters of the crystal lattice of hafnium were determined from x-ray diffraction data: $a = (0.31950 \pm 5 \cdot 10^{-5})$ nm and $c = (0.50542 \pm 5 \cdot 10^{-5})$ nm (at 298 K), which corresponds to a density $\rho = 13.263$ g/cm³ and an axial ratio $c/a = 1.5819$ [17].

CONCLUSIONS

The work investigates the possibilities of effective refining of zirconium and hafnium by the zone recrystallization method, including the experiments in an electric field. It is shown that zone melting with the variability of connecting the direction of the electric field makes it possible to obtain refined samples with a reduced content of metal and gas-forming impurities. The best degree of purification was achieved when zone melting took place in an electric field directed opposite to the movement of the zone. As a result of the experiments, zirconium samples with a purity of 99.89 wt. % and hafnium with a purity of 99.85 wt. % were obtained. The use of an integrated approach to refining made it possible to obtain and study single-crystal samples of hafnium.

ACKNOWLEDGMENTS

The authors express their gratitude and deep appreciation to the junior researcher Yu.P. Bobrov for many years of cooperation, advice and valuable remarks when discussing the experimental results.

ORCID IDs

Oleh E. Kozhevnikov, <https://orcid.org/0000-0002-9690-8931>; Mykola M. Pylypenko <https://orcid.org/0000-0001-8113-8578>
 Maryna F. Kozhevnikova, <https://orcid.org/0000-0003-2464-3847>

REFERENCES

- [1] D.L. Douglass. *The Metallurgy of Zirconium*, (Vienna: IAEA, 1971), pp. 466.
- [2] A.S. Zaimovsky, E.V. Nikulina, N.G. Reshetnikov, *Циркониевые сплавы в атомной энергетике [Zirconium Alloys in Atomic Energetics]*, (Energoatomizdat, Moscow, 1994), pp. 453. (in Russian)
- [3] D.E. Thomas, and E.T. Hayes, *Металлургия гафния [The Metallurgy of Hafnium]*, (Metallurgy, Moscow, 1967), pp. 310. (in Russian)

- [4] P.N. Vjugov, O.E. Kozhevnikov, and T.Yu. Rudycheva, PAST, 6(18), 19-24 (2009), https://vant.kipt.kharkov.ua/ARTICLE/VANT_2009_6/article_2009_6_19.pdf. (in Russian)
- [5] W.G. Pfann, *Зонная плавка [Zone Melting]*, (Mir, Moscow, 1970), pp. 366. (in Russian)
- [6] L.A. Niselson, and A.G. Yaroshevsky, *Межфазовые коэффициенты распределения [Interphase distribution coefficients]*, (Nauka, Moscow, 1992), pp. 390. (in Russian)
- [7] N.P. Lyakishev, *Диаграммы состояния Т.2 [State diagrams Vol.2]*, (Mashinostroyeniye, Moscow, 1997), pp. 1024. (in Russian)
- [8] R.A. Laudise, and R.L. Parker, *Рост монокристаллов [The Growth of Single Crystals]*, (Mir, Moscow, 1974), pp. 540. (in Russian)
- [9] Sh.I. Peizulaev, *Учет испарения примесей при зонной плавке [Taking into Account the Evaporation of Impurities in Zone Melting]*, Bulletin of the Academy of Sciences, Series "Inorganic Materials", 3(9), 1523-1532 (1967) (in Russian)
- [10] G.F. Tikhinski, G.P. Kovtun, and V.M. Azhazha, *Получение сверхчистых редких металлов [Obtaining of ultrapure rare metals]*, (Metallurgy, Moscow, 1986), pp. 160. (in Russian)
- [11] O.E. Kozhevnikov, M.M. Pylypenko, Yu.S. Stadnik, V.D. Virich, M.F. Kozhevnikova, and I.G. Tantsyura, PAST, 5(117), 62-68 (2018), https://vant.kipt.kharkov.ua/ARTICLE/VANT_2018_5/article_2018_5_62r.pdf. (in Russian)
- [12] L. Kuchaf, B. Wozniakova and J. Dräpala. *Segregation behavior during the zone melting of refractory metals*, Journal of Crystal Growth, 52, 359-366 (1981), [https://doi.org/10.1016/0022-0248\(81\)90219-0](https://doi.org/10.1016/0022-0248(81)90219-0).
- [13] F.A. Schmidt, O.N. Carlson, and C.E. Swanson, Metallurgical Transactions, 1, 1371-1374 (1970), <https://doi.org/10.1007/BF02900257>.
- [14] O.E. Kozhevnikov, M.M. Pylypenko, Yu.S. Stadnik, and R.V. Azhazha, PAST, 1(125), 27-34 (2020), https://vant.kipt.kharkov.ua/ARTICLE/VANT_2020_1/article_2020_1_27.pdf. (in Russian)
- [15] O.E. Kozhevnikov, P.N. Vjugov, M.M. Pylypenko, and V.D. Virich, The Journal of Kharkiv National University, Series "Nuclei, Particles, Fields", 4(60), 81-86 (2013), <https://periodicals.karazin.ua/eejp/article/view/12908/12230>. (in Russian)
- [16] O.E. Kozhevnikov, P.N. Vjugov, and M.M. Pylypenko, PAST, 2(96), 89-94 (2015), https://vant.kipt.kharkov.ua/ARTICLE/VANT_2015_2/article_2015_2_89r.pdf. (in Russian)
- [17] O.E. Kozhevnikov, M.M. Pylypenko, A.S. Bulatov, P.N. Vjugov, V.S. Klochko, and A.V. Korniets. PAST, 1(113), 54-61 (2018), https://vant.kipt.kharkov.ua/ARTICLE/VANT_2018_1/article_2018_1_54r.pdf. (in Russian)

ЗОННА ПЕРЕКРИСТАЛІЗАЦІЯ ЦИРКОНІЮ ТА ГАФНІЮ

О.Є. Кожевніков, М.М. Пилипенко, М.Ф. Кожевнікова

Національний науковий центр «Харківський фізико-технічний інститут», НАНУ
вул. Академічна, 1, 61108, Харків, Україна

В роботі вивчено можливості отримання високочистих зразків цирконію та гафнію методом зонної перекристалізації круглих стрижнів з електронно-променевим нагрівом у вакуумі $1 \cdot 10^{-4}$ Па. Частина плавок було проведено в постійному електричному полі з варіативністю його підключення. Показано, що одночасне проходження декількох рафінуючих процесів (випаровування легковидаляємих металевих домішок, зонна перекристалізація зі спрямованим зміщенням домішок в кінцеву частину зразка, електроперенос) дозволили провести ефективне рафінування цирконію як від металевих домішок, так і від домішок впровадження. Найкращої ступені очищення було досягнуто при проведенні зонного плавлення в електричному полі, направленому протилежно руху зони. В цьому випадку зміщення іонів домішок впровадження збіглося з напрямком пересування рідкої зони. Було отримано зразки цирконію з чистотою 99,89 мас. % (концентрація алюмінію було знижено в 5, заліза - 11, міді - 45, хрому - 75, кремнію - 10, титану - 2,5, кисню - 3,3, азоту - 3, вуглецю - 2 рази). Рафіновані методом зонної перекристалізації зразки гафнію характеризувалися чистотою 99,85 мас. %. Було значно знижено концентрації як усіх металевих домішок, так і домішок впровадження (концентрація в мас.% кисню склала 0,011, вуглецю - 0,0018, азоту - $5 \cdot 10^{-5}$). Проведено дослідження газовиділення із зразків йодидного та рафінованого гафнію. З'ясовано, що максимальний пік газовиділення припадав на температурний інтервал 500...550 °С. Застосування комплексного підходу, який включає високотемпературний прогрів, етапи зонного плавлення з різною швидкістю і термоцикування в області температури поліморфного перетворення, дозволило отримати монокристалічні зразки гафнію. По результатам рентгеноструктурного аналізу було визначено параметри кристалічної решітки гафнію: $a = (0,31950 \pm 5 \cdot 10^{-5})$ нм і $c = (0,50542 \pm 5 \cdot 10^{-5})$ нм (при 298 К), що відповідає щільності $\rho = 13,263$ г/см³ та осьовому співвідношенню $c/a = 1,5819$.

КЛЮЧОВІ СЛОВА: цирконій, гафній, зонна перекристалізація, електроперенос, термоцикування, домішковий склад, мікротвердість.

PACS: 31.15.A-; 46.70.-P; 62.20.D-; 62.20.de; 65.40.De; 65.40.-b ; 65.60.+a ; 71.20.-b

STRUCTURE AND PROPERTIES OF ZnSnP₂ WITH THE APPLICATION IN PHOTOVOLTAIC DEVICES BY USING CdS AND ZnTe BUFFER LAYERS

 Neeraj^a,  Ajay S. Verma^{b,*}

^aDepartment of Physics, Banasthali Vidyapith, Rajasthan 304022 (India)

^bDepartment of Natural and Applied Sciences, School of Technology, Glocal University Saharanpur, Uttar Pradesh, 247232 (India)

*Corresponding Author: ajay_phy@rediffmail.com, Mobile: +91 9412884655

Received November 1, 2020; revised December 15, 2020; accepted February 13, 2021

Here in, we present the extensive analysis of the parameters associated with structural, electronic, optical and mechanical properties of zinc-based chalcopyrite material by using full potential linearized augmented plane wave method (FP-LAPW) within framework on the density functional theory. Ab initio calculations have been performed by the linearized augmented plane wave (LAPW) method as implemented in the WIEN2K code within the density functional theory to obtain the structural, electronic and optical properties of ZnSnP₂ in the body centered tetragonal (BCT) phase. The six elastic constants (C_{11} , C_{12} , C_{13} , C_{33} , C_{44} and C_{66}) and mechanical parameters have been presented and compared with the available experimental data. The thermodynamic calculations within the quasi-harmonic approximation is used to give an accurate description of the pressure-temperature dependence of the thermal-expansion coefficient, bulk modulus, specific heat, Debye temperature, entropy Grüneisen parameters. Based on the semi-empirical relation, we have determined the hardness of the material; which attributed to different covalent bonding strengths. Further, ZnSnP₂ solar cell devices have been modeled; device physics and performance parameters have analyzed for ZnTe and CdS buffer layers. Simulation results for ZnSnP₂ thin layer solar cell show the maximum efficiency (22.9%) with ZnTe as the buffer layer. Most of the investigated parameters are reported for the first time. The result of the present study further validates the prospects of using this chalcopyrite that would be inherently persistent and consistent with flexible substratum, those are the main features of commercialization chalcopyrite solar cells. Thus, promoting the evolution of this material, for achieving high performance based optoelectronic devices will pave a new path in solar cell industry.

KEYWORDS: Ab-initio calculations; electronic properties; elastic constants; thermodynamic properties

ZnSnP₂ is a member of A^{II}B^{IV}C^V₂ group ternary compound semiconductors, which has with chalcopyrite structure as a new solar absorber. The growth of ZnSnP₂ thin films has been prepared by co-evaporation and in ultra-high vacuum by molecular beam epitaxy (MBE). Recently [1], ZnSnP₂ based thin-film solar cell is fabricated and also prepared energy band gap by phosphidation method under the variation of Zn/Sn atomic ratio. Defects introduce localized levels in the energy gap of ZnSnP₂ and other compound semiconductors through which they control solar cell device performance, efficiency and reliability. In ZnSnP₂ thin film, zinc vacancies or zinc-on-tin sites are considered as acceptor. This is responsible for p-type conductivity. ZnSnP₂ is focused as a solar absorbing material consisting of safe and earth-abundant elements. Investigated the structures of interfaces related to the absorbing material ZnSnP₂ to clarify the origin of high resistance and improve the photovoltaic performance in ZnSnP₂ solar cells. The absorption coefficient of ZnSnP₂ was reported to be approximately 10^5 cm^{-1} in visible light range; ZnSnP₂ has a promising property for a solar absorbing material. ZnSnP₂ crystals for solar cells were prepared by mechanical-polishing [2,3].

Martinez et al [4], the A^{II}B^{IV}C^V₂ materials have similarly compelling electronic properties to their A^{II}B^V counter parts. Materials can typically be doped both n-type and p-type using extrinsic impurities, and mobilities can be extremely high, with multiple reports. The phosphide and arsenide in A^{II}B^{IV}C^V₂ compounds have been synthesized in bulk form by three primary techniques; while optical properties have been studied using a combination of theory and experiment. Experimental work has been used to examine photoluminescence and absorption edge, while calculations can provide insight into physical mechanisms underlying these measurements [4]. ZnSnP₂ has been proposed as a promising candidate for a solar absorbing material consisting of earth-abundant and safe elements. Solar absorbing materials composed of earth-abundant and safe elements have been investigated and Cu₂ZnSnS_{4-x}Se_x, Cu₂SnS₃, Cu₂O, SnS, Fe₂S, and Zn₃P₂ solar cells have been developed with a conversion efficiency of 12.6% [5]. The chalcopyrite compound ZnSnP₂ is a promising candidate as a light absorber in solar cells since it has a direct band gap of 1.6 eV [6]. Ternary A^{II}B^{IV}C^V₂ chalcopyrite semiconductors (Zn,Cd)(Si,Ge,Sn)(P,As)₂ have band gap energies ranging from 2.1 eV (ZnSiP₂) to 0.67 eV (ZnSnAs₂) [6]. These materials have structural as well as electronic anomaly with higher energy gaps and lower melting points relative to their binary analogues, because of which they are considered to be important in crystal growth studies and device applications. Apart from it, the other important technological applications of these materials are in light emitting diodes, infrared detectors, infrared oscillations, etc [4-8]. ZnSnP₂ semiconductors open up the possibility of fabricating a graded multi-junction solar cell using the ordered chalcopyrite as the top layer, with progressively more disordered layers underneath, free from lattice matching problems [7-10]. A considerable amount of experimental and theoretical work related to the prediction of crystal structures, lattice constants, phase diagrams and related properties of these compounds has been done during the last few years [9-13]. In spite of all these works, it has been seen that the theoretical results obtained for elastic constants which experimentally need single crystals of these compounds differ considerably with the available experimental data [4-8].

In the present article, we have been investigated the structural, electronic, optical, elastic and thermal properties of ZnSnP_2 in chalcopyrite phase. We have presented the theoretical study of expansion coefficient (α), heat capacities (C_v and C_p), bulk modulus (B and B'), Debye temperature (θ_D), hardness (H) and Gruneisen parameter (γ) of ZnSnP_2 ; which are nevertheless scarce in literature. Calculated ground-state structural properties of the aforementioned crystals have been compared with available experimental and theoretical data. The outline of the paper is as follows. In section II we have given a brief review of the computational scheme used. The calculations of the fundamental physical properties have been described with the application point of view in solar cell device in section III; while the summary and conclusions are drawn in section VI.

COMPUTATIONAL METHODS

The calculations were done using FP-LAPW computational scheme [14, 15] as implemented in the WIEN2K code [16]. The FP-LAPW method expands the Kohn-Sham orbitals as atomic like orbitals inside the muffin-tin (MT) atomic spheres and plane waves in the interstitial region. The Kohn-Sham equations were solved using the recently developed Wu-Cohen generalized gradient approximation (WC-GGA) [17, 18] for the exchange-correlation (XC) potential. It has been shown that this new functional is more accurate for solids than any existing GGA and meta-GGA forms. For a variety of materials, it improves the equilibrium lattice constants and bulk moduli significantly over local-density approximation [19] and Perdew-Burke-Ernzerhof (PBE) [20] and therefore is a better choice. For this reason, we adopted the new WC approximation for the XC potential in studying the present systems. Further for electronic structure calculations modified Becke-Johnson potential (mBJ) [21] as coupled with WC-GGA is used.

The valence wave functions inside the atomic spheres were expanded up to $l=10$ partial waves. In the interstitial region, a plane wave expansion with $R_{\text{MT}}K_{\text{max}}$ equal to seven was used for all the investigated systems, where R_{MT} is the minimum radius of the muffin-tin spheres and K_{max} gives the magnitude of the largest K vector in the plane wave expansion. The potential and the charge density were Fourier expanded up to $G_{\text{max}} = 10$. We carried out convergence tests for the charge-density Fourier expansion using higher G_{max} values. The R_{MT} (muffin-tin radii) are taken to be 2.2, 2.15 and 1.7 (in atomic unit) for Zn, Sn and P respectively. The modified tetrahedron method [22] was applied to integrate inside the Brillouin zone (BZ) with a dense mesh of 5000 uniformly distributed k-points (equivalent to 405 in irreducible BZ) where the total energy converges to less than 10^{-6} Ry.

The computer simulation tool AMPS-1D (Analysis of Microelectronic and Photonic Structures) was employed by specifying semiconductor parameters as input in each layers of the cell.

RESULTS AND DISCUSSION

Structural Properties

The ternary chalcopyrite semiconductor crystallizes in the chalcopyrite structure with space group $I-42d$ (D_{2d}^{12}). The Zn atom is located at (0,0,0); (0,1/2,1/4), Sn at (1/2,1/2,0); (1/2,0,1/4) and P at (u,1/4,1/8); (-u,3/4,1/8); (3/4,u,7/8); (1/4,-u,7/8). Two unequal bond lengths $d_{\text{Zn-P}}$ and $d_{\text{Sn-P}}$ result in two structural deformations, first is characterized by u parameter defined as $u=0.25 + (d_{\text{Zn-P2}} - d_{\text{Sn-P2}})/a^2$ where a is the lattice parameter in x and y direction, and the second parameter $\eta=c/a$, where c is lattice parameter in z direction which is generally different from 2a.

To determine the best energy as a function of volume, we minimized the total energy of the system with respect to the other geometrical parameters. The minimization is done in two steps, first parameter u is minimized by the calculation of the internal forces acting on the atoms within the unit cell until the forces become negligible, for this MINI task is used which is included in the WIEN2K code. Second, the total energy of crystal is calculated for a grid of volume of the unit cell (V) and c/a values, where each point in the grid involves the minimization with respect to u. Five values of c/a are used for each volume and a polynomial is then fitted to the calculated energies to calculate the best c/a ratio. The result is an optimal curve (c/a, u) as a function of volume. Further a final optimal curve of total energy is obtained by minimizing the energy verses [V, c/a (V), u (V)] by FP-LAPW calculations and Murnaghan equation of state [23]. Table 1 present the lattice parameters (a, c and u) and obtained along with the bulk modulus (B) and its pressure derivative (B'). The calculated total energy per unit as a function of volume is shown in Figure 1 (a).

Electronic and optical properties

The present calculations using the WC-mBJ method yields a direct band gap of 1.9 eV. As clear from the Figure 1 (b), that the obtained electronic band gap matches well with the experimental data predicted by Shaposhnikov et al [24]. Sahin et al [3] reported an estimate of the theoretical band gap as 1.06 eV. The comparison of the theoretical band gaps with available experimental data shows that mBJ correlation potential allows the prediction of band gap values much closer to the experimental values. The mBJ potential gives results in good agreement with experimental values that are similar to those produced by more sophisticated methods but at much lower computational costs [21].

To describe the general features of bonding in more detail the partial and total density for states (PDOS and DOS) at 0 GPa pressure are calculated using the mBJ potential together with WC-GGA for the correlation (Figure 2). The DOS of different compounds considered share the similar features. For a clear understanding we divided the valence band region (VB) into three zones: low, intermediate and higher energy bands. For a better analysis, we have decomposed the total density of states into s, p and d orbital contribution. Clearly, the low set of VBs ranging from -11 eV to -10 eV arise

mainly from hybridized P s states, Sn p states and Sn s states. The intermediate energy sub bands situated at about -9 eV and -5 eV consists mainly of Zn d states. The upper valence band mainly consists of P p-states Sn p and Zn p states. The conduction bands near Fermi level are composed of strongly hybridized Sn s s-states and P p states with a few contributions of Sn p-states and P s states.

Table 1. Structural equilibrium parameters, a, c, u, B and B' calculated in WC-GGA and thermal properties at 300 K; isothermal bulk modulus (B in GPa), Hardness (H in GPa), Gruneisen parameter (γ), Debye temperature (θ_D in K) and thermal expansion coefficient (α in $10^{-5}/K$) of ZnSnP₂.

Structural Analysis	a (Å)	c (Å)	u	B (GPa)	B'
	5.69, 5.65 ^{a,*}	11.30, 11.30 ^{a,*}	0.253, 0.25 ^{b,*}	72, 73 ^{b,*}	4.59
Thermal Analysis	B (GPa)	H (GPa)	γ	θ_D (K)	α ($10^{-5}/K$)
	67	4.82	1.863	354, 352 ^j	4.512

^a Reference [6]; ^b Reference [3]; ^j Reference [51]; *Experimental

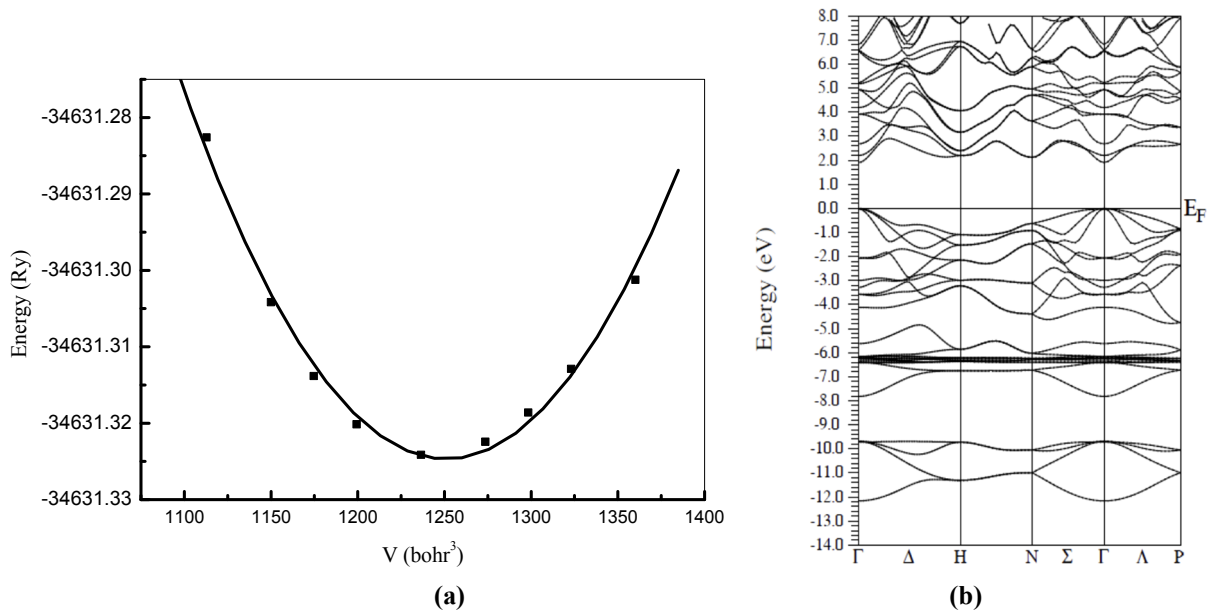


Figure 1. (a) Calculated total energies as a function of volume and (b) Band structures of ZnSnP₂

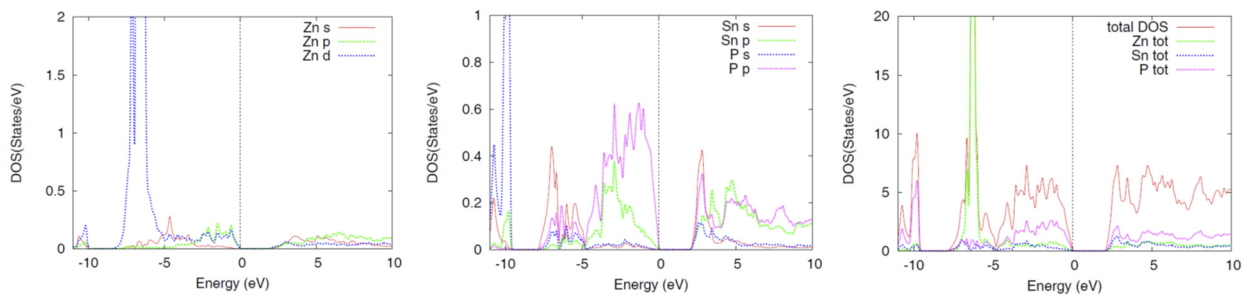


Figure 2. The calculated partial and total density of states (DOS) for ZnSnP₂.

The linear response to an external electromagnetic field with a small wave vector is measured through the complex dielectric function,

$$\epsilon(\omega) = \epsilon_1(\omega) + i\epsilon_2(\omega) \quad (1)$$

which is related to the interaction of photons with electrons [25]. The imaginary part $\epsilon_2(\omega)$ of the dielectric function could be obtained from the momentum matrix elements between the occupied and unoccupied wave functions and is given by [26]

$$\epsilon_2(\omega) = \frac{2\pi^2 e^2}{\Omega \epsilon_0} \sum_{i \in c, f \in v} \sum_k \left| \langle \Psi_k^c | \hat{\mu} \cdot r | \Psi_k^v \rangle \right|^2 \delta[E_k^c - E_k^v - \hbar\omega]. \quad (2)$$

The real part $\epsilon_1(\omega)$ can be evaluated from $\epsilon_2(\omega)$ using the Kramer-Kronig relations and is given by [27]

$$\epsilon_1(\omega) = 1 + \left(\frac{2}{\pi}\right) \int_0^{\infty} \frac{\omega'^2 \epsilon_2(\omega')}{\omega'^2 - \omega^2} d\omega'. \quad (3)$$

All of the other optical properties, including the absorption coefficient $\alpha(\omega)$, the refractive index $n(\omega)$, the extinction coefficient $k(\omega)$, and the energy-loss spectrum $L(\omega)$, can be directly calculated from $\epsilon_1(\omega)$ and $\epsilon_2(\omega)$ [26, 28,29].

Figure 3 (a) and (b) displays the real and imaginary parts respectively of the electronic dielectric function $\epsilon(\omega)$ spectrum for the photon energy ranging up to 40 eV, respectively.

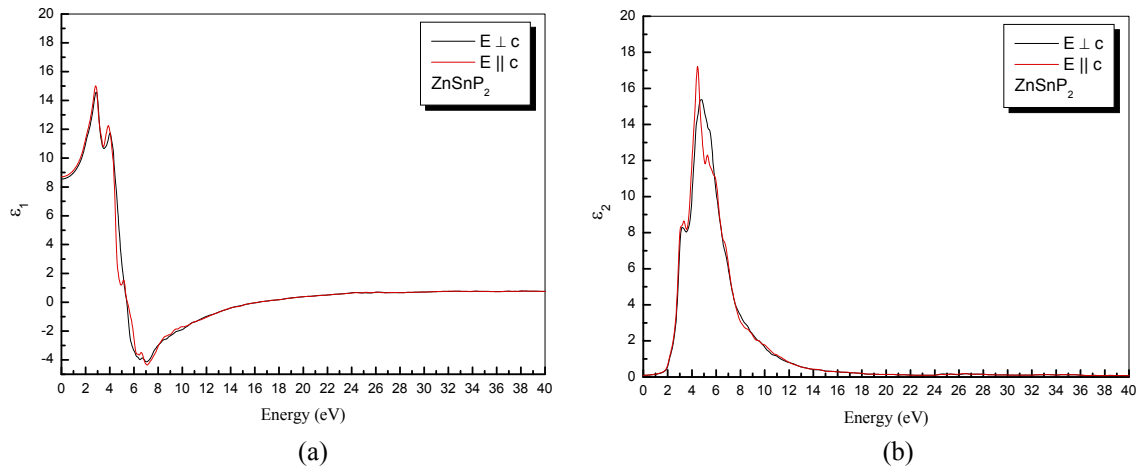


Figure 3. The calculated real $\epsilon_1(\omega)$ and imaginary $\epsilon_2(\omega)$ parts of complex dielectric constant for ZnSnP₂.

The main peaks of $\epsilon_1(\omega)$ which is mainly generated by electronic transition from the top of the valence band to the bottom of conduction band, occurs at 2.84 eV (14.90) and $\epsilon_1(\omega)$ spectra further decreases up to 7.10 eV. Optical spectra exhibit anisotropy in two directions (along basal-plane and z-axis) with a very small difference (0.1543 eV) in the static limit. The imaginary part of the dielectric constant $\epsilon_2(\omega)$ is the fundamental factor of the optical properties of a material. Figure 3 (b) displays the imaginary (absorptive) part of the dielectric function $\epsilon_2(\omega)$ up to 40 eV. Our analysis shows that the critical points of the $\epsilon_2(\omega)$ occurs at 1.80 eV. These points correspond to the $\Gamma_c - \Gamma_v$ splitting which gives the threshold for the direct optical transitions between the absolute valence band maximum and the first conduction band minimum and is known as fundamental adsorption edge. The obtained fundamental edges are closely related to the obtained energy band gap values 1.9 eV.

Figure 4 (a) presents the refractive index $n(\omega)$ along with the extinction coefficient $k(\omega)$. The refractive index spectrum shows an anisotropic behavior ($\Delta n(0 \text{ eV}) = 0.0263$), hence only the averages are listed in (2.93737) Table 2. The peak value of refractive indices for ZnSnP₂ is 3.88 at 2.94 eV.

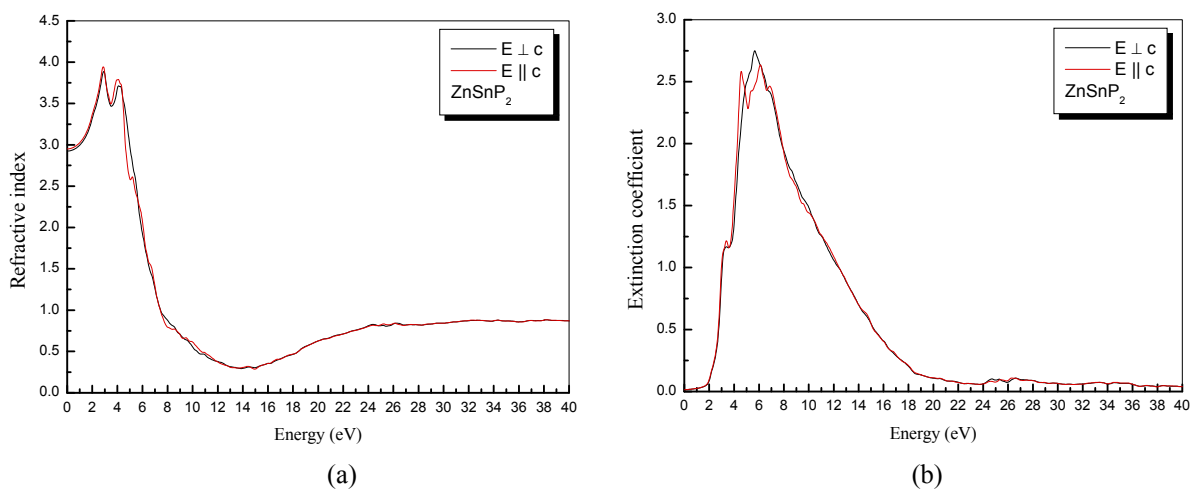


Figure 4. The calculated (a) refractive index and (b) extinction coefficient for ZnSnP₂.

Figure 4 (b) show extinction coefficient $k(\omega)$ is related to the decay or damping of the oscillation amplitude of the incident electric field, the extinction coefficient $k(\omega)$ decreases with increasing the incident photon energy. The peak values obtained for the extinction coefficient occur at the points where the dispersive part of dielectric constant ($\epsilon_1(\omega)$) has a zero value (Figure 3) for all the compounds. The calculated optical reflectivity $R(\omega)$ is displayed in Figure 5 (a).

These materials have small reflectivity in the low energy range. The maximum reflectivity occurs in region 4.54-13.92 eV [30].

Table 2. The calculated minimum band gaps E_g (eV), refractive index (n) and dielectric constant for ZnSnP₂ compared with other experimental and theoretical data.

Crystals	E_g (eV) this work	n this work	ϵ_∞ this work
ZnSnP ₂	1.9, 1.5-1.7 ^{d,*} , 1.06 ^c , 1.66 ^e	2.93, 2.90 ^{f,*}	8.62, 9.7 ^g

^d Reference [24]; ^c Reference [3]; ^e Reference [52]; ^f Reference [53]; ^g Reference [54]; *Experimental

The absorption coefficient is a parameter, which indicates the fraction of light lost by the electromagnetic wave when it passes through a unit thickness of the material. These have been plotted in Figure 5 (b). It is clear that polarization has a minor influence on the spectrum. From the absorption spectrum, we can easily find the absorption edges located at 1.89 eV. It is clear from the above discussion that both chalcopyrites are excellent mid-IR transparent crystal materials as they transparent to low energy photons showing zero value of the absorption coefficient in that region. When the photon energy is more than the absorption edge value, then adsorption coefficient increases. The absorption coefficients further decrease rapidly in the high energy region, which is the typical characteristic of semiconductors. Optical conductivity parameters are closely related to the photo-electric conversion efficiency and mainly used to measure the change caused by the illumination. Figure 5 (c) shows the optical conductivities of ZnSnP₂. It's clear that the maximum photoconductivity of the materials lies in the u-v region of electromagnetic spectrum.

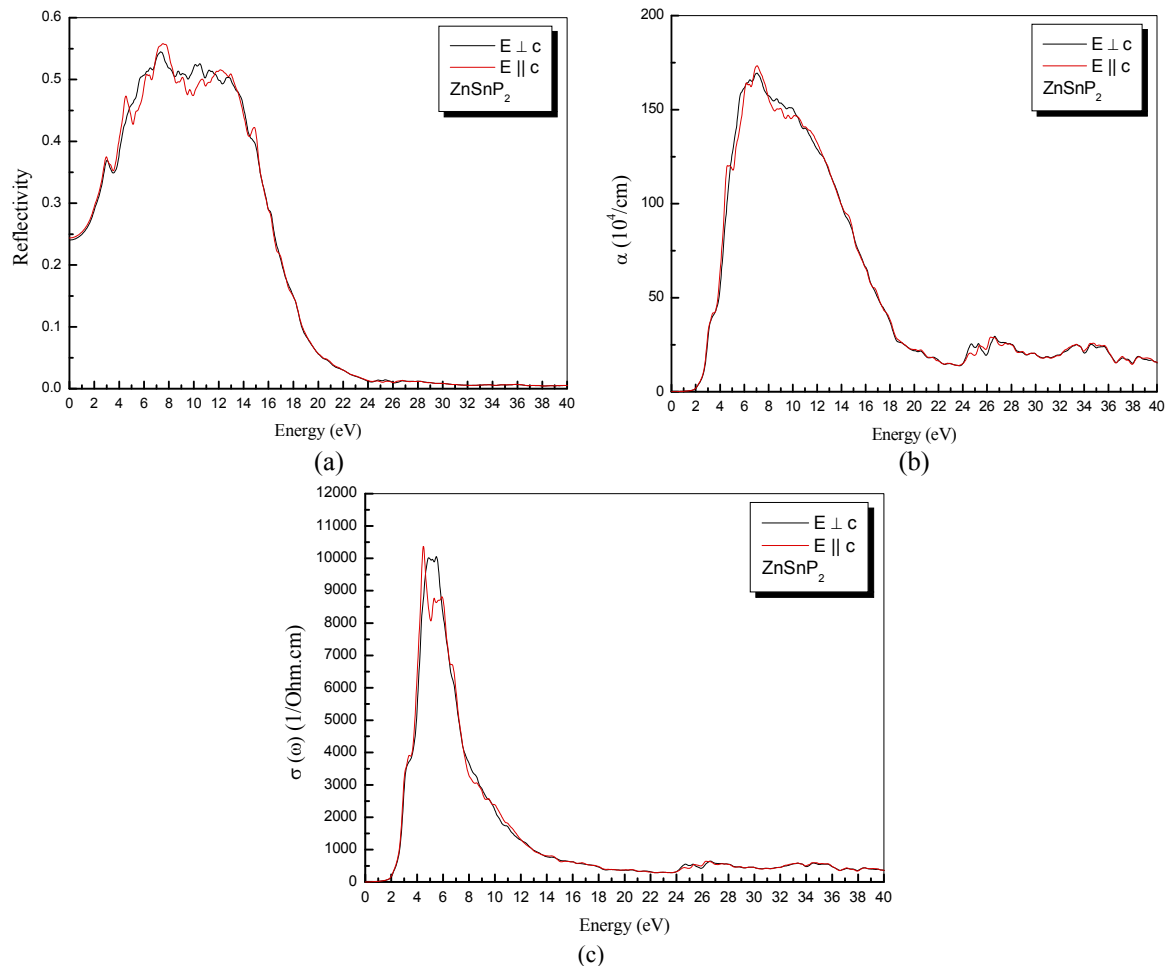


Figure 5. The calculated (a) reflectivity ($R(\omega)$), (b) absorption coefficient ($\alpha(\omega)$) and (c) photoconductivity ($\sigma(\omega)$) for ZnSnP₂.

Elastic Properties

The elastic properties of a solid are among the most fundamental properties that can be predicted from the first-principles ground-state total-energy calculations. The determination of the elastic constants requires knowledge of the curvature of the energy curve as a function of strain for selected deformations of the unit cell. The deformations [31] are shown in Table 3 and chosen such that the strained systems have the maximum possible symmetry. The system has been optimized for each deformed cell geometry. The WIEN2K package [16] facilitates this task by providing a force-driven optimization of the internal cell geometry. The elastic stiffness tensor of chalcopyrite compounds has six independent

components because of the symmetry properties of the D_{2d}^{12} space group, namely C_{11} , C_{12} , C_{13} , C_{33} , C_{44} and C_{66} in Young notation. The calculated elastic constant for the tetragonal phase of $ZnSnP_2$ are listed in Table 4.

Table 3. The lattice parameters of the deformed tetragonal unit cell, the expression relating the δ and ε variables, the finite Lagrangian strain tensor (Voigt notation) and the value of the second derivative, $(1/2V)(d^2E/d\varepsilon^2)$, in terms of the elastic constants (ε being deformation coordinate and E the energy).

Strained cell	ε	Strain (η)	$dE^2/d\varepsilon^2$
$(a + \delta, a + \delta, \frac{c + c\delta}{a}, 90, 90, 90)$	$\frac{(a + \delta)^2}{a^2} - 1$	$(\frac{\varepsilon}{2}, \frac{\varepsilon}{2}, \frac{c\varepsilon}{2a}, 0, 0, 0)$	$\frac{1}{4}(C_{11} + C_{12}) + \frac{1}{8}C_{33} + \frac{1}{2}C_{13}$
$(a + \delta, a + \delta, c, 90, 90, 90)$	$\frac{(a + \delta)^2}{a^2} - 1$	$(\frac{\varepsilon}{2}, \frac{\varepsilon}{2}, 0, 0, 0, 0)$	$\frac{1}{4}(C_{11} + C_{12})$
$(a, a, \frac{c + c\delta}{a}, 90, 90, 90)$	$\frac{(c + \delta)^2}{c^2} - 1$	$(0, 0, \frac{\varepsilon}{2}, 0, 0, 0)$	$\frac{1}{8}C_{33}$
$(a, a + \delta, c, 90, 90, 90)$	$\frac{(a + \delta)^2}{a^2} - 1$	$(0, \frac{\varepsilon}{2}, 0, 0, 0, 0)$	$\frac{1}{8}C_{11}$
$(a, a, c, 90, 90 + \delta, 90)$	$\sin \delta$	$(0, 0, 0, 0, \varepsilon, 0)$	C_{44}
$(a, a, c, 90, 90, 90 + \delta)$	$\sin \delta$	$(0, 0, 0, 0, 0, \varepsilon)$	C_{66}

Table 4. Elastic constants C_{ij} (in GPa) of the $ZnSnP_2$ compared with available data.

C_{11}	C_{12}	C_{13}	C_{33}	C_{44}	C_{66}
105, 110 ^c	53, 53 ^c	53, 51 ^c	103, 106 ^c	50, 47 ^c	50, 49 ^c
B (GPa)	G (GPa)	Y (GPa)	ν	κ_a (GPa ⁻¹)	κ_c (GPa ⁻¹)
70	39	98	0.27	0.0047	0.0048

^c Reference [3];

In general, the proposed results are in good agreement with the available data, in particular if we consider, shear constants (C_{44} and C_{66}) appear to be no worse than the rest of the elastic constants, even though the inner strain component is particularly difficult in those constants. The comparison with other theoretical calculations also shows an important dispersion of values. The calculated elastic constants fulfill the mechanical stability criteria for the tetragonal systems:

$$C_{11} > |C_{12}|, (C_{11} + C_{12}) C_{33} > 2C_{13}^2, C_{44} > 0, \text{ and } C_{66} > 0$$

In order to check the internal consistency of calculated elastic constants we can compare the bulk modulus reported on Table 1 & 4 with an equivalent combination of the C_{ij} 's.

Bulk modulus should be found from above by the Voigt approximation (uniform strain assumption) [32, 33]:

$$B_V = \frac{1}{9}(2C_{11} + C_{33} + 2C_{12} + 4C_{13}) \tag{4}$$

Reuss found lower bounds for all lattices [34]

$$B_R = \frac{(C_{11} + C_{12})C_{33} - 2C_{13}^2}{C_{11} + C_{12} + 2C_{33} - 4C_{13}} \tag{5}$$

Voigt and Reuss approximations provide, in fact, an estimation of the elastic behaviour of an isotopic material, for instance a polycrystalline sample. Such a medium would have a single shear constant, G, upper bounded by

$$G_V = \frac{1}{30}(M + 3C_{11} - 3C_{12} + 12C_{44} + 6C_{66}) \tag{6}$$

and lower bounded by

$$G_R = 15 \left\{ \frac{18B_V}{C^2} + \frac{6}{(C_{11} - C_{12})} + \frac{6}{C_{44}} + \frac{3}{C_{66}} \right\}^{-1} \tag{7}$$

where $C^2 = (C_{11} + C_{12})C_{33} - 2C_{13}^2$

In the Voigt-Reuss-Hill approximation [35], the B and G of the polycrystalline material are approximated as the arithmetic mean of the Voigt and Reuss limits:

$$B = \frac{B_V + B_R}{2} \tag{8}$$

$$G = \frac{G_V + G_R}{2} \quad (9)$$

Finally the Poisson ratio and the Young modulus are obtained as

$$\nu = \frac{3B - 2G}{2(3B + G)} \quad (10)$$

$$Y = \frac{9BG}{3B + G} \quad (11)$$

Using the single crystal C_{ij} data, one can evaluate the linear compressibilities along the principles axis of the lattice. For the tetragonal structure, the linear compressibilities κ_a and κ_c along the a- and c-axis respectively are given in term of elastic constants by the following relations:

$$\kappa_a = -\frac{1}{a} \frac{\partial a}{\partial p} = \frac{C_{33} - C_{13}}{C_{33}(C_{11} + C_{12}) - 2C_{13}^2} \quad (12)$$

$$\kappa_c = -\frac{1}{c} \frac{\partial c}{\partial p} = \frac{C_{11} + C_{12} - 2C_{13}}{C_{33}(C_{11} + C_{12}) - 2C_{13}^2} \quad (13)$$

Pugh [36] proposed that the resistance to plastic deformation is related to the product Gb, where ‘b’ is the Burgers vector, and that the fracture strength is proportional to the product Ba, where ‘a’ corresponds to the lattice parameter. As b and a are constants for specific materials, the Ba/Gb can be simplified into B/G. This formula was recently exploited in the study of brittle vs ductile transition in intermetallic compounds from first-principles calculations [37, 38]. A high B/G ratio is associated with ductility, whereas a low value corresponds to the brittle nature. The critical value which separates ductile and brittle material is around 1.75, i.e., if $B/G > 1.75$, the material behaves in a ductile manner otherwise the material behaves in a brittle manner. We have found that B/G ratios is 1.82 for ZnSnP₂, classifying the materials is ductile.

Thermal Properties

To investigate the thermodynamic properties of Zn-chalcopyrite, we have used Gibbs program. The obtained set of total energy versus primitive cell volume determined in previous section has been used to derive the macroscopic properties as a function of temperature and pressure from the standard thermodynamic relations. Gibbs program is based on the quasi-harmonic Debye model [39], in which the non-equilibrium Gibbs function $G^*(V; P, T)$ can be written in the form of:

$$G^*(V; P, T) = E(V) + PV + A_{vib}[\theta_D; T] \quad (14)$$

where $E(V)$ is the total energy per unit cell, PV corresponds to the constant hydrostatic pressure condition, θ_D is the Debye temperature, and A_{vib} is the vibrational term, which can be written using the Debye model of the phonon density of states as [40, 41]:

$$A_{vib}[\theta_D; T] = nkT \left[\frac{9\theta}{8T} + 3 \ln(1 - e^{-\theta/T}) - D\left(\frac{\theta}{T}\right) \right] \quad (15)$$

where n is the number of atoms per formula unit, $D(\theta/T)$ represents the Debye integral, and for an isotropic solid, θ is expressed as [40]:

$$\theta_D = \frac{\hbar}{k} \left[6\pi^2 V^{1/2} n \right]^{1/3} f(\sigma) \sqrt{\frac{B_s}{M}} \quad (16)$$

M being the molecular mass per unit cell and B_s the adiabatic bulk modulus, approximated by the static compressibility [39]:

$$B_s \cong B(V) = V \frac{d^2 E(V)}{dV^2} \quad (17)$$

$f(\sigma)$ is given by Refs. [39, 42, 43]; where σ is the Poisson ratio.

Therefore, the non-equilibrium Gibbs function $G^*(V; P, T)$ as a function of (V; P, T) can be minimized with respect to volume V,

$$\left(\frac{\partial G^*(V; P, T)}{\partial V} \right)_{P, T} = 0 \quad (18)$$

By solving Eq. (18), one can obtain the thermal equation of state (EOS) $V(P, T)$. The heat capacity C_V and the thermal expansion coefficient α are given by [35],

$$C_V = 3nk \left[4D \left(\frac{\theta}{T} \right) - \frac{3\theta/T}{e^{\theta/T} - 1} \right] \quad (19)$$

$$S = nk \left[4D \left(\frac{\theta}{T} \right) - 3 \ln(1 - e^{-\theta/T}) \right] \quad (20)$$

$$\alpha = \frac{\gamma C_V}{B_T V} \quad (21)$$

where γ is the Grüneisen parameter, which is defined as:

$$\gamma = - \frac{d \ln \theta(V)}{d \ln V} \quad (22)$$

Through the quasi-harmonic Debye model, one could calculate the thermodynamic quantities of any temperatures and pressures of compounds from the calculated E–V data at T = 0 and P = 0.

We can also provide a prediction of the hardness (H in GPa) by using the semi-empirical equations developed by Verma and co-authors [44],

$$H = K B^{K+1} \quad (23)$$

B = Bulk modulus; K = 0.59 for $A^{II}B^{IV}C_2V$

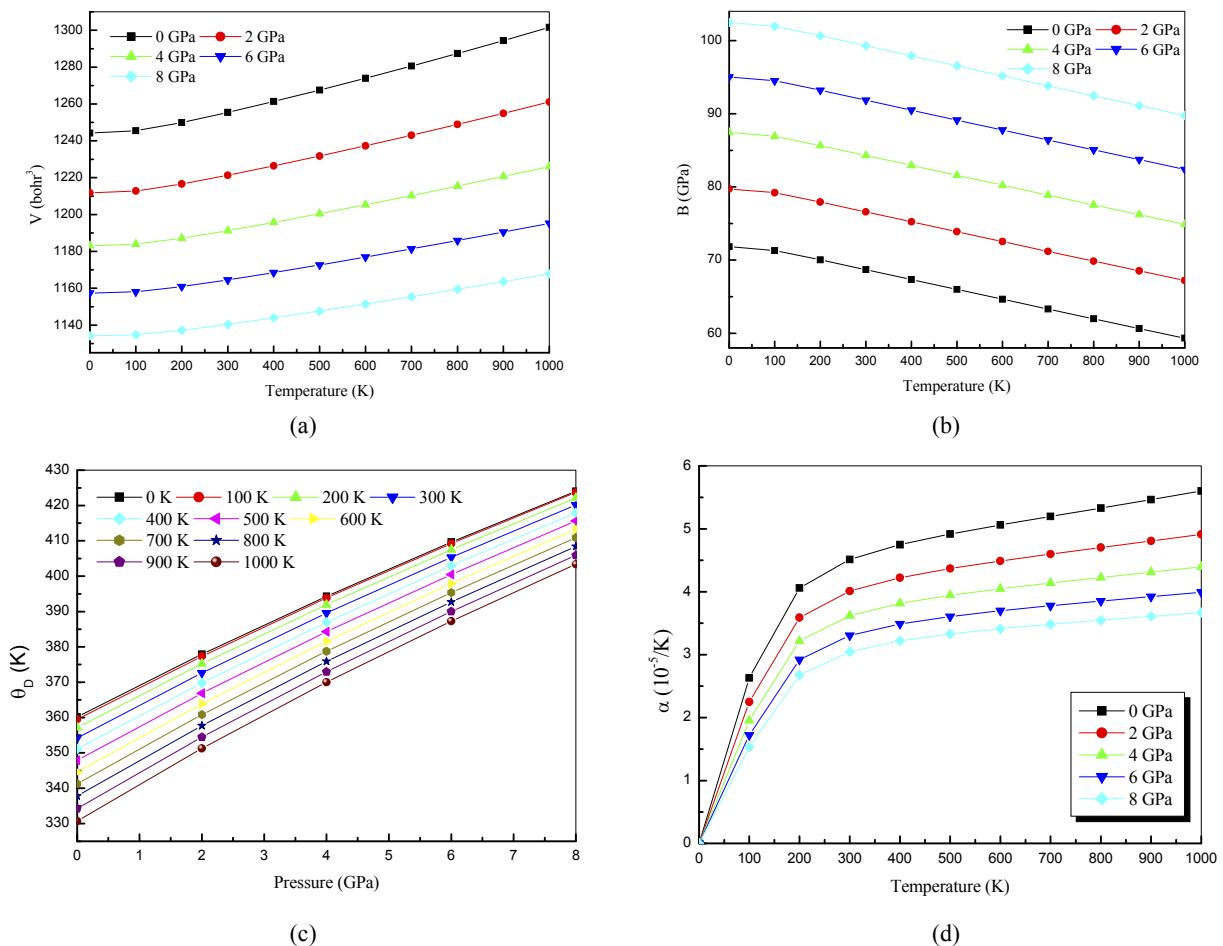


Figure 6. (a) Volume vs temperature at various pressures (b) Bulk modulus vs temperature at various pressures, (c) Debye temperature vs pressure at various temperatures (d) Thermal expansion coefficients vs temperature at various pressures for ZnSnP₂.

To determine the thermodynamic properties through the quasi-harmonic Debye model, a temperature range 0 K-1000 K has been taken. The pressure effects are studied in the 0–8 GPa range. Figure 6 (a) presents relationships between the equilibrium volume V (bohr³) and pressure at various temperatures. Meanwhile, V increases slightly as the temperature increases, whereas the equilibrium volume V decreases dramatically as the pressure P increases at a given temperature. This account suggests that the ZnSnP₂ under loads turns to be more compressible with increasing pressure than decreases temperature. Furthermore, it is noted that the relationship between the bulk modulus and temperature for ZnSnP₂ in Figure 6 (b). The bulk modulus slightly decreases with increasing temperature at a given pressure and increases with increasing pressure at a given temperature.

The variation of the Debye temperature θ_D (K) of ZnSnP₂ as a function of pressure and temperature illustrated by proposed results is displayed in Figure 6 (c). With the applied pressure increasing, the Debye temperatures are almost linearly increasing. Figure 6 (d) shows the volume thermal expansion coefficient θ_D ($10^{-5}/K$) at various pressures, from which it can be seen that the volume thermal expansion coefficient θ_D increases quickly at a given temperature particularly at zero pressure below the temperature of 300 K. After a sharp increase, the volume thermal expansion coefficient is nearly insensitive to the temperature above 300 K due to the electronic contributions.

As very important parameters, the heat capacities of a substance not only provide essential insight into the vibrational properties, but are also mandatory for many applications. The proposed calculation of the heat capacities C_P and C_V of ZnSnP₂ versus temperature at pressure range 0-8 GPa is shown in Figure 7.

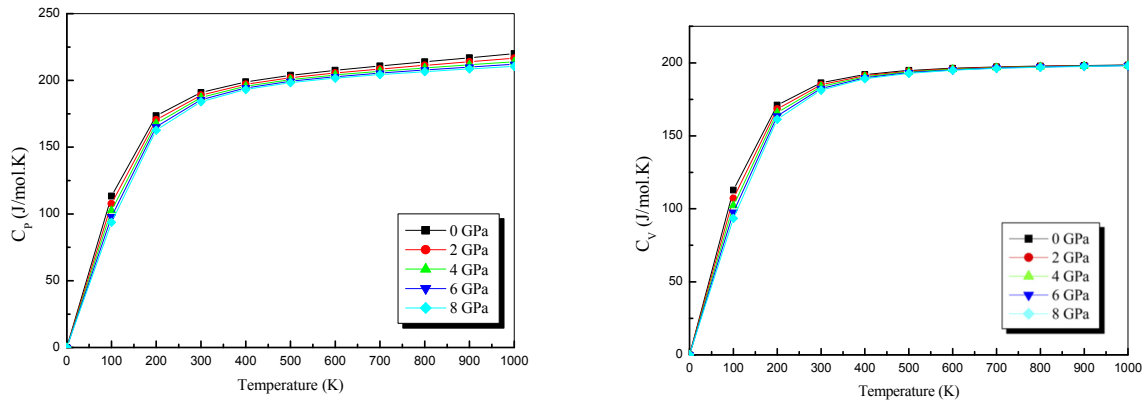


Figure 7. Heat capacities (C_P and C_V) vs temperature at various pressures for ZnSnP₂

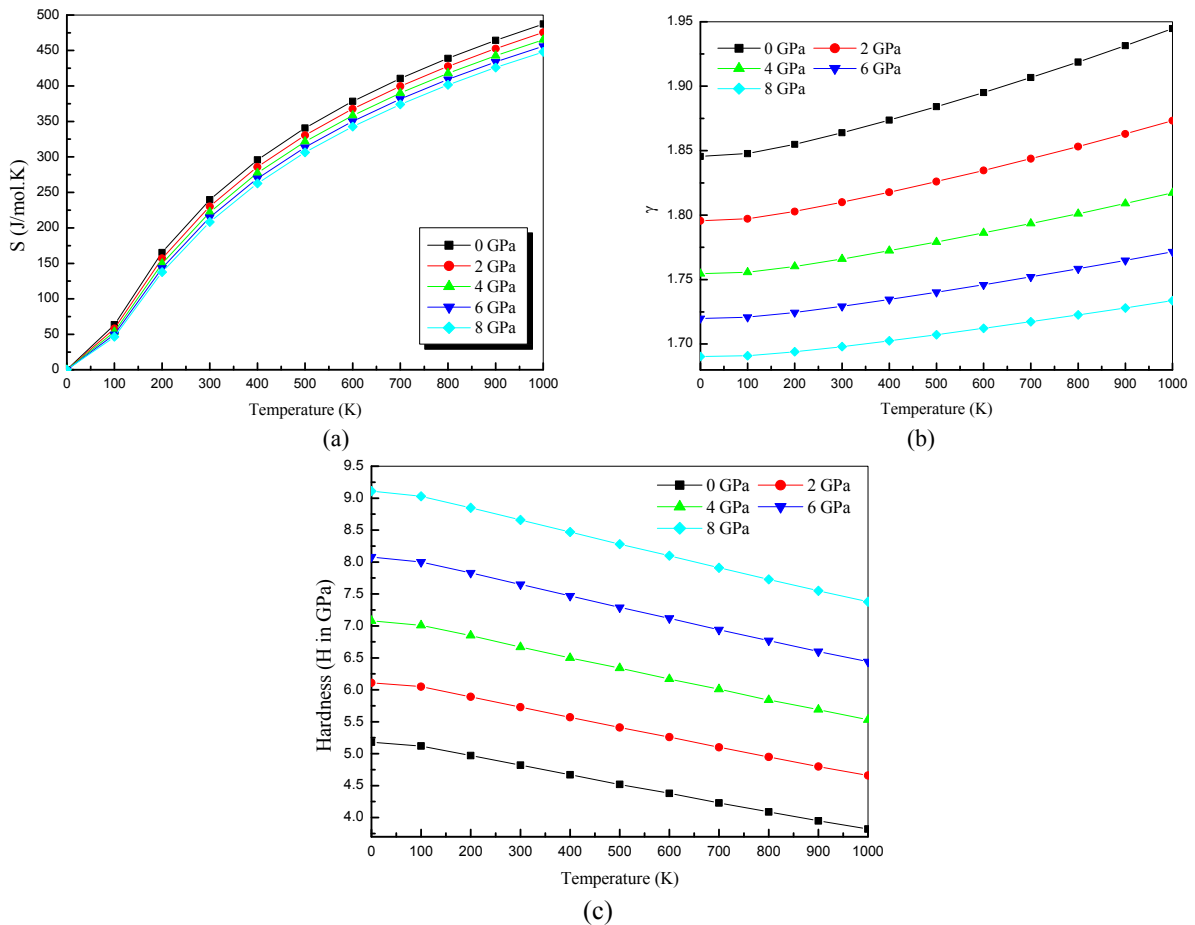


Figure 8. (a) Entropy vs temperature at various pressures, (b) Gruneisen parameter vs temperature at various pressures, (c) Hardness vs temperature at various pressures for ZnSnP₂.

From these figures, we can see that the constant volume heat capacity C_V and the constant pressure capacity C_P are very similar in appearance and both of them are proportional to T^3 at low temperatures. At high temperatures, the

anharmonic effect on heat capacity is suppressed; which is called Dulong-Petit limit, with the increasing of the temperature, whereas C_p increases monotonically with the temperature.

Figure 8 (a) shows the entropy vs temperature at various pressures. The entropies are variable by power exponent with increasing temperature but the entropies are higher at low pressure than that at high pressure at same temperature. The Grüneisen parameter γ is another important quantity for the materials. In Figure 8 (b), we have shown the values of Grüneisen parameter γ at different temperatures and pressures. It shows the value γ increases as the temperature increases at a given pressure and decreases as the pressure increases at a given temperature.

In Figure 8 (c), we have shown the values of hardness (H in GPa) at different temperatures and pressures. It shows the hardness decreases as the temperature increases at a given pressure and increases as the pressure increases at a given temperature. The values of hardness are reported for the first time at different pressure and temperature. Table 1 present the thermal properties such as isothermal bulk modulus, hardness, Grüneisen parameter, Debye temperature and thermal expansion coefficient at 300 K.

CELL STRUCTURE, MATERIAL PARAMETERS AND CELL PERFORMANCE

The modeled cell structure is shown in Figure 9 (a). The simulated structure starts with 2500 nm ZnSnP₂ layer over a Molybdenum substrate followed by 50 nm CdS/ZnTe buffer and 50 nm intrinsic ZnO window layer with 300 nm Al doped ZnO layer.

The device simulation is based on the solution of a set of equations, which provide a mathematical model for device operation. Using this model, the influence of the modeling parameters over the efficiency of the device can be examined, which is a tedious task by experimental method. The simulation is based on the solution of one-dimensional Poisson equation and the continuity equations for free charge carriers. These equations are expressed as follows:

$$\frac{d}{dx} \left(-\varepsilon(x) \frac{d\psi}{dx} \right) = q \left[p(x) - n(x) + N_D^+(x) - N_A^-(x) + p_t(x) - n_t(x) \right] \quad (24)$$

$$\frac{dp_n}{dt} = G_p - \frac{p_n - p_{n0}}{\tau_p} - p_n \mu_p \frac{dE}{dx} - \mu_p E \frac{dp_n}{dx} + D_p \frac{d^2 p_n}{dx^2} \quad (25)$$

$$\frac{dn_p}{dt} = G_n - \frac{n_p - n_{p0}}{\tau_n} + n_p \mu_n \frac{dE}{dx} + \mu_n E \frac{dn_p}{dx} + D_n \frac{d^2 n_p}{dx^2} \quad (26)$$

Where ε the permittivity, q the charge, Ψ the electrostatic potential, n the free electron density, p the free hole density, $p_t(x)$ the trapped hole density, $n_t(x)$ the trapped electron density, N_D^+ the donor atom density, N_A^- the acceptor atom density, E the electric field and G the generation rate, D the diffusion coefficient, τ the lifetime and μ the mobility of charge carriers. With the help of solution of these equations current density/voltage (J/V) characteristics are determined and performance of solar cell with different buffer layers is compared. In Table 5 we have presented description for the parameters; which was used in the simulation. The terrestrial spectrum AM 1.5 (Air Mass 1.5 Global 1000W/m²) is used for illumination. The schematic energy band diagram under equilibrium condition for the thin layer solar cell has been illustrated in Figure 9 (b).

Table 5. Material properties for the ZnSnP₂ solar cells simulation.

Parameters \ Layers	1-n+ZnO	2-n(i) ZnO	3-CdS	3-ZnTe	4-ZnSnP ₂
Thickness (nm)	300	50	50 ^k	50	2500
ε (dielectric constant)	9.26 ^a	9 ^{g,c}	9.4 ^a	14 ^m	8.62*
μ_n (electron mobility in 10cm ² /Vs)	65.6 ^b	230 ^h	265 ^l	70 ^m	55 ⁿ
μ_p (hole mobility in 10cm ² /Vs)	65 ^c	70 ⁱ	15 ^l	50 ^m	35 ^o
n/p (carrier density in cm ⁻³)	1×10 ²¹ ^c	5×10 ¹⁷ ^j	1×10 ¹⁷ ^j	7.5×10 ¹⁹ ^m	1×10 ¹⁶ ^o
E_g (eV) (optical band gap)	3.228 ^d	3.29 ^d	2.42 ^j	2.25 ^m	1.9*
N_c (electron density in cm ⁻³)	1×10 ¹⁹ ^e	1×10 ¹⁹ ^e	1×10 ¹⁹ ^e	1×10 ¹⁵ ^m	6.8×10 ¹⁷
N_v (effective density in cm ⁻³)	1×10 ¹⁹ ^e	1×10 ¹⁹ ^e	1.6×10 ¹⁹ ^e	1.5×10 ¹⁹ ^m	1.5×10 ¹⁹
χ electron affinity (eV)	4.2 ^f	4.445 ^j	4.3 ^e	3.65 ^m	4.25 ⁿ

^a Reference [55]; ^b Reference [56]; ^c Reference [57]; ^d Reference [58]; ^e Reference [59]; ^f Reference [60]; ^g Reference [61]; ^h Reference [62]; ⁱ Reference [63]; ^j Reference [64]; ^k Reference [65]; ^l Reference [66]; ^m Reference [67]; ⁿ Reference [68]; ^o Reference [69]; *This work

The band diagram is drawn according to Anderson's affinity rule, which shows conduction band offset is $\Delta E_c = \chi_2 - \chi_1$ and valance band offset is $\Delta E_v = (\chi_1 + E_{g1}) - (\chi_2 + E_{g2})$. The band diagram shows that this is a type II heterostructure. The difference in band gaps creates discontinuity spikes in the conduction- and valance bands [45]. These

spikes can create extra barriers for the electrons to overcome or tunnel through, and may also work as potential wells with discrete energy states [46].

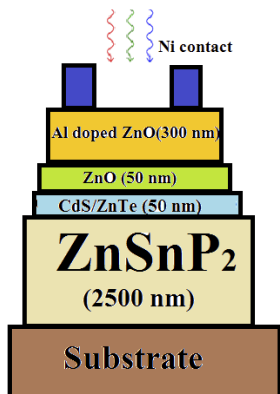


Figure 9 (a). The layer structure of ZnSnP₂ solar cell.

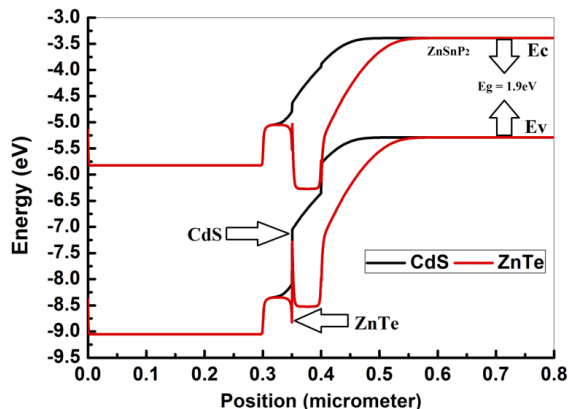


Figure 9 (b). The schematic energy-band diagram of a typical ZnSnP₂/CdS or ZnTe solar cell under equilibrium condition.

The Figure 9 (c) shows the illuminated characteristics *J-V* curve of the proposed solar cell structures. The performance parameters open circuit voltage (*V*_{oc}), short circuit current density (*J*_{sc}), Fill Factor (*FF*) and efficiency (*η*) have been calculated from *J-V* characteristics for different considered buffer layers. The simulation results have been presented in Table 6. These results show that both the buffer layers provide good efficiency (>20%); but the fill factor for ZnTe buffer layer is considerably high. A maximum density of current (>29 mA/cm²) has been obtained with both the buffer layers, which ensures the suitability of CdS and ZnTe buffer layers in ZnSnP₂ solar cells.

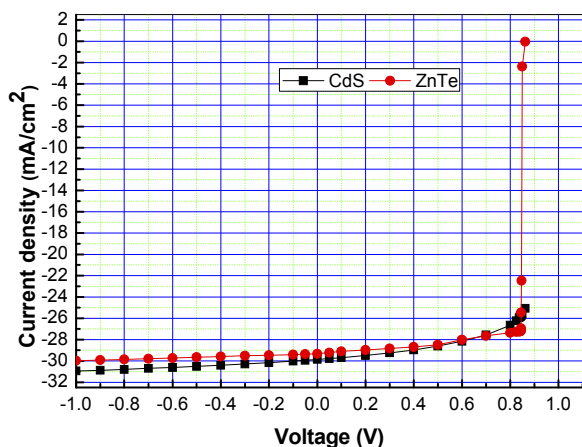


Figure 9 (c). Photo-current density-voltage (*J-V*) curves for the simulated results for 50nm thickness of buffer layers.

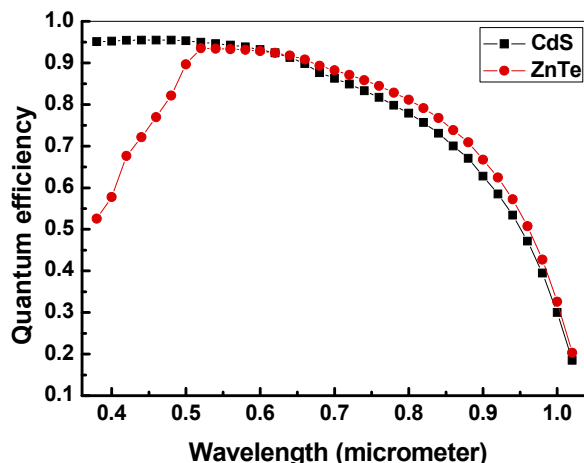


Figure 9 (d). Quantum efficiency curves for ZnSnP₂/CdS or ZnTe solar cell for 50 nm thickness of buffer layer

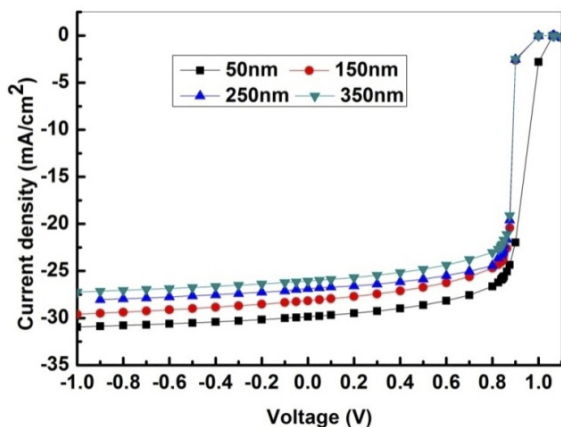


Figure 9 (e). Effect of thickness of buffer layer over *J-V* characteristics of ZnSnP₂/CdS solar cell.

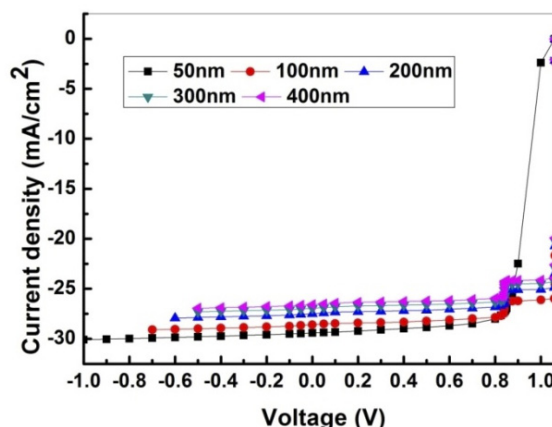


Figure 9 (f). Effect of thickness of buffer layer over *J-V* characteristics of ZnSnP₂/ZnTe solar cell.

Table 6. Simulated performance parameters of the solar cells for absorption layer ZnSnP₂

Buffer layer	E _g	□(%)	V _{oc} (mV)	J _{sc} (mA/cm ²)	FF(%)
CdS	1.06	13.186	604	29.235	74.6
	1.9	21.748	1066	29.864	68.3
ZnTe	1.06	14.055	603	29.121	80.1
	1.9	22.926	1062	29.415	73.4

Further, the analysis of photoconductivity of cell structure is done in terms of quantum efficiency (QE) as shown in Figure 9 (d). The spectral response of the device is studied within the spectral range of 0.4 μm to 1.0 μm. Quantum efficiency is a measure of collection of charge carriers with respect to number of incident photons. As CdS buffer layer has higher band gap, it provides a wider window for absorption of photons, thus creating larger number of charge carriers and resulting in higher quantum efficiency in lower wavelength region, whereas in higher wavelength region QE of CdS becomes lower which ensures higher recombination in this structure. The higher values of quantum efficiencies are found for blue region of the light. Since blue light is absorbed closer to the junction, recombination effect is less effective for this wavelength region whereas at higher side of wavelength high recombination occurs, since the free carrier generated deeper in the bulk have to travel longer before being collected. This results higher recombination loss and in turn lower quantum efficiency in long wavelength region. Moreover, the absorption coefficient decreases with the increasing of the photon wavelength, so the loss in absorption causes the spectral response to decrease quickly and thus the quantum efficiency.

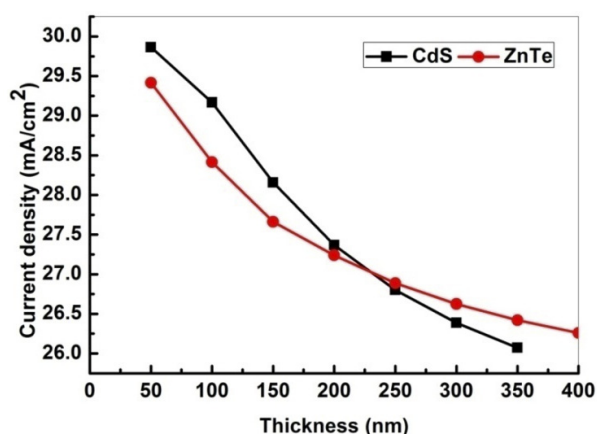
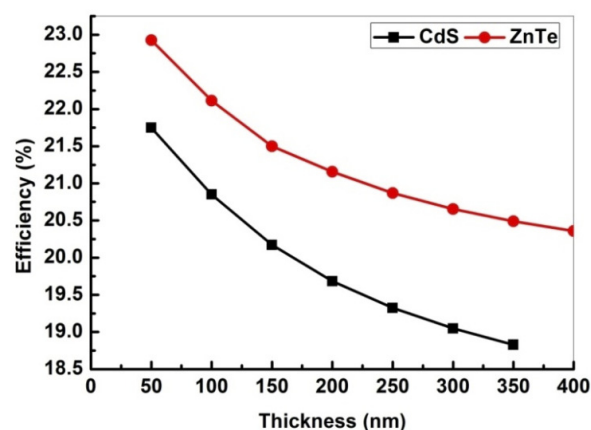
Effect of buffer layer thickness

The effect of thickness of buffer layer on J-V characteristics for the two cell structures are shown in Figures 9 (e)-9 (f). With the help of these characteristics J_{sc} , V_{oc} , η and FF are calculated at different thickness of buffer layers. The effect of thickness of buffer layer over performance parameters of these cell structures is shown in Figures 10 (a)-10 (c).

Figure 10 (a) and 10 (b) shows that as thickness of buffer layer increases, the current density as well as efficiency start to decrease for both the structures. This shows that at 50 nm the ratio of diffusion length to the thickness of the buffer layer is appropriate for collection of minority carriers. After this thickness all the photogenerated carriers are not able to reach the depletion region, which in turn decreases the current density and efficiency. The decrement in current density at lower thickness values is fast in ZnSnP₂/CdS structure, which shows that rate of recombination is higher in ZnSnP₂/CdS solar cell structure.

Further, the effect of thickness over open circuit voltage for all the three buffer layers is shown in Figure 10 (c). At 50 nm thickness a significant value of V_{oc} is found whereas for higher values of thickness it decreases for both the structures. At higher thickness the separated charge carriers starts to recombine before reaching the electrodes, which causes decrement in V_{oc} .

Effect of thickness over fill factor for the two structures is shown in Figure 10 (d). It is a measure of maximum power that can be achieved by a cell. As both the structures are showing the highest FF at 50nm thickness, ensures that at lower values of thickness charge collection is good because charge carriers are able to reach the electrodes. After this thickness charge collection suffers due to low values of diffusion length than the thickness of buffer layer. Further, with increment in thickness FF becomes almost constant because maximum effect of recombination over charge collection is achieved.

**Figure 10 (a).** Effect of thickness of buffer layer over current density of ZnSnP₂/CdS or ZnTe solar cell.**Figure 10 (b).** Effect of thickness of buffer layer over efficiency of ZnSnP₂/CdS or ZnTe solar cell.

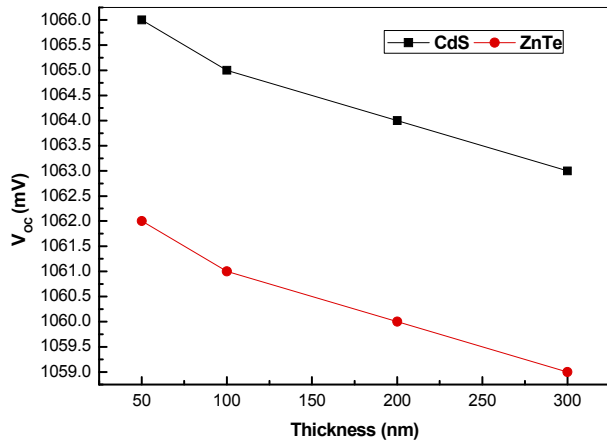


Figure 10 (c). Effect of thickness of buffer layer over V_{oc} of ZnSnP₂/ZnSnP₂/CdS or ZnTe solar cell.

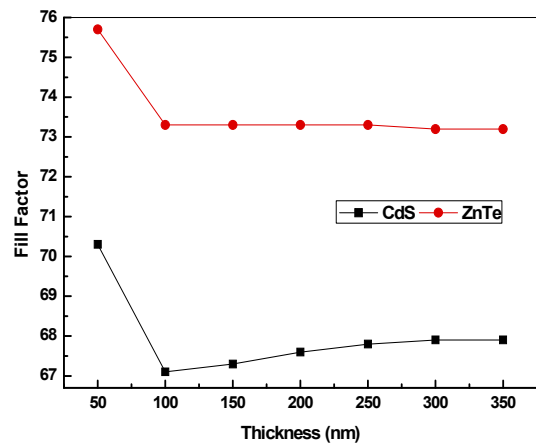


Figure 10 (d). Effect of thickness of buffer layer over fill factor of ZnSnP₂/CdS or ZnTe solar cell

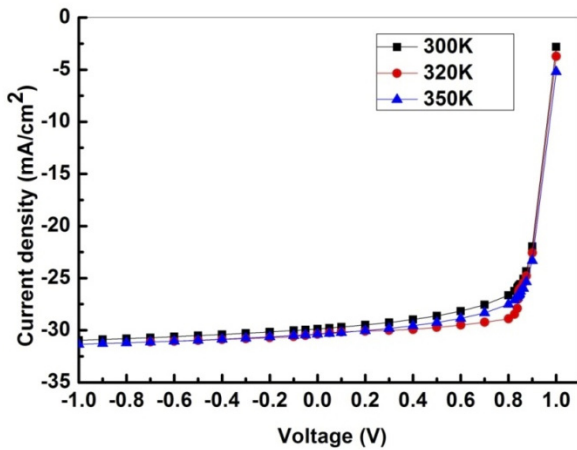


Figure 10 (e). Effect of temperature over J-V characteristics of ZnSnP₂/CdS solar cell.

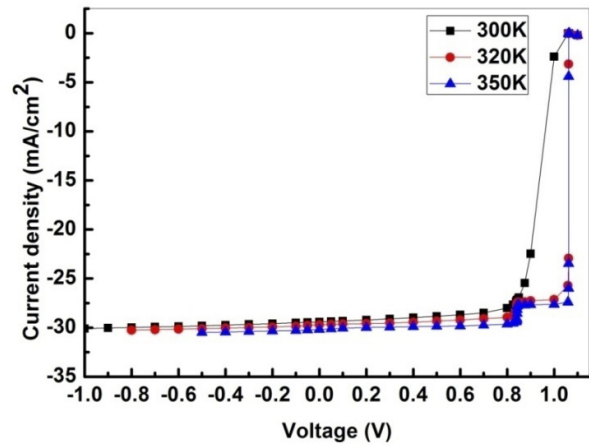


Figure 10 (f). Effect of temperature over J-V characteristics of ZnSnP₂/ZnTe solar cell.

Effect of temperature

The effect of temperature over J-V characteristics for both the three structures is shown in Figure 10 (e) and 10 (f). Further, Figures 11(a)-11(e) shows the effect of temperature over performance parameters for the two cell structures.

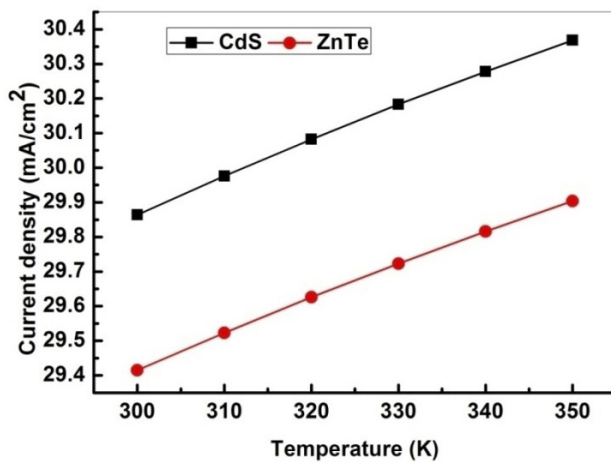


Figure 11 (a). Effect of temperature over current density of ZnSnP₂/CdS or ZnTe solar cell structures.

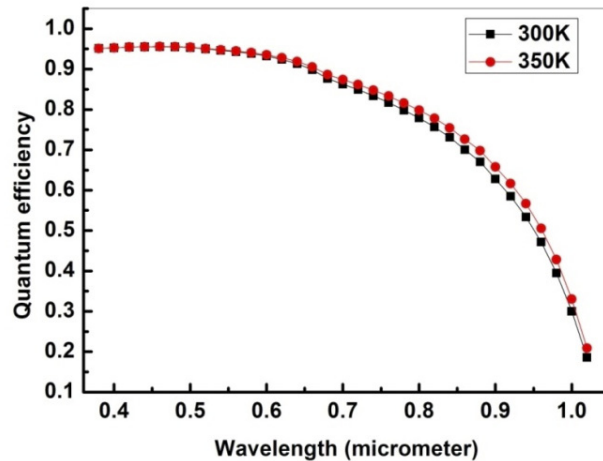


Figure 11 (b). Effect of temperature over quantum efficiency of ZnSnP₂/CdS solar cell.

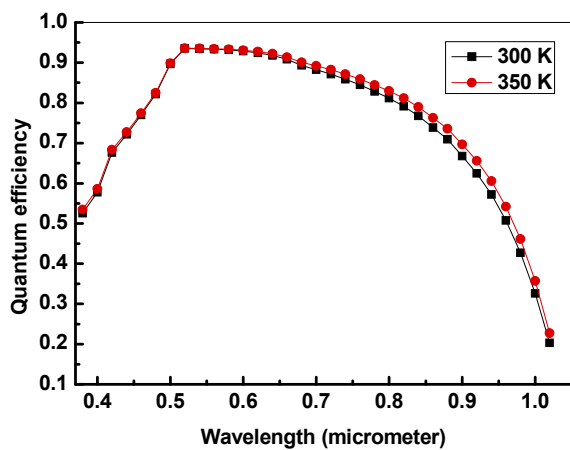


Figure 11 (c). Effect of temperature over quantum efficiency of ZnSnP₂/ZnTe solar cell.

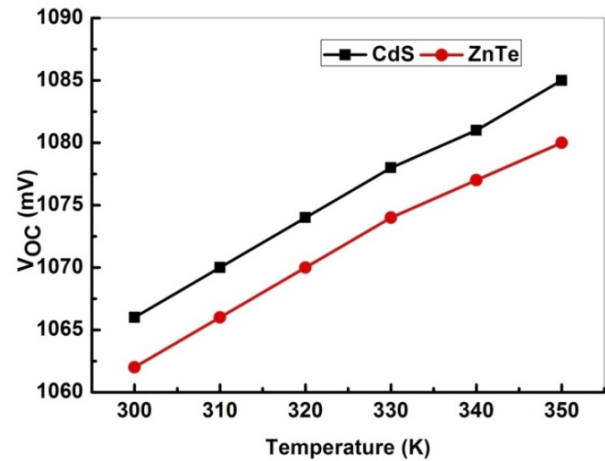


Figure 11 (d). Effect of temperature over open circuit voltage of ZnSnP₂/CdS or ZnTe solar cell structures.

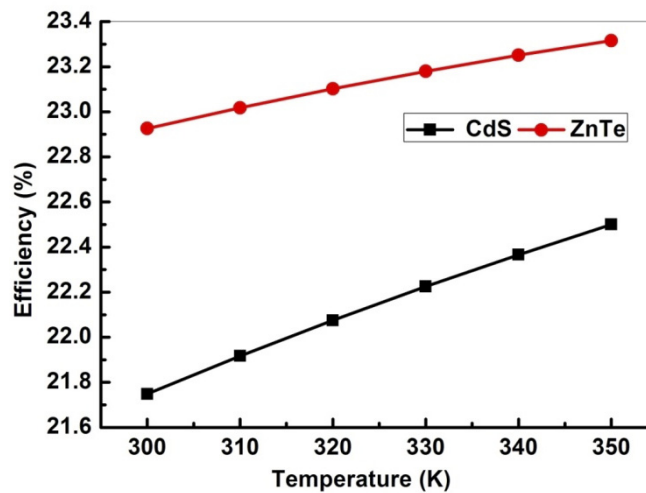


Figure 11 (e). Effect of temperature over efficiency of ZnSnP₂/CdS or ZnTe solar cell structures.

In Figure 11 (a), J_{sc} increases with temperature for both the structures considered. This effect can be understood in terms of band gap. The effect of temperature over energy band gap, E_g is given by Varshni equation [47]

$$E_g(T) = E_g(0) - \frac{\alpha T^2}{T + \beta} \tag{27}$$

Where $E_g(0)$ is the band gap energy at absolute zero on the Kelvin scale in the given material, and α and β are material-specific constants. This decrement in band gap is responsible for enhancement in current density values at higher temperature. Increase in temperature can be viewed as increase the energy of the charge carriers. Thus less energy is required to break the bond and conduction increases.

As a consequence of the increase in temperature, there is a shift in quantum efficiency curves (Figure 11(b),11(c)). When the temperature of the cell is increased, thermal vibrations of the lattice becomes stronger, which causes reduction in lifetime and mobility of minority charge carriers. This in turn reduces the diffusion length and process of recombination becomes stronger. But with increase in temperature, the band gap is reduced, which enhances the production of charge carriers. In low and middle temperature range, there is equilibrium in between the phenomenon of charge generation and recombination.

But with temperature, the absorption in wide band gap materials is improved for long wavelength region because of the phonons multiplication phenomenon [48]. So, the minority carriers production is increased with temperature in the range of long wavelengths, thus the photocurrent increases and consequently, the quantum efficiency. Further with temperature a sharp increment is found in V_{oc} (Figure 11 (d)).

The effect over V_{oc} can be understood as a measure of the amount of recombination in the device. As the temperature increases, the number of thermally generated carriers can exceed the number of dopant-generated carriers. Though the concentration of intrinsic carriers is very small; but it has very strong temperature dependence [49]. This increment in intrinsic carrier concentration causes the increase in reverse saturation current. The increment in reverse saturation current is responsible for decrement in open circuit voltage values.

Also, the temperature dependence of V_{oc} is given by [50]

$$\frac{dV_{oc}}{dT} \approx \frac{dE_g/q}{dT} + \frac{V_{oc} - E_g/q}{T} \tag{28}$$

From eq. (28) it is inferred that the temperature dependence is mainly related to the term $\frac{V_{oc} - E_g/q}{T}$; which after integration provides a linear relationship $V_{oc} \propto -T$ as observed experimentally [50].

Therefore, the tendency of V_{oc} to decrease and J_{sc} to increase with increasing temperature in the solar cells are determining factor for efficiency with variation in temperature. The overall effect of temperature has been studied for η as shown in figure 11 (e).

Effect of Band gap of absorption layer

The effect of band gap of absorption layer over performance parameters is studied. To find the effect of band gap, the results of ZnSnP₂ absorption layer with band gap 1.06 eV and 1.9 eV are compared. The effect of band gap of absorption layer over J-V characteristics of the cell are shown in Figure 12 (a)-12 (d). These results show that the increment in band gap results in an increment in absorption of light, thus an increment in performance parameters is found (Table 6). This improvement in parameters is due to the enhancement of absorption in longer wavelength region. This effect can be seen in quantum efficiency curves in Figure 12 (c) and 12 (d).

Hence, the study shows that ZnSnP₂ as absorption layer with CdS and ZnTe buffer can be promising solar cell model. ZnTe can be used as an option for CdS buffer layer, which is not only beneficial on the energy basis, but also helps in overcoming the serious environmental related problems due to the toxic nature of cadmium.

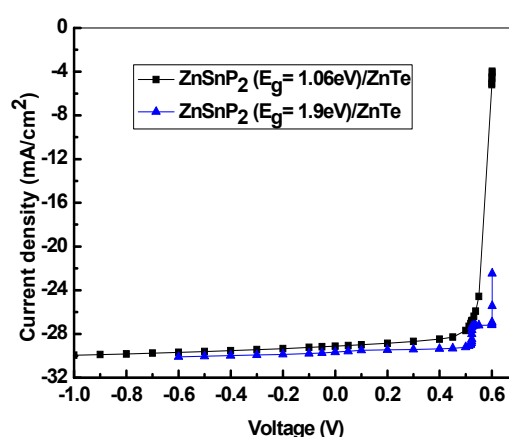
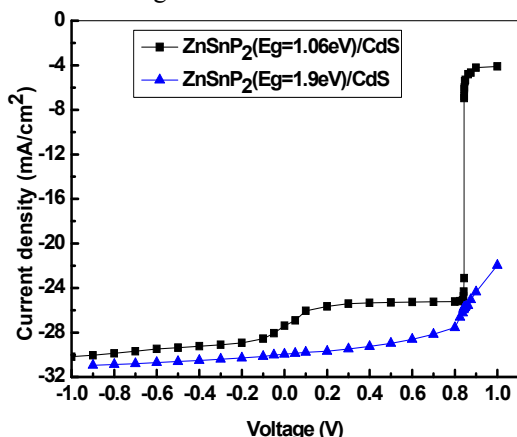


Figure 12 (a). Effect of band gap of absorption layer over J-V curves of ZnSnP₂/CdS solar cell.

Figure 12 (b). Effect of band gap of absorption layer over J-V curves of ZnSnP₂/ZnTe solar cell.

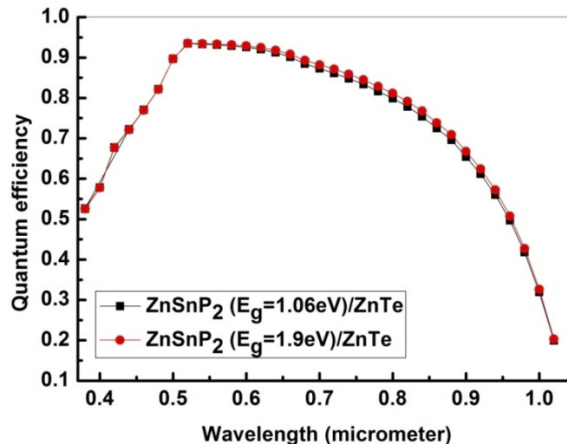
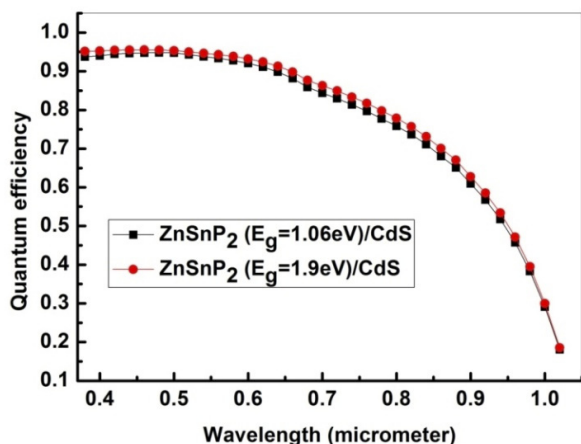


Figure 12 (c): Effect of band gap of absorption layer over quantum efficiency of ZnSnP₂/CdS solar cell.

Figure 12 (d): Effect of band gap of absorption layer over quantum efficiency of ZnSnP₂/ZnTe solar cell.

SUMMARY AND CONCLUSIONS

To conclude, results have been presented for the solid state properties such as structural, electronic, optical, elastic and thermal properties of the ZnSnP₂ semiconductor using the first-principles calculation. The structural properties in the

chalcopyrite structure are obtained using the total energy as a function of volume; the derived equilibrium parameters are compared with experimental data. We compared electronic and optical properties calculated with the mBJ functional and spectroscopic ellipsometry data. We find that the mBJ functional provides an accurate description of the electronic and optical properties. The ZnSnP₂ has a direct band gap. We have also derived the static refractive index. Thermal properties such as Gruneisen parameter, volume expansion coefficient, bulk modulus, specific heat, entropy, debye temperature and hardness are calculated successfully at various temperatures and pressures, and trends are discussed. The ground state parameters of interest were obtained and showed good agreement with published experimental and theoretical data. An application of the material in solar cell device has been presented; here we have used AMPS-1D to investigate the dependence of the buffer layer for thin layer ZnSnP₂ solar cells. A device modelling and detailed simulation study have been carried out over single junction ZnSnP₂ solar cell with a variety of buffer layers. The performance parameters of solar cells as open-circuit voltage (V_{oc}), the short-circuit current density (J_{sc}), the conversion efficiency η , Fill factor (FF) and quantum efficiency (QE) have been calculated. Also the effect of temperature and band gap of absorption layer is studied and it is found that higher band gap of absorption layer improves the performance of solar cell. Thus the study shows that ZnTe can be considered as an alternative to CdS buffer layer and assumes greater significance under this scenario. To the best of our knowledge, most of the investigated parameters are reported for the first time and will further stimulate the research in the related field.

ORCID IDs

 Neeraj, <https://orcid.org/0000-0001-9205-3246>;  Ajay Singh Verma, <https://orcid.org/0000-0001-8223-7658>

REFERENCES

- [1] S. Mukherjee, T. Maitra, A. Nayak, A. Pradhan, M. K. Mukhopadhyay, B. Satpati, and S. Bhunia, *Materials Chemistry and Physics* **204**, 147-153 (2018), <https://doi.org/10.1016/j.matchemphys.2017.10.014>.
- [2] S. Sharma, and A.S. Verma, *Eur. Phys. J. B*, **87**, 159 (2014), <https://doi.org/10.1140/epjb/e2014-41097-2>.
- [3] S. Sahin, Y.O. Ciftci, K. Colakoglu and N. Korozlu, *J. Alloy. Comp.* **529**, 1-7 (2012), <https://doi.org/10.1016/j.jallcom.2012.03.046>.
- [4] A.D. Martinez, E.L. Warren, P. Gorai, K.A. Borup, D. Kuciauskas, P.C. Dippo, and S.W. Boettcher, *Energy & Environmental Science*, **9**, 1031-1041 (2016), <https://doi.org/10.1039/C5EE02884A>.
- [5] A.D. Martinez, A.N. Fioretti, E.S. Toberer, and A.C. Tamboli, *J. Materials Chemistry A*, **5**, 11418-11435 (2017), <https://doi.org/10.1039/C7TA00406K>.
- [6] K. Miyauchi, T. Minemura, K. Nakatani, H. Nakanishi, M. Sugiyama, and S. Shirakata, *Phys. Stat. Sol. C*, **6**, 1116 (2009), <https://doi.org/10.1002/pssc.200881170>.
- [7] S. Nakatsuka, S. Akari, J. Chantana, T. Minemoto, and Y. Nose, *ACS Applied Materials & Interfaces*, **9**, 33827-33832 (2017), <https://doi.org/10.1021/acsami.7b08852>.
- [8] S. Nakatsuka, N. Yuzawa, J. Chantana, T. Minemoto, and Y. Nose, *Physica Status Solidi A*, **214**, 1600650 (2017), <https://doi.org/10.1002/pssa.201600650>.
- [9] D.O. Scanlon, and A. Walsh, *Appl. Phys. Letts.* **100**, 251911 (2012), <https://doi.org/10.1063/1.4730375>.
- [10] P.C. Sreeparvathy, V. Kanchana, and G. Vaitheeswaran, *J. Appl. Phys.*, **119**, 085701 (2016), <https://doi.org/10.1063/1.4942011>.
- [11] A.S. Verma, *Mat. Chem. Phys.* **139**, 256 (2013), <https://doi.org/10.1016/j.matchemphys.2013.01.032>.
- [12] N. Yuzawa, J. Chantana, S. Nakatsuka, Y. Nose, and T. Minemoto, *Curr. Appl. Phys.* **17**, 557-564 (2017), <https://doi.org/10.1016/j.cap.2017.02.005>.
- [13] Y. Zhang, *Comp. Mat. Sci.* **133**, 152-158 (2017), <https://doi.org/10.1016/j.commatsci.2017.03.016>.
- [14] G.K.H. Madsen, P. Blaha, K. Schwarz, E. Sjöstedt, and L. Nordström, *Phys. Rev. B*, **64**, 195134 (2001), <https://doi.org/10.1103/PhysRevB.64.195134>.
- [15] K. Schwarz, P. Blaha, and G.K.H Madsen, *Comput. Phys. Commun.* **147**, 71 (2002), [https://doi.org/10.1016/S0010-4655\(02\)00206-0](https://doi.org/10.1016/S0010-4655(02)00206-0).
- [16] P. Blaha, K. Schwarz, G.K.H. Madsen, D. Kvasnicka, and J. Luitz, in: *WIEN2K, An Augmented Plane Wave Plus Local Orbitals Program for Calculating Crystal Properties*, edited by K. Schwarz (Techn. Universität Wien, Austria, 2001).
- [17] Z. Wu, and R.E. Cohen, *Phys. Rev. B*, **73**, 235116 (2006), <https://doi.org/10.1103/PhysRevB.73.235116>.
- [18] F. Tran, R. Laskowski, P. Blaha, and K. Schwarz, *Phys. Rev. B*, **75**, 115131 (2007), <https://doi.org/10.1103/PhysRevB.75.115131>.
- [19] W. Kohn, and L.J. Sham, *Phys. Rev.* **140**, A1133 (1965), <https://doi.org/10.1103/PhysRev.140.A1133>.
- [20] J.P. Perdew, K. Burke, and M. Ernzerhof, *Phys. Rev. Lett.* **77**, 3865 (1996), <https://doi.org/10.1103/PhysRevLett.77.3865>.
- [21] F. Tran and P. Blaha, *Phys. Rev. Letts.* **102**, 226401 (2009), <https://doi.org/10.1103/PhysRevLett.102.226401>.
- [22] P.E. Blochl, O. Jepsen, and O.K. Andersen, *Phys. Rev. B*, **49**, 16223 (1994), <https://doi.org/10.1103/PhysRevB.49.16223>.
- [23] F.D. Murnaghan, *Proc. Natl. Acad. Sci. USA* **30**, 244-247 (1947), <https://doi.org/10.1073/pnas.30.9.244>.
- [24] V.L. Shaposhnikov, A.V. Krivosheeva, V.E. Borisenko, J.L. Lazzari, and F.A. Avitaya, *Phys. Rev. B*, **85**, 205201 (2012), <https://doi.org/10.1103/PhysRevB.85.205201>.
- [25] J. Sun, H.T. Wang, N.B. Ming, J. He, and Y. Tian, *Appl. Phys. Letts.* **84**, 4544 (2004), <https://doi.org/10.1063/1.1758781>.
- [26] S. Saha, and T.P. Sinha, *Phys. Rev. B*, **62**, 8828 (2000), <https://doi.org/10.1103/PhysRevB.62.8828>.
- [27] P.Y. Yu, and M. Cardona, *Fundamentals of Semiconductors*, (Springer-Verlag, Berlin, 1996).
- [28] M.Q. Cai, Z. Yin, and M.S. Zhang, *Appl. Phys. Letts.* **83**, 2805 (2003), <https://doi.org/10.1063/1.1616631>.
- [29] S. Sharma, A.S. Verma, R. Bhandari, S. Kumari, and V.K. Jindal, *Materials Science in Semiconductor Processing*, **27**, 79-96 (2014), <https://doi.org/10.1016/j.mssp.2014.06.015>.
- [30] J.C. Rife, R.N. Dexter, P.M. Bridenbaugh, and B.W. Veal, *Phys. Rev. B*, **16**, 4491 (1977), <https://doi.org/10.1103/PhysRevB.16.4491>.
- [31] J.F. Nye, *Physical Properties of Crystals, Their Representation by Tensors and Matrices*, (Oxford Univ. Press, Oxford, USA, 1985).
- [32] W. Voigt, *Lehrbuch der Kristallphysik*, (Teubner, Leipzig, 1928).
- [33] I.R. Shein, and A.L. Ivanovskii, *Scripta Materiali*, **59**, 1099-1002 (2008), <https://doi.org/10.1016/j.scriptamat.2008.07.028>.
- [34] A. Reuss, and Z. *Angew. Math. Mech.* **9**, 55 (1929), <https://doi.org/10.1002/zamm.19290090104>.
- [35] R. Hill, *Proc. Phys. Soc. Lond. A*, **65**, 349 (1952), <https://doi.org/10.1088/0370-1298/65/5/307>.

- [36] S.F. Pugh, *Philos. Mag.* **45**, 823-843 (1953), <https://doi.org/10.1080/14786440808520496>.
- [37] K. Chen, L. Zhao, and J.S. Tse, *J. Appl. Phys.* **93**, 2414 (2003), <https://doi.org/10.1063/1.1540742>.
- [38] K. Chen, L. Zhao, J.S. Tse, and J.R. Rodgers, *Phys. Lett. A*, **331**, 400 (2004), <https://doi.org/10.1016/j.physleta.2004.09.034>.
- [39] M.A. Blanco, E. Francisco, and V. Luaña, *Comput. Phys. Commun.* **158**, 57 (2004), <https://doi.org/10.1016/j.comphy.2003.12.001>.
- [40] M.A. Blanco, A. Martín Pendás, E. Francisco, J.M. Recio, and R. Franco, *J. Mol. Struct. Theochem.* **368**, 245 (1996), [https://doi.org/10.1016/S0166-1280\(96\)90571-0](https://doi.org/10.1016/S0166-1280(96)90571-0).
- [41] M. Flórez, J.M. Recio, E. Francisco, M.A. Blanco, and A.M. Pendás, *Phys. Rev. B*, **66**, 144112 (2002), <https://doi.org/10.1103/PhysRevB.66.144112>.
- [42] E. Francisco, M.A. Blanco, and G. Sanjurjo, *Phys. Rev. B*, **63**, 094107 (2001), <https://doi.org/10.1103/PhysRevB.63.094107>.
- [43] J.P. Poirier, *Introduction to the Physics of Earth's Interior*, (Cambridge University Press, Oxford, 2000), pp. 39.
- [44] A.S. Verma, and S.R. Bhardwaj, *J. Phys: Condensed Matter*, **19**, 026213 (2007), <https://doi.org/10.1088/0953-8984/19/2/026213>.
- [45] R. Gautam, P. Singh, S. Sharma, S. Kumari, and A.S. Verma, *Superlattices and Microstructures*, **85**, 859-871 (2015), <https://doi.org/10.1016/j.spmi.2015.07.014>.
- [46] B.G. Streetman, and S.K. Banerjee, *Solid State Electronic Devices' 6th ed.* (Pearson College Div, 2010), pp. 581.
- [47] Y.P. Varshni, *Physica*, **34**, 149 (1967), [https://doi.org/10.1016/0031-8914\(67\)90062-6](https://doi.org/10.1016/0031-8914(67)90062-6).
- [48] B.O. Seraphin, editor, *Solar Energy Conversion—Solid State Physics Aspects Topics in Applied Physics, Volume 31*, (Springer-Verlag, Heidelberg, 1979), <https://doi.org/10.1007/3-540-09224-2>.
- [49] S.M. Sze, *Physics of semiconductor devices, 2nd ed.* (John Wiley and Sons, NY, 1981), pp. 880.
- [50] P. Würfel, *Physics of Solar Cells*, (Wiley-VCH Verlag, Weinheim, 2005), pp. 188.
- [51] V. Kumar, A.K. Shrivastava, R. Banerji, and D. Dhirhe, *Solid State Communications*, **149**, 1008-1011 (2009), <https://doi.org/10.1016/j.ssc.2009.04.003>.
- [52] A.S. Verma, S. Sharma, and V.K. Jindal, *Mod. Phys. Letts. B*, **24**, 2511 (2010), <https://doi.org/10.1142/S0217984910024821>.
- [53] A.S. Verma, *Phys. Status Solidi B*, **246**, 192 (2009), <https://doi.org/10.1002/pssb.200844242>.
- [54] A.S. Verma, and D. Sharma, *Phys. Scr.* **76**, 22 (2007), <https://doi.org/10.1088/0031-8949/76/1/004>.
- [55] K.F. Young, and H.P.R. Fredrikse, *J. Phys. Chem. Ref. Data* **2**, 313 (1973), <https://doi.org/10.1063/1.3253121>.
- [56] K.K. Kima, S. Niki, J.Y. Oh, J. Song, T.Y. Seong, S.J. Park, S. Fujita, and S.W. Kimb, *J. Appl. Phys.* **97**, 066103 (2005), <https://doi.org/10.1063/1.1863416>.
- [57] M.A. Bodea, G. Sbarcea, G.V. Naik, A. Boltasseva, T.A. Klar, and J.D. Pedarnig, *Appl. Phys. A*, **110**, 929 (2013), <https://doi.org/10.1007/s00339-012-7198-6>.
- [58] S. Mondal, S.R. Bhattacharyya, and P. Mitra, *Pramana J. Physics*, **80**, 315 (2013), <https://doi.org/10.1007/s12043-012-0463-6>.
- [59] R.K. Swank, *Phys. Rev.* **153**, 844 (1967), <https://doi.org/10.1103/PhysRev.153.844>.
- [60] Z.C. Feng, editor, *Handbook of Zinc Oxide and Related Materials: Devices and Nano Engineering, Volume 2*, (CRC Press/Taylor & Francis, Boca Raton, FL, 2012).
- [61] M.A. Olopade, O.O. Oyebola, and B.S. Adeleke, *Adv. Appl. Sci. Res.* **3**, 3396 (2012), https://www.researchgate.net/profile/Muteeu_Olopade/publication/283294216_Investigation_of_some_materials_as_buffer_layer_in_copper_zinc_tin_sulphide_Cu_2ZnSnS4_solar_cells_by_SCAPS-1D/links/5699290108aea14769432a39.pdf.
- [62] X. Yang, C. Xu, and N.C. Giles, *J. Appl. Phys.* **104**, 073727 (2008), <https://doi.org/10.1063/1.2996032>.
- [63] B.K. Meyer, ZnO: electron and hole mobilities, *Landolt-Börnstein-Group III, Condensed Matter*, **44D**, 610 (2011).
- [64] M. Burgelman, K. Decock, S. Khelifi, A. Abass, *Thin Solid Films*, **535**, 296 (2013), <https://doi.org/10.1016/j.tsf.2012.10.032>.
- [65] M.A. Green, *Solar Cells, Operating Principles, Technology and System Applications*, Prentice Hall Inc., (1982)
- [66] W.E. Spear, J. Mort, *Proc. Phys. Soc.* **81**, 130 (1963), <https://doi.org/10.1088/0370-1328/81/1/319>.
- [67] M.S. Hossain, M.M. Aliyu, M.A. Matin, M.A. Islam, M.R. Karim, T. Razykov, K. Sopian, and N. Amina, *Int. J. Mech. Mater. Eng.* **6**, 350 (2011).
- [68] H.J. Moller, *Progress in Materials Science* **35**, 205-418 (1991), [https://doi.org/10.1016/0079-6425\(91\)90001-A](https://doi.org/10.1016/0079-6425(91)90001-A).
- [69] S. Siebentritt, U. Rau, *Wide-Gap Chalcopyrites*, (Springer, 2006).

СТРУКТУРА І ВЛАСТИВОСТІ ZnSnP₂ ДЛЯ ЗАСТОСУВАННЯ В ФОТОЕЛЕКТРИЧНИХ ПРИСТРОЯХ З ВИКОРИСТАННЯМ БУФЕРНИХ ШАРІВ НА ОСНОВІ CdS І ZnTe

Нирадж^а, Аджай С. Верма^б

^аФізичний факультет, Банастанлі Від'яніт, Раджастан 304022 (Індія)

^бФакультет природничих та прикладних наук, Школа технологій, Глокал університет
Сахаранпур, Уттар Прадеш, 247232 (Індія)

Тут ми представляємо розширений аналіз параметрів, пов'язаних із структурними, електронними, оптичними та механічними властивостями халькопіритового матеріалу на основі цинку, використовуючи повний потенціал лінеаризованого методу доповненої плоскої хвилі (FP-LAPW) в рамках теорії функціональності щільності. Розрахунки ab initio виконувались методом лінеаризованої розширеної плоскої хвилі (LAPW), реалізованого в коді WIEN2K в рамках теорії функціоналу щільності, щоб отримати структурні, електронні та оптичні властивості ZnSnP₂ у об'ємно-центрованій тетрагональній (ВСТ) фазі. Представлено шість пружних констант (C₁₁, C₁₂, C₁₃, C₃₃, C₄₄ і C₆₆) та механічні параметри, які порівнюються з наявними експериментальними даними. Для точного опису залежності від тиску і температури коефіцієнта теплового розширення, об'ємного модуля, питомої теплоти, температури Дебая, параметрів ентропії Грюнайзена використовуються термодинамічні розрахунки в квазігармонічному наближенні. На основі напівемпіричного співвідношення ми визначили твердість матеріалу; що пояснюється різною силою ковалентного зв'язку. Крім того, змодельовані сонячних елементи на основі ZnSnP₂ також проаналізовано фізику пристрою та параметри продуктивності для буферних шарів ZnTe та CdS. Результати моделювання для тонкошарової сонячної батареї ZnSnP₂ показують максимальну ефективність (22,9%) із ZnTe в якості буферного шару. Більшість досліджуваних параметрів повідомляється вперше. Результат цього дослідження додатково підтверджує перспективи використання цього халькопіриту, який за своєю суттю був би стійким та відповідав би гнучкому субстрату, що є найважливішими характеристиками для комерціалізації сонячних елементів на основі халькопіриту. Таким чином, сприяння еволюції цього матеріалу для досягнення високоефективних оптоелектронних пристроїв відкриває новий шлях у галузі створення сонячних елементів.

КЛЮЧОВІ СЛОВА: Ab-initio розрахунки; електронні властивості; пружні константи; термодинамічні властивості

PACS: 71.15.Mb; 71.20.-b; 71.55.Ak; 71.20.Nr

OPTOELECTRONIC PROPERTIES OF TERNARY TETRAHEDRAL SEMICONDUCTORS

Rajesh C. Gupta^a, Ajay S. Verma^{b,*}, Khushvant Singh^a^aDepartment of Physics, B. S. A. College, Mathura 281004 (India)^bDepartment of Natural and Applied Sciences, School of Technology, Glocal University, Saharanpur 247121 (India)*Corresponding Author: ajay_phy@rediffmail.com

Received December 5, 2020; revised February 16, 2021; accepted February 17, 2021

The dielectric interpretation of crystal ionicity evolved by Phillips and Van Vechten (P.V.V) has been utilized to evaluate various ground state properties for broad range of semiconductors and insulators. Although, the relevance of P.V.V dielectric theory has been restricted to only simple $A^N B^{8-N}$ structured compounds, which have a particular bond. Levine has broadened P.V.V. theory of ionicity to multiple bond and complex crystals and evaluated many bond parameters for ternary tetrahedral semiconductors. Some other researchers have extended Levine's work with a concept of ionic charge product and nearest neighbour distance to binary and ternary tetrahedral crystals to evaluate the ground state properties. In this paper, a new hypothesis of average atomic number of the elements in a compound has been used to understand the some electronic and optical properties such as ionic gap (E_c), average energy gap (E_g), crystal ionicity (f_i), electronic susceptibility (χ), and dielectric constant (ϵ) of ternary tetrahedral ($A^{II}B^{IV}C_2^V$ and $A^{I}B^{III}C_2^{VI}$) semiconductors. A reasonably acceptable agreement has been noticed between our evaluated values and other researchers reported values.

KEYWORDS: crystal ionicity, average atomic number, chalcopyrites

Optical and electronic properties of a material are the important parameters for device fabrication in almost all the fields of present-time electronics. The ternary tetrahedral ($A^{II}B^{IV}C_2^V$ and $A^{I}B^{III}C_2^{VI}$) structured compounds have brought significant curiosity of researchers' fraternity due to their exciting semiconducting, optical, electrical, mechanical and structural properties. These properties are of underlying significance for the conduct of charge carriers, dopants, impurities and defects in insulators and semiconductors. In contrast to binary analogues these semiconductors have high energy direct band gaps and lower melting points with tetragonal chalcopyrite structure. Structurally chalcopyrite semiconductors are extracted from that of binary sphalerite structure ($A^{II}B^{VI}$ and $A^{III}B^V$) with a slight distortion in the chemical composition. Therefore, similar to their binary analogues ternary tetrahedral semiconductors have a high non-linear susceptibility. Although due to presence of two different types of bonds in ternary tetrahedral semiconductors they show anisotropy, which increases high birefringence. High non-linear susceptibility appeared with high birefringence in ternary tetrahedral semiconductors make them very helpful for efficient second harmonic generation and phase matching. Except this, the other major technological applications of these compounds are in photo-voltaic detectors, infrared oscillators, modulators, filters, solar cells, light emitting diodes and lasers etc [1-13].

Theory of crystal ionicity is essential in analyzing the problems in the area of cohesive energy, heat formation, elastic constants, bulk modulus and crystal structure [14]. Van Vechten [15, 16], Phillips [16, 17], Levine [14] and many other workers [18, 19] have brought to light various theories and evaluated crystal ionicity for the elementary compounds. Phillips and Van Vechten have computed the heteropolar and homopolar parts to the chemical bond in binary $A^N B^{8-N}$ crystals. Penn [18] suggested one electron model to separate the average energy gap into heteropolar and homopolar parts. Here, homopolar energy gap (E_h) is used as the function of bond length. Levine [14] has broadened Phillips and Van Vechten (P.V.V) theory of ionicity for ternary tetrahedral semiconductors including the effect of 'd' core electrons. Validation of Levine's theory has been given by Singh and Gupta [19]. According to Levine's modified theory of crystal ionicity heteropolar energy gap (E_c) depends on bond length and ionic charges involved in bond formation. Kumar et al. [20-22] have evaluated heteropolar and homopolar energy gaps with reference to plasmon energy and it depends directly on the ionic charge of the compound. Ionic charge depends on atomic number of an element in a compound.

Due to difficulties associated with the experimental procedure and its high cost, also intricacies in obtaining correct values of physical properties, researchers have found theoretical methods more appropriate in calculating the physical properties of solids. However due to the lengthy procedure, as well complicated computational methods needed a series of approximation; those methods have always been complex and developed for only certain semiconductors [23]. Hence, we thought it would be of great interest to suggest an another probable interpretation of the ionic gap (E_c), average energy gap (E_g), crystal ionicity (f_i), dielectric constant (ϵ) and electronic susceptibility (χ) for ternary tetrahedral ($A^{II}B^{IV}C_2^V$ and $A^{I}B^{III}C_2^{VI}$) semiconductors.

Several other researchers have made an effort to compute optical and electronic properties of ternary tetrahedral semiconductors with the help of ionic charge and valance electrons. Besides it considering the different screening factors present in compound crystallography, we have used a new concept of average atomic number of interacting elements in a compound and found excellent outcomes comparable to previous workers for the ionic gap (E_c), average energy gap (E_g), crystal ionicity (f_i), dielectric constant (ϵ) and electronic susceptibility (χ) in ternary tetrahedral

(A^{II}B^{IV}C₂^V and A^IB^{III}C₂^{VI}) semiconductors. In the proposed relations only a few variables such as atomic number and ionic charge on cation and anion are prerequisite; to calculate many electronic and optical properties of these compounds the method emerge relevant to other materials, too.

THEORY, RESULTS AND DISCUSSION

Covalency and ionicity of the materials have been studied for long as a result researchers have got clear concept of those. The covalent concept involves contribution of electrons between atoms in place of charge transfer, while the ionic concept involves transfer of electron in actual from one atom to another which promotes interaction of two closed shell ions mainly due to short range repulsion and Coulomb force. Pauling [24] has pioneered the concept of crystal ionicity derived from thermo-chemical effect. According to one electron model of Penn [18], the average energy gap ($E_g = E_p$) may be given as,

$$E_p = \hbar\omega_p S_0 / (\epsilon_\infty - 1)^{1/2} \quad (1)$$

where $\hbar\omega_p$ is valance electron plasmon energy, ϵ_∞ is the optical dielectric constant and $S_0 = 1$. Plasmon energy of valance electron oscillations both in metal and compound is given as [25],

$$\hbar\omega_p = 28.8 \sqrt{ND/M} \quad (2)$$

where N is the number of valance electrons participating in plasma oscillations, D and M are density and molecular weight, respectively. Relation (2) is applicable for valance electrons in semiconductors and insulators up to first approximation. Philipp and Ehrenreich [26], and Raether [27] have found that the plasmon energy for semiconductors and insulators is represented by,

$$\hbar\omega_{pd} = \hbar\omega_p / \sqrt{1 - \delta\epsilon_0} \quad (3)$$

where $\delta\epsilon_0$ is a very small correction to valance electron plasmon energy $\hbar\omega_p$ may be overlooked to a first approximation. Philipp and Ehrenreich [26] have expressed that the evaluated values of $\hbar\omega_p$ and $\hbar\omega_{pd}$ are in good agreement with their observed values of plasmon energy in dielectrics. Kittel [28] has also been shown that plasmon energy in dielectrics is actually the same as in metals.

It is stated in modified theory of dielectric of solids [15-17,29; 19,30] for tetrahedral coordinated compounds, average energy gap (E_g), relating bonding and anti bonding (sp^3) hybridized orbital can be decomposed into two parts because of the symmetric and anti symmetric contribution to the potential in a unit cell. These two parts are covalent or homopolar gap (E_h) and ionic or heteropolar gap (E_c), which can be expressed in the following relation:

$$E_g^2 = E_c^2 + E_h^2 \quad (4)$$

The ionic or heteropolar gap (E_c) is inversely related to the bond length 'd' as:

$$E_c = K_1 d^{-1} e^{-K_s r_0} \quad (5)$$

where K_1 is an arbitrary constant and depends on the difference between valance states of an atom and is given by $K_1 = bc^2 \Delta z$, where prescreening factor b depends on the coordination number [14] around the cation i.e. $b = 0.089 N_c^2$, here N_c is average coordination number and c-electronic charge, $\Delta z = 4$ for IIB chalcogenides. The values of $N_c = 4$, $b = 1.424$ and hence $K_1 = 262.784$ are for zinc blende type structure. Thomas-Fermi screening parameter K_s has been ascertained taking into account eight electrons per molecule (two for Zn, Cd & Hg and six for O, S, Se & Te) and $r_0 = d/2$.

The covalent or homopolar gap (E_h) is related to the bond length 'd' as [16]:

$$E_h = A d^{-K_2} \quad (6)$$

Here A and K_2 are constants, which remain unaffected in different crystal structures with values $A = 40.468 \text{ eV}/\text{\AA}^{2.5}$ and $K_2 = 2.5$. These values are $A = 39.74$ and $K_2 = 2.48$ as reported by PVV theory. Therefore, the values of E_c and E_h depend on number of bonds emerge from cations and bond length.

The crystal ionicity f_i of the chemical bond is expressed as the fraction of ionic character as follows.

$$f_i = E_c^2 / E_g^2 \quad (7)$$

V. Kumar [20-22] has expressed those electronic properties of ternary tetrahedral (A^{II}B^{IV}C₂^V and A^IB^{III}C₂^{VI}) crystals in terms of plasmon energy $\hbar\omega_p$ (eV) as follows:

For the A-C bond in A^{II}B^{IV}C₂^V:

$$E_{h,AC} \text{ (eV)} = 0.05118(\hbar\omega_{p,AC})^v, \quad (8)$$

$$E_{c,AC} \text{ (eV)} = 5.904b_{AC}(\hbar\omega_{p,AC})^\mu \times \exp[-5.971(\hbar\omega_{p,AC})^{-\mu^2}] \quad (9)$$

For the B-C bond in $A^{II}B^{IV}C_2^V$:

$$E_{h,BC} \text{ (eV)} = 0.04158(\hbar\omega_{p,BC})^v, \quad (10)$$

$$E_{c,BC} \text{ (eV)} = 1.81b_{BC}(\hbar\omega_{p,BC})^\mu \times \exp [-6.4930(\hbar\omega_{p,BC})^{-\mu/2}] \quad (11)$$

For the A-C bond in $A^I B^{III} C_2^{VI}$:

$$E_{h,AC} \text{ (eV)} = 0.0246(\hbar\omega_{p,AC})^v, \quad (12)$$

$$E_{c,AC} \text{ (eV)} = 7.3208b_{AC}(\hbar\omega_{p,AC})^{2/3} \times \exp [-8.026(\hbar\omega_{p,AC})^{-1/3}((\hbar\omega_{p,AC})^{-2/3})] \quad (13)$$

For the B-C bond in $A^I B^{III} C_2^{VI}$:

$$E_{h,BC} \text{ (eV)} = 0.0416(\hbar\omega_{p,BC})^v, \quad (14)$$

$$E_{c,BC} \text{ (eV)} = 5.53b_{BC}(\hbar\omega_{p,BC})^{2/3} \times \exp [-6.5058(\hbar\omega_{p,BC})^{-2/3}] \quad (15)$$

where v is a constant. E_c and E_h are the ionic and homopolar gaps, respectively. The authors of above theory have used constants μ , v and prescreening factor b to evaluate the parameters mentioned therein.

Jayaraman et al. [31], Srideshmukh et al. [32], and Krishnan et al. [33] established that significantly reduced ionic charges must be used to obtain better agreement with experimental values of these parameters. Verma et al. [34] have been applied this concept for obtaining better agreement with theoretical data for ionic gap (E_c), average energy gap (E_g), crystal ionicity (f_i) dielectric constant (ϵ) and susceptibility (χ) of ternary tetrahedral ($A^{II}B^{IV}C_2^V$ and $A^I B^{III} C_2^{VI}$) semiconductors, which can be expressed in terms of product of ionic charges and bond length as follows:

For A-C bond in ternary tetrahedral ($A^{II}B^{IV}C_2^V$ and $A^I B^{III} C_2^{VI}$) semiconductors:

$$E_{c,AC} \text{ (eV)} = 90 d^2 / (Z_1 Z_2)^{0.7}, \quad (16)$$

$$E_{g,AC} \text{ (eV)} = 96 d^{2.12} / (Z_1 Z_2)^{0.5} \quad (17)$$

For B-C bond in ternary tetrahedral ($A^{II}B^{IV}C_2^V$ and $A^I B^{III} C_2^{VI}$) semiconductors:

$$E_{c,BC} \text{ (eV)} = 275 d^2 / (Z_1 Z_2)^{1.25}, \quad (18)$$

$$E_{g,BC} \text{ (eV)} = 106 d^{2.12} / (Z_1 Z_2)^{0.5} \quad (19)$$

where, Z_1 and Z_2 are the ionic charges and d is the bond length in Å. On solving equations (7) and (16-19), crystal ionicity f_i can be expressed as follows:

For A-C bond in ternary tetrahedral ($A^{II}B^{IV}C_2^V$ and $A^I B^{III} C_2^{VI}$) semiconductors:

$$f_i = 0.87891 d^{0.24} / (Z_1 Z_2)^{0.4} \quad (20)$$

For B-C bond in ternary tetrahedral ($A^{II}B^{IV}C_2^V$ and $A^I B^{III} C_2^{VI}$) semiconductors:

$$f_i = 6.731 d^{0.24} / (Z_1 Z_2)^{1.5} \quad (21)$$

V. Kumar [35] has given the relation for electronic susceptibility χ as follows:

$$\chi_{XY} = (\hbar\omega_{p,XY})^2 / (E_{g,XY})^2, \quad (22)$$

and dielectric constant

$$\epsilon_{XY} = 1 + \chi_{XY}. \quad (23)$$

As, the plasmon energy ($\hbar\omega_p$) and ionic charge depend on the number of valance electrons, which depend on atomic number in an atom. But in a compound this may depend on the atomic numbers of the constituent atoms. Hence, we have proposed the idea of average atomic number of the atoms in a compound to study the ground state properties. As, this parameter of average atomic number includes all the distribution laws of electrons in an atom and various screening factors. So, taking into account the above empirical relations and applying the concept of product of ionic charges given by Verma et al. [34] and our hypothesis of average atomic number of elements in the ternary tetrahedral semiconductors, the crystal ionicity (f_i) of ternary tetrahedral semiconductors manifests a nearly linear dependence when traced against average atomic number.

However crystal ionicity falls on two closely parallel straight lines according to the product of ionic charge of the compounds and this is presented in the Fig. 1 and 2. Applying this concept to reach better agreement with theoretical data, we have introduced following empirical relations for electronic and optical properties such as ionic gap (E_c), average energy gap (E_g), crystal ionicity (f_i), electronic susceptibility (χ) and dielectric constant (ϵ) and further evaluated their values. The evaluated values are in excellent agreement with the values reported by Levine [14], V. Kumar [21, 35, 36]. Our endeavour of determining those has not been required experimental values of the dielectric constant although the previous models needed this value in their computations except Verma et al. [34]. These values are presented in the Table 1-5.

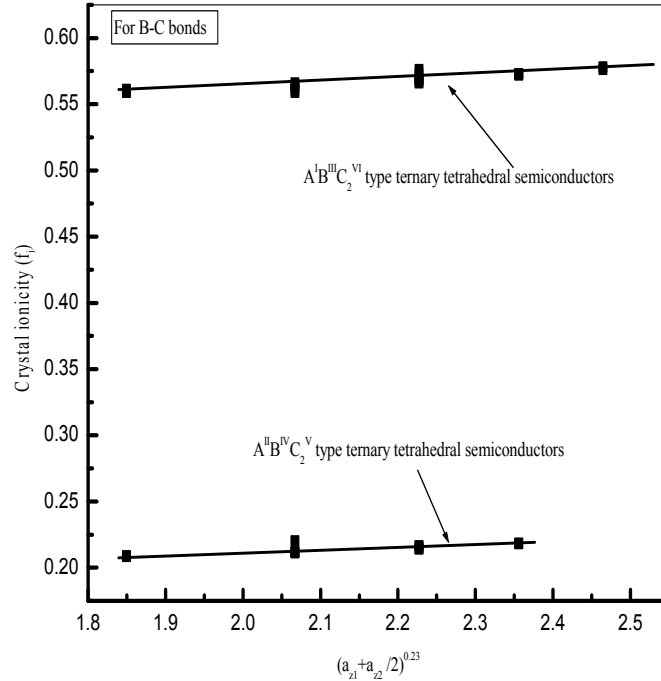


Figure 1. Plot of crystal ionicity versus average atomic number for A-C bonds in ternary tetrahedral ($A^{II}B^{IV}C_2^V$ and $A^I B^{III}C_2^{VI}$) semiconductors. Here, crystal ionicity of $A^{II}B^{IV}C_2^V$ lies on a line closely parallel to the line of $A^I B^{III}C_2^{VI}$. In this figure values of (f_i) taken from V. Kumar [35,36].

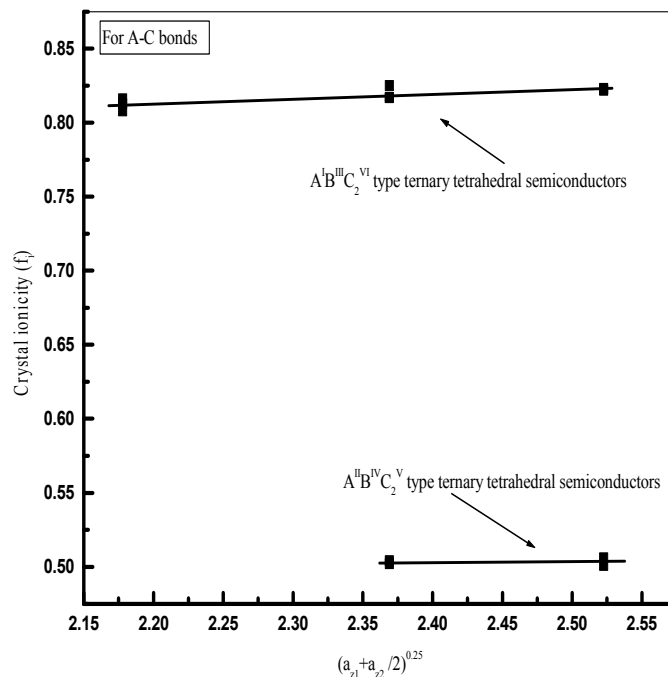


Figure 2. Plot of crystal ionicity versus average atomic number for B-C bonds in ternary tetrahedral ($A^{II}B^{IV}C_2^V$ and $A^I B^{III}C_2^{VI}$) semiconductors. Here, crystal ionicity of $A^{II}B^{IV}C_2^V$ lies on a line closely parallel to the line of $A^I B^{III}C_2^{VI}$. In this figure values of (f_i) taken from V. Kumar [35,36].

For A-C bond in ternary tetrahedral ($A^{II}B^{IV}C_2^V$ and $A^I B^{III}C_2^{VI}$) semiconductors:

$$E_{c,AC} \text{ (eV)} = 88 / (Z_1 Z_2)^{0.8} \left(\frac{a_{z1} + a_{z2}}{2} \right)^{0.5}, \tag{24}$$

$$E_{g,AC} \text{ (eV)} = 95 / (Z_1 Z_2)^{0.8} \left(\frac{a_{z1} + a_{z2}}{2} \right)^{0.5}, \tag{25}$$

$$f_{i,AC} = 0.4 \left(\frac{a_{z1} + a_{z2}}{2} \right)^{0.25} / (Z_1 Z_2)^{0.3}. \tag{26}$$

For B-C bond in ternary tetrahedral ($A^I B^{IV} C_2^V$ and $A^I B^{III} C_2^{VI}$) semiconductors:

$$E_{c,BC} \text{ (eV)} = 90 / (Z_1 Z_2)^{0.8} \left(\frac{a_{z1} + a_{z2}}{2} \right)^{0.49}, \tag{27}$$

$$E_{g,BC} \text{ (eV)} = 122 / (Z_1 Z_2)^{0.8} \left(\frac{a_{z1} + a_{z2}}{2} \right)^{0.43}, \tag{28}$$

$$f_{i,BC} = 4 \left(\frac{a_{z1} + a_{z2}}{2} \right)^{0.23} / (Z_1 Z_2)^{1.5}. \tag{29}$$

while, we have found electronic susceptibility (χ_{xy}) same as given in relation (22) and can be calculated for AC and BC bonds by using the values of E_g obtained from relations (25) and (28), thereafter dielectric constant (ϵ_{xy}) by the relation (23). Here, Z_1, Z_2 are ionic charges and a_{z1}, a_{z2} are atomic numbers of the elements in the compound.

Table 1. This table presents the values of ionic gaps E_c (eV) and average energy gaps E_g (eV) for A-C bond of ternary tetrahedral ($A^I B^{III} C_2^{VI}$ and $A^I B^{IV} C_2^V$) semiconductors.

Solids	a_{z1}	a_{z2}	E_c [14]	E_c [35,36]	E_c [34]	E_c [This work]	E_g [14]	E_g [35,36]	E_g [34]	E_g [This work]
CuAlS ₂	29	16		10.575	10.565	10.655		11.728	11.719	12.941
CuAlSe ₂	29	34		9.435	9.46	9.005		10.436	10.425	10.938
CuAlTe ₂	29	52		8.035	8.196	7.942		8.859	8.954	9.646
CuGaS ₂	29	16	9.95	9.673	9.699	10.655	10.964	10.705	10.704	12.941
CuGaSe ₂	29	34	7.87	8.807	8.936	9.005	8.888	9.692	9.813	10.938
CuGaTe ₂	29	52		7.945	8.133	7.942		8.758	8.881	9.646
CuInS ₂	29	16	8.52	8.523	8.936	10.655	9.617	9.478	9.813	12.941
CuInSe ₂	29	34		9.333	9.382	9.005		10.321	10.334	10.938
CuInTe ₂	29	52		6.635	7.83	7.942		7.516	8.531	9.646
AgAlS ₂	47	16		9.32	8.587	9.005		10.117	9.408	10.938
AgAlSe ₂	47	34		8.393	7.83	7.942		9.096	8.531	9.646
AgAlTe ₂	47	52		7.51	7.117	7.184		8.128	7.71	8.725
AgGaS ₂	47	16	9.87	9.103	8.388	9.005	10.6	9.877	9.177	10.938
AgGaSe ₂	47	34	8.56	8.405	7.83	7.942	9.275	9.11	8.531	9.646
AgGaTe ₂	47	52		7.649	7.22	7.184		8.281	7.829	8.725
AgInS ₂	47	16		9.608	8.794	9.005		10.434	9.648	10.938
AgInSe ₂	47	34	8.15	8.662	8.01	7.942	8.862	9.392	8.739	9.646
AgInTe ₂	47	52		7.554	7.117	7.184		8.176	7.71	8.725
ZnSiP ₂	30	15	4.1	4.584	4.552	4.425	6.119	6.53	6.263	6.477
ZnGeP ₂	30	15	4.08	4.541	4.499	4.425	6.134	6.465	6.186	6.477
ZnSnP ₂	30	15	4.07	4.414	4.399	4.425	6.038	6.273	6.04	6.477
ZnSiAs ₂	30	33	3.73	4.225	4.229	3.739	5.655	5.989	5.793	5.474
ZnGeAs ₂	30	33	3.71	4.157	4.168	3.739	5.582	5.887	5.705	5.474
ZnSnAs ₂	30	33	3.68	4.061	4.082	3.739	5.48	5.744	5.58	5.474
CdSiP ₂	48	15	4.17	3.875	3.915	3.739	5.682	5.647	5.338	5.474
CdGeP ₂	48	15	4.12	3.882	3.921	3.739	5.652	5.478	5.347	5.474
CdSnP ₂	48	15	4.04	3.785	3.834	3.739	5.519	5.334	5.221	5.474
CdSiAs ₂	48	33	3.98	3.618	3.684	3.298	5.354	5.088	5.005	4.828
CdGeAs ₂	48	33	3.94	3.612	3.679	3.298	5.317	5.08	4.997	4.828
CdSnAs ₂	48	33	3.87	3.527	3.602	3.298	5.205	4.983	4.887	4.828

Table 2. This table presents the values of ionic gaps E_c (eV) and average energy gaps E_g (eV) for B-C bond of ternary tetrahedral ($A^I B^{III} C_2^{VI}$ and $A^{II} B^{IV} C_2^V$) semiconductors.

Solids	a_{z1}	a_{z2}	E_c [14]	E_c [35,36]	E_c [34]	E_c [This work]	E_g [14]	E_g [35,36]	E_g [34]	E_g [This work]
CuAlS ₂	29	16		5.746	5.584	5.790		7.671	7.471	9.214
CuAlSe ₂	29	34		5.165	5.084	4.570		6.863	6.764	7.487
CuAlTe ₂	29	52		4.479	4.469	3.899		5.902	5.899	6.512
CuGaS ₂	29	16	5.6	5.684	5.536	4.570	7.45	7.584	7.402	7.487
CuGaSe ₂	29	34	5.1	5.103	5.001	3.899	6.8	6.777	6.646	6.512
CuGaTe ₂	29	52		4.336	4.366	3.458		5.725	5.755	5.862
CuInS ₂	29	16	5.49	4.898	4.839	3.899	6.39	6.494	6.419	6.512
CuInSe ₂	29	34		4.466	4.469	3.458		5.902	5.899	5.862
CuInTe ₂	29	52		3.96	4.017	3.141		5.215	5.269	5.388
AgAlS ₂	47	16		5.939	5.734	5.790		7.943	7.683	9.214
AgAlSe ₂	47	34		5.381	5.258	4.570		7.162	7.009	7.487
AgAlTe ₂	47	52		4.43	4.434	3.899		5.853	5.85	6.512
AgGaS ₂	47	16	5.64	5.887	5.683	4.570	7.47	7.869	7.611	7.487
AgGaSe ₂	47	34	5.02	5.235	5.127	3.899	6.7	6.959	6.824	6.512
AgGaTe ₂	47	52		4.316	4.332	3.458		5.698	5.708	5.862
AgInS ₂	47	16		4.835	4.8	3.899		6.408	6.364	6.512
AgInSe ₂	47	34	4.71	4.378	4.4	3.458	6.7	5.783	5.802	5.862
AgInTe ₂	47	52		3.758	3.844	3.141		4.944	5.029	5.388
ZnSiP ₂	30	15	2.45	2.72	2.424	3.325	5.84	5.95	5.463	5.292
ZnGeP ₂	30	15	2.6	2.546	2.28	2.625	5.56	5.54	5.12	4.300
ZnSnP ₂	30	15	2.71	2.183	1.994	2.239	4.97	4.7	4.443	3.740
ZnSiAs ₂	30	33	2.54	2.478	2.23	2.625	5.41	5.38	5.001	4.300
ZnGeAs ₂	30	33	2.12	2.347	2.125	2.239	4.97	5.07	4.753	3.740
ZnSnAs ₂	30	33	1.53	2.045	1.883	1.986	4.16	4.38	4.182	3.367
CdSiP ₂	48	15	2.59	2.739	2.439	3.325	5.94	6	5.5	5.292
CdGeP ₂	48	15	2.68	2.538	2.278	2.625	5.59	5.52	5.116	4.300
CdSnP ₂	48	15	2.71	2.181	1.992	2.239	4.96	4.69	4.439	3.740
CdSiAs ₂	48	33	2.64	2.543	2.233	2.625	5.46	5.42	5.01	4.300
CdGeAs ₂	48	33	2.21	2.317	2.101	2.239	4.95	5	4.695	3.740
CdSnAs ₂	48	33	1.59	2.017	1.861	1.986	4.14	4.32	4.13	3.367

Table 3. This table presents the values of crystal ionicity f_i for A-C and B-C bonds of ternary tetrahedral ($A^I B^{III} C_2^{VI}$ and $A^{II} B^{IV} C_2^V$) semiconductors.

Solids	f_i [14]	f_i [35,36]	f_i [37]	f_i [34]	f_i [This work]	f_i [14]	f_i [35,36]	f_i [37]	f_i [34]	f_i [This work]
	A-C Bond					B-C Bond				
CuAlS ₂		0.813	0.78	0.813	0.708		0.561	0.62	0.559	0.503
CuAlSe ₂		0.817	0.79	0.824	0.770		0.566	0.65	0.565	0.563
CuAlTe ₂		0.822	0.75	0.838	0.820		0.576	0.56	0.574	0.606
CuGaS ₂	0.825	0.816	0.77	0.821	0.708	0.565	0.561	0.55	0.559	0.563
CuGaSe ₂	0.784	0.825	0.76	0.829	0.770	0.563	0.567	0.55	0.566	0.606
CuGaTe ₂		0.823	0.81	0.839	0.820		0.573	0.51	0.576	0.641
CuInS ₂	0.785	0.808	0.77	0.829	0.708	0.636	0.569	0.6	0.569	0.606
CuInSe ₂		0.817	0.77	0.824	0.770		0.572	0.6	0.574	0.641
CuInTe ₂		0.779	0.76	0.842	0.820		0.576	0.57	0.581	0.671
AgAlS ₂		0.848	0.85	0.833	0.770		0.559	0.61	0.557	0.503
AgAlSe ₂		0.851	0.86	0.842	0.820		0.564	0.63	0.563	0.563
AgAlTe ₂		0.853	0.84	0.852	0.862		0.573	0.57	0.575	0.606

Solids	f_i	f_i	f_i	f_i	f_i	f_i	f_i	f_i	f_i	f_i
	[14]	[35,36]	[37]	[34]	[This work]	[14]	[35,36]	[37]	[34]	[This work]
A-C Bond					B-C Bond					
AgGaS ₂	0.867	0.849	0.86	0.835	0.770	0.57	0.559	0.54	0.558	0.563
AgGaSe ₂	0.852	0.851	0.85	0.842	0.820	0.561	0.566	0.54	0.565	0.606
AgGaTe ₂		0.853	0.86	0.851	0.862		0.573	0.51	0.576	0.641
AgInS ₂		0.847	0.85	0.831	0.770		0.569	0.61	0.569	0.606
AgInSe ₂	0.846	0.85	0.85	0.84	0.820	0.604	0.573	0.6	0.575	0.641
AgInTe ₂		0.853	0.84	0.852	0.862		0.578	0.58	0.584	0.671
ZnSiP ₂	0.438	0.493		0.528	0.509	0.117	0.2088		0.197	0.178
ZnGeP ₂	0.442	0.493		0.529	0.509	0.219	0.2112		0.198	0.199
ZnSnP ₂	0.455	0.495		0.53	0.509	0.298	0.2162		0.202	0.214
ZnSiAs ₂	0.436	0.498		0.533	0.554	0.22	0.2122		0.199	0.199
ZnGeAs ₂	0.446	0.499		0.534	0.554	0.182	0.214		0.2	0.214
ZnSnAs ₂	0.45	0.5		0.535	0.554	0.135	0.218		0.203	0.227
CdSiP ₂	0.539	0.502		0.538	0.554	0.191	0.2085		0.197	0.178
CdGeP ₂	0.532	0.502		0.538	0.554	0.231	0.2113		0.198	0.199
CdSnP ₂	0.536	0.504		0.539	0.554	0.298	0.2163		0.202	0.214
CdSiAs ₂	0.553	0.506		0.542	0.589	0.234	0.2202		0.199	0.199
CdGeAs ₂	0.549	0.506		0.542	0.589	0.199	0.2144		0.2	0.214
CdSnAs ₂	0.553	0.501		0.543	0.589	0.148	0.2184		0.203	0.227

Table 4. This table presents the values of electronic susceptibility χ for A-C and B-C bonds of ternary tetrahedral ($A^I B^{III} C_2^{VI}$ and $A^I B^{IV} C_2^{VI}$) semiconductors and plasmon energy $\hbar\omega_p$ are taken from [35,36].

Solids	$\hbar\omega_p$	χ	χ	χ	χ	$\hbar\omega_p$	χ	χ	χ	χ
		[14]	[35]	[34]	[This work]		[14]	[35]	[34]	[This work]
A-C Bond					B-C Bond					
CuAlS ₂	25.110		4.584	4.591	3.765	18.295		4.955	5.997	3.942
CuAlSe ₂	23.231		5.24	4.966	4.511	17.041		5.908	6.347	5.181
CuAlTe ₂	20.859		5.262	5.427	4.676	15.518		7.102	6.92	5.678
CuGaS ₂	23.626	4.43	4.248	4.872	3.333	18.163	6.07	5.485	6.021	5.886
CuGaSe ₂	22.176	5.76	4.838	5.107	4.111	16.906	7.04	6.573	6.471	6.739
CuGaTe ₂	20.703		5.305	5.434	4.607	15.195		7.951	6.971	6.718
CuInS ₂	22.231	5.53	4.824	5.132	2.951	16.453	5.99	6.537	6.57	6.383
CuInSe ₂	23.061		4.607	4.98	4.445	15.489		7.867	6.984	6.981
CuInTe ₂	20.167		6.939	5.588	4.371	14.332		9.114	7.399	7.076
AgAlS ₂	21.536		4.138	5.24	3.877	18.708		4.829	5.929	4.122
AgAlSe ₂	20.090		4.767	5.546	4.338	17.51		5.461	6.241	5.470
AgAlTe ₂	18.681		5.349	5.871	4.584	15.408		7.073	6.937	5.598
AgGaS ₂	21.201	3.68	4.209	5.337	3.757	18.598	5.84	5.338	5.971	6.171
AgGaSe ₂	20.110	4.28	4.762	5.557	4.346	17.193	7.04	6.443	6.348	6.970
AgGaTe ₂	18.905		5.275	5.831	4.695	15.149		7.978	7.044	6.677
AgInS ₂	21.979		4.048	5.19	4.038	16.313		6.601	6.571	6.275
AgInSe ₂	20.513	4.53	4.658	5.51	4.522	15.291	7.41	7.888	6.946	6.803
AgInTe ₂	18.751		5.325	5.915	4.619	13.86		9.494	7.596	6.617
ZnSiP ₂	15.294			5.963	5.575	18.757			11.789	12.562
ZnGeP ₂	15.198			6.036	5.505	17.944			12.283	17.415
ZnSnP ₂	14.907			6.091	5.296	16.203			13.3	18.766
ZnSiAs ₂	14.473			6.242	6.990	17.62			12.414	16.792
ZnGeAs ₂	14.316			6.3	6.839	16.997			12.788	20.651
ZnSnAs ₂	14.094			6.38	6.628	15.524			13.78	21.257

CdSiP ₂	13.659			6.55	6.225		18.845			11.74	12.681
CdGeP ₂	13.675			6.54	6.240		17.905			12.249	17.340
CdSnP ₂	13.446			6.633	6.033		16.194			13.309	18.746
CdSiAs ₂	13.050			6.799	7.306		17.642			12.4	16.834
CdGeAs ₂	13.035			6.805	7.290		16.85			12.88	20.295
CdSnAs ₂	12.831			6.894	7.063		15.388			13.882	20.886

Table 5. This table presents the values of dielectric constant ϵ for A-C and B-C bonds of ternary tetrahedral ($A^I B^{III} C_2^V$ and $A^{II} B^{IV} C_2^V$) semiconductors.

Solids	ϵ	ϵ	ϵ	ϵ	ϵ	ϵ	ϵ	ϵ	ϵ
	[14]	[35,36]	[34]	[This work]	[14]	[35,36]	[34]	[This work]	
	A-C Bond				B-C Bond				
CuAlS ₂			5.591	4.765			6.997	4.942	
CuAlSe ₂			5.966	5.511			7.347	6.181	
CuAlTe ₂			6.427	5.676			7.92	6.678	
CuGaS ₂	5.43		5.872	4.333	7.07		7.021	6.886	
CuGaSe ₂	6.76		6.107	5.111	8.04		7.471	7.739	
CuGaTe ₂			6.434	5.607			7.971	7.718	
CuInS ₂	6.53		6.132	3.951	6.99		7.57	7.383	
CuInSe ₂			5.98	5.445			7.894	7.981	
CuInTe ₂			6.588	5.371			8.399	8.076	
AgAlS ₂			6.24	4.877			6.929	5.122	
AgAlSe ₂			6.546	5.338			7.241	6.470	
AgAlTe ₂			6.871	5.584			7.937	6.598	
AgGaS ₂	4.68		6.337	4.757	6.84		6.971	7.171	
AgGaSe ₂	5.28		6.557	5.346	8.04		7.348	7.970	
AgGaTe ₂			6.831	5.695			8.044	7.677	
AgInS ₂			6.19	5.038			7.571	7.275	
AgInSe ₂	5.53		6.51	5.522	8.41		7.946	7.803	
AgInTe ₂			6.915	5.619			8.596	7.617	
ZnSiP ₂	6.84	6.486	6.963	6.575	10.41	10.931	12.789	13.562	
ZnGeP ₂	6.84	6.526	7.036	6.505	11.55	11.494	13.283	18.415	
ZnSnP ₂	6.84	6.648	7.091	6.296	12.65	12.93	14.3	19.766	
ZnSiAs ₂	7.95	6.839	7.242	7.990	11.8	11.731	13.414	17.792	
ZnGeAs ₂	7.95	6.913	7.3	7.839	14.29	12.223	13.788	21.651	
ZnSnAs ₂	7.95	7.021	7.38	7.628	18.08	13.568	14.78	22.257	
CdSiP ₂	6.99	7.239	7.55	7.225	10.41	10.874	12.74	13.681	
CdGeP ₂	6.99	7.232	7.54	7.240	11.55	11.521	13.249	18.340	
CdSnP ₂	6.99	7.355	7.633	7.033	12.65	12.922	14.309	19.746	
CdSiAs ₂	8.22	7.579	7.799	8.306	11.8	11.603	13.4	17.834	
CdGeAs ₂	8.22	7.588	7.805	8.290	14.29	12.343	13.88	21.295	
CdSnAs ₂	8.22	7.73	7.894	8.063	18.08	13.71	14.882	21.886	

SUMMARY AND CONCLUSION

It is obvious from the results introduced in the tables 1 to 5 that the values obtained for the proposed properties for ternary tetrahedral semiconductors are in close agreement to the values reported so far for the same properties by earlier researchers. So, we draw an inference that average atomic number in addition to product of ionic charges of the elements in a compound plays a vital role in determining the electronic and optical properties of the ternary tetrahedral ($A^I B^{III} C_2^V$ and $A^{II} B^{IV} C_2^V$) compounds. The proposed empirical relations for the ionic gap (E_c) and average energy gap (E_g) have been found inversely related to average atomic number and the product of ionic charges of the elements in the ternary tetrahedral semiconductors. The crystal ionicity (f_i) is directly related to the average atomic number and inversely to the product of ionic charges of the elements in the compound, while the electronic susceptibility (χ) and dielectric constant (ϵ) are directly related to both the criterion. It is noteworthy that the proposed relations are simple and widely applicable and the values obtained for electronic and optical properties are in accordance to the earlier

workers reported. The new idea conceptualized herein will be encouraging to the material scientists for exploring new homologous compounds with desired ionic gap (E_c), average energy gap (E_g), crystal ionicity (f_i), electronic susceptibility (χ) and dielectric constant (ϵ), which may revolutionized modern microelectronic industry.

ORCID IDs

 Rajesh C. Gupta, <https://orcid.org/0000-0002-0560-7077>;  Khushvant Singh, <https://orcid.org/0000-0002-1957-4384>
 Ajay S. Verma, <https://orcid.org/0000-0001-8223-7658>

REFERENCES

- [1] Neeraj, Pravesh, R. Gautam, S. Pal, C. Mohan, S. Kumari, S.R. Bhardwaj, and A.S. Verma, *J. Nanoelectronics and Optoelectronics*, **14**, 759 (2019), <https://doi.org/10.1166/jno.2019.2553>.
- [2] S. Tomar, R. Gautam, Pravesh, C. Mohan, S.K. Gupta, S.R. Bhardwaj, and A.S. Verma, *Chalcogenide Letters*, **16**, 1 (2019), https://chalcogen.ro/1_TomarS.pdf.
- [3] J.L. Shay, and J.H. Wernick, *Ternary Chalcopyrite Semi-conductors: Growth, Electronic Properties and Applications* (Pergamon Press, Oxford, 1975), pp.11, 12 and 73.
- [4] N. Yamamoto, Ph.D. Thesis, University of Osaka, Japan (1976).
- [5] J.E. Jaffe, and A. Zunger, *Phys. Rev. B*, **20**, 1882 (1984), <https://doi.org/10.1103/PhysRevB.29.1882>.
- [6] R. Marquez, and C. Rincon, *Phys. Stat. Sol. (b)*, **191**, 115 (1995), <https://doi.org/10.1002/pssb.2221910112>.
- [7] M.I. Alonso, K. Wakita, J. Pascual, and N. Yamamoto, *Phys. Rev. B*, **63**, 75203 (2001), <https://doi.org/10.1103/PhysRevB.63.075203>.
- [8] Xiaoshu Jiang, and W.R.L. Lambrecht, *Phys. Rev. B*, **69**, 035201 (2004), <https://doi.org/10.1103/PhysRevB.69.035201>.
- [9] F. Chiker, B. Abbar, A. Tadjer, S. Bresson, B. Khelifa, and C. Mathieu, *Physica B*, **349**, 181 (2004), <https://doi.org/10.1016/j.physb.2004.03.087>.
- [10] V. Kumar, and B.S.R. Sastry, *J. Phys. Chem. Solids*, **66**, 99 (2005), <https://doi.org/10.1016/j.jpcs.2004.08.034>.
- [11] A.H. Reshak, *Physica B*, **369**, 243 (2005), <https://doi.org/10.1016/j.physb.2005.08.038>.
- [12] L.K. Samanta, and S. Chatterjee, *Infrared Phys. Technol.* **46**, 370 (2005), <https://doi.org/10.1016/j.infrared.2004.06.009>.
- [13] A. Chahed, O. Benhelal, H. Rozale, S. Laksari, and N. Abbouni, *Phys. Status Solidi B*, **244**, 629 (2007), <https://doi.org/10.1002/pssb.200642050>.
- [14] B.F. Levine, *Phys. Rev. B*, **7**, 2591, 2600 (1973), <https://doi.org/10.1103/PhysRevB.7.2591>.
- [15] J.A. van Vechten, *Phys. Rev.* **182**, 891 (1969), <https://doi.org/10.1103/PhysRev.182.891>.
- [16] J.C. Phillips, and J.A. Van Vechten, *Phys. Rev. B*, **2**, 2147 (1970), <https://doi.org/10.1103/PhysRevB.2.2147>.
- [17] J.C. Phillips, *Rev. Mod. Phys.* **42**, 317 (1970), <https://doi.org/10.1103/RevModPhys.42.317>.
- [18] D.R. Penn, *Phys. Rev.* **128**, 2093 (1962), <https://doi.org/10.1103/PhysRev.128.2093>.
- [19] O.P. Singh, and V.P. Gupta, *Phys. Stat. Sol. (b)*, **137**, 97 (1986), <https://doi.org/10.1002/pssb.2221370112>.
- [20] V. Kumar, and G.M. Prasad, *J. Phys. Chem. Solids*, **50**, 899 (1989), [https://doi.org/10.1016/0022-3697\(89\)90037-1](https://doi.org/10.1016/0022-3697(89)90037-1).
- [21] V. Kumar Srivastava, *J. Phys. C: Solid State Phys.* **19**, 5689 (1986), <https://doi.org/10.1088/0022-3719/19/28/019>.
- [22] V. Kumar Srivastava, *Phys. Rev. B*, **29**, 6993 (1984), <https://doi.org/10.1103/PhysRevB.29.6993>.
- [23] A.S. Verma, *Solid State Commun.* **149**, 1236 (2009), <https://doi.org/10.1016/j.ssc.2009.04.011>.
- [24] L. Pauling, *The Nature of Chemical Bond* (Ithaca, NY: Cornell University Press, 1906).
- [25] L. Marton, L.B. Leder, and H. Mendlowitz, in: *Advances in Electronics and Electron Physics, Vol. 7*, edited by L. Marton (Academic Press, New York, 1955), p. 225.
- [26] H.R. Philipp, and H. Ehrenreich, *Phys. Rev.* **129**, 1530 (1963), <https://doi.org/10.1103/PhysRev.129.1550>.
- [27] H. Raether, *Ergeb. Exakten Naturwiss. (Germany)* **38**, 84 (1965).
- [28] C. Kittel, *Introduction to Solid State Physics*, 4th ed. (Wiley, New York, 1971), (Second Wiley Eastern Re-print, New Delhi, 1974), pp. 227.
- [29] J.C. Phillips, *Bonds and Bands in Semiconductors* (Academic Press, New York, 1973).
- [30] O.P. Singh, and V.P. Gupta, *Phys. Status Solidi (b)*, **129**, K153, (1985).
- [31] A. Jayaraman, B. Batlogg, R.G. Maines, and H. Bach, *Phys. Rev. B*, **26**, 3347 (1982), <https://doi.org/10.1103/PhysRevB.26.3347>.
- [32] D.B. Srideshmukh, and K.G. Subhadra, *J. Appl. Phys.* **59**, 276 (1986), <https://doi.org/10.1063/1.336826>.
- [33] K.S. Krishnan, and S.K. Roy, *Proc. R. Soc. London*, **210**, 481 (1952), <https://doi.org/10.1098/rspa.1952.0014>.
- [34] A.S. Verma, and S.R. Bhardwaj, *Phys. Stat. Sol. (b)*, **243**, 4025 (2006), <https://doi.org/10.1002/pssb.200642229>.
- [35] V. Kumar, *J. Phys. Chem. Solids*, **48**, 827 (1987), [https://doi.org/10.1016/0022-3697\(87\)90033-3](https://doi.org/10.1016/0022-3697(87)90033-3).
- [36] V. Kumar Srivastava, *Phys. Rev. B*, **36**, 5044 (1987), <https://doi.org/10.1103/PhysRevB.36.5044>.
- [37] H. Neumann, *Cryst. Res. Technol.* **18**, 1299, 1391, 665, 901 (1983), <https://doi.org/10.1002/crat.2170181016>.

ОПТОЕЛЕКТРОННІ ВЛАСТИВОСТІ ПОТРІЙНИХ ТЕТРАЕДРИЧНИХ НАПІВПРОВІДНИКІВ

Р.С. Гупта^a, А.С. Верма^b, К. Сінгх^a^aФізичний факультет, коледж Б.С.А., Матхура, 281004 (Індія)^bФакультет природничих та прикладних наук, Школа технологій, Університет Глокал, Сахаранпур 247121 (Індія)

Діелектрична інтерпретація іонності кристалів, розроблена Філіпсом та Ван Вехтенем (P.V.V), була використана для оцінки різних властивостей основного стану для широкого спектра напівпровідників та ізоляторів. Однак актуальність теорії діелектриків P.V.V. обмежена лише простими структурованими сполуками $A^N B^{8-N}$, які мають певний зв'язок. Левін розширив P.V.V. теорію іонності для кристалів з багатьма зв'язками та комплексних кристалів та оцінив багато параметрів зв'язку для потрійних тетраедричних напівпровідників. Деякі інші дослідники розширили роботу Левіна за допомогою концепції іонного заряду та відстані до найближчого оточення на бінарні та потрійні тетраедричні кристали для оцінки властивостей основного стану. У цій роботі для розуміння деяких електронних та оптичних властивостей, таких як іонний зазор (E_c), середня енергетична щільність (E_g), іонність кристалів (f_i), електронна сприйнятливість (χ) та діелектрична проникність (ϵ) потрійних чотиригранних напівпровідників ($A^{IV} B^V C_2^V$ and $A^{IV} B^{III} C_2^{VI}$) була використана нова гіпотеза середнього атомного числа елементів у сполуках. Відмічається досить прийнятна відповідність оцінених значень з оцінками зробленими іншими іншими дослідниками.

КЛЮЧОВІ СЛОВА: іонність кристалів, середній атомний номер, халькопірити

PACS: 71.15.Mb; 71.20.-b; 71.55.Ak

EMPIRICAL RELATION FOR ELECTRONIC AND OPTICAL PROPERTIES OF BINARY TETRAHEDRAL SEMICONDUCTORS

 **Rajesh C. Gupta**^a,  **Khushvant Singh**^a,  **Ajay S. Verma**^{b,*}

^aDepartment of Physics, B. S. A. College, Mathura 281004 (India)

^bDepartment of Natural and Applied Sciences, School of Technology, Glocal University, Saharanpur 247121 (India)

*Corresponding Author: ajay_phy@rediffmail.com

Received December 13, 2020; revised February 19, 2021; accepted February 20, 2021

The concept of ionicity developed by Phillips and Van Vechten originated from the dielectric analysis of the semiconductors and insulators have been used to evaluate various bond parameters of binary tetrahedral ($A^{II}B^{VI}$ and $A^{III}B^V$) semiconductors. An overview of the understanding of correlation between atomic number and the opto-electronic properties of zinc blende crystal structured solids is presented here. In this paper, an advance hypothesis of average atomic number of the elements in a compound has been used to evaluate intrinsic electronic and optical parameters such as ionic gap (E_c), average energy gap (E_g), crystal ionicity (f_i) and dielectric constant (ϵ) of binary tetrahedral semiconductors.

KEYWORDS: Ionicity; atomic number; zinc blende; energy gap

The largest part of modern technology on the earth is based on solid state materials. Ample research dedicated to the physics and chemistry of solids during the past four decades has produced sizeable breakthroughs in comprehending the properties of solids as a whole. So, it is captivating to go through the behaviour and various properties of other solids. The modern microelectronic industry uses the semiconductors of particular omnitriangular nature in zinc blende crystallographic structure. This nature gives rise to unique physical properties in materials. A great amount of theoretical and experimental work has been completed in recent past on mechanical, structural and optical properties of zinc blende ($A^{III}B^V$ and $A^{II}B^{VI}$) semiconductors [1-7]. It is due to their exciting semiconducting properties and various practical applications in the area of non-linear optical laser devices, photovoltaic detectors, light emitting diodes, solar cells, and integrated optical devices such as switches, filters and modulators. The hypothesis of crystal ionicity of chemical bonding has been demonstrated its potential in the characterization of molecular and solid state properties. This proposed various ionicity scales to associate with a broad spectrum of physical and chemical properties such as cohesive energy, elastic constants, heat of formation, crystal structure, bulk modulus etc [8]. Levine [8], Phillips and Van Vechten [9-11], and many more researchers [12-16] have evolved several theories and evaluated ionicity in the case of basic compounds.

Because of the trouble related to the experimental procedure and its price, also complications in getting correct values of physical properties, researchers moved to evaluating the physical properties of solids by means of theoretical methods. But owing to the elaborated process, as well difficult computational methods require a sequence of approximation; these methods have always been complex and developed for only limited semiconductors [17]. Consequently, we realized it would be of immense interest to present an another possible interpretation of the ionic gap (E_c), average energy gap (E_g), crystal ionicity (f_i) and dielectric constant (ϵ) in binary tetrahedral ($A^{II}B^{VI}$ and $A^{III}B^V$) semiconductors.

Numerous researchers have attempted to evaluate electronic and optical parameters of binary tetrahedral semiconductors with the help of ionic charge and valance electrons. But considering the different screening factors present in compound crystallography, we have used a new concept of average atomic number of interacting elements in a compound and found excellent results comparable to previous workers for the ionic gap (E_c), average energy gap (E_g), crystal ionicity (f_i) and dielectric constant (ϵ) in binary tetrahedral ($A^{II}B^{VI}$ and $A^{III}B^V$) semiconductors. In our suggested relations only few variables such as atomic number and ionic charge on cation and anion are needed as input data, to calculate many electronic and optical properties of these compounds and the method emerge relevant to other materials, too.

THEORY, RESULTS AND DISCUSSION

As stated in modified theory of dielectric of solids [9-11, 18-20] for tetrahedral coordinated compounds, average energy gap (E_g), connected bonding and anti binding (sp^3) hybridized orbital can be separated into two shares due to symmetric and anti symmetric portions of the potential inside a unit cell. These shares are ionic or heteropolar (E_c) and covalent or homopolar (E_h), which can be expressed in the following relation:

$$E_g^2 = E_c^2 + E_h^2 \quad (1)$$

The ionic or heteropolar share E_c is inversely related to the bond length d as:

$$E_c = K_1 d^{-1} e^{-K_s r_0} \quad (2)$$

where K_1 is an arbitrary constant and depends on the difference between valence states of an atom and is given by $K_1 = bc^2 \Delta z$, where prescreening factor b depends on the coordination number [21] around the cation i.e. $b = 0.089 N_C^2$, here

N_c is average coordination number and c-electronic charge, $\Delta z = 4$ for IIB chalcogenides. The values of $N_c = 4$, $b=1.424$ and hence $K_1 = 262.784$ are for zinc blende type structure. Thomas-Fermi screening parameter K_s has been ascertained taking into account eight electrons per molecule (two for Zn, Cd & Hg and six for O, S, Se & Te) and $r_0 = d/2$.

The covalent or homopolar share E_h is related to the bond length d as:

$$E_h = Ad^{-K_2} \tag{3}$$

where A and K_2 are constants, which remain unaffected in different crystal structures with values $A = 40.468 \text{ eV/\AA}^{2.5}$ and $K_1 = 2.5$. These values are $A= 39.74$ and $K_1 = 2.48$ as reported by PVV [10]. Therefore, the values of E_c and E_h depend on number of bonds emerge from cations and bond length.

The crystal ionicity f_i of the chemical bond is expressed as the fraction of ionic character as follows.

$$f_i = E_c^2/E_g^2 \tag{4}$$

V. Kumar [22-24] has expressed those electronic properties of zinc blende ($A^{II}B^{VI}$ and $A^{III}B^V$) crystals in terms of Plasmon energy $\hbar\omega_p$ as follows:

$$E_h \text{ (eV)} = 0.04584(\hbar\omega_p)^v, \tag{5}$$

$$E_c \text{ (eV)} = 10.722(\hbar\omega_p)^{2/3} \times \exp[-6.2554(\hbar\omega_p)^{-1/3}] \tag{6}$$

Here $\hbar\omega_p$ is in eV, v is a constant. E_c and E_h are the ionic and homopolar gaps, respectively.

Jayaraman et al. [25], Srideshmukh et al. [26], and Krishnan et al. [27] established that significantly reduced ionic charges must be used to obtain better agreement with experimental values of these parameters. Verma et al. [28] have been applied this concept for obtaining better agreement with theoretical data for ionic gap (E_c), average energy gap (E_g), crystal ionicity (f_i) and dielectric constant (ϵ) of binary tetrahedral ($A^{II}B^{VI}$ and $A^{III}B^V$) semiconductor, which can be expressed in terms of product of ionic charges as follows:

For binary tetrahedral (zinc blende) semiconductors:

$$E_c = 90 d^2 / (Z_1 Z_2)^{0.7} \text{ eV}, \tag{7}$$

$$E_g = 90 d^{2.12} / (Z_1 Z_2)^{0.5} \text{ eV} \tag{8}$$

Here, Z_1 and Z_2 are the ionic charges and d is the bond length in Å. On solving equations (2) and (7, 8), crystal ionicity f_i can be expressed as follows:

$$f_i = 0.87891 d^{0.24} / (Z_1 Z_2)^{0.4} \tag{9}$$

Levine and Penn [8, 29] have given the relation for dielectric constant ϵ as follows:

$$\epsilon = 1 + (\hbar\omega_p)^2 / (E_g)^2 \tag{10}$$

Considering the above empirical relations and using the concept of product of ionic charges given by Verma et al. [28] and our hypothesis of average atomic number of elements in the binary tetrahedral semiconductor, we have proposed following empirical relations for electronic and optical parameters such as ionic gap (E_c), average energy gap (E_g), crystal ionicity (f_i) and dielectric constant (ϵ) and further evaluated their values. The evaluated values are in excellent agreement with the values reported by Levine [8], V. Kumar [22-24]. Our endeavour of determining ionic gap E_c , average energy gap E_g , crystal ionicity f_i , and dielectric constant ϵ has not been required experimental values of the dielectric constant although the previous models needed this value in their computations except Verma et al. [28]. These values are presented in the table 1 and 2.

$$E_c = 65 / (Z_1 Z_2)^{0.8} \left(\frac{a_{Z1} + a_{Z2}}{2} \right)^{0.6}, \tag{11}$$

$$E_g = 91 / (Z_1 Z_2)^{0.6} \left(\frac{a_{Z1} + a_{Z2}}{2} \right)^{0.5}, \tag{12}$$

$$f_i = 1.6 \left(\frac{a_{Z1} + a_{Z2}}{2} \right)^{0.25} / (Z_1 Z_2)^{0.25}, \tag{13}$$

We have found dielectric constant (ϵ) same as given in relation (10). Here, Z_1, Z_2 are ionic charges and a_{Z1}, a_{Z2} are atomic numbers of the elements in the compound.

Table 1. This table presents the values of ionic gap E_c and average energy gap E_g of binary tetrahedral semiconductors.

Solids	a_{z1}	a_{z2}	E_c [8]	E_c [24,30]	E_c [28]	E_c [This work]	E_g [8]	E_g [24,30]	E_g [28]	E_g [This work]
AIP	13	15	3.76	3.31	3.47	4.00	6.04		5.18	6.50
AlAs	13	33	3.82	3.36	3.27	3.29	5.81		4.87	5.07
AlSb	13	51	3.08	2.71	2.73	2.90	4.68		4.02	4.30
GaP	31	15	3.3	2.9	3.47	3.29	5.76		5.18	5.07

Solids	a_{z1}	a_{z2}	E_c [8]	E_c [24,30]	E_c [28]	E_c [This work]	E_g [8]	E_g [24,30]	E_g [28]	E_g [This work]
GaAs	31	33	2.92	2.51	3.22	2.90	5.21		4.79	4.30
GaSb	31	51	2.13	1.87	2.75	2.63	4.14		4.05	3.80
InP	49	15	3.35	2.95	3.0	2.90	5.16		4.44	4.30
InAs	49	33	2.74	2.41	2.84	2.63	4.58		4.19	3.80
InSb	49	51	2.15	1.89	2.45	2.43	3.76		3.58	3.44
ZnS	30	16	6.16	6.05	6.23	6.31	7.82	7.73	7.92	8.25
ZnSe	30	34	5.51	5.57	5.64	5.55	6.98	7.09	7.12	7.00
ZnTe	30	52	4.38	4.54	4.89	5.03	5.66	5.75	6.13	6.18
CdS	48	16	5.78	5.1	5.29	5.55	7.01	6.47	6.65	7.00
CdSe	48	34	5.31		4.97	5.03	6.42		6.23	6.18
CdTe	48	52	4.43	4.19	4.32	4.66	5.40	5.29	5.37	5.60
HgS	80	16		5.08	5.33	4.73		6.45	6.71	5.71
HgSe	80	34		4.14	4.93	4.43		5.22	6.18	5.24
HgTe	80	52			3.97	4.18			4.92	4.87

Table 2. This table presents the values of dielectric constant ϵ and crystal ionicity f_i of the binary tetrahedral semiconductors.

Solids	a_{z1}	a_{z2}	$h\omega_p$ [32]	ϵ [5]	ϵ [31]	ϵ [28]	ϵ [This work]	f_i [8]	f_i [24]	f_i [28]	f_i [This work]
GaP	31	15	16.8	9.495	9.11	11.52	11.95	0.328	0.325 ^d	0.449	0.379
GaAs	31	33	16	12.302	10.88	12.16	14.82	0.315	0.303 ^d	0.453	0.394
GaSb	31	51	14.9		14.44	14.53	16.35	0.265	0.264 ^d	0.461	0.404
InP	49	15	13.9	9.706	9.61	10.8	11.43	0.421	0.419 ^d	0.457	0.394
InAs	49	33	13.7	13.55	12.03	11.69	13.98	0.359	0.357 ^d	0.46	0.404
InSb	49	51	13.2		15.68	14.6	15.69	0.329	0.327 ^d	0.468	0.413
ZnS	30	16	16.68 ^b	5.7 ^c	5.2 ^a	5.44	5.08	0.621	0.613	0.619	0.593
ZnSe	30	34	15.78 ^b	5.9 ^c	6 ^a	5.91	6.08	0.623	0.617	0.627	0.615
ZnTe	30	52	13.8 ^b	6.7 ^c	7.28	6.07	5.98	0.599	0.626	0.637	0.632
CdS	48	16	14.87 ^b		5.3 ^a	6	5.51	0.679	0.621	0.631	0.615
CdTe	48	52	13.09 ^b		7.21	6.94	6.46	0.675	0.629	0.647	0.646
HgS	80	16	14.85 ^b			5.9	7.75		0.622	0.631	0.643
HgSe	80	34	12.98 ^b			5.41	7.12		0.629	0.637	0.655

^aRef. [8], ^bRef. [24], ^cRef. [33], ^dRef. [30]

SUMMARY AND CONCLUSIONS

The suggested empirical relations have been applied to calculate ionic gap E_c , average energy gap E_g , crystal ionicity f_i , and dielectric constant ϵ of binary tetrahedral ($A^{II}B^{VI}$ and $A^{III}B^V$) semiconductors. This shows average atomic number of the elements in the compounds is a crucial parameter for evaluating electronic and optical properties. The ionic gap (E_c) and average energy gap (E_g) of these compounds have been found inversely proportional to the average atomic number and product of ionic charges of the compounds. The crystal ionicity (f_i) is directly related to average atomic number and inversely to product of ionic charges, while dielectric constant (ϵ) is directly related to both the parameters. This is interesting to note that the suggested relations are straightforward, extensively relevant and values obtained are in good agreement with published values as compared to earlier workers. The hypothesis proposed herein will be supportive to the researchers for exploring new analogous materials with aimed ionic gap (E_c), average energy gap (E_g), crystal ionicity (f_i) and dielectric constant (ϵ). Arguably this hypothesis may easily be broadened to ternary tetrahedral semiconductors, for which work in progression out comes will be revealed in expected paper.

ORCID IDs

 **Rajesh C. Gupta**, <https://orcid.org/0000-0002-0560-7077>;  **Khushvant Singh**, <https://orcid.org/0000-0002-1957-4384>
 **Ajay S. Verma**, <https://orcid.org/0000-0001-8223-7658>

REFERENCES

- [1] M.B. Kanoun, S. Goumri-Said, A.E. Merad, G. Merad, J. Ciberti, and H. Aourang, *Semicond. Sci. Technol.* **19**, 1220 (2004), <https://doi.org/10.1088/0268-1242/19/11/002>.
- [2] S.Q. Wang, H.Q. Ye, *J. Phys.: Condens. Matter*, **17**, 4475 (2005), <https://doi.org/10.1088/0953-8984/17/28/007>.
- [3] V. Kumar, and B.S.R. Sastry, *J. Phys. Chem. Solids* **66**, 99-102 (2005), <https://doi.org/10.1016/j.jpcs.2004.08.034>.
- [4] N. Guezmir, J. Ouerfelli, and S. Belgacem, *Mater. Chem. Phys.* **96**, 116 (2006), <https://doi.org/10.1016/j.matchemphys.2005.06.059>.
- [5] M.S. Omar, *Mater. Res. Bull.* **42**, 961 (2007), <https://doi.org/10.1016/j.materresbull.2006.08.008>.
- [6] A.E. Merad, M.B. Kanoun, G. Merad, J. Ciberti, and H. Aourag, *Mater. Chem. Phys.* **92**, 333 (2005), <https://doi.org/10.1016/j.matchemphys.2004.10.031>.

- [7] H.M. Tutuncu, S. Bagci, G.P. Srivastava, A.T. Albudak, and G. Ugur, Phys. Rev. B, **71**, 195309 (2005), <https://doi.org/10.1103/PhysRevB.71.195309>.
- [8] B.F. Levine, Phys. Rev. B, **7**, 2591 (1973), <https://doi.org/10.1103/PhysRevB.7.2591>.
- [9] J.A. Van Vecheten, Phys. Rev. B, **1**, 3351 (1970), <https://doi.org/10.1103/PhysRevB.1.3351>.
- [10] J.C. Phillips and Van Vecheten, Phys. Rev. B, **2**, 2147 (1970), <https://doi.org/10.1103/PhysRevB.2.2147>.
- [11] J.C. Phillips, *Bonds and Bands in Semiconductors* (Academic Press, New York, (1973).
- [12] A.C. Sharma, and S. Auluck, Phys. Rev. B, **28**, 965 (1983), <https://doi.org/10.1103/PhysRevB.28.965>.
- [13] P.R. Sarode, Phys. Stat. Sol. (b), **88**, K35 (1978), <https://doi.org/10.1002/pssb.2220880152>.
- [14] A. Garcia, and M.L. Cohen, Phys. Rev. B, **47**, 4215 (1993), <https://doi.org/10.1103/PhysRevB.47.4215>.
- [15] D.R. Penn, Phys. Rev. **128**, 2093 (1962), <https://doi.org/10.1103/PhysRev.128.2093>.
- [16] M. Ferhat, A. Zaoui, M. Certier, and B. Khelifa, Phys. Stat. Sol. (b), **195**, 415 (1996), <https://doi.org/10.1002/pssb.2221950210>.
- [17] A.S. Verma, Solid State Commun. **149**, 1236 (2009), <https://doi.org/10.1016/j.ssc.2009.04.011>.
- [18] O.P. Singh, and V.P. Gupta, Phys. Status Solidi (b), **129**, K153, (1985).
- [19] O.P. Singh, and V. Gupta, Phys. Status Solidi (b), **137**, 97 (1986).
- [20] D.V. Singh, and V.P. Gupta, Phys. Status Solidi (b), **171**, K71, (1992).
- [21] B.F. Levine, Phys. Rev. B, **7**, 2600 (1973), <https://doi.org/10.1103/PhysRevB.7.2600>.
- [22] V. Kumar Srivastava, Phys. Rev. B, **36**, 5044 (1987), <https://doi.org/10.1103/PhysRevB.36.5044>.
- [23] V. Kumar, J. Phys. Chem. Solids, **48**, 827 (1987), [https://doi.org/10.1016/0022-3697\(87\)90033-3](https://doi.org/10.1016/0022-3697(87)90033-3).
- [24] V. Kumar Srivastava, J. Phys. C, Solid State Phys. **19**, 5689 (1986), <https://doi.org/10.1088/0022-3719/19/28/019>.
- [25] A. Jayaraman, B. Batlogg, R.G. Maines, and H. Bach, Phys. Rev. B, **26**, 3347 (1982), <https://doi.org/10.1103/PhysRevB.26.3347>.
- [26] D.B. Srideshmukh, and K.G. Subhadra, J. Appl. Phys. **59**, 276 (1986), <https://doi.org/10.1063/1.336826>.
- [27] K.S. Krishnan, and S.K. Roy, Proc. R. Soc. London, **210**, 481 (1952), <https://doi.org/10.1098/rspa.1952.0014>.
- [28] A.S. Verma, and S.R. Bhardwaj, Phys. Stat. Sol. (b), **243**, 4025 (2006), <https://doi.org/10.1002/pssb.200642229>.
- [29] D.R. Penn, Phys. Rev. **128**, 2093 (1962), <https://doi.org/10.1103/PhysRev.128.2093>.
- [30] W.K. Kucharczyk, Phys. Stat. Sol. (b), **180**, K27 (1993), <https://doi.org/10.1002/pssb.2221800133>.
- [31] B.R. Nag, Appl. Phys. Lett. **65**, 1938 (1994), <https://doi.org/10.1063/1.112823>.
- [32] S. Sen, D.N. Bose, and M.S. Hegde, Phys. Stat. Sol. (b), **129**, K65 (1985), <https://doi.org/10.1002/pssb.2221290162>.
- [33] S.V. Adhyapak, S.M. Kanetkar, and A.S. Nigavekar, Nuovo Cimento, **35**, B179 (1976).

ЕМПІРИЧНЕ СПІВВІДНОШЕННЯ ЕЛЕКТРОННИХ ТА ОПТИЧНИХ ВЛАСТИВОСТЕЙ БІНАРНИХ ТЕТРАЕДРИЧНИХ НАПІВПРОВІДНИКІВ

Раджеш С. Гупта^a, Хушвант Сінгх^a, Аджай С. Верма^b

^aФізичний факультет, В.С.А. коледж, Матура 281004 (Індія)

^bФакультет природничих та прикладних наук, Школа технологій, Глокальний університет, Сахаранпур 247121 (Індія)

Концепція іонності, розроблена Філіпсом та Ван Вехтенем, виникла в результаті діелектричного аналізу напівпровідників, а ізолятори використовувались для оцінки різних параметрів зв'язку двійкових чотиригранних напівпровідників (АІВVI та АІВV). Тут представлений огляд розуміння кореляції між атомним номером та оптоелектронними властивостями твердих кристалів із змішаною кристалічною структурою цинку. У цій роботі попередня гіпотеза середнього атомного числа елементів у сполуці була використана для оцінки власних електронних та оптичних параметрів, таких як іонна щільність (E_c), середня заборонена зона (E_g), іонність кристалів (f_i) та діелектрична проникність (ϵ) подвійних тетраедричних напівпровідників.

КЛЮЧОВІ СЛОВА: іонність; атомний номер; цинкова обманка; заборонена зона

PACS: 71.15.Mb, 71.20.-b, 71.20

STUDY OF STRUCTURAL AND ELECTRONIC PROPERTIES OF INTERCALATED TRANSITION METAL DICHALCOGENIDES COMPOUND MTiS_2 ($M = \text{Cr, Mn, Fe}$) BY DENSITY FUNCTIONAL THEORY

Vandana B. Parmar[†],  Aditya M. Vora*

Department of Physics, University School of Sciences, Gujarat University, Navrangpura
Ahmedabad 380 009, Gujarat, India

*Corresponding Author: voraam@gmail.com

[†]E-mail: vandanaparmar3996@gmail.com

Received December 31, 2020; accepted February 26, 2021

In the present work, we have studied intercalated Transition Metal Dichalcogenides (TMDC) MTiS_2 compounds ($M = \text{Cr, Mn, Fe}$) by Density Functional Theory (DFT) with Generalized Gradient Approximation (GGA). We have computed the structural and electronic properties by using first principle method in QUANTUM ESPRESSO computational code with an ultra-soft pseudopotential. A guest 3d transition metal M (viz; Cr, Mn, Fe) can be easily intercalated in pure transition metal dichalcogenides compound like TiS_2 . In the present work, the structural optimization, electronic properties like the energy band structure, density of states (DoS), partial or projected density of states (PDoS) and total density of states (TDoS) are reported. The energy band structure of MTiS_2 compound has been found overlapping energy bands in the Fermi region. We conclude that the TiS_2 intercalated compound has a small band gap while the doped compound with guest 3d-atom has metallic behavior as shown from its overlapped band structure.

KEYWORDS:—Density Functional Theory (DFT), Transition metal dichalcogenide compounds (TMDCs), Generalized Gradient Approximation (GGA), Quantum ESPRESSO code, Intercalated compound, ultra-soft pseudopotential.

During several years, the Transition Metal Dichalcogenides (TMDC) materials of group IV-b, V-b and VI-b have received significant consideration because of their uses particularly as electrodes in photoelectrochemical (PEC) solar cell for conversion of solar energy into electrical energy as well as photonic devices in numerous electronic applications. We have work on MTiS_2 intercalated compound [1]. While, different atoms may be intercalated into van der Waal's gap with TMDC TX_2 ($T = \text{group IV, V, VI transition metal, X = S, Se, Te}$) compounds and a great deal of effort has been made to obtain new functional content. In TiS_2 , Ti has a sandwiched layer between two Sulphur layers with very weak van der Waal's force. Because of such weak attraction between interlayer, a guest 3d atom can be easily intercalated in the TMDC TiS_2 [2]. The effect of charge transfer from guest 3d-transition metal to self-intercalated compound TiS_2 has been studied by Kim *et al.* [3]. Also, based on self-consistent APW method the d-orbitals of intercalant M atoms hybridize strongly with p-orbitals of 'S' in such a way that the Ti-S bonds become weaker than the M-S bonds [4, 5]. Therefore, the M-S bonds are much stronger than Ti-S bonds [5]. Also, a strong hybridization takes place in the states like 3d states of M , 3d-states of Ti and 3p-states of S [6-8]. However, the TiS_2 has a very small indirect bandgap as a semiconductor [4]. Also, in the band structure of MTiS_2 , the energy band lines are overlapped near at the Fermi region.

The Density Functional Theory (DFT) based formulation is commonly used for investigating the structural and electronic properties of the materials and found successful [9-12]. The molecular-orbital (MO) method is found useful to examine the nature of chemical bonding in intercalated MTiS_2 compound [3]. The intercalates MTiS_2 ($M = \text{Cr, Mn, Fe}$) compounds depending on the guest atom M (viz; Cr, Mn, Fe), which are supported by various experimental techniques such as X-Ray photoemission spectroscopy (XPS), Angle Resolved Resonant Photoemission Spectroscopy (ARPES), Angle Resolved Inverse Photoemission Spectroscopy (ARIPES) and high field magnetization measurements [13,14].

Very recently, Sharma *et al.* [6] have reported transport properties and electronic structure of intercalated compounds CrTiS_2 by employing full potential linearized augmented plane wave (LAPW) with local orbitals (LO) method, in the outline of DFT with Generalized Gradient Approximations (GGA) [15] under Wien2K code [16] environment. They have constrained their studies up to band structure, density of states (DOS), charge density and specific heat calculations only. But, they have not reported theoretical fallouts of MnTiS_2 and FeTiS_2 compounds in their research work thoroughly. Also, they concluded that all CrTiS_2 , MnTiS_2 and FeTiS_2 compounds have same electronic band structure and DOS. However, all above mentioned materials have different band structure and DOS.

Hence, looking to the technological aspects of the said materials, we though it undertakes in the present work, the structural optimization and electronic properties like energy band structure, density of states (DOS), partial or projected density of states (PDOS), total density of states (TDOS) of MTiS_2 compounds using GGA [15] with Perdew-Burke-Ernzerhof (PBE) exchange and correlation effect [17] and ultra-soft pseudopotential [18] through Quantum ESPRESSO code [19] under DFT environment. The prime novelty of our current work is that, we have compared our computed results of the studied materials and their properties after and before the interaction process, which gives us good assessments and nature of aforementioned materials briefly.

COMPUTATIONAL METHODOLOGY

All the calculations are performed in our computational laboratory based on density functional theory (DFT) of intercalated compound $MTiS_2$ by solving Kohn-Sham equations [20] with Burai software [21]. Here, we have adopted Generalized Gradient Approximations (GGA) with Perdew-Burke-Ernzerhof (PBE) exchange and correlation effect [17] and ultra-soft pseudopotential [18] through Quantum ESPRESSO code [19]. The structural optimization and the electronic properties such as band structure, density of states (DOS), partial density of states (PDOS) and total density of states (TDOS) are reported for intercalated $MTiS_2$ compound.

RESULT AND DISCUSSION

Structural Optimization

The $MTiS_2$ has the CdI_2 -type layer structure, in which, Ti layer is inserted among two Sulfur layers. In this structure, the unit cell of it comprises four atoms with the unit cell positioned for Ti is a 1a; the two S atoms are positioned in 2d ($1/3, 1/3, 0.2501$) and ($2/3, 1/3, -0.2501$), respectively. The structure consists of S-Ti-S sandwich, separated in Z-direction by the van der Waals gap [22]. In very weak van der Waals attraction between the Ti and S layers, guest 3d atom like Cr, Mn and Fe can be easily intercalated in pure TiS_2 . In the $MTiS_2$ atom, the lattice position is 1b ($0, 0, 0.5$) in the structure and also has a hexagonal crystal structure with space group $P\bar{3}m1$ [164] as shown in Fig. (1), (2) and (3). In $MTiS_2$ has the lattice parameters $a = 3.4395\text{\AA}$ and $c = 5.9303\text{\AA}$. The Brillouin zone (BZ) for hexagonal structure is shown in Fig. (4).

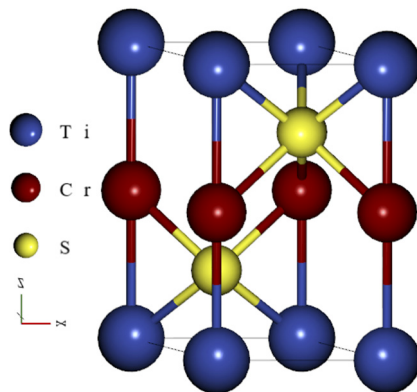


Figure 1. Crystal structure of $CrTiS_2$

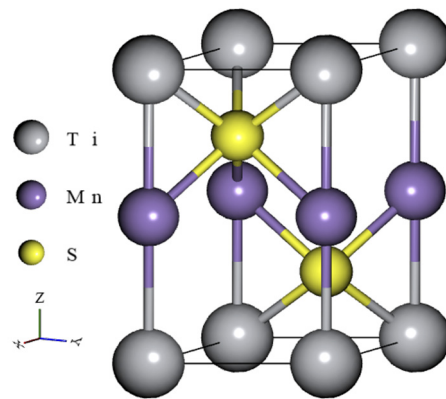


Figure 2. Crystal structure of $MnTiS_2$

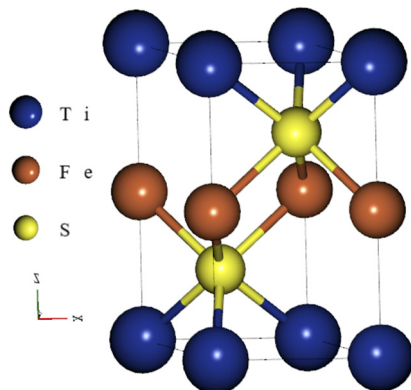
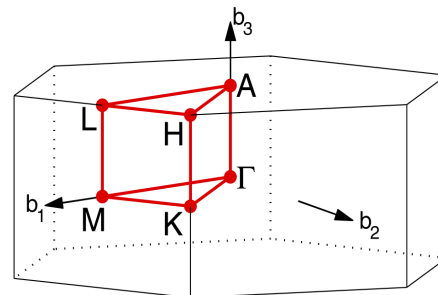


Figure 3. Crystal Structure of $FeTiS_2$



HEX path: Γ -M-K- Γ -A-L-H-A|L-M|K-H

Figure 4. Brillouin zone for Hexagonal structure

Electronic properties

In electronic properties, the energy band structure, density of states (DOS), total density of states (TDOS) and partial or projected density of states (PDOS) are computed and studied.

Band Structure

In the energy band structure calculation, the path of k -points is considered at the high symmetry path viz; $\Gamma \rightarrow M \rightarrow K \rightarrow \Gamma \rightarrow A \rightarrow L \rightarrow H \rightarrow A$ in irreducible Brillouin zone (IBZ). The Band structures of the said materials are plotted in the energy range of -10.0 eV to 10.0 eV. Also, we have calculated the energy band structure with spin polarized calculation of said material with spin up and spin down band structure as shown in the same figure.

In Fig. (5) and (6) shows the electronic band structure of $CrTiS_2$ compound with spin up and spin down configuration for taking K path is $\Gamma \rightarrow M \rightarrow K \rightarrow \Gamma \rightarrow A \rightarrow L \rightarrow H \rightarrow A$. The valance band and the conduction band are overlapped in the

energy range of -5.0 eV to 5.0 eV. From that, we have concluded that the intercalated compound like CrTiS_2 has a metallic characteristic. Here, the maximum band is overlapped at the Fermi level. According to the spin up and spin down band structure of CrTiS_2 , the paramagnetic nature of the studied compound successfully observed.

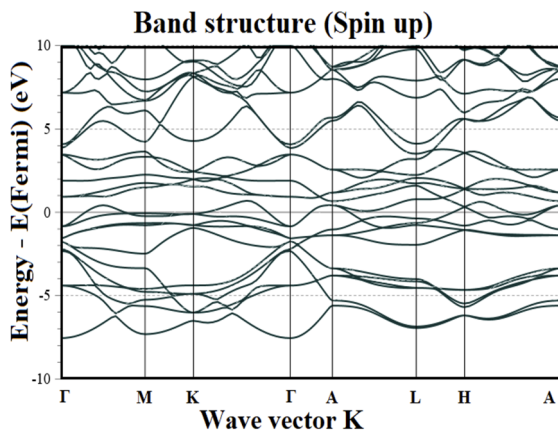


Figure 5. Electronic band structure of CrTiS_2 Spin up

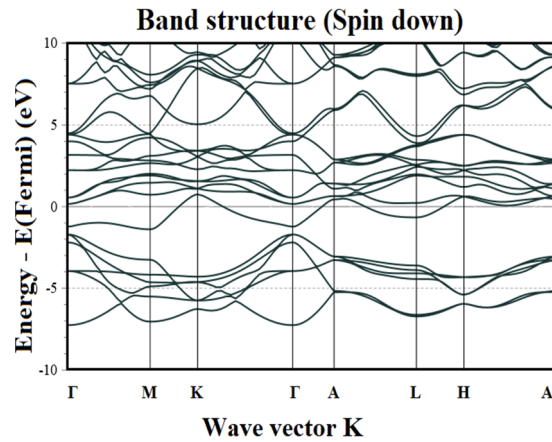


Figure 6. Electronic band structure of CrTiS_2 Spin down

Fig. (7) and (8) shows the electronic band structure with spin up and spin down configuration for MnTiS_2 compound for K path taking is $\Gamma \rightarrow \text{M} \rightarrow \text{K} \rightarrow \Gamma \rightarrow \text{A}$. The valance band and the conduction bands are overlapped in the energy range between -5.0 eV to 5.0 eV. In MnTiS_2 , the energy band lines are overlapped more than that of the CrTiS_2 material. From that, we have concluded that the intercalated compound like MnTiS_2 has a metallic characteristic. Here also, one can observe the maximum band is overlapped at the Fermi level. According to the spin up and spin down band structure of MnTiS_2 , it is having a paramagnetic material in nature.

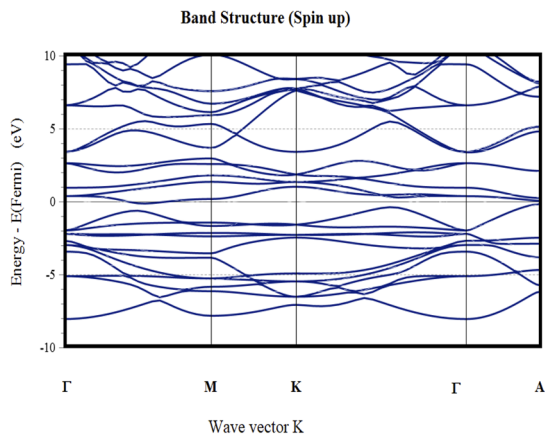


Figure 7. Electronic band structure of MnTiS_2 Spin up

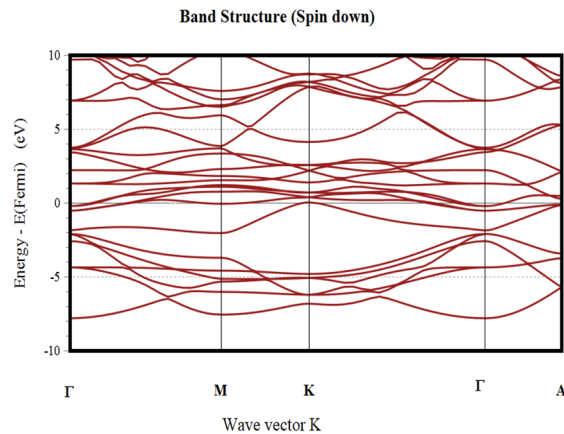


Figure 8. Electronic band structure of MnTiS_2 Spin down

Fig. (9) and (10) shows the electronic band structure with spin up and spin down configuration in the K path of $\Gamma \rightarrow \text{M} \rightarrow \text{K} \rightarrow \Gamma \rightarrow \text{A} \rightarrow \text{L} \rightarrow \text{H} \rightarrow \text{A}$.

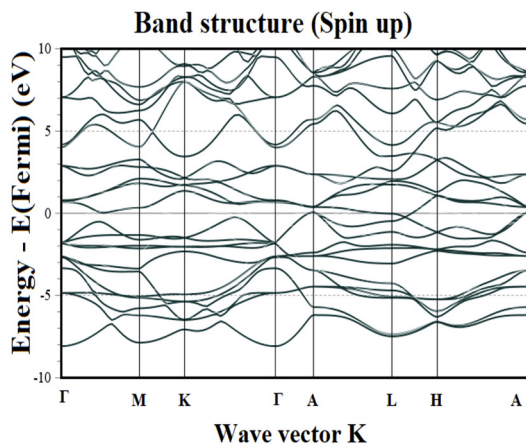


Figure 9. Electronic band structure of FeTiS_2 Spin up

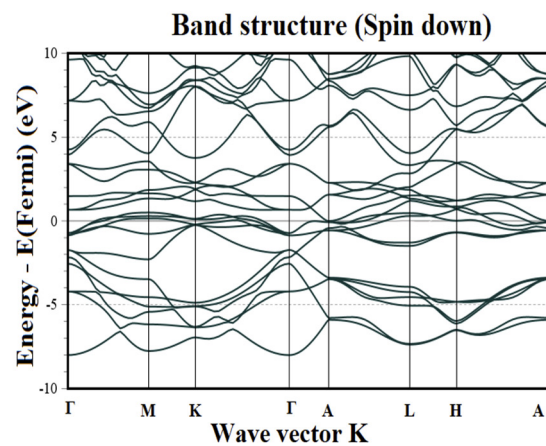


Figure 10. Electronic band structure of FeTiS_2 Spin down

The valance band and the conduction bands are met in the energy range of -5.0 eV to 5.0 eV. In FeTiS₂, the energy band lines are overlapped more than that of CrTiS₂ and MnTiS₂ compounds. From that, we have noted that, FeTiS₂ intercalated compound has a metallic nature. Here also, the band is overlapped maximum at the Fermi level. From the spin up and spin down band structures of FeTiS₂, one can say that, the materials has a ferromagnetic in nature.

Density Of States (DOS)

From the partial or projected DOS, the contributions from the individual orbitals of different materials like s, p, d and f can be checked [19]. We have used here the tetrahedral method for integration over the Brillouin zone to estimate the DOS. Both DOS and PDOS are computed for spin up and spin down configuration.

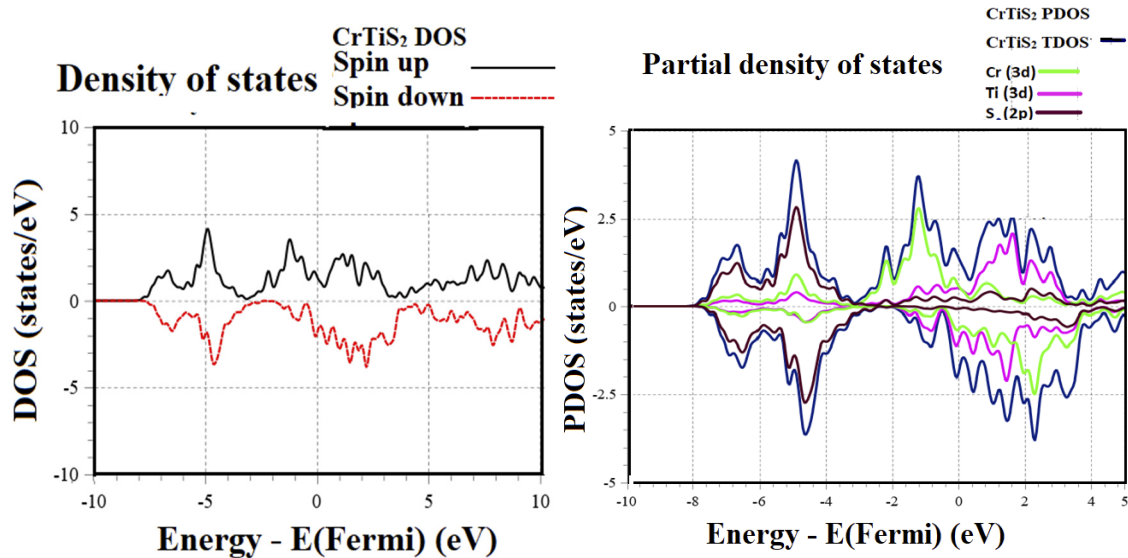


Figure 10. Total DoS of CrTiS₂

Figure 11. Partial DOS of CrTiS₂

The TDOS of CrTiS₂ is shown in Fig. 10. While, Fig. 11 displays the energy contributions from the individual orbitals like s, p, d and f in PDOS for CrTiS₂ compound. It is plotted in the energy range between -10.0 eV to 10.0 eV in both spin up and spin down energy states. In TDOS below the Fermi region, the electron density shows maximum at 6.0 states/eV at a point -5.0 eV in spin up DOS and 3.5 states/eV at a point -4.5 eV in spin down DOS. Above the Fermi region, the electron density maximum at 1.0 states/eV at a point 2.0 eV in spin up and 1.5 eV in spin down DOS. However, the DOS at the Fermi region is 1.5 states/eV. In PDOS of CrTiS₂ is drawn in the states of Cr (3d-state), Ti (3d-state) and S (2p-state), respectively. Such 3d-states are mainly paid attention to the conduction band, while S-2p states are mainly contributed to the valance band. Because of these, the CrTiS₂ is having a metallic compound.

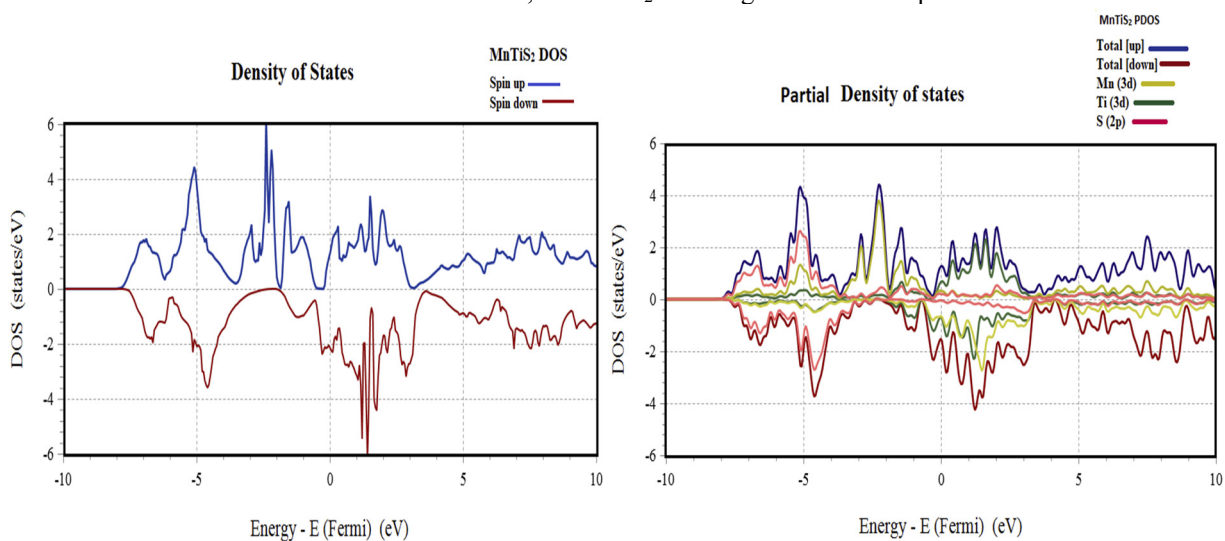


Figure 12. Total DoS of MnTiS₂

Figure 13. Partial DOS of MnTiS₂

Figs. 12 and 13, show the TDOS and PDOS for MnTiS₂ compound, which are plotted in the energy range between -10.0 eV to 10.0 eV in both spin up and spin down energy states. In TDOS below the Fermi region, the electron density shows maximum at 6.0 states/eV at a point -5.0 eV in spin up DOS and 3.5 states/eV at a point -4.5 eV in spin down

DOS. Above the Fermi region, the electron density maximum at 1.0 states/eV at a point 2.0 eV in spin up and 1.5 eV in spin down DOS graphs. The DOS at the Fermi region is shown at a 1.5 states/eV. In PDOS of MnTiS₂ is drawn in the states of 3d-state of Mn, 3d-state of Ti and 2p-state of S, respectively. In PDOS, 3d-states of Mn and Ti are mainly contributed to the conduction band, while 2p-state of S is mainly contributed to the valance band. Hence, the MnTiS₂ is showing a metallic nature.

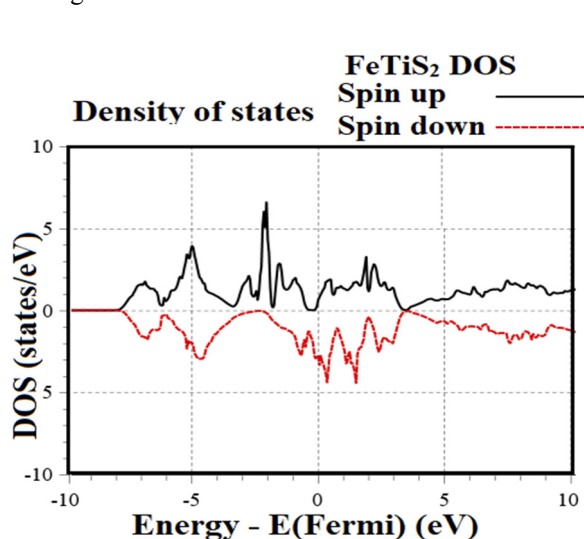


Fig. 14. Total DoS of FeTiS₂

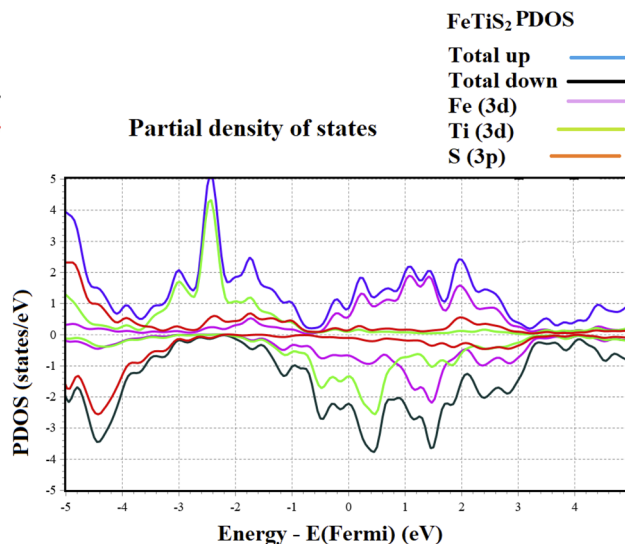


Fig. 15. Partial DOS of FeTiS₂

Figs. 14 and 15, display the TDOS and PDOS for FeTiS₂ compound with spin up and spin down configuration. It is drawn in the energy range between -10.0 eV to 10.0 eV in both spin up and spin down energy states. In TDOS below the Fermi region, the electron density found maximum at 6.0 states/eV at a point -5.0 eV in spin up DOS and 3.5 states/eV at a point -4.5 eV in spin down DOS. While, above the Fermi region, the electron density shown maximum at 1.0 states/eV at a point 2.0 eV in spin up and 1.5 eV in spin down DOS. However, the DOS at the Fermi region is found at 1.5 states/eV. The 3d-states Fe, Ti and 2p-state of such compound is represented in PDOS, in which 3d-states are mainly donated to the conduction band, while 2p state is mainly contributed to the valance band only, which shows a metallic nature.

Above the reference paper, Sharma, Y., Shukla, S., Dwivedi, S., Sharma, R.: Transport properties and electronic structure of intercalated compounds MTiS₂ (M = Cr, Mn and Fe), she says all the materials have same electronic properties. In our research paper calculation, we can say all the material have not same electronic properties. Some changes in energy band lines and density of states shown the above figure.

CONCLUSION

Lastly, we conclude here that, the DFT based simulation is used to compute the structural analysis, electronic properties like electronic band structure, total and projected density of states (TDOS and PDOS) of MTiS₂ (M = Cr, Mn and Fe) intercalated compound using GGA and PBE exchange correlation effects. Whole computations are performed with Quantum Espresso code. From the structural optimization, the guest atom is placed between the interlayer of TiS₂ and shows significant variations in the studied properties. From the electronic band structure data of the all the compounds, it is noticed that the conduction and valance bands are overlapped with each other and shows metallic nature. Also, spin up and spin down natures are easily reported from the band structure data and DOS data of the aforementioned materials. Such type of results is not reported by Sharma et al. [6] earlier. Also, it is observed that, 3d-states of M and Ti atoms are mainly contributed to the conduction band and 2p-state of S atom is mainly contributed to the valance band, respectively. While, metallic nature of FeTiS₂ material is found more than MnTiS₂ and CrTiS₂ compounds. Also, spin polarized configuration with spin up and spin down electronic band structure are observed for aforesaid compounds. It is concluded from that, the CrTiS₂ and MnTiS₂ compounds are having paramagnetic in nature, while FeTiS₂ is having ferromagnetic in nature. According to their such type of properties, the TiS₂ compound is used for making rechargeable lithium batteries and fabrication of photo electronic devices. The prime novelty of this compound is that, it can be easily intercalated by any guest 3d atom.

ACKNOWLEDGMENTS

We sincerely acknowledge the computational facility developed under DST-FIST programme from the Department of Science and Technology, Government of India, New Delhi, India and financial assistance under DRS-SAP-II from University Grants commission, New Delhi, India.

ORCID IDs

 Aditya M. Vora, <https://orcid.org/0000-0002-2520-0266>

REFERENCES

- [1] K. Motizuki, and N. Suzuki, Phys. New Mater., Springer Series in Material Sciences Volume 27, Ed. by F. E. Fujita, 106-138 (1994), https://doi.org/10.1007/978-3-662-00461-6_5.
- [2] N. Suzuki, Y. Yamasaki, K. Motizuki, J. De Physique. Solid State Phys. C. **8**, 49201-49202 (1998), <https://doi.org/10.1051/jphyscol:1988887>.
- [3] Y.-S. Kim, J. Li, I. Tanaka, Y. Koyama, and H. Adachi, Mat. Trans. Jim. **41**(8), 1088-1091 (2000), <https://www.jim.or.jp/journal/e/pdf3/41/08/1088.pdf>
- [4] Q. Bin, Z. Guo-Hua, LI Di, W. Jiang-Long, Q. Xiao-Ying, Z. Zhi, Phys. Lett. **24**, 1050-1053 (2007), <https://doi.org/10.1088/0256-307X/24/4/056>.
- [5] T. Yamasaki, N. Suzuki, K. Motizuki, J. Phys. C: Solid State Phys. **20**, 395-404 (1987), <https://doi.org/10.1088/0022-3719/20/3/010>.
- [6] Y. Sharma, S. Shukla, S. Dwivedi, and R. Sharma, Adv. Mater. Lett. **6**(4), 294-300 (2015). <https://doi.org/10.5185/amlett.2015.5608>.
- [7] R.H. Friend, and A.D. Yoffe, Adv. Phys. **36**, 1-94 (1987), <https://doi.org/10.1080/00018738700101951>.
- [8] J.A. Wilson, and A.D. Yoffe, Adv. Phys. **18**, 193-335 (1969), <https://doi.org/10.1080/00018736900101307>.
- [9] V.B. Zala, A.M. Vora, and P.N. Gajjar, AIP Conf. Proc. 2100, 020027(1)-020027(4) (2019), <https://doi.org/10.1063/1.5098581>.
- [10] H.S. Patel, V.A. Dabhi, A.M. Vora, In: Singh D., Das S., Materny A. (Eds) Advances in Spectroscopy: Molecules to Materials. Springer Proceedings in Physics, **236**, 389-395 (2019), https://doi.org/10.1007/978-981-15-0202-6_30.
- [11] V.A. Dabhi, H.S. Patel, and A.M. Vora, AIP Conf. Proc. 2224 (2020) 030003(1)-030003(4), <https://doi.org/10.1063/5.0000484>.
- [12] H.S. Patel, V.A. Dabhi and A.M. Vora, AIP Conf. Proc. 2224 (2020) 030006(1)-030006(4), <https://doi.org/10.1063/5.0000485>.
- [13] T. Matssushita, S. Suga, and A. Kimuta, Phys. Rev. B. **60**, 1678-1686 (1999), <https://doi.org/10.1103/PhysRevB.60.1678>.
- [14] Y. Ueda, H. Negishi, and M. Koyana, M. Inoue, Solid State Comm. **57**, 839-842 (1986), [https://doi.org/10.1016/0038-1098\(86\)90188-2](https://doi.org/10.1016/0038-1098(86)90188-2).
- [15] J.P. Perdew, J. Chevary, S. Vosko, K. Jackson, M. Perderson, D. Singh, and C. Fiolhais, Phys. Rev. B. **48**, 6671-6687 (1993), DOI: <https://doi.org/10.1103/PhysRevB.46.6671>.
- [16] P. Blaha, K. Schwarz, F. Tran, R. Laskowski, G.K.H. Madsen, and L.D. Marks, WIEN2k. J. Chem. Phys. **152**, 074101(1)-074101(30) (2020), <https://doi.org/10.1063/1.5143061>.
- [17] J.P. Perdew, K. Burke, and M. Ernzerhof, Phys. Rev. Lett. **77**, 3865-3868 (1996), <https://doi.org/10.1103/PhysRevLett.77.3865>.
- [18] <http://www.quantum-espresso.org/pseudopotential>
- [19] P. Giannozzi, S. Baroni, N. Bonini, M. Calandra, R. Car, C. Cavazzoni, D. Ceresoli, G. Chiarotti, M. Cococcioni, I. Dabo, and A. Dal Corso, J. Phys. Condens. Matter, **21**, 395502 (2009), <https://doi.org/10.1088/0953-8984/21/39/395502>.
- [20] W. Kohn, L.J. Sham, Phys. Rev. **140**, A1133-A1138 (1965), DOI: <https://doi.org/10.1103/PhysRev.140.A1133>.
- [21] <http://nisihara.wixsite.com/burai>.
- [22] C.M. Fang, R.A. De Groot, C. Hass, Phys. Rev. B. **56**, 4455-4463 (1997), <https://doi.org/10.1103/PhysRevB.56.4455>.

**ВИВЧЕННЯ СТРУКТУРНИХ І ЕЛЕКТРОННИХ ВЛАСТИВОСТЕЙ ІНТЕРКАЛЬОВАНИХ
ДИХАЛКОГЕНІДНИХ КОМПАУНДІВ ПЕРЕХІДНИХ МЕТАЛІВ MTiS₂ (M = Cr, Mn, Fe)
ЗА ТЕОРІСІЮ ФУНКЦІОНАЛЬНОЇ ЩІЛЬНОСТІ**

Вандана Б. Пармар, Адітья М. Вора

*Фізичний факультет, Університетська школа наук, Університет Гуджарат, Наврангура
Ахмедабад 380009, Гуджарат, Індія*

У цій роботі ми вивчали інтеркальовані дихалкогеніди перехідних металів (TMDC) MTiS₂ (M = Cr, Mn, Fe) за допомогою теорії функціональної щільності (DFT) із узагальненою апроксимацією градієнта (GGA). Ми обчислили структурні та електронні властивості, використовуючи метод першопринципу в обчислювальному коді QUANTUM ESPRESSO з надм'яким псевдопотенціалом. 3d-перехідні метали M (а саме; Cr, Mn, Fe) можуть бути легко інтеркальовані у сполуку чистого дихалкогеніду перехідного металу, як TiS₂. У цій роботі повідомляється про структурну оптимізацію, електронні властивості, такі як: структура забороненої зони, щільність станів (DoS), часткова або прогнозована щільність станів (PDoS) та загальна щільність станів (TDoS). Було виявлено, що структура забороненої зони сполуки MTiS₂ перекриває енергетичні смуги в регіоні Фермі. Ми прийшли до висновку, що інтеркальована сполука TiS₂ має малу заборонену зону, тоді як легувана сполука з 3d-атомом має металеву поведінку, як видно з забороненої зони що перекривається.

КЛЮЧОВІ СЛОВА: теорія функціональної щільності (DFT), дихалкогенідні сполуки перехідних металів (TMDC), узагальнене градієнтне наближення (GGA), квантовий код ESPRESSO, інтеркальований компаунд, надм'який псевдопотенціал.

PACS: 52.75.-d,52.77.-j,52.80.Hc,52.90.+z,82.33.Xj

PLASMA CHEMICAL METHOD OF DECREASING THE ETHYLENE IMPURITIES IN THE AIR

 Leonid M. Zavada[†],  Dmytro V. Kudin^{*}

*Institute of Plasma Electronics and New Acceleration Methods
National Scientific Center "Kharkiv Institute of Physics and Technology" NASU
Kharkiv, 61108, st. Akademicheskaya 1, Ukraine*

**Corresponding Author: kudin@kipt.kharkov.ua*

[†]E-mail: zavadal@kipt.kharkov.ua

tel./fax +38(057)335-61-87

Received December 21, 2020; revised January 18, 2021; accepted February 19, 2021

The efficiency of ethylene impurities decomposition in barrierless plasma-chemical system during artificial injection into the air of a sea container has been studied. The experimental study was performed at the air temperature 5°C in container volume 65 m³. The initial level of ozone in the air was 100 ppb. This concentration is below concentration which audible to humans. It has been established that the use of a carbon filter after a plasma chemical system allows to maintain the ozone content in the air at an acceptable level (in terms of human health and food storage). During 24 hours the ethylene concentration increases until an equilibrium concentration is reached. After the plasma chemical reactor was switched on, the ethylene concentration in the container began to decrease due to decomposition in the low-temperature plasma and interaction with ozone until new equilibrium concentration was reached. The ozone concentration after plasma chemical reactor was switched to begin increased. After 1 hour, the new minimum equilibrium ethylene and ozone concentration was established. The decrease in concentration occurred exponentially and reached a new equilibrium concentration above zero, which is consistent with the theory. The increase in ozone concentration occurs by about 20-25%. It has been shown that using plasma chemical system based on barrierless plasma chemical reactors can reduce the ethylene concentration by up to 10 times, even for low concentrations of ethylene in the air.

KEYWORDS: ethylene, plasma chemistry barrierless reactor.

During storage and transportation of many types of fruits and vegetables there is an increase in the concentration of ethylene due to biochemical reactions [1]. The concentration of ethylene that can be generated in this way during storage of vegetables and fruits varies in a wide range from 1.3-1.5 ppm for tomatoes [2] to 30-40 ppm for eggplants [3] or plums [4]. Increasing the ethylene concentration in the air significantly accelerates the processes of maturation and spoilage [5]. And the task of controlling the level of ethylene is difficult due to low concentrations (1-40 ppm) and large volumes of air to be treated [6]. As shown in [7], low-temperature plasma of barrierless gas discharge can be used to control the content of ethylene in the air of a sea container used for the transportation of fruits and vegetables. In gas discharge atmospheric pressure in air is also generated ozone. For effective use of this method in transportation and storage of vegetables and fruits requires a more detailed study of the efficiency and stability of oxidation of ultra-low concentrations of ethylene by plasma chemical reactors and ozone influence. It should be noted that a significant number of fruits are sensitive to ozone and it can have both positive (mold suppression [8,9]) and negative (spoilage of products and loss of attractive appearance) effect. The air can be purified from ozone with a filter based on carbon or oxide catalysts. However, reducing the filter load and the cost-effectiveness of using a plasma chemical system to oxidize ethylene impurities in air to levels below harmful levels requires a study of the effect of concomitant low ozone concentrations on the efficiency of ethylene oxidation.

EXPERIMENTAL SETUP AND METHODS

The experimental study was performed in a 40-foot sea container with a volume of 65 m³, which was cooled to 5 °C. Figure 1 shows a diagrammatic representation of a container with a plasma chemical system.

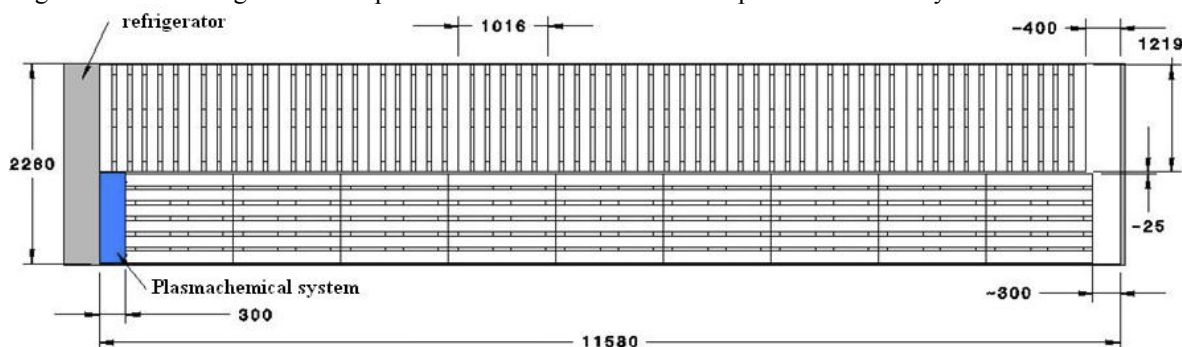


Figure 1. The diagrammatic representation of a container with a plasma chemical system.

The plasma chemical system consisted of two units, each of which included 12 plasma chemical reactors (PCRs) with 10 star-shaped [9] electrodes and a high-voltage power supply unit with a capacity of 285 W each. The photo (Fig. 2) shows a general view of the plasma chemical system.



Figure 2. The photos of plasma chemical system with closed and open outer cover.

The plasma chemical oxidation system of ethylene operated in three modes: standby mode (plasma chemical system off, fans off), ventilation mode (3 fans on), operating mode (plasma chemical system on, 1 or 3 fans on depending on the ozone system setting). The carbon filter consisted of 8 containers. The total weight of activated carbon was 70 kg.

Figure 3 shows the photo of the container with the distribution of sensors for measuring the concentration of ozone and ethylene to determine the uniformity of air treatment in the middle and a photo of the location of the plasma chemical system in the container.



Figure 3. Distribution of sensors inside the container and location of the plasma chemical system.

The ethylene concentration values were averaged for all sensors located in the container. The ethylene was fed into the container from a 40-liter cylinder through a reducer and a control flow meter “Alicat scientific”. The air in the container was forcibly circulated by an external air pump at a rate of 1 l/min. The ethylene and ozone concentrations, as well as air temperature and moisture content were measured by sensors located in the container. The ethylene concentration was measured with an ICA56 meter and monitored by sampling from a circulating line, which was analyzed by a Thermo Scientific “Trace 1310” gas chromatograph with a flame ionization detector. Samples were taken in different control points of the circulation line (in the middle of the container, near the door and at the end, at different heights) with a 1 ml syringe. The chromatograph was pre-calibrated with calibration gas mixtures with ethylene content of 10 and 100 ppm.

RESULTS AND DISCUSSIONS

At the first stage of research the change of ozone concentration in the container depending on time at the maximum power which applied to plasma chemical reactor with system of recirculation of air through the carbon filter is measured (Fig. 4).

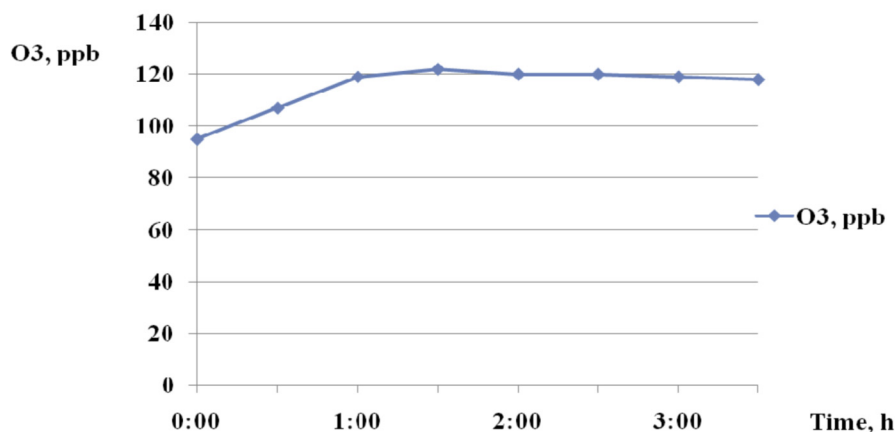


Figure 4. Dependences of ozone concentration inside the container on time. Power 820 W.

The initial level of ozone in the air was higher than 0, but below the concentrations audible to humans. Reaching the maximum value of ozone concentration occurs within 1 hour. The ozone concentration level after switch on plasma chemical reactor increase in occurs by about 20-25%. It is seen that the carbon filter is quite effective in reducing the concentration of ozone, keeping it at a low level.

The concentration of ozone and ethylene in an empty container by artificially filling ethylene at a flow rate of 1 and 4 cm³/min was measured. On Fig. 5 is shown graphs of the dependence of the concentration of ozone and ethylene on time at different flows of C₂H₄ and at the applied power to the plasma chemical reactor 820 W.

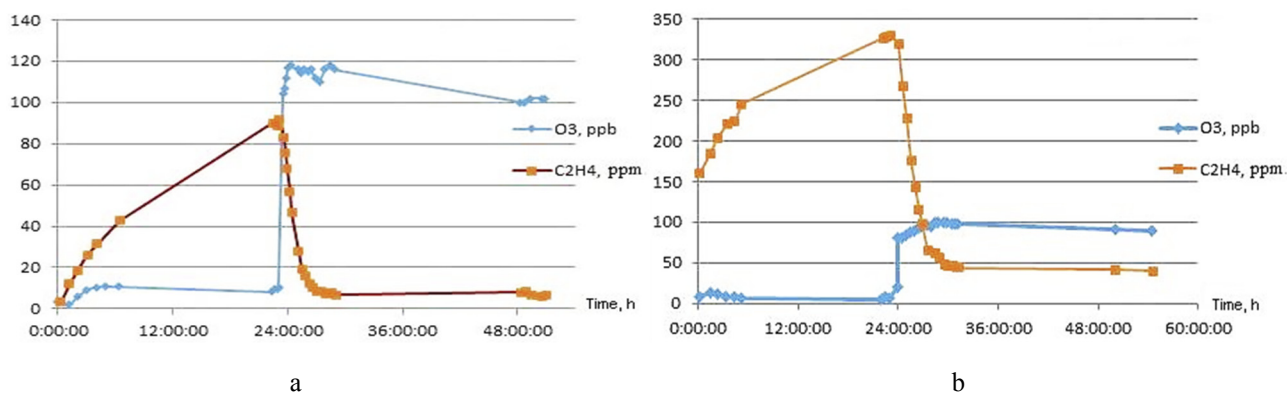


Figure 5. The dependence of ozone and ethylene concentration on the time (a - ethylene flow rate 1 sccm, b - 4 sccm).

The graphs show that the concentration of ethylene initially increases, until an equilibrium concentration is reached in the container (approximately 24 hours). After reaching the equilibrium concentration of ethylene, the plasma chemical reactor was switched on, the ozone concentration in the container began to increase until equilibrium was reached, and the ethylene concentration decreased due to decomposition in the plasma chemical reactor and interaction with ozone. After approximately 1 hour, the minimum equilibrium concentration of ethylene was established, which was determined by the rate of ethylene supply to the container.

To determine the law of decreasing ethylene concentration, the part of the dependence where the significant decrease occurs was considered. The graph (Fig. 6) shows the dependence of the rate of decrease of the reduced concentration of ethylene ($[C_2H_4]/[C_2H_4]_0$) on time at different consumption of ethylene.

It can be seen that the graphs of decline are exponential in nature and agree well with the theoretical calculation.

The dependence of the decrease in the reduced concentration of ethylene on time is analyzed.

$$[C_2H_4]/[C_2H_4]_0 = \exp\{-t/t_0\}, \quad (1)$$

where $[C_2H_4]_0$ - equilibrium concentration C₂H₄ without plasma reactors, t_0 - half-life C₂H₄.

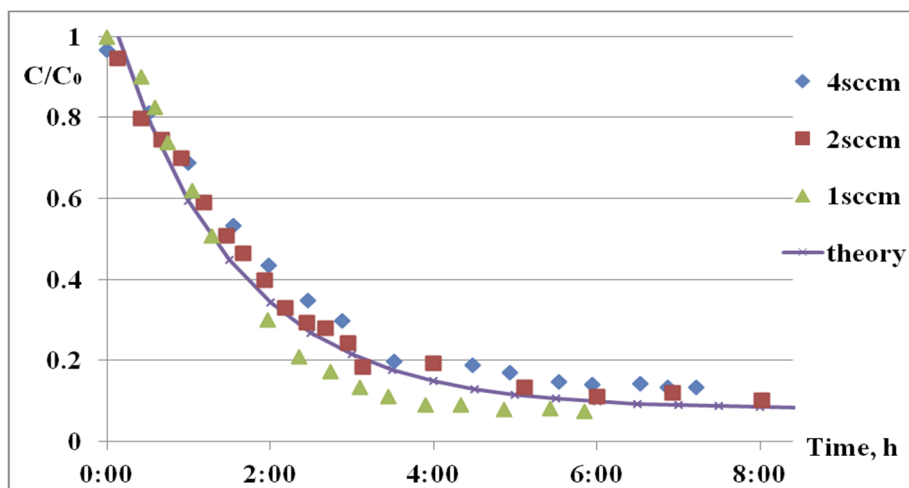


Figure 6. The rate of decrease of ethylene concentration at different injection rates (1-4 sccm).

In Table 2 is shown the data on the maximum (excluding the plasma chemical system) and minimum ethylene content in the sea container at different injection of ethylene.

Table 2. The degree of decomposition of ethylene in the plasma chemical system.

	1 sccm C ₂ H ₄	2 sccm C ₂ H ₄	4 sccm C ₂ H ₄
Applied power, W	800	820	820
O ₃ , ppb	105	115	140
Max C ₂ H ₄ , ppm	7,2	11,2	31,1
Min C ₂ H ₄ , ppm	0.5	1,1	3,8

The table shows that the presence of a plasma chemical system reduces the ethylene content in the container by about 10 times at different injection of ethylene.

The graph (Fig. 7) shows the dependence of the ethylene concentration decrease rate in the container on time at different concentrations of residual ozone (5, 1 and 0 ppm).

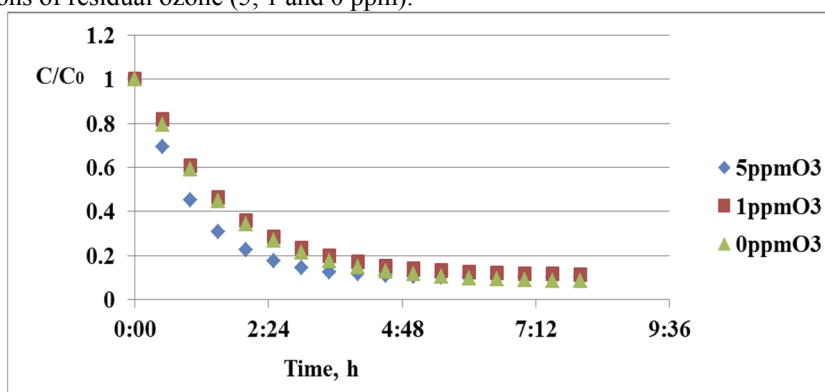


Figure 7. The rate of ethylene concentration decrease after the inclusion of the plasma chemical system at different concentrations of residual ozone.

From the above graphs it is seen that with increasing residual ozone concentration, the rate of decline of ethylene concentration increases, but over time it reaches the same stationary concentration, according to the theory [11].

Table 3 shows the half-life of ethylene at different concentrations of residual ozone.

Table 3. The half-life of ethylene in the container.

O ₃	0 ppm	1 ppm	5ppm
t ₀ , min	91	86	57

The table shows that the presence of residual ozone in the container reduces the half-life of ethylene by 40%. Thus, the presence of a small concentration of residual ozone can accelerate the process ethylene impurities

decomposition with the inclusion of the plasma chemical system. For some vegetables and fruits, the harmful effects of ethylene become noticeable from concentrations much higher than those that can be obtained using the plasma chemical method of ethylene decomposition, so they may have more energy-efficient regimes that reduce either the power applied in the discharge or the plasma chemical system is switched on with some periodicity, which requires additional methodological instructions for the use of the described method in the storage of a specific type of fruit and vegetable products.

CONCLUSIONS

It has been shown that using a plasma chemical system based on barrierless plasma chemical reactors can reduce the ethylene concentration by 10 times or more, even for low concentrations of ethylene in the air. It has been established that the use of a carbon filter after a plasma chemical system allows to maintain the ozone content in the air at an acceptable level (in terms of human health and food storage).

For each type of fruit and vegetable products it is necessary to form methodological guidelines for the use of plasma-chemical method of ethylene oxidation to increase its energy efficiency and economic feasibility.

ORCID IDs

 Leonid M. Zavada, <https://orcid.org/0000-0002-7248-1400>;  Dmytro V. Kudin, <https://orcid.org/0000-0002-6704-1582>

REFERENCES

- [1] A.A. Kolesnik *Factors of long-term storage of fruits and vegetables*, (Gostorgizdat, Moscow, 1959), pp. 356. [in Russian]
- [2] A. Nakatsuka, S. Murachi, H. Okunishi, S. Shiomi, R. Nakano, Y. Kubo, and A. Inaba, *Plant Physiol*, **118**, 1295–1305 (1998), <https://doi.org/10.1104/pp.118.4.1295>.
- [3] A. Concellón, María C. Añón, and A.R. Chaves, *Food Chemistry*, **92**, 63–69 (2005), <https://doi.org/10.1016/j.foodchem.2004.04.048>.
- [4] Li Dong, Susan Lurie, Hong-Wei Zhou, *Postharvest Biology and Technology*, **24**, 135–145 (2002), [https://doi.org/10.1016/S0925-5214\(01\)00130-2](https://doi.org/10.1016/S0925-5214(01)00130-2).
- [5] W. Crocker, A.E. Hitchcock, and P.W. Zimmerman, Similarities in the effects of ethylene and the plant auxins, in: *Contrib. Boyce Thompson Inst.* **7**(3), 1935, pp. 231-248.
- [6] K. Golden, *Asian Journal of Biological Sciences*, **7**(4), 135-143 (2014), <https://doi.org/10.3923/ajbs.2014.135.143>.
- [7] V.I. Golota, D.V. Kudin, O.V. Manuilenko, G.V. Taran, L.M. Zavada, M.O. Yegorov, and V.F. Khmelevskaya, *Problems of Atomic Sci. and Technol. Ser. Plasma Electronics and New Methods of Acceleration*, **4**(116), 160-163 (2018), https://vant.kipt.kharkov.ua/ARTICLE/VANT_2018_4/article_2018_4_160.pdf.
- [8] G.V. Taran, V.A. Breslavets, A.A. Zamuriev, M.O. Yaroshenko, P.O. Opalev, and O.V. Maiboroda, *PAST*, **4**(122), 198-202 (2019), https://vant.kipt.kharkov.ua/ARTICLE/VANT_2019_4/article_2019_4_198.pdf.
- [9] V.I. Golota, G.V. Taran, A.A. Zamuriev, P.O. Opalev, S.G. Pugach, S.N. Mankovskyi, V.P. Petrenkova, and I.N. Nyska, *PAST*, **116**(4), 185-188 (2018), https://vant.kipt.kharkov.ua/ARTICLE/VANT_2018_4/article_2018_4_185.pdf.
- [10] V. Golota, O. Yegorov, V. Mykhaylov, V. Mukhin, G. Taran, and S. Shilo, US Patent No. 6,544,486 B2 (18 April, 2003).
- [11] O.V. Manuilenko, D.V. Kudin, A.Y. Dulphan, V.I. Golota, *PAST*, **116**(4), 139-143 (2018), https://vant.kipt.kharkov.ua/ARTICLE/VANT_2018_4/article_2018_4_139.pdf

ПЛАЗМОХІМІЧНИЙ МЕТОД ЗМЕНШЕННЯ ДОМШКИ ЕТИЛЕНУ У ПОВІТРІ

Завада Л.М., Кудін Д.В

Інститут плазмової електроніки та нових методів прискорення

Національний Науковий Центр "Харківський Фізико-Технічний Інститут», Харків, Україна

Досліджено ефективність окиснення домішки етилену безбар'єрною плазмохімічною системою при штучному ін'єктуванні у повітря морського контейнеру. Експериментальне дослідження проводилось при температурі повітря 5 °C в об'ємі 65 м³. Початковий рівень озону в повітрі становив 100 ppb. Ця концентрація нижча за концентрацію, яка чутна для людей. Таким чином встановлено, що використання вугільного фільтру після плазмохімічної системи дозволяє підтримувати вміст озону у повітрі на припустимому (з точки зору здоров'я людей та зберігання продуктів) рівні. Протягом 24 годин концентрація етилену зростає до досягнення рівноважної концентрації. Після включення плазмохімічного реактора концентрація етилену в контейнері почала зменшуватися через розкладання в низькотемпературній плазмі та взаємодію з озоном до досягнення нової рівноважної концентрації. Концентрація озону після включення плазмохімічного реактора почала зростати. Через 1 годину було встановлено нову мінімальну рівноважну концентрацію етилену та озону. Спадання концентрації відбувалося за експоненціальним законом та досягало нової рівноважної концентрації вище нуля, що відповідає теорії. Збільшення концентрації озону відбувається приблизно на 20-25%. Продемонстровано, що при використанні плазмохімічної системи на базі безбар'єрних плазмохімічних реакторів можливо зниження концентрації етилену до 10 разів навіть для низьких концентрацій етилену у повітрі.

КЛЮЧОВІ СЛОВА: етилен, плазмохімічний безбар'єрний реактор

Алла Таньшина*

До 55-річниці фундації

Інституту теоретичної фізики імені М.М. Боголюбова НАН України

ОЛЕКСІЙ ГРИГОРОВИЧ СИТЕНКО: КЕРМАНИЧ, УЧЕНИЙ, ГРОМАДЯНИН

Академік НАН України Олексій Григорович Ситенко (наукова школа академіка О.І. Ахієзера) збагатив теоретичну ядерну фізику і теорію плазми відкриттям низки ефектів, що нині носять його ім'я. Підґрунтям фундації його наукової школи були 50-ті роки минулого століття, коли він працював у Харківському фізико-технічному інституті та викладав у Харківському державному університеті. Подальшого розвитку його наукова школа набула в Києві. Завдячуючи спогадам його учнів, колег та родини академіка О.Г. Ситенка, викладено життєпис ученого раніш не оприлюдненими фактами про його родовід, дитячі й юнацькі роки, а також реконструйовано витоки його наукових уподобань, чинники формування наукового світогляду, напрями наукової, педагогічної і науково-організаційної діяльності, пріоритетні наукові результати.

КЛЮЧОВІ СЛОВА: наукова школа академіка О.І. Ахієзера, Олексій Григорович Ситенко, ХФТІ, ІТФ ім. М.М. Боголюбова НАН України, Анатолій Глібович Загородній.

Олексій Григорович Ситенко народився 12 лютого 1927 року в селі Нові Млини Батуринського району Чернігівської області [1].

1935 року його батька було призначено інженером на Новокраматорський машинобудівний завод. У Краматорську Олексій пішов до першого класу середньої школи. Навчався охоче, був відмінником.

У молодших класах став постійним відвідувачем міської бібліотеки. Його родина згадує, як у працівників бібліотеки були сумніви: чи насправді цей малюк читає такі серйозні як на його вік книжки, чи можливо просто бере та повертає їх непрочитаними. Почали розпитувати... і були вражені, почувши у відповідь змістовні й обґрунтовані розповіді Олексія щодо прочитаного.

1944 року Олексій блискуче закінчує середню школу та мріє присвятити себе поезії й філософії. Батьки підтримали його бажання продовжити освіту, але, як на їхнє переконання, сину треба було навчитися конкретній справі – здобути спеціальність інженера.

Олексій вагається. Тож спільно з двома друзями-однокурсниками він їде “на розвідку” до Києва. Зруйноване місто справило на нього гнітюче враження. Олексій повертається до рідного Донбасу й вступає до електромеханічного факультету Донецького гірничого інституту.

На початку першого курсу Олексій занедужав: напівголодне життя та застуди призвели до тяжкої хвороби – ревмоендокардиту.

Майже півроку Олексій був прикутий до ліжка. Програму першого курсу він опановував удома самотужки: сестра Галина, яка навчалася тоді в Донецькому медичному інституті, привозила братові необхідні підручники.

Утім, сумніви щодо фаху не полишали його...

Склавши на відмінно іспити за перший курс, він нарешті остаточно усвідомив: його покликання – це фундаментальна наука, а саме фізика.

Олексій вирушає до Харкова, щоб вступити на заочне відділення фізико-математичного факультету Харківського державного університету. Завдяки блискуче складеним іспитам його зараховують одразу ж на другий курс денного відділення.

Закінчивши 1949 року з відзнакою університет, Олексій Ситенко вступає до аспірантури кафедри теоретичної ядерної фізики. Його науковим керівником був призначений Олександр Ілліч Ахієзер (харківський учень Лева Давидовича Ландау; упродовж 1945-1975 рр. – зав. каф. теор. ядерної фізики Харківського державного університету, 1938-1988 рр. – керманіч теоретичного відділу Харківського фізико-технічного інституту).

Після успішного закінчення аспірантури О.Г. Ситенко розпочинає працювати в Харківському фізико-технічному інституті та викладати в Харківському державному університеті. Відтоді й розпочинається стрімке наукове зростання молодого вченого: в 25-річному віці він захистив кандидатську дисертацію, у 32 – вже доктор фізико-математичних наук, а у віці 33 років стає наймолодшим професором Харківського державного університету.

Од 1968 року О.Г. Ситенко – завідувач відділу теорії ядерних реакцій Інституту теоретичної фізики АН УРСР.

1982 року його обирають академіком АН УРСР, а через 6 років він очолив Інститут теоретичної фізики АН УРСР.

Окрім того, Олексій Григорович Ситенко був блискучим педагогом, котрий значну частину свого життя присвятив вихованню наукової зміни.

*Стаття підготовлена до друку за матеріалами докторської дисертації (науковий куратор – академік Віктор Григорович Бар'яхтар)

Майже 10 років він очолював зорганізовану за підтримки академіка АН СРСР М. М. Боголюбова кафедру теорії ядра і елементарних частинок Київського державного університету. Зокрема, 44 учня академіка О. Г. Ситенка стали кандидатами фізико-математичних наук, 21 – докторами. 3-посеред його вихованців – відомі фізики-теоретики України, Росії, Грузії, Узбекистану, В'єтнаму та Китаю.

Наразі маємо можливість оприлюднити маловідомі широкому загалу біографічні факти зі спогадів учнів, колег та родини академіка О. Г. Ситенка.

Академік НАН України, Герой України Віктор Григорович Бар'яхтар: «Олексій Григорович – видатний фізик, справжній інтелігент і патріот України. Свою наукову діяльність розпочав у Харкові за керівництва О. І. Ахієзера. Видатний Вчитель виховав видатного Фізика. Він залучив молодого науковця до дослідження плазми (флуктації у плазмі, комбінаційне розсіювання і трансформація хвиль) та ядерної фізики (дифракційна теорія ядерних процесів)...

За того часу він отримав формулу Ситенка-Глаубера в ядерній фізиці, побудував тензор діелектричної проникності плазми (за співавторства зі К. М. Степановим)...

Ситенко зорганізував у Харкові, а згодом й у Києві наукові школи...

Монографія з фізики плазми (співатори – О.І. Ахієзер, І.О. Ахієзер, О.Г. Ситенко, К.М. Степанов, Р.В. Половін) вважається однією з найкращих книг за цією проблематикою у світі, та, безумовно, найкращою в Україні...» [2].

Зі спогадів старшого сина – Юрія Олексійовича Ситенка, члена-кореспондента НАН України, завідувача відділу теорії ядра і квантової теорії поля Інституту теоретичної фізики імені М. М. Боголюбова НАН України: «Я згадую, як у юнацькі роки запекло дискутував з батьком щодо місця особистості в суспільстві.

Особистість, справжній талант, твердив я, відмежовуються від суспільства, “сірого натовпу”, прагнучи зберегти себе у протистоянні буденщині. Як приклад, наводив філософа Діогена, який жив у бочці. Батько заперечував і наводив інший приклад: Арістотель був царедворцем (вихователем майбутнього імператора Олександра Македонського), і його здобуток до філософії виявився вагомим за Діогена.

Батькова позиція полягала в тому, що справжня особистість прагне найповнішої реалізації своїх здібностей за наявних обставин і не витрачає себе на протистояння тому, чого не подолати. Існують люди, які вбачають сенс життя в боротьбі, існують ті, котрі вбачають сенс у творчості. Батько, безумовно, належав до останніх, але й принципи людської моралі та наукової етики для нього стояли на чільному місці.

Він розповідав мені, як юнаком обирав життєвий шлях. Душа тяжіла до гуманітарної царини (філософії та поезії), але вибір був зроблений на користь точних наук, оскільки в цій галузі (зокрема, в ядерній фізиці, опосередковано пов'язаній зі завданнями оборони держави) можна було зберегти незалежність поглядів і свободу творчості. Саме тому й існує думка, що лави фізиків поповнювалися найбільш обдарованими особистостями і являли собою еліту радянського суспільства. Про це говорив батько, і в цьому я зміг перекопатися сам ще досить давно: од раннього шкільного віку батько з мамою почали брати мене на всесоюзні наукові конференції...

Не спиняючись на здобутках Олексія Григоровича в ядерній фізиці і фізиці плазми, відзначу лише, що для його наукового стилю і методу характерне прагнення досконалості, довершеності. Саме такими якостями відзначаються, зокрема, його численні монографії (17) та підручники.

Мої колеги погодяться зі мною, що часом трапляються наукові книги, цікаві і популярні з-посеред науковців, але які є компіляцією матеріалу: буває, що і формули з помилками, і позначення, і навіть поняття в різних місцях не узгоджені.

Із книг Олексія Григоровича видно, з якою вимогливістю автора до себе і повагою до читача вони написані: формули вивірені, позначення продумані, матеріал викладений зі граничною прозорістю і чіткістю, лаконічно і водночас обгрунтовано. На кожен рядок таких книг можна покладатися як на вірогідний, і тому за своєю бездоганністю, на мою думку, їх слід зарахувати до шедеврів наукової літератури.

Батько згадував, що теоретична фізика була його власним вибором. Однак, як на мою думку, в тому, що він став видатним науковцем, велику роль відіграли його батьки – Григорій Павлович і Парасковія Олексіївна. Це вони зростили його в любові, виховали і навчили не шукати легких шляхів у житті, а наполегливо працювати і обрати собі роботу до душі. Адже справжні фахівці потрібні завжди і будь-якому суспільству.

І ще, як мені здається, батько наслідував нашим козацьким предкам, котрі кожну справу робили старанно, досконало і винахідливо – чи то ставили засіки в степу, чи то майстрували “чайки” на узбережжі, чи то відливали гармати перед походом. І берегли свою честь і гідність за будь-яких обставин» [2].

Зі спогадів дружини академіка – Жанни Григорівни Ситенко: «Вперше я побачила Олексія Григоровича у Харківському державному університеті, де навчалася на фізико-математичному факультеті. У нас викладали вже знані метри науки – академіки О.І. Ахієзер, І. М. Ліфшиць, А.К. Вальтер, блискучий математик В.О. Марченко.

І посеред них – зовсім молодий (32-річний) професор Олексій Григорович Ситенко. Викладацький талант, його виняткова відповідальність робили лекції цікавими і головне – зрозумілими.

Все життя педагогічну діяльність Олексій Григорович поєднував з науковою. Його курси лекцій увійшли до підручників, які й досі вважаються одними з найкращих. Ось уривок з рецензії американський професора

Дж.Л. Хіршвельда на монографію О.Г. Ситенка “Електромагнітні флуктуації у плазмі”: “Ця книга – педагогічний шедевр... Цю монографію настійно рекомендую читачам, запитуючи: де книги, схожі на неї, написані західними фізиками?”.

Професор Київського національного університету імені Т.Г. Шевченка Ю.І. Чутов, перебуваючи в службовому відрядженні в Японії, був приємно вражений, побачивши підручник О.Г. Ситенка в руках японського студента.

Чому Олексій Григорович став саме фізиком, він пояснював так: “Незважаючи на свій потяг до гуманітарних наук, і, зокрема, до українознавства (ще в шкільні роки не менш сильний вплив справила на мене заборонена “Історія українського письменства” Сергія Єфремова), я обрав, навчаючись в Харківському університеті, фізико-математичний факультет. Мені здавалося, що фізика дозволить зберегти внутрішню незалежність і гідність в умовах заполітизованої радянської дійсності...”

Фізика виявилася дуже цікавою наукою. Харківська фізична школа znana в усьому світі. Теоретична фізика полонила мене і я в подальшому присвятив своє життя науковій роботі, зосередившись на проблемах ядерної фізики та фізики плазми”.

Ми прожили з Олексієм Григоровичем тільки 34 роки, але то найкращі роки мого життя. Олексій Григорович був, є і назавжди залишиться для мене і для тих, хто його знав, взірцем освіченості, багатогранності таланту, широти духовного світу.

Будучи талановитою людиною, він не обмежувався тільки наукою, умів радіти життю, особливо любив весняний квітучий сад, музику, літературу, мистецтво.

Найбільша пристрасть його життя – це книги. Олексій Григорович зібрав велику бібліотеку, що яскраво віддзеркалює широке коло його інтересів. Він захоплювався мистецтвом, відвідував художні музеї країн, де перебував, зібрав величезну колекцію альбомів з репродукціями різних митців. Олексій Григорович переймався знаннями з історії, філософії і літератури на щаблі фахівця. Маючи унікальну пам’ять, енциклопедичну обізнаність, щиро ділився своїми знаннями, був цікавим співрозмовником, залишаючись при цьому скромною людиною.

Олексій Григорович не полюбляв пусті розмови, принцип його життя – “Не треба слів, хай буде тільки діло” – стосувався як роботи, так і взаємин у родині.

Мені хочеться підкреслити найголовнішу рису Олексія Григоровича – незламність духу і силу волі.

Смерть його улюбленої донечки Алли у 18-річному віці завдала йому тяжких страждань. І все ж таки він зміг знайти у собі сили продовжувати жити і плідно працювати.

Ці невиліковні рани підірвали здоров’я, Олексій Григорович почав важко хворіти. Однак він ніколи не обговорював свій стан, не скаржився і навіть намагався приховати від мене свої проблеми.

Можна сказати, що в останній рік життя Олексій Григорович виборював у хвороби кожен день. Ці страждання не зламали його волі до життя. Він продовжував працювати, пам’ять залишалася потужною, а розум світлим.

Ще наприкінці січня Олексій провів Вчену раду в Інституті, засідання редколегії “Українського фізичного журналу”, головним редактором якого залишався до останнього дня свого життя.

У ті дні Олексій Григорович показав мені і Григорію свою поетичну спадщину і погодився опублікувати збірку вибраних віршів за назвою “Поетичні округлини”. Згодом цю книгу я видала до роковин смерті Олексія Григоровича за підтримки Інституту теоретичної фізики. Не кожна людина може прожити життя так мужньо і так гідно, як прожив його Олексій Григорович Ситенко.

Кожна людина живе доти, поки її пам’ятають. Олексій Григорович й надалі житиме в спогадах рідних та учнів. Його життя продовжується в підручниках, якими користуються студенти, в статтях, на які посилаються науковці в усьому світі, а також у поезіях, які він встиг залишити» [2].

Зі спогадів чинного директора Інституту теоретичної фізики імені М. М. Боголюбова НАН України – академіка Анатолія Глібовича Загороднього: «Олексій Григорович є, безумовно, одним із тих яскравих представників українських учених, завдяки яким Україна сьогодні сприймається в світі як держава з високим рівнем фундаментальної науки.

Його любили і шанували не лише на теренах України, а й далеко за її межами. Маючи щасливу нагоду супроводжувати Олексія Григоровича в його відрядженнях за кордон, я неодноразово був свідком того, як найавторитетніші вчені зі світовими іменами віддавали йому найвищі почесті й поцінювали його наукові здобутки як такі, що великою мірою визначали рівень розвитку теоретичної ядерної фізики і фізики плазми. Так було у В’єтнамі, Нідерландах, Канаді, Великій Британії, Росії.

Ймовірно, не випадково Олексія Григоровича було обрано до Королівської Шведської академії наук та Угорської академії наук. Це був один з титанів теоретичної фізики, який не лише мав глибокі знання з більшості її розділів, а й сам долучався до творення найсучасніших напрямів цієї науки.

Вихованець харківської школи теоретичної фізики, він завжди пам’ятав про своє наукове коріння, з великою повагою ставився до харківських колег, глибоко шанував вчителя – Олександра Ілліча Ахієзера, який до останніх днів залишався для нього науковим авторитетом і порадником з усіх питань – як наукових, так і життєвих.

З благословення свого Вчителя Олексій Григорович у 1963 році переїздить до Києва, де продовжує розвивати традиції харківської школи. Олексій Григорович ніколи не зупинявся на досягнутому – оволодівав новими методами, продовжував творчий пошук. Можливо, тому його творчості притаманний і дух наукових ідей ще одного патріарха теоретичної фізики – Миколи Миколайовича Боголюбова. Цей дух простежується в багатьох роботах О.Г. Ситенка, і, мабуть, буде правильним вважати його послідовником Боголюбова.

Олексію Григоровичу притаманна широка наукова ерудиція, але найбільше він зробив для теоретичної ядерної фізики і теорії плазми. Внесок його в ці галузі є, без перебільшення, видатним.

Досить згадати теорію взаємодії високоенергетичних частинок з ядрами. Така теорія вкрай необхідна задля отримання інформації про характер ядерної взаємодії та ядерні процеси на основі результатів експериментів з розсіяння окремих частинок (протонів, нейтронів, α -частинок) атомними ядрами. Це єдина можливість здобути нові знання про атомне ядро, особливості його будови та властивості ядерних сил. Саме розроблена Олексієм Григоровичем загальна теорія багаторазового дифракційного розсіяння (теорія, що описує розсіяння частинок з довжиною хвилі Дебройля, значно меншою за розмір ядерної системи, на якій відбувається розсіяння, і враховує взаємний вплив усіх складових системи при розсіянні) сформувала сучасні уявлення про процеси ядерних зіткнень за високих енергій з участю складних частинок. Розвинутий метод застосовується не лише в ядерній фізиці, а й у фізиці елементарних частинок та атомній фізиці

Ця теорія запропонована і розвинута О.Г. Ситенком у 1958 році. Вперше вона була оприлюднена 1959 року в “Українському фізичному журналі”. Одночасно і незалежно аналогічний підхід запропонував Р. Глаубер (США). Дуже швидко дифракційна теорія ядерних процесів знайшла широке визнання і отримала у світовій літературі назву “теорія Ситенка-Глаубера”. І вже понад чотири десятиліття лавина наукових публікацій теоретичного й експериментального характеру з дифракційних ядерних процесів невпинно зростає. Міжнародні конференції з ядерної фізики та фізики елементарних частинок приділяють значну увагу розробці застосуванню теорії Ситенка-Глаубера до найрізноманітніших процесів.

До найвагоміших результатів О.Г. Ситенка з ядерної фізики варто віднести також передбачення ним разом зі своїм учителем академіком О.І. Ахієзером нового фізичного явища – дифракційного розщеплення дейтрона (розпаду високоенергетичного дейтрона на протон і нейтрон під час його розсіяння на ядрах). Цей ефект підтверджено експериментально, зокрема українськими фізиками-ядерниками.

Значне місце в наукових працях О. Г. Ситенка з ядерної фізики посідають дослідження електродинаміки ядер (розділ ядерної фізики, що вивчає взаємодію електронів та інших заряджених частинок з ядрами), відображені в монографії “Електродинаміка ядер” за співавторством О.І. Ахієзера, О.Г. Ситенка та В.К. Тартаковського.

Разом з учнями він розвинув теорію квазіпружного розсіяння високоенергетичних електронів на ядрах, непружного розсіяння і процесів електродезінтеграції (розвал ядра високоенергетичними електронами), інклюзивних процесів з електронами, побудував теорію електророзщеплення малонуклонних систем.

Окремо варто відзначити праці Олексія Григоровича, в яких для квантових частинок різної природи були знайдені точні розв’язки низки задач ядерної фізики. Зокрема, О.Г. Ситенко вперше отримав точний розв’язок проблеми розсіяння протонів на протонах за припущення, що взаємодія задається нелокальним ядерним потенціалом і кулоновим відштовхуванням. Ці точні результати, отримані для модельних систем, є еталоном під час розгляду реалістичних ядерних задач і важливі для розуміння та інтерпретації фізики різноманітних явищ.

Не менш вагомий внесок О.Г. Ситенка і до теоретичної фізики плазми. Як відомо, властивості плазми значною мірою залежать від умов, за яких вона перебуває, зокрема від її стану, що визначається наявністю зовнішніх полів. При цьому важливо якомога точніше описати поведінку плазми, враховуючи тепловий рух електронів й іонів, просторові розподіли густини і температури плазми та нерівноважність їх розподілів за швидкостями (відхилення цих розподілів від рівноважного розподілу Максвелла). Такий опис можна здійснити на основі кінетичних рівнянь – рівнянь для функцій розподілу. О. Г. Ситенко разом з К.М. Степановим виконав піонерські роботи з кінетичної теорії плазми у зовнішньому магнітному полі.

Вперше в кінетичному наближенні було знайдено тензор діелектричної проникності такої плазми, що дозволило сформулювати в найзагальнішому вигляді дисперсійні рівняння для хвиль у магнітоактивній плазмі з урахуванням теплового руху частинок. Це відкрило шлях для опису електродинамічних властивостей такої плазми, зокрема для послідовного опису різноманітних хвиль у магнітоактивній плазмі.

Основоположним є внесок О.Г. Ситенка до розвитку статистичної теорії електромагнітних процесів у плазмоподібних середовищах. Одне з головних завдань тут – дослідження флуктуацій, тобто випадкових відхилень фізичних величин від їх середніх значень, оскільки поведінка флуктуацій пов’язана з електромагнітними і термодинамічними властивостями плазми. Саме таку теорію розвинули О.І. Ахієзер та О.Г. Ситенко.

Зокрема, були розраховані спектри флуктуацій багатьох фізичних величин (густина електронів та іонів, напруженості електричного і магнітного полів, мікроскопічних функцій розподілу частинок), знайдені перерізи розсіяння і трансформації хвиль на флуктуаціях у плазмі та виявлені особливості спектрів розсіяного випромінювання, зумовлені колективними явищами у плазмі. Уперше було передбачено явище комбінаційного

розсіяння хвиль у плазмі. Запропонована О.І. Ахієзером, І.Г. Проходою, О.Г. Ситенком теорія розсіяння хвиль у плазмі (1957 рік) отримала суттєвий розвиток у роботах Олексія Григоровича та його учнів.

Вона стала основою нового перспективного методу діагностики плазми, що широко застосовується для вивчення природної та лабораторної плазми, зокрема експериментального визначення її параметрів. Практично усі наукові публікації за цією тематикою містять посилання на піонерські роботи О.Г. Ситенка або відповідні розділи його монографій.

Чільне місце в науковій діяльності Олексія Григоровича посідають дослідження нелінійної взаємодії хвиль у плазмі та впливу таких взаємодій на флуктуації. Він розрахував нелінійні діелектричні сприйнятливості (як скалярні, так і тензорні) і сформулював нелінійні рівняння для електромагнітних полів та послідовності кореляційних функцій флуктуаційних величин. На основі таких рівнянь досліджено нелінійне насичення критичних флуктуацій у нестійкій плазмі, вивчено процеси резонансної взаємодії хвиль у плазмі. Тим самим були закладені основи теорії флуктуацій у слаботурбулентній плазмі.

Значні результати отримав О.Г. Ситенко і в дослідженні плазми, що перебуває у так званому сильнотурбулентному стані, який характеризується великими енергіями колективних коливань плазми порівняно з тепловою енергією частинок. Ці умови реалізуються, зокрема в установках для керованого термоядерного синтезу. Побудова послідовної теорії флуктуацій у такій плазмі потребує перенормування функцій діелектричного відгуку і кореляційних функцій джерел флуктуацій з урахуванням усіх порядків теорії збурень – на відміну від слаботурбулентної плазми, коли таке перенормування можна здійснити на основі опису нелінійної взаємодії скінченної кількості (трьох, чотирьох) хвиль. З метою побудови цієї теорії О.Г. Ситенко розвинув перенормовану електродинаміку плазми, що дало змогу розрахувати стаціонарні спектри конвективних і дрейфових збуджень у плазмі та дослідити процеси аномального перенесення у турбулентній плазмі з просторово-неоднорідними параметрами.

Наведені результати з теорії плазми аж ніяк не вичерпують наукового доробку Олексія Григоровича за цією галуззю. Їхній перелік можна продовжувати. Це і теорія поляризаційної взаємодії заряджених частинок з плазмою, і флуктуаційний підхід до розрахунку кінетичних коефіцієнтів та інтегралів зіткнень для плазми, і теорія плазмового відлуння, і послідовна кінетична теорія флуктуацій у плазмі зі зіткненнями.

Багато сил і енергії Олексій Григорович віддавав науково-організаційній роботі. Впродовж 1988-2002 років він очолював Інститут теоретичної фізики імені М.М. Боголюбова НАН України, був головним редактором “Українського фізичного журналу”, директором Міжнародного Центру фізики при Відділенні фізики і астрономії НАН України.

За ініціативи О.Г. Ситенка започатковано міжнародні конференції з теорії плазми. Перша та друга конференції відбулися в Києві в Інституті теоретичної фізики ім. М.М. Боголюбова НАН України в 1971 та 1974 роках.

Враховуючи великий успіх цих конференцій, їм було надано назву “Київських”. Починаючи з 1977 року саме за цією назвою міжнародні конференції з теорії плазми проходять в різних країнах світу.

О.Г. Ситенко був одним з ініціаторів Першої міжнародної конференції “Фізика в Україні” (Київ, 1993) та міжнародної боголюбовської конференції “Проблеми теоретичної та математичної фізики” (Москва-Дубна-Київ, 1999).

Розповідь про Олексія Григоровича як науковця не буде повною, якщо хоча б коротко не зупинитися на особливостях його підходу до наукової праці. Передусім – це глибоке розуміння наукової проблеми, яку потрібно розв’язати. По-друге, вибір відповідної, якомога послідовнішої моделі, що допускає точне розв’язання. По-третє, пошук тих граничних випадків, у яких складна теорія стає фізично прозорою і які дають змогу зрозуміти сутність загальних результатів. Можливо, що саме завдяки цим особливостям наукова діяльність Олексія Григоровича була надзвичайно плідною.

Він завжди був відкритий для обговорення будь-яких наукових питань. При цьому наполегливо і аргументовано відстоював свої погляди.

Нове для себе О.Г. Ситенко охоче сприймав, але вимагав обґрунтування не нижчого рівня строгості, аніж його власні аргументи.

Все це робило наукові дискусії з Олексієм Григоровичем надзвичайно корисними і цікавими. Вони були цінними й з огляду знайомства з історією тієї чи іншої наукової проблеми, оскільки впродовж багатьох років він був свідком і особисто причетним до творення сучасної теоретичної фізики. Спілкування з ним було живим спілкуванням з класиком теоретичної фізики, можливістю доторкнутися до історії нашої науки.

О.Г. Ситенко – яскрава, всебічно обдарована особистість. Він був великим знавцем української та світової культури, широко обізнаним в літературній класиці – від стародавньої до новітньої. Глибоко розумівся на живописі, архітектурі. Його знанням з української та всесвітньої історії могли позаздрити фахівці. Це була світла і надзвичайно талановита особистість, прекрасна і добра людина» [2].

Згадає ще один учень Олексія Григоровича Ситенка – Іван Васильович Сименюк, доктор фізико-математичних наук, завідувач відділу прикладних проблем теоретичної фізики Інституту теоретичної фізики імені М.М. Боголюбова НАН України: «Олексій Григорович був цілісною особистістю з унікально широким

кругозором і високою культурою. Я майже не знаю науковців (природознавчого напрямку) такого щабля, які були б такою мірою вірними своєму народові.

Олексій Григорович ґрунтовно переймався українською мовою. Інколи це дивувало навіть близьких до нього людей. Для мене все стало зрозумілим, коли ми дізналися у день прощання з Олексієм Григоровичем, що він усе життя писав вірші й був у цьому неймовірно вимогливим до себе.

Наразі ми усвідомлюємо, що Олексій Григорович був не тільки корифеєм у теоретичній фізиці, а й непересічним українським поетом, знавцем української і всесвітньої історії, глибоким поціновувачем світового образотворчого мистецтва. Душу Олексія Григоровича завжди зігрівали думки, що обраний науковий шлях і незавершені наукові задуми продовжує його старший син Юрій.

Широта світогляду О.Г. Ситенка виявилась і в тому, що він усіляко заохочував сина до роботи на передньому краї сучасної фізики – квантовій теорії поля і теорії елементарних частинок, хоча безпосередні інтереси Олексія Григоровича і не належали до цієї площини.

Людиною з великої літери, порядною і принциповою, щедро обдарованою талантами, – таким запам'ятали О.Г. Ситенка його сучасники» [2].

Наукові надбання О.Г. Ситенка було поціновано як вітчизняною, так і міжнародною науковою спільнотою. Зокрема, академік Національної академії наук України Олексій Григорович Ситенко – лауреат премії імені К.Д. Синельникова НАН України, Державної премії України в галузі науки і техніки [4], премії імені М. М. Боголюбова НАН України та міжнародної премії імені Вальтера Тіррінга (Австрія).

Окрім того, він був обраний почесним іноземним членом Королівської Шведської академії наук (1991), Української Могиллянсько-Мазепинської Академії наук (Канада, 1992), Угорської Академії наук та Нью-Йоркської Академії наук (1998).

Олексій Григорович входив до складу Українського та Американського фізичних товариств, а також був членом-кореспондентом Міжнародного радіосоюзу.

Од 1991 року О.Г. Ситенко – директор Міжнародного центру фізики при Відділенні фізики і астрономії Національної академії наук України, а впродовж 1991-1995 років – голова Київського фізичного товариства.

Вчений нагороджений орденами Трудового Червоного Прапора (1977) і Дружби народів (1987).

1997 року Олексію Григоровичу Ситенку Указом Президента України за значний особистий внесок у розвиток науки і створення національних наукових шкіл присвоєно почесне звання «Заслужений діяч науки і техніки» [3].

2000 року постановою Президії Академії наук вищої школи України його відзначено нагородою Ярослава Мудрого за вагомі досягнення в галузі науки і техніки.

2002 року Верховна Рада України нагородила академіка О.Г. Ситенка Почесною Грамотою – за особливі заслуги перед українським народом. Цю звістку він одержав у лікарні, за лічені години до смерті.

Останні роки свого життя Олексій Григорович Ситенко важко хворів. Утім, його не залишали учні та колеги: біля ліжка хворого обговорювали різноманітні питання науки, мистецтва, політики.

Коли хвороба трохи відступала, Олексій Григорович переймався науковими вишукуваннями. Від неймовірних фізичних і моральних страждань рятувала й поезія: після тривалої перерви він знов розпочав писати вірші.

Олексій Григорович Ситенко пішов зі життя 11 лютого 2002 року, за день до свого 75-річчя [1].

REFERENCES

- [1] https://uk.wikipedia.org/wiki/%D0%A1%D0%B8%D1%82%D0%B5%D0%BD%D0%BA%D0%BE_%D0%9E%D0%BB%D0%B5%D0%BA%D1%81%D1%96%D0%B9_%D0%93%D1%80%D0%B8%D0%B3%D0%BE%D1%80%D0%BE%D0%B2%D0%B8%D1%87.
- [2] А.М. Tanshyna, D.Sci. Thesis, Історія становлення і розвитку теоретичних досліджень в УФТІ – ХФТІ – ННЦ «ХФТІ», Центр досліджень науково-технічного потенціалу та історії науки імені Г.М. Доброва НАН України [Center for Research of Scientific and Technical Potential and History of Science named after G.M. Dobrova NAS of Ukraine, Kyiv.
- [3] <https://zakon.rada.gov.ua/laws/show/168/96#Text>
- [4] <https://zakon.rada.gov.ua/laws/show/611/92>

OLEKSIY HRYHOROVYCH SYTENKO: MANAGER, SCIENTIST, CITIZEN

Alla Tanshyna

NSC "Kharkiv Institute of Physics & Technology" NASU, Kharkiv, 61108, st. Akademicheskaya 1, Ukraine

Academician of the National Academy of Sciences of Ukraine Oleksiy Hryhorovych Sytenko (Scientific School of Academician O.I. Akhiezer) enriched theoretical nuclear physics and plasma theory by discovering a number of effects that now bear his name. The base of the foundation of his scientific school was the 50-th of the last century, when he worked at the Kharkiv Institute of Physics and Technology and taught at Kharkiv State University. His scientific school was further developed in Kyiv. Thanks to the memories of his students, colleagues and family of Academician O.G. Sitenko, the biography of the scientist with previously unpublished facts about his pedigree, childhood and adolescence, as well as reconstructed the origins of his scientific preferences, factors shaping the scientific worldview, areas of scientific, pedagogical and scientific-organizational activities, priority scientific results.

KEYWORDS: scientific school of Academician O.I. Akhiezer, Oleksiy Hryhorovych Sytenko, KIPT, M.M. Bogolyubov ITF NAS of Ukraine, Anatoliy Hlibovych Zagorodniy



УДК 53.01

П 78

Серія «Проблемы теоретической и математической физики. Научные труды»

під загальною редакцією академіка А. Г. Загороднього, академіка М Ф. Шульги

Рецензенты:

академік НАН України **Бакай О. С.**;

академік НАН України **Семиноженко В. П.**

Проблемы теоретичної фізики. Наукові праці. Випуск 3 / Ю. Л. Болотін, В. С. Захаров, В. І. Карась, В. М. Куклін, Е. А. Пашицький, В. І. Пентегов, В. І. Соколенко, А. В. Тур, А. А. Туркін, В. В. Яновський; під загальною редакцією А. Г. Загороднього, М. Ф. Шульги, ред. вип. В. В. Яновський. – Х. : ХНУ імені В. Н. Каразіна, 2019. – Вип. 3. – 398 с. (Сер. «Проблемы теоретичної і математичної фізики».)

ISBN 978-966-285-594-4

Обговорюється нерівноважна кінетика електрон-фононої підсистеми кристала при наявності змінних електричних і магнітних полів. Розглянуто результати досліджень кінетики фазових перетворень і стабільності фаз у опромінених сплавах.

Обговорюються механізми виникнення скалярних полів і

формування просторово неоднорідною великомасштабної структури сучасного Всесвіту, а також походження «темної енергії» і «темної матерії». Розглянута фізика планківських масштабів і гранично досяжні величини в нашому Всесвіті. Обговорюється розвиток модуляційної нестійкості інтенсивних періодичних структур у хвильових і нехвильових середовищах.

Для вчених в області природознавства, викладачів, аспірантів і студентів старших курсів фізичних факультетів.

<http://dspace.univer.kharkov.ua/handle/123456789/15830>

УДК 53.01

ISBN 978-966-285-594-4 (вып. 3)

© Национальная академия наук Украины, 2019

© Харьковский национальный университет имени В. Н. Каразина, 2019

© Ю. Л. Болотін, В. С. Захаров, В. І. Карась, В. М. Куклін, Е. А. Пашицький, В. І. Пентегов, В. І. Соколенко, А. В. Тур, А. А. Туркін, В. В. Яновський, 2019

© Дончик І. М., макет обкладинки, 2019

PACS: specify PACS code(s) here

INSTRUCTIONS FOR PREPARING MANUSCRIPT IN EAST EUROPEAN JOURNAL OF PHYSICS

Nikita F. Author^{a,*}, Peter V. Co-author(s)^{b,†}

^aAffiliation of first author

^bAffiliation of second author (if different from first Authors)

*Corresponding Author: corresponding_authors@mail.com, ^aORCID ID

[†]E-mail: co_authors@mail.com, ^bORCID ID

Received October 25, 2020; revised November 25, 2020 accepted December 5, 2020

Each paper must begin with an abstract. The abstract should be typed in the same manner as the body text (see below). Please note that these Instructions are typed just like the manuscripts should be. The abstract must have at least **1800 phonetic symbols**, supplying general information about the achievements, and objectives of the paper, experimental technique, methods applied, significant results and conclusions. Page layout: the text should be printed on the paper **A4** format, at least **5 pages**, with margins of: **Top - 3, Bottom, Left and Right - 2 cm**. The abstract, keywords should be presented in **English** (only for foreign authors), and **Ukrainian**.

KEYWORDS: there, must, be, 5-10 keywords

This is introduction section. This paper contains instructions for preparing the manuscripts. The text should be prepared in “**doc**” or “**docx**” format.

INSTRUCTIONS

The text should be typed as follows:

- **title:** Times New Roman, 12 pt, ALL CAPS, bold, 1 spacing, centred;
- **authors:** name, initials and family names; Times New Roman, 12 pt, bold, 1 spacing, centred;
- **affiliation(s):** Times New Roman, 9 pt, italic, 1 spacing, centred;
- **abstract:** Times New Roman, 9 pt, 1 spacing, justified;
- **body text:** Times New Roman, 10 pt, 1 spacing, justified; paragraphs in sections should be indented right (tabulated) for 0.75 cm;
- **section titles:** Times New Roman, 10 pt, bold, 1 spacing, centred, without numbering, one line should be left, blank above section title;
- **subsection titles:** Times New Roman, 10 pt, bold, 1 spacing, centred, without numbering in accordance to the section (see below), one line should be left blank above subsection title;
- **figure captions:** width of the figure should be 85 or 170 mm, Figures should be numbered (**Figure 1.**) and titled below Figures using sentence format, Times New Roman, 9 pt, 1 spacing, centred (if one line) or justified (if more than one line); one line should be left blank below figure captions;
- **table captions:** width of the table should be 85 or 170 mm, tables should be numbered (**Table 1.**) and titled above tables using sentence format, Times New Roman, 10 pt, 1 spacing, justified, Tables should be formatted with a single-line box around the outside border and single ruling lines between rows and columns; one line should be left blank below tables;
- **equations:** place equations centred, numbered in Arabic (1), flush right, equations should be specially prepared in **MathType** or “**Microsoft Equation**” one line should be left blank below and above equation.

Additional instructions

Numerated figures and tables should be embedded in your text and placed after they are cited. Only sharp photographs and drawings are acceptable. Letters in the figures should be 3 mm high. The figures should be presented in one of the following graphic formats: jpg, gif, pcx, bmp, tif.

REFERENCES

Cite references in AIP style (<https://guides.lib.monash.edu/citing-referencing/aip>). Numbering in the order of referring in the text, e.g. [1], [2-5], etc. References should be listed in numerical order of citation in the text at the end of the paper (justified), Times New Roman, 9 pt, 1 spacing.

Journal Articles

- [1] T. Mikolajick, C. Dehm, W. Hartner, I. Kasko, M.J. Kastner, N. Nagel, M. Moert, and C. Mazure, *Microelectron. Reliab.* **41**, 947-950 (2001), [https://doi.org/10.1016/S0026-2714\(01\)00049-X](https://doi.org/10.1016/S0026-2714(01)00049-X).
- [2] S. Bushkova, B.K. Ostafiychuk, and O.V. Copenaiev, *Physics and Chemistry of Solid State.* **15**(1), 182-185 (2014), <http://page.if.ua/uploads/pccs/vol15/11501-27.pdf>. (in Ukrainian)
- [3] M. Yoshimura, E. Nakai, K. Tomioka, and T. Fukui, *Appl. Phys. Lett.* **103**, 243111 (2013), <http://dx.doi.org/10.7567/APEX.6.052301>.

E-print Resources with Collaboration Research or Preprint

- [4] M. Aaboud et al. (ATLAS Collaboration), *Eur. Phys. J. C*, **77**, 531 (2017), <http://dx.doi.org/10.1140/epjc/s10052-017-5061-9>
- [5] Sjöstrand et al., *Comput. Phys. Commun.* **191**, 159-177 (2015), <https://doi.org/10.1016/j.cpc.2015.01.024>.
- [6] Boudreau, C. Escobar, J. Mueller, K. Sapp, and J. Su, (2013), <http://arxiv.org/abs/1304.5639>.

Books

- [7] S. Inoue, and K.R. Spring, *Video Microscopy: The fundamentals*, 2nd ed. (Plenum, New York, 1997), pp. 19-24.
- [8] I. Gonsky, T.P. Maksymchuk, and M.I. Kalinsky, *Біохімія Людини [Biochemistry of Man]*, (Ukrmedknyga, Ternopil, 2002), pp. 16. (in Ukrainian)

Edited Books

- [9] Z.C. Feng, editor, *Handbook of Zinc Oxide and Related Materials: Devices and Nano Engineering, vol. 2*, (CRC Press/Taylor & Francis, Boca Raton, FL, 2012)

Book Chapters

- [10] P. Blaha, K. Schwarz, G.K.H. Madsen, D. Kvasnicka, and J. Luitz, in: *WIEN2K, An Augmented Plane Wave Plus Local Orbitals Program for Calculating Crystal Properties*, edited by K. Schwarz (Techn. Universität Wien, Austria, 2001).
- [11] M. Gonzalez-Leal, P. Krecmer, J. Prokop, and S.R. Elliot, in: *Photo-Induced Metastability in Amorphous Semiconductors*, edited by A.V. Kolobov (Wiley-VCH, Weinheim, 2003), pp. 338-340.
- [12] A. Kochelap, and S.I. Pekar, in: *Теорія Спонтанної у Стимульованій Хемілюмінесценції Газів [Theory of Spontaneous and Stimulated Gas Chemiluminescence]* (Naukova dumka, Kyiv, 1986), pp. 16-29. (in Russian)

Conference or Symposium Proceedings

- [13] C. Yaakov, and R. Huque, in: *Second International Telecommunications Energy Symposium Proceedings*, edited by E. Yow (IEEE, New York, 1996), pp. 17-27.
- [14] V. Nikolsky, A.K. Sandler, and M.S. Stetsenko, in: *Автоматика-2004: Матеріали 11 Міжнародної Конференції по Автоматичному Управлінню [Automation-2004: Materials of the 11th International Conference on Automated Management]* (NUHT, Kyiv, 2004), pp. 46-48. (in Ukrainian)

Patent

- [15] I.M. Vikulin, V.I. Irha, and M.I. Panfilov, Patent Ukraine No. 26020 (27 August 2007). (in Ukrainian)

Thesis / Dissertation

- [16] R.E. Teodorescu, Ph.D. dissertation, The George Washington University, 2009.

Special Notes

1. Use International System of Units (SI system). 2. It is undesirable to use acronyms in the titles. Please define the acronym on its first use in the paper. 3. Refer to isotopes as ¹⁴C, ³H, ⁶⁰Co, etc.

Наукове видання

СХІДНО-ЄВРОПЕЙСЬКИЙ ФІЗИЧНИЙ ЖУРНАЛ

Номер 1, 2021

EAST EUROPEAN JOURNAL OF PHYSICS

No 1, 2021

Збірник наукових праць
англійською та українською мовами

Коректор – Коваленко Т.О.
Технічний редактор – Гірник С.А.
Комп'ютерне верстання – Гірник С.А.

Підписано до друку 22.02.2021. Формат 60×84/8. Папір офсетний.

Друк цифровий.

Ум. друк. арк. 9,6. Обл.-вид. арк. 9,9

Тираж 50 пр. Зам. № . Ціна договірна

Видавець і виготовлювач

Харківський національний університет імені В.Н. Каразіна

61022, Харків, майдан Свободи, 4

Свідоцтво суб'єкта видавничої справи ДК № 3367 від 13.01.09

Видавництво Харківський національний університет імені В.Н. Каразіна
тел. +380-057-705-24-32